Conception et modélisation de circuits monolithiques à diode Schottky sur substrat GaAs aux longueurs d'onde millimétriques et submillimétriques pour des récepteurs hétérodynes multi-pixels embarqués sur satellites et dédiés à l'aéronomie ou la planétologie.

Hui Wang

THESE DE DOCTORAT
DE L'UNIVERSITE PIERRE ET MARIE CURIE

Spécialité: Méthodes Instrumentales en Astrophysique et leurs Applications Spatiales

(Ecole Doctorale Astronomie et Astrophysique d'île-de-France)

Présentée par

Hui WANG

Pour obtenir le grade de DOCTEUR de l'UNIVERSITÉ PIERRE ET MARIE CURIE

Conception et modélisation de circuits monolithiques à diode Schottky sur substrat GaAs aux longueurs d'onde millimétriques et submillimétriques pour des récepteurs hétérodynes multi-pixels embarqués sur satellites et dédiés à l'aéronomie ou la planétologie.

Soutenue le 7 Mai 2009 devant le jury composé de:

Mr. Aziz BENLARBI DELAI	Président
Mr. Imran MEHDI	Rapporteur
Mr. Didier LIPPENS	Rapporteur
Mr. Gérard BEAUDIN	Directeur de thèse
Mr. Alain MAESTRINI	Codirecteur de thèse
Mr. Philippe GOY	Examinateur
Mr. Jean-Marc GOUTOULE	Examinateur
Mr. François MATTIOCCO	Examinateur

Thèse préparée au Laboratoire d'Etude du Rayonnement de la Matière en Astrophysique – Observatoire de Paris

Summary

This research work proposes a novel approach and topology of a compact two-pixel heterodyne integrated receiver front-end working at room temperature dedicated to planetary and atmospheric sciences. Large arrays of millimeter and submillimeter wave heterodyne Schottky diode-based receivers can offer higher mapping speed and mapping consistency while avoiding the use of cryogenic receivers in planetary and atmospheric sciences.

To reduce the size, the weight and the power consumption of a multi-pixel receiver it is necessary to optimize the interface between the mixers and the local oscillator (LO) unit. Only highly integrated components make building large array heterodyne receivers possible. One solution consists in integrating in the same mechanical block a frequency multiplier and one or several mixers to create a compact sub-array. We studied a configuration featuring one single solid state LO source pumps two 183GHz mixers simultaneously by using an in phase waveguide power divider. The mixers and the frequency multiplier are integrated in a same waveguide block to reduce the extra LO losses. However, the mixer chip and the frequency multiplier were both optimized independently for two stand-alone circuits.

The 183GHz Monolithic Microwave Integrated Circuit (MMIC) subharmonic mixer and the 30/90GHz frequency tripler that integrated in the two-pixel receiver front-end have been fabricated and measured respectively. The mixer circuits have been fabricated with three different European Schottky diode processes. The best measured DSB mixer noise temperature of the single 183GHz subharmonic mixer was 793K at 161GHz. Maximum efficiency of 5% and more than 1mW output power has been measured over the band 80-95GHz for the 30/90GHz tripler. The two-pixel integrated receiver has been optimized with a predicted result of DSB mixer noise temperature of 750K at 183GHz for single pixel.

This is the first published demonstration of a multi-pixel heterodyne receiver working at room temperature with integrated LO source in a same block; this compact topology could be applied for higher frequency and extended linearly for larger array heterodyne receiver.

Résumé

Ce travail de recherche propose une nouvelle approche et la topologie d'un récepteur hétérodyne en ondes millimétrique intégré à deux pixels fonctionnant à la température ambiante, dédié aux sciences planétaire et de l'atmosphère. Des récepteurs hétérodynes multi pixels à diode Schottky aux longueurs d'onde millimétriques et submillimétriques peuvent permettre une cartographie plus rapide et plus cohérente tout en évitant d'utiliser des systèmes cryogéniques.

Pour réduire la taille, le poids et la consommation électrique d'un récepteur à multi pixels, il est nécessaire d'optimiser l'interface entre les mélangeurs et l'oscillateur local. Seulement des microcomposants intégrés permettent de construire des récepteurs hétérodynes à grand nombre de pixels. Une solution consiste à intégrer un multiplicateur de fréquence et un ou plusieurs mélangeurs dans une même structure et créer une sous-unité compacte. Dans notre configuration, une seule source d'oscillateur local pompe deux mélangeurs simultanément en utilisant un diviseur de puissance en guide d'onde. Les mélangeurs et le multiplicateur de fréquence sont intégrés dans une même structure en guide d'ondes afin de réduire les pertes supplémentaires. En outre, le mélangeur et le multiplicateur de fréquence ont tous été optimisés de façon indépendante pour deux circuits indépendants.

Le mélangeur subharmonique monolithique à 183GHz et le tripleur à 30/90GHz intégrés dans le récepteur à deux pixels ont été fabriqués et mesurés. Le chip du mélangeur a été réalisé en utilisant trois différents procédés de fabrication de diodes Schottky européennes et dont la meilleur température de bruit de 793K DSB a été mesurée à 161GHz. Un maximum d'efficacité de 5% et plus de 1mW de puissance couvrant la bande 80-95GHz ont été mesurés pour le tripleur. Le récepteur intégré à deux pixels a été optimisé et une température de bruit du mélangeur de 750K DSB a été prédite par simulation.

Ce sera la première démonstration de récepteur hétérodyne à multi-pixels intégrant la chaine oscillateur local dans une structure, cette topologie compacte peut être appliquée aux plus hautes fréquences et étendue linéairement pour des récepteurs aux plus grand nombre pixels.

Acknowledgements

Thanks are also due to Dr. David Matheson of Millimetre Wave Technology Group at Rutherford Appleton Laboratory (RAL) in UK, his kindness invitation for me to work during two months in his group. I wish to thank all other members of the group for their enthusiasms made me feel like members of their group, and specially thank to Dr. Byron Alderman for teaching me the basics of micro-assembly operation and his assistance throughout my PhD period.

I am grateful to other members of our group at LERMA who are not only great collaborators but also provide enjoyable atmosphere: Dr. Yan Delorme, Miss. Jeanne Treuttel, Miss. Cécile Jung, Mr. Jean-Michel Krieg, Dr. Maurice Gheudin, Mr. Alexandre Féret, Dr. Rolant Lefevre, Mr. Frédéric Dauplay, Mr. Benoît Lecomte, Dr. Faouzi Boussaha, Dr. Jean-Marie Munier, Ms. Michèle Ba-Trung. With them I shared useful discussions and found an invaluable assistance. Thanks are also due to Mr. Patrice Landry and Ms. Marie-Claude Lemonnier for providing technical documentations. I would also like to thank other members of LERMA, specially, Dr. François Viallefond, Mr. Michel Caillat, Dr. Alain Coulais, and Dr. Frédéric Boone. I enjoyed many conversations we had over lunchtime and thanks for your daily encouragements during last years.

I would also like to thank Ms. Annick Gassais, Ms. Chantal Levivier, Mr. Laurent Girot and Ms. Valérie Audon who made so many and so often-incredible efforts to help me for my administration work.

Finally, I would like to thank my parents for all of their love and support since I was born. Thanks to all of my family and friends who I haven't mentioned. Without their encouragements and supports, I couldn't have done it.

Table of Contents

Purpose of the work

The purpose of this thesis is to study and design monolithic Schottky diode-based circuits for large arrays of heterodyne receivers working at millimeter and submillimeter wavelength dedicated to planetary and atmospheric sciences.

In planetary and atmospheric sciences large arrays of millimeter and submillimeter wave heterodyne Schottky diode-based receivers can offer higher mapping speed and mapping consistency while avoiding the use of cryogenic receivers. To reduce the size, the weight and the power consumption of a multi-pixel receiver it is necessary to optimize the interface between the mixers and the local oscillator unit. Only highly integration components make building large array heterodyne receivers possible.

My research has included designing three millimeter wave MMIC Schottky diode-based circuits: a 183GHz MMIC subharmonic mixer, a 30/90GHz MMIC frequency tripler, and a two-pixel integrated heterodyne Schottky diode receiver front-end at 183GHz. Novel techniques intended to improve further the performance of receivers or to provide new ways for receiver circuit implementation have been studied.

One solution consists in integrating in the same mechanical block a frequency multiplier and one or several mixers to create a compact sub-array. A novel approach of designing a multi-pixel heterodyne receiver is demonstrated in this thesis. In our configuration, one single solid state LO source pump two mixers simultaneously by using a waveguide power divider. In addition, the mixers and the frequency multiplier are integrated in a same waveguide block. However, they were both optimized independently for two stand-alone circuits.

All the circuits have been fabricated thanks to a research project financed by ESA (European Space Agency) and CNES (Centre National D'Etudes Spatiales) to study the possibilities of developing Schottky MMICs (Monolithic Microwave Integrated Circuit) for high frequencies based on the European industrial process from UMS (United Monolithic Semiconductors). These developments are dedicated for future airborne and space borne atmospheric limb sounding instruments in planetary and atmospheric applications.

Thesis structure

The work presented in this thesis relates to the study and design of three millimeter-wave circuits using commercial foundry planar Schottky diodes from UMS. During this research work, a fixed-tuned broadband subharmonic mixer working at 183 GHz and a MMIC frequency tripler working at 90 GHz were designed, fabricated and measured respectively. Further study based on these two circuits has been accomplished on the development of a novel two-pixel integrated heterodyne receiver front-end. New topology has been analyzed with predicted results.

Before going deep into the details of the work that was carried out, the contents of this manuscript are summarized here.

Chapter 1 gives a general review of the state-of-the-art millimeter and submillimeter wavelength heterodyne techniques, the development of large array heterodyne receiver and general description of the Schottky diode technology.

In the second chapter, three circuits designed within this thesis are discussed individually, including the knowledge necessary to approach each design, simulation results, measured results and the comparison between simulated and measured results. The 183 GHz MMIC subharmonic mixer chip that designed for UMS diodes has been fabricated with two other different Schottky diode processes from the University of Bath and the RAL, the mixer shares the same circuit layout and mechanical block. Measured results and detailed analyses are discussed.

Chapter 3 gives a summary and overview of this research work. Suggestions for future study include several topologies for developing larger array receiver based on the two-pixel integrated receiver that was proposed and developed in this thesis have been proposed.

1 Introduction

1.1 Millimeter and Submillimeter Heterodyne Receiver

In view of the great significance of millimeter and submillimeter waves for the science community, the techniques and instrumentation used for sensitive millimeter and submillimeter wave astronomical observations and planetary remote sensing have been increasingly developed during the last thirty years.

The millimeter domain is at wavelengths ranging from 10mm to 1mm, covers the range of frequencies from 30 to 300GHz. This band is commonly used in radio astronomy and remote sensing. Then the submillimeter domain is at wavelength ranging from 1mm to 0.1mm, or from 300GHz to 3THz in the frequency domain, which is located between the regions observed by radio telescopes and infrared/optical telescopes.

For astrophysics, the millimeter wave range is especially useful for studying the characteristics of cold molecular clouds in which stars form. And the submillimeter band contains spectral and spatial information on the cosmic background, on very distant newly formed galaxies, and on the early stages of star formation within gas clouds in our own galaxy [Phillips92]. For the past four decades submillimeter wave heterodyne spectroscopy techniques have been widely used for molecular line spectroscopy; the detection, identification and mapping of thermal emission and absorption signatures from lightweight low pressure gases; the study of new star formation; and analysis the composition, and map of distribution, of gas and dust within our own galaxy and the constituents in the cores of distant galaxies [Phillips92, Siegel06a, Siegel07].

The human eye is sensitive only to visible light, which is a tiny fraction of the electromagnetic spectrum; in addition, only a small fraction of the radiation produced by astronomical objects actually reaches the ground, because of atmospheric opacity. Certain atmospheric gases absorb radiation very efficiently at some wavelength, which lead to opacity variation of the atmosphere along the spectrum. For example, water vapor (H_2O) and oxygen (O_2) absorb radio waves having wavelengths less than about a centimeter, whereas water vapor and carbon dioxide (CO_2) are strong absorbers of infrared radiation. Ultraviolet, X-ray, and gamma-ray radiation are

completely blocked by the ozone layer high in Earth's atmosphere (see Figure 1.1). In the millimeter and submillimeter portion of the spectrum, the Earth's atmosphere emits strongly at frequencies corresponding to a number of H_2O, O_2, O_3, and $O_{18}O$ transitions.
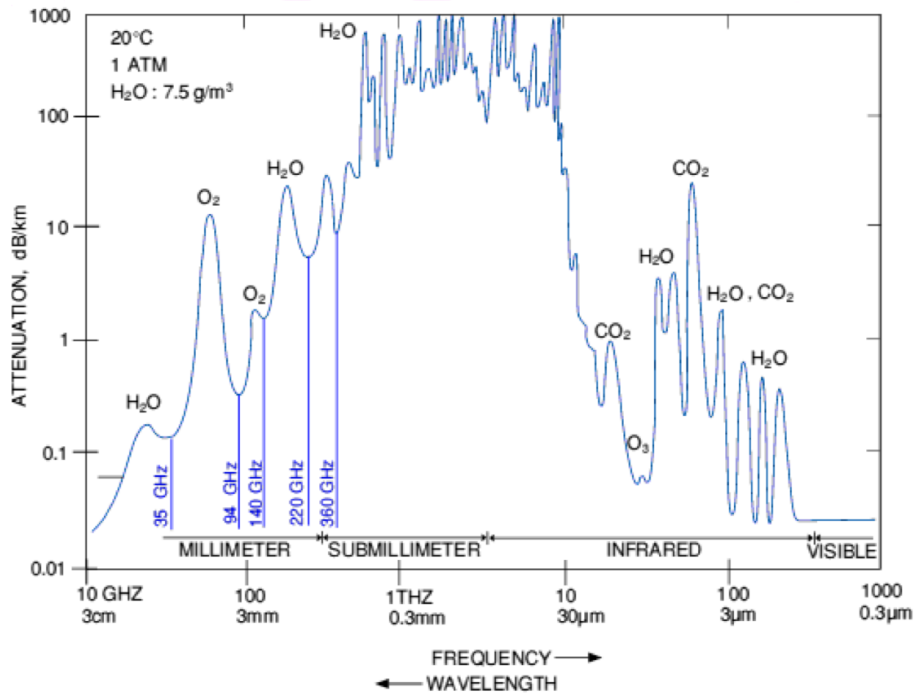
Figure 1.1: Atmospheric attenuation properties over a wide frequency range at sea level.

The most significant limitation to the detection of astronomical emission at submillimeter wavelengths with ground-based observatories is atmospheric emission, noise and attenuation. At submillimeter wavelengths, ambient atmospheric water vapor absorbs incoming light. At low altitudes (see Figure 1.2), where most water vapor resides, the atmosphere is very opaque at submillimeter wavelengths; the abundant water vapor absorbs any incoming submillimeter photons before they can reach the telescope. At higher altitudes (see Figure 1.3 & Figure 1.4), however, the water content decreases substantially. Owing to atmospheric absorption issues, ground-based millimeter and submillimeter wave astronomy telescope is limited to high altitude sites such as the site on Mauna Kea, in Chile and the South Pole.
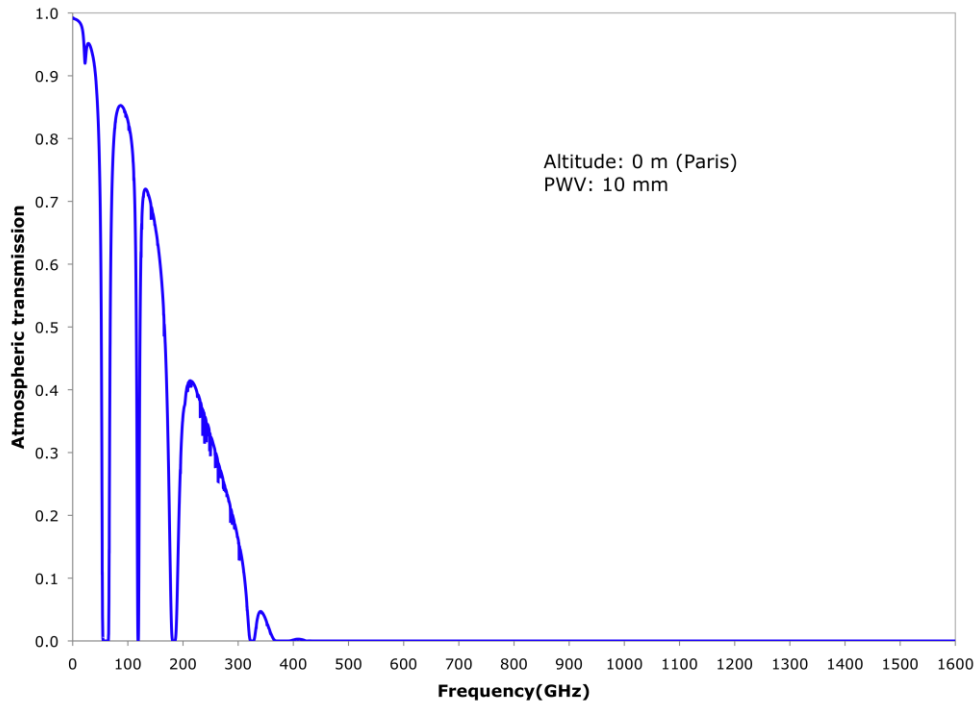
Figure 1.2: The Earth's atmospheric transmission observed from the ground of Paris with 10 mm of perceptible water vapour above the ground (adapted from [Pardo08]).
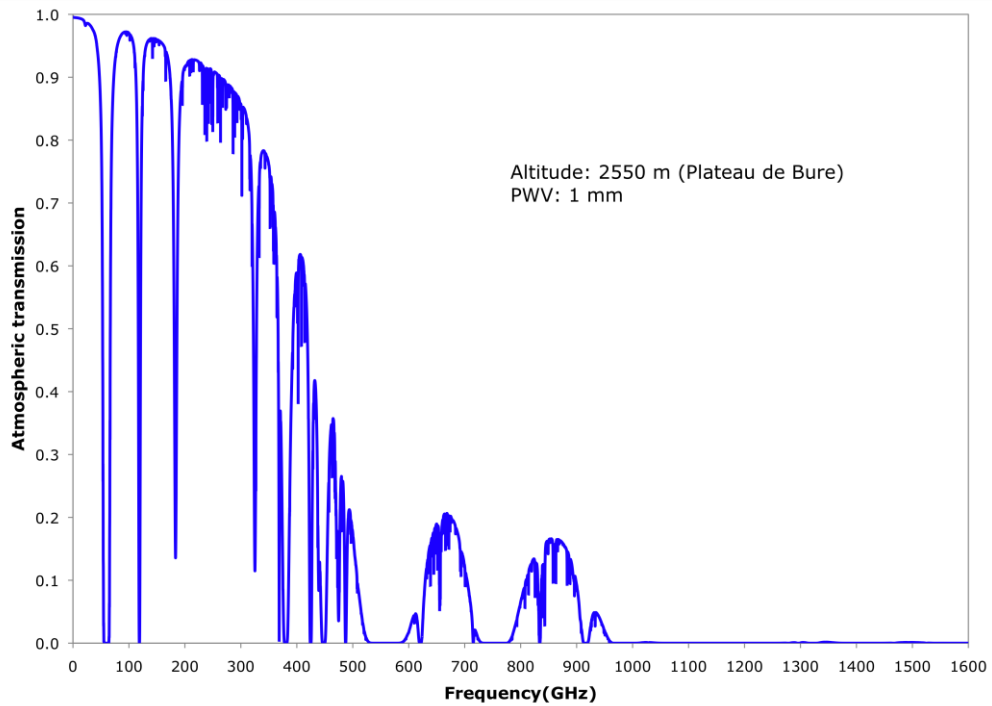
Figure 1.3: The Earth's atmospheric transmission observed from Plateau de Bure (Haute-Alpes, France) with 1 mm of perceptible water vapour above the ground (adapted from [Pardo08]).
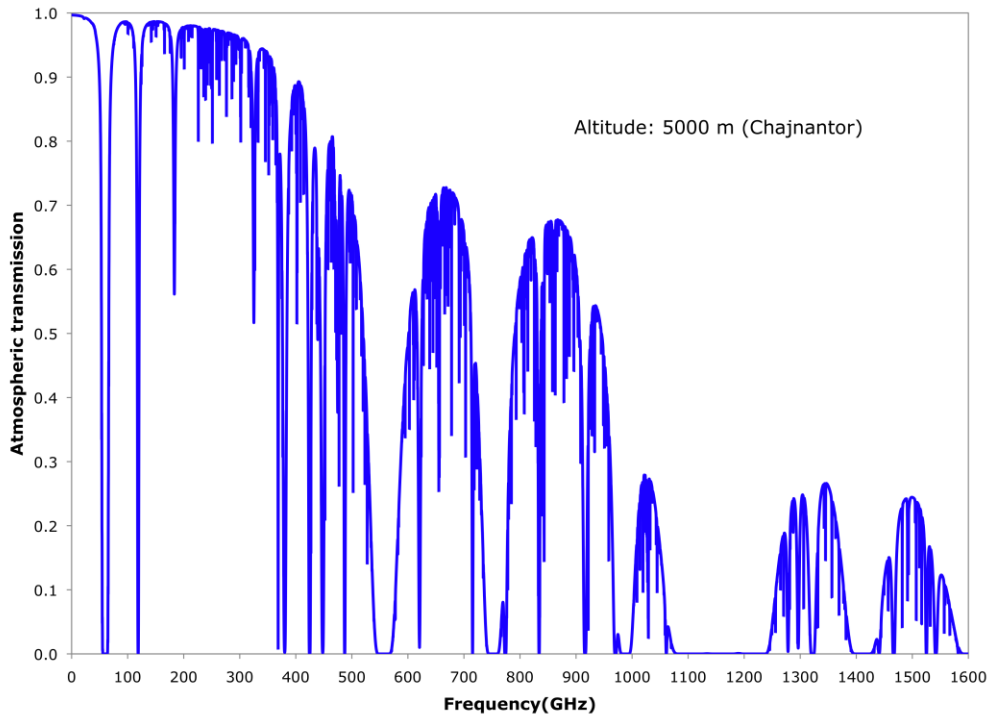
Figure 1.4: Earth's atmospheric transmission observed from Chajnantor (site of ALMA, Chile) with 0.3 mm of perceptible water vapour above the ground (adapted from [Pardo08]).

To overcome these drawbacks, several approaches have been used to get above the atmosphere. One approach has been to use telescope carried to high altitude by balloons [Garnier05]. Another approach has been to use the airborne telescope [Boreiko96] to observe from above most of the atmosphere. While not able to reach altitudes comparable to those of balloons, airborne astronomy and balloon astronomy get above most, but not the entire atmosphere. To avoid the absorption of the Earth's atmosphere, the only solution is to go into space [Phillips02, Goldsmith07].

1.1.1 Millimeter and Submillimeter Wave Techniques

There are two classes of detectors used in the millimeter and submillimeter region, namely direct and heterodyne instruments. Being situated at the transition region between the heterodyne detection techniques used at radio wavelengths and the direct photo detection techniques used for infrared, optical, ultraviolet, and X-ray astronomy, the submillimeter-wave astronomy benefit the techniques from both regimes.

Direct detections such as bolometers [Richards94], are thermal radiation detectors: an absorber absorbs the incident electromagnetic radiation; its temperature

rises and a resistance thermometer measures the change of temperature. Bolometers have very wide bandwidths and offer better continuum sensitivities; consequently, they are generally useful for continuum detection.

Whereas heterodyne techniques are preferred to direct detection involve the need for high spectral resolution studies in astrophysics and planetary remote sensing [Blaney78, Phillips02, Siegel02, Chattopadhyay04]. Future large telescopes or interferometers in space need very high spatial resolution, which implies relatively small velocity dispersion and therefore high spectral resolution [Phillips02]. In general, heterodyne detection offers higher spectral resolution ($\lambda / \Delta\lambda \approx 10^6$) over direct detection [Phillips02, Chattopadhyay05].

Low noise pre-amplifiers are just being available at shorter millimeter wavelength less than 3 mm [Weinreb99, Archer01a, Archer01b, Raja01, Gaier07, Tessmann07] from past few years, MMIC low noise amplifier (LNA) in submillimeter range [Deal07a, Pukala08, Samoska08a] are just becoming to be developed recently. Thus, the typical solution for detecting signals at millimeter and submillimeter wavelengths is to bring the signal down in frequency, without losing information. This is accomplished by a heterodyne receiver in which the signal from the sky called radio frequency (RF) is mixed with a monochromatic signal called local oscillator (LO). The frequency of the LO is very close to the frequency of the signal. In performing such a mixing, the resulting signal is at much lower frequency (at the difference of the two frequencies), while still having all the spectral information of the original signal from the sky (See Figure 1.5).
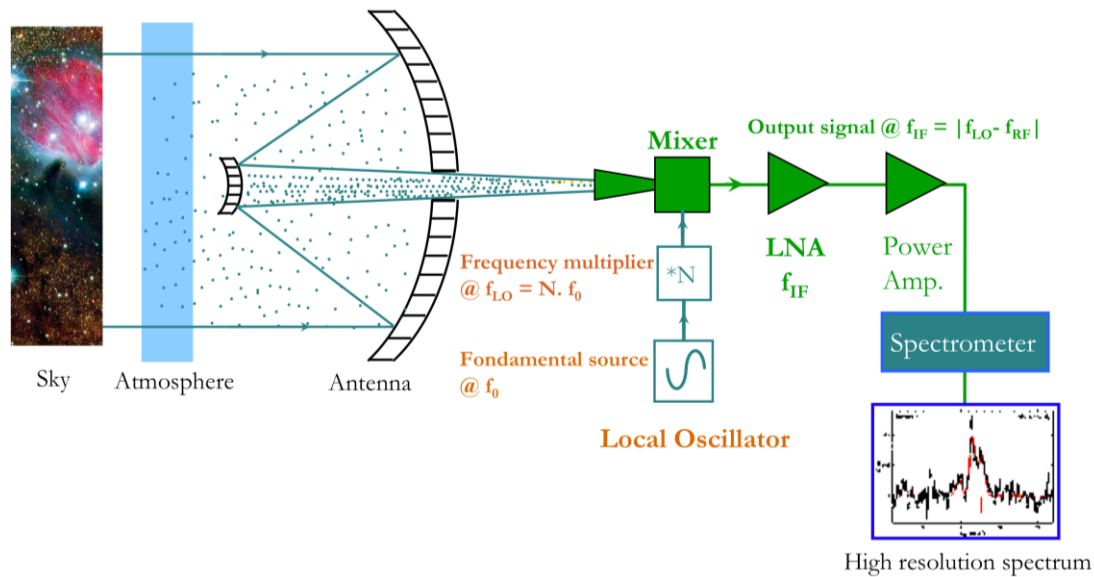
Figure 1.5: A block diagram of a heterodyne receiver chain (redrawn from [Maestrini99]).

Only heterodyne techniques are briefly described here; more details for submillimeter astronomy techniques could be found in [Phillips87, Charlstrom96, Siegel02, Zmuidzinas07].

Increased progress in millimeter and submillimeter heterodyne receiver technology has been achieved over the last three decades, including the front-end segment, the intermediate frequency (IF) output, the back-end processing [Charlstrom96, Benz05, Klein06] (spectrometer or correlator) and micromachining [Lubecke98, Kirby06, Li08, Bruneau08]. The detectors and LO sources used in heterodyne receiver front-ends are summarized below.

1.1.1.1 Detectors

Heterodyne receivers using cooled HEMT LNA have been employed in radio astronomy since 1980's [Weinreb88, Pospieszalski93]. As described previously steady improvement has been achieved at millimeter MMIC LNAs especially for high frequency during last few years, furthermore, the highest frequency MMIC LNA has been reported recently up to 360GHz [Samoska08a]. Thus, MMIC LNAs are increasingly being used as receiver front-end in the millimeter wave range particularly for array and imaging applications involving Earth science and planetary [Siegel03]. A Q-band (38-50GHz) MMIC receiver [Kangaslahti06] has been developed for application to detection of the cosmic microwave background (CMB) radiation in astrophysics. At E-band, a multichannel receiver for imaging radar was

8

reported [Schellenberg07], at W-band, a dual-channel receiver was demonstrated [Tessmann06], and a G-band Multi-chip MMIC T/R module for radar applications was recently reported [Samoska08b]. MMICs are appealing for array receivers.

At millimeter and submillimeter wavelength, three types of mixer technologies are mainly used in heterodyne receivers: Schottky diode mixers, Superconductor insulator superconductor (SIS) mixers and hot electron bolometer (HEB) mixers.

Schottky diode mixers can operate at frequencies up to 5THz [Betz96], which use the nonlinear current voltage characteristic of a metal-semiconductor junction. In the early days of submillimeter astronomy, whisker-contacted GaAs Schottky diode mixers were been commonly used either in a waveguide mount or in an open structure. They have been employed in Submillimeter Wave Astronomical Satellite (SWAS) launched by NASA in 1998 [Melnick00] and Odin launched by teams from Sweden, Canada, France and Finland in 2001[Odin]; they were the two first submillimeter space heterodyne instruments. However, whisker-contacted devices show reliability and handling problems, and space qualification is very difficult. Furthermore, whiskered diodes cannot be integrated. For these reasons, the planar Schottky diode technology has been developed and improved for the last two decades. In the aspect of receiver sensitivities, typical DSB noise temperature of room temperature Schottky diode mixers is about 1800K at 500GHz with approximately 8dB of conversion loss [Chattopadhyay04], improved performance can be achieved when cooled. Last reported subharmonic Schottky diode mixer working at 874GHz [Thomas08a] showed minimum DSB noise temperature of 3000K. The highest Schottky diode mixer has been demonstrated up to 2.5THz [Gaidis00] flown on Aura satellite and 4.744THz flown aboard the Kuiper Airborne Observatory (KAO) [Boreiko96].

In order to develop far more sensitive submillimeter and THz mixers, at least two different superconducting heterodyne detectors have been developed, including the superconducting tunnel junction (SIS) [Dolan79, Richards79, Tucker79] and HEB [Phillips73]. SIS mixers are widely used throughout the millimeter wave bands up to 700GHz, the SIS tunnel junction have already been proven to operate close to the quantum limit ($T_n \geq hv/k$)[Zmuidzinas04], and extending recently up to frequencies as high as 1.4THz [Karpov07] for heterodyne spectrometry [Edgar00] on the

Stratospheric Observatory For Infrared Astronomy (SOIFA) [SOFIA] and the Heterodyne Instrument for the Far-Infrared (HIFI) on Herschel Space Observatory [Herschel]. However, reverse photon sets a hard upper frequency limit for SIS mixer operation, for all-niobium SIS junctions the limit is around 1.4THz and possible 1.6THz for junctions incorporating higher critical temperature materials [Zmuidzinas04].

At yet higher frequencies, HEB mixers now offer excellent performance at frequencies in the terahertz region that are beyond the reach of SIS mixers, excellent performance has been reported at 2.84THz [Gao07] with a receiver noise temperature of 1050K (below ten times of quantum noise), and at 4.3THz with a DSB receiver noise temperature of 1300K [Khosropanah07].

The SIS and HEB mixers both operate at temperatures well below the superconductor critical temperature (2 to 4K), the requirement of cryogenic lead a significant limitation for remote and long lifetime space operation. One major advantage of Schottky mixers is that they can operate over a very wide temperature range, including room temperature, and can therefore be used in applications in which cryogenic cooling is undesirable or prohibitively expensive. The Schottky diode mixers could be deployed for the Earth observation, planetary science and ground atmospheric research, which do not require sensitivities as high as for astrophysics. However, Schottky diode mixer requires higher local oscillator (LO) pump power, which is at least 1mW, while the required LO power for HEB mixers is in the 1-100nW range, and for SIS mixers is on the order of µW [Siegel03].

Consequently, the particular choice is mostly dictated by the available LO power, operating frequency, receiver sensitivity criteria and whether the mixer will operate at room temperature or cryogenic temperatures.

1.1.1.2 Local oscillators

The development of powerful, tunable, monochromatic sources is currently one of the most important issues for the development of high frequency heterodyne instrument particularly in the terahertz frequency range (0.3-10 THz). Solid-state LO chains have rapidly replaced sources using molecular lasers and vacuum tube oscillators such as klystrons, carcinotrons. Direct sources such as carcinotrons or Backward Wave Oscillator (BWO) can operate at frequencies between a few GHz

and 1.2 THz producing substantial output power. However, the disadvantages of these sources lay in their large size, high voltage requirements, low reliability and short lifetimes as well their commercial availability. To overcome the limitations of such direct sources, two successful frequency conversion approaches have been widely used for the power generation at millimeter and submillimeter wavelength: either up to higher frequency from low frequency, or down from the optical or infrared frequencies [Siegel03].

Up conversion from microwave sources is currently the most efficient technique. Gunn oscillators and amplifiers are usually used as the fundamental source with harmonic generation resulting from a nonlinear device such as Schottky diode varactor or heterostructure barrier varactor (HBV) [Kollberg89]. Schottky diode technology is mature and high frequency multipliers have been progressed combing with several related technologies, which include membrane technology, improved micromachining, powerful simulators and increased drive power from MMIC power amplifiers [Maestrini08a]. Frequency multipliers using GaAs Schottky diodes have reported tens of microwatts of output power up to 1.9THz [Maestrini04a] for the Herschel Space Telescope. To increase the power handling of given source, a power-combined frequency tripler at 300GHz has been demonstrated recently in [Maestrini08b], it delivers a peak power of 26mW with 11% conversion efficiency at 318GHz. This approach should be the future trend to improve the power handling of frequency multiplier. Another demonstration of tripler at 900GHz has been reported in [Maestrini08c]; and is expected to be capable of pumping a 2.7THz tripler [Maestrini08b] in near future.

HBVs have a symmetric capacitance-voltage and anti-symmetric current-voltage characteristics; because of these characteristics no even-order harmonics are generated. The odd-order frequency multiplier design is therefore simplified. Furthermore, dc bias is not needed because the capacitance modulation region is centered at zero-bias. HBV multipliers have made significant advances, an output power of 6.5mW and conversion efficiency of 7.2% at 270GHz for a tripler was reported in [Xiao07], an output power of 195mW and conversion efficiency of 15% at 113GHz for a tripler was demonstrated in [Vukusic07], other recent demonstrations could be found in [Melique00, David02, Xiao04, Xiao05, Vukusic06]. However the reported state of the art performances of HBV multipliers

are lower than the power produced by Schottky diode multipliers.

The devices used for up conversion described above need to be driven by a fundamental source at lower frequency. At millimeter wave range, the solid-state power amplifiers (PAs) are frequently used to drive the diode multiplier chain to increase output power and bandwidth for a local oscillator chain [Samoska06]. The commercial W-band PAs [Wang01, RPG] are only available for a few years. Significant progress has been made in increasing the operating frequency of millimeter wave solid-state (PAs) in the past few years, which was pushed by applications including millimeter and submillimeter/THz receivers for astrophysics and earth remote sensing. Increasing the operating frequency of solid-state amplifiers would potentially reduce the number of successive multiplications necessary to reach a particular frequency, and therefore offer significant improvements in total dc efficiency and improve final output power [Deal08, Maestrini08a]. For the novel application in high-resolution submillimeter wave radars [Dengler07], PAs could be used as the fundamental source. Several PAs operating at G-band [Samoska01, Samoska04, Paidi05, Huang06, Deal07b, Deal07c] and even above (>300GHz) have been reported in the last few years; a new submillimeter wave PA topology has been recently reported at 260GHz [Deal08] giving more than 5.9mW output power and is expected to reach the operating frequencies around 340GHz in the near future.

In 2001, a new type of solid-state THz source was developed based on quantum cascade laser (QCL) structures [Köhler02]. Rapid improvement has been achieved over the past few years. QCLs can provide high output power levels, are compact compared to other sources and can achieve frequencies as low as 1.2THz without magnetic field [Williams07]. They have been demonstrated as LO source with superconducting HEB mixers [Gao05, Hübers05]. However, cryogenic cooling is required for continuous wave operation below 2THz. A record operation temperature of 178K has been reported recently for a 3THz QCLs [Belkin08]. Furthermore, their main drawback is the limited frequency tunability [Hindle08].

Photomixers use down conversion from the optical regime for generating millimeter and submillimeter power. The short carrier lifetime, high electrical breakdown field, and high carrier mobility make the Low Temperature Growth (LTG) GaAs suitable for operation well into the THz range. Results have been reported for frequencies up to 3.8THz [Brown95], however poor output power of

about 50μW has been achieved at 100GHz and decreased 12dB/octave beyond 500GHz. More recently, a maximum output power of 10.9μW at 1.04THz photomixer was reported in [Ito05].

Other commonly used sources at submillimeter wave are FIR-pumped gas lasers [Hodges77], which usually can deliver tens of milliwatts in the terahertz range. However, such lasers are generally massive, bulky and require a lot of DC power, though one 2.5THz gas laser [Mueller98] is currently operating on the NASA AURA Satellite, they are therefore appropriate for ground based applications [Gao07, Maestrini08a].

To conclude, tremendous progress has been made in solid-state LO development at submillimeter wavelengths over last few years, which is being driven by space application such as Herschel.

1.2 Why does one need large array receivers?

With the much-improved performance of state-of-the-art millimeter and submillimeter heterodyne instruments, the dynamic range of ground-based millimeter and submillimeter observations are restricted by the partial transparency and turbulence of the atmosphere that relates to the water vapor content of the atmosphere. To use better the rare appropriate observing conditions and improve the efficiency of ground based or airborne telescope observing time, it is conceivable to perform multiple observations at the same time, requiring arrayed receivers in the focal plane of telescope [Rabanus02].

The array receivers used in millimeter astronomy [Gillespie79] has been discussed for more than two decades, in order to improve the speed mapping of extended molecular line sources. A large amount of observing time at millimeter-wave telescopes with single beam was necessary to observe both the intensity and velocity distribution of the constituents of large molecular clouds [Payne88].

These molecular clouds can be as extended as one to several square degrees in some cases. The parabolic antenna operated at millimeter wavelength has a narrow beam size. It requires a long observation time to map extended sources with a single beam of a small angular size. The observing time required to map a given object may be reduced by adding more beams to the telescope system merely by adding receivers

at the focal plane [Payne88]. Table 1.1 gives minimum observing time in order to map astronomical object with a wide range of sizes with a multi-beam receiver in the range 460-490GHz, and shows that a molecular cloud could be mapped in much less time with array receivers.

Table 1.1 Observing time for the JCMT (i.e. no without calibration) for a 3Jy source at the 3σ detection level for different field sizes and number of array elements (Reproduced from [Ardenn87]).

Field size (arcmin)	#HPBW's	Min Observ. time (hrs), for 3 Jy sources (3σ) Array size		
		8 (2x4)	16 (4x4)	64 (8x8)
1 x 1	33	240 sec	120 sec	120 sec
4 x 4	532	0.6	0.15	240 sec
12 x 12	4.810^3	4.6	2.3	0.6
30 x 30	3.010^4	29	15	3.6
60 x 60	1.210^5	4.8 days	2.4 days	14.3
180 x 180	$1.07.10^6$	43 days	21.5 days	5.4 days

In addition to this fundamental advantage in mapping speed on extended objects, array receivers offer several secondary advantages. With a multi-beam array, a larger region of the sky can be mapped under identical conditions, allowing for better internal consistency, which is especially notable for extragalactic observations. Because the absorbing water vapor changes rapidly with time at submillimeter wavelengths in space and in time, conditions when a map is started may not be at all the same as when the map is finished. Mapping image quality is to be greatly improved due to the homogenous baseline of array receivers. In addition, relative calibration of individual pixels is more accurate since data are taken simultaneously through the same atmospheric path.

1.2.1 Actual status of the development of large array heterodyne receivers

Historically, the basis of focal plane array systems was discussed by [Gillespie79], and an experimental system was developed by [Murphy88]. Then, an array employing SIS mixers working at 345GHz was reported by [Ardenn87]. The first complete millimeter wavelength focal plane array operating on a telescope, which used cooled Schottky diode mixers at 230GHz, was described by [Payne 88].

Many factors determine the viability of the receiver array. The most important

are cost, size, complexity, availability of local oscillator power and operating temperature of receiver array [Gillespie79]. Fortunately, recent breakthroughs in detector technology, micromachining, local oscillators, amplifier technology, and backend spectrometers now make the construction of large arrays of heterodyne receivers possible [Walker02]. However, there are many challenges and considerations in developing large array heterodyne receiver, such as the array architecture, mixer configuration, local oscillator power coupling, IF layout and backend processing [Chattopadhyay04, Chattopadhyay05a, Chattopadhyay05b].

The choice of mixer technology used in array receiver is dictated by the available LO power, requirement of receiver sensitivity, and the operating temperature of the mixer. Different mixer technologies have been described previously. Available LO power is the major concern for developing the heterodyne array receivers at submillimeter wavelengths [Chattopadhyay04]. HEB mixers require the lowest LO power but tend to have a narrow IF bandwidth. SIS mixers are the most sensitive mixers available today in the 100-1200GHz range and require a reasonable amount of LO power (in order of μW). Both HEB and SIS mixers need to be cooled below 4K. On the other hand, Schottky diode mixer can operate at room temperatures and have moderated noise performance, however, they need at least around 1 mW LO power.

Array architecture is critical for the design of the instrument, to improve the LO power distribution and reduce the losses, only high integrated array structure is possible to built large array receiver [Chattopadhyay04]. Various techniques could be employed for multiplexing LO power to a number of mixers simultaneously in a large array receiver, such as beam splitter used in [Groppi00a], direct waveguide coupler employed in [Schuster00], Dammann grating used in [Gusten98] and Fourier grating used in [Graf 03]. With beam splitters, losses show up in absorption and reflection of a few percent due to finite refraction indices, in grating, lost power is scatted away statistically or appears in higher unwanted orders [Rabanus02]. The losses in the LO circuit can be reduced by integrating the last stages of the frequency multiplier chain in the array mixer blocks [Narayanan 02, Chattopadhyay04]. The approach consisting in using individual LO source for each mixer was discussed in [Chattopadhyay04], which means each mixer is pumped with an independent LO source. More recently, a single quartz-based combined Schottky diodes mixer/double working at 380GHz has

been reported in [Thomas08c].

Large multichannel backend became feasible; this leap in spectrometer ability is driven by the rapid expansion in the capabilities of high speed Analog to Digital Converters (ADCs) and Field Programmable Gate Arrays (FPGAs).

Currently, there are only a handful of millimeter and submillimeter wave heterodyne array receivers in operation on ground-based telescope. Table 1.2 summarizes the heterodyne array receivers used in the past, current and under development.

Table 1.2 Past, Current and Future heterodyne array receivers operate in the world.

Receiver	Telescope	Frequency (GHz)	Beams	Technology	Year
RETIRED					
NRAO [Payne88]	12m-NRAO	230	8	Schottky	1987
QUAARY [Erickson92]	14m-FCRAO	86-115	15	Schottky	1990
S115Q	45m-NRO	100-116	4	SIS	1992
NRAO [Payne95]	12m-NRAO	230	8	SIS	1994
SISYFOS	20m-OSO	85-115	16	SIS	1998
CHAMP [Gusten98]	10.4m-CSO	460	15(x2)[1]	SIS	1999
OPERATIONAL					
BEARS [Sunada00] [Yamaguchi00]	45m-NRO	82-116	25	SIS	1998
SEQUOIA [Sequoia]	14m-FCRAO, MA	86-115.6	32	SIS	2000
PoleStar	1.8m-	810	4	SIS	2001

[Groppi00a]	AST/RO				
HERA [Schuster04]	IRAM 30m	215-272	9(x2)[1]	SIS	2001(May.)
SMART [Graf03]	3m-KOSMA	490/810	8x2	SIS	2001(Sep.)
DesertSTAR [Groppi00b]	10m-HHT	345	7	SIS	2005
HARP [Dent00]	15m-JCMT	325-375	16	SIS	2005(Dec.)
CHAMP+ [Kasemann06]	12M-APEX	660/810	14	SIS	2006
Under Development					
SuperCam [Groppi07]	10m-HHT/ 25m-CCAT	330-360	64	SIS	since 2004
STAR [Michael02]	SOFIA	1600-1900	16	HEB	

Notes

1 Dual polarization

1.3 Planar Schottky diode technology

1.3.1 Structure and principle

The Schottky diode is one of the components most largely used to build mixers and frequency multipliers at millimeter and submillimeter wavelengths. The principle of the Schottky diode resides in the use of a metal contact deposited on a semiconductor substrate of type N. This component has the fundamental advantage to function only with majority carriers that enable it to function at high speed and very high frequency.

Figure 1.6 shows the general structure of an Schottky-barrier diode. The diode is fabricated on a high-conductivity substrate (*n*-type) that offers high electron mobility, then a very pure high-conductivity buffer layer is gown up on the top of the

substrate to assure low series resistance and to prevent impurities in the substrate from diffusing into the epitaxial layer during processing; the buffer and substrate are doped as heavily as possible, usually on the order of 10^{18} cm^{-3} for GaAs. An n epitaxial layer is grown on top of the buffer and doped to 5.10^{16} to 5.10^{17} cm^{-3}. The contact of the metal anode to the epitaxial layer forms the Schottky contact. Platinum and titanium are the most common anode materials for GaAs diodes. A gold layer is usually plated onto the metal anode to prevent corrosion and to facilitate a bond wire, ribbon, air bridge, or whisker connection [Maas03].
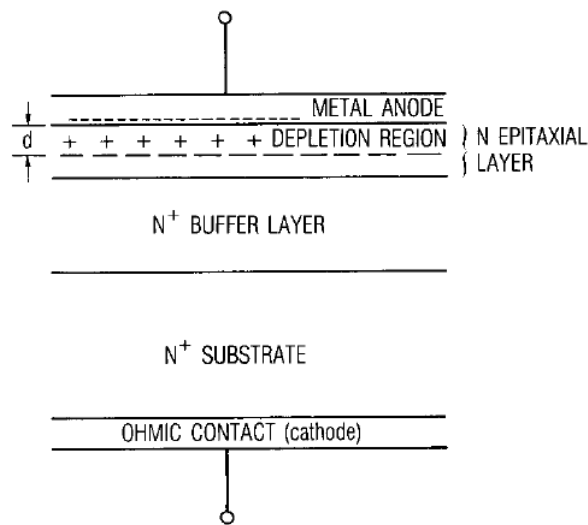
Figure 1.6: Cross section of a Schottky-barrier diode (reproduced from [Maas03]).

When the metal and the semiconductor are in contact, some of the free electrons in the semiconductor move to the surface of the metal. The semiconductor immediately under the anode that is named the depletion region is depleted of electrons. The uncompensated ions are positive on the semiconductor side and negative on the metal side, this creates an electric field, which opposes further movement of electrons, is set up between the anode and the semiconductor, and a dynamic equilibrium is reached (shown in Figure 1.7 (a)). Because of this electric field, a potential difference, called the diffusion potential or built-in voltage, exists between the neutral semiconductor and the anode.

Depletion width describes the width of the depletion region in the semiconductor, which can be found from the doping density and material parameters of the semiconductor. The depletion width d of an ideal junction having uniform epitaxial doping is:

$$d = \sqrt{\frac{2V_b\varepsilon_s}{qN_d}} \qquad (1\text{-}1)$$

where V_b is the built-in voltage; ε_s is the electric permittivity of the semiconductor; N_d is the doping density; and q is the electron charge. The depletion width changes when the junction is polarized (DC voltage V_j), which becomes:

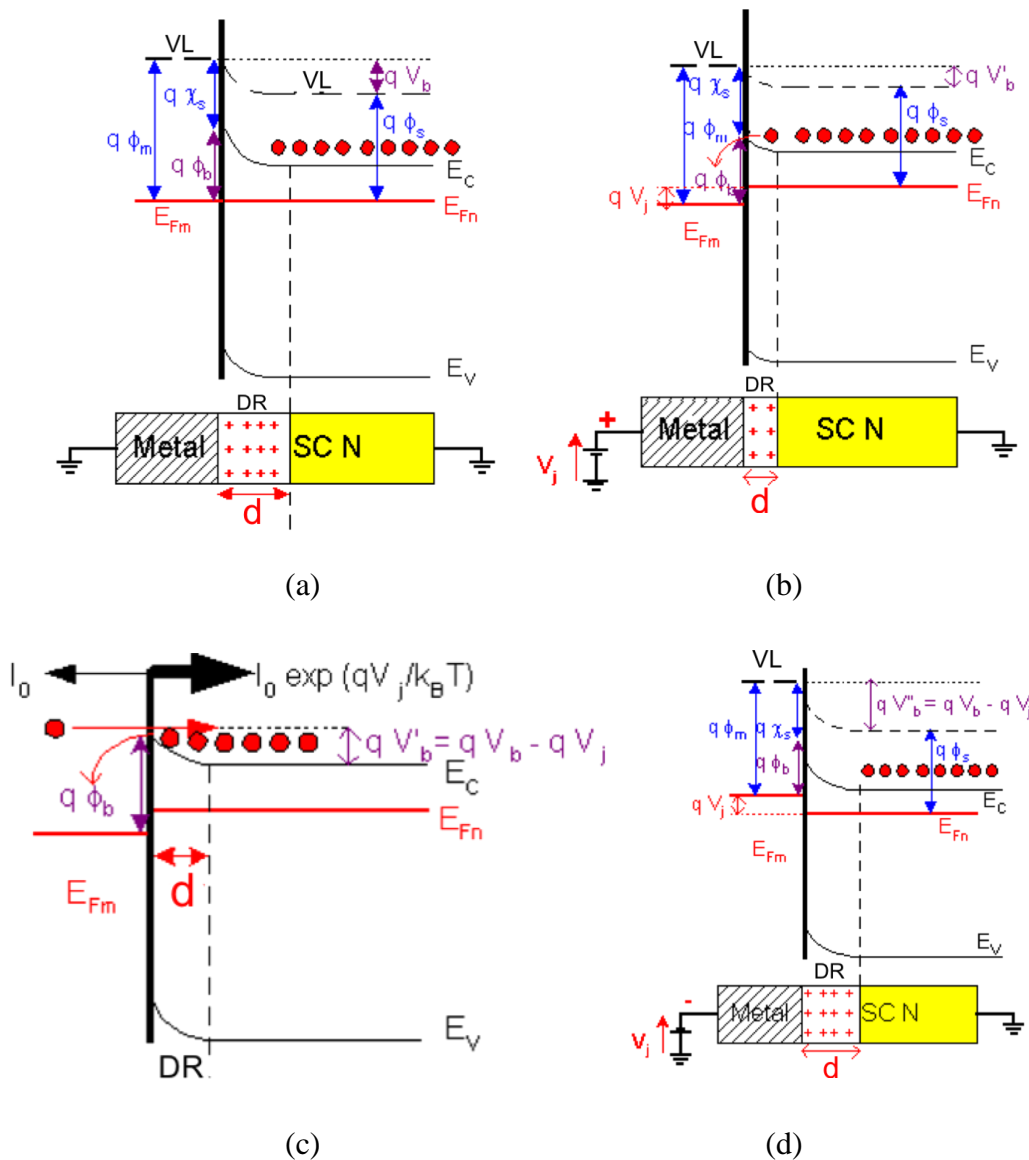$$d = \sqrt{\frac{2(V_b - V_j)\varepsilon_s}{qN_d}} \qquad (1\text{-}2)$$

(a)

(b)

(c)

(d)

Figure 1.7: Band diagram of Schottky diode when (a) in dynamic equilibrium, (b)&(c) forward biased, (d) reverse biased.

E_{Fm} : *Fermi energy of the metal* E_C : *Energy of conduction band*

E_{Fn} : Fermi energy of the semiconductor E_V : Energy of valence band

$q\Phi_m = VL - E_{Fm}$: Work function of the metal $q\chi_S = VL - E_C$: Electron affinity

$q\Phi_S = VL - E_{Fn}$: Work function of the semiconductor d : depletion region

$q\Phi_b = q\Phi_m - q\chi_S$: Barrier metal $\rightarrow$ semiconductor V_j : Voltage polarization

$qV_b = q\Phi_m - q\Phi_S$: Barrier semiconductor $\rightarrow$ metal VL : Vacuum Level

If the Schottky junction is forward biased ($V_j>0$), the depletion region narrows (see Figure 1.7 (b)&(c)) and less charge is stored. The carrier density is large making a large forward current. While the junction is reverse biased (see Figure 1.7 (d)), the depletion region gets wider that increases the drift component of current and decrease the diffusion component. Therefore, the Schottky diode operates as a nonlinear capacitor.

1.3.2 The Schottky Diode Model

Figure 1.8 shows the equivalent circuit of a Schottky diode. Which consist of two nonlinear elements junction resistance R_j and junction capacitance C_j in parallel, and the parasitic series resistance R_s in series.
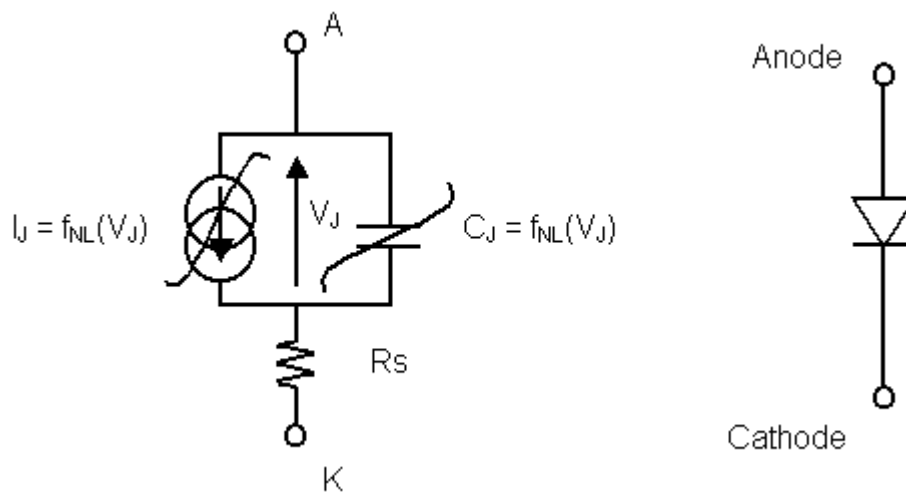
Figure 1.8: Equivalent circuit of a Schottky-barrier diode.

The junction capacitance of a Schottky diode depends on the voltage applied to the junction, the relationship is:

$$C_j(V) = \frac{dQ}{dV} = \frac{C_{j0}}{(1 - \frac{V_j}{V_b})^\gamma} \qquad (1\text{-}3)$$

where V_b is the built-in voltage or diffusion potential and C_{j0} is the zero voltage junction capacitance, V is the junction voltage shown in Figure 1.8 ($V_j > 0$ if the junction is forward biased), and $\gamma = 0.5$ if the junction is uniformed doped. The zero voltage junction capacitance is:

$$C_j(0) = S\left[\frac{q\varepsilon_{epi}N_d}{2V_b}\right]^{1/2} \qquad (1\text{-}4)$$

where S is the surface of the anode; q is the electron charge; ε_{epi} is the electric permittivity of the epilayer; N_d is the doping density of the epilayer.

The current-voltage characteristic of a Schottky diode can be expressed by the diode equation, which is similar for a *pn* junction diode (see in Figure 1.7 (c)):

$$I(V) = I_s\left[\exp\left(\frac{qV_j}{\eta kT}\right) - 1\right] \qquad (1\text{-}5)$$

where $kT/q = 25.8mV$ for T= 293 K (absolute temperature), k is Boltzmann's constant, $1.37 \cdot 10^{-23} J/K$, I_s is the saturation current which is a proportionality constant, and η is the ideality factor ($\eta > 1$) that accounts for unavoidable imperfection in the junction and for other secondary phenomena that thermionic emission theory cannot predict.

1.3.3 Varistor and Varactor Schottky diodes

The varistor (Figure 1.9 (left)) and varactor diodes (Figure 1.9 (right)) are based respectively on nonlinear resistance characteristic and nonlinear capacitance characteristic of the Schottky-barrier diode.

When the Schottky junction is forward-biased as shown in Figure 1.9 (left), it works as a Varistor diode. The nonlinearity of the resistance allows the Varistor to be used as mixer. The noise mechanism of varistor mixer will be detailed in Chapter 2.4.

When a reverse voltage is applied to the junction, the holes in the p-region are attracted to the anode terminal and electrons in the n-region are attracted to the cathode terminal creating the depletion region where there is little current. The

depletion region increases as reverse voltage across it increases; and since capacitance varies inversely as dielectric thickness, the junction capacitance will decrease as the voltage across the junction increases. By varying the reverse voltage across the junction, the junction capacitance can be varied. This is shown in the typical varactor voltage-capacitance curve shown in Figure 1.9 (right). Notice the nonlinear increase in capacitance as the reverse voltage is decreased. This nonlinearity allows the varactor to be used as a harmonic generator, like frequency multiplier.

The structure of a Schottky-barrier varactor is qualitatively the same as that of a varistor diode. Since the series resistance consists largely of the undepleted epilayer, the series resistance likewise varies significantly. At high frequencies the importance of minimizing series resistance and maximizing capacitance variation becomes progressively greater. In order to achieve both good efficiency and high output power, varactors require higher breakdown voltages than mixer diodes. The higher the doping level, the less negative the breakdown voltage (lower in absolute value); the larger the epilayer, the more negative the breakdown voltage (higher in absolute value). In lightly doped varactors, electrons may approach saturated drift velocity in the resistive epilayer. This phenomenon increases the incremental resistance in a nonlinear manner.

$$i(V) = i_s \cdot \left[e^{\frac{q \cdot V}{\eta \cdot k \cdot T}} - 1 \right]$$
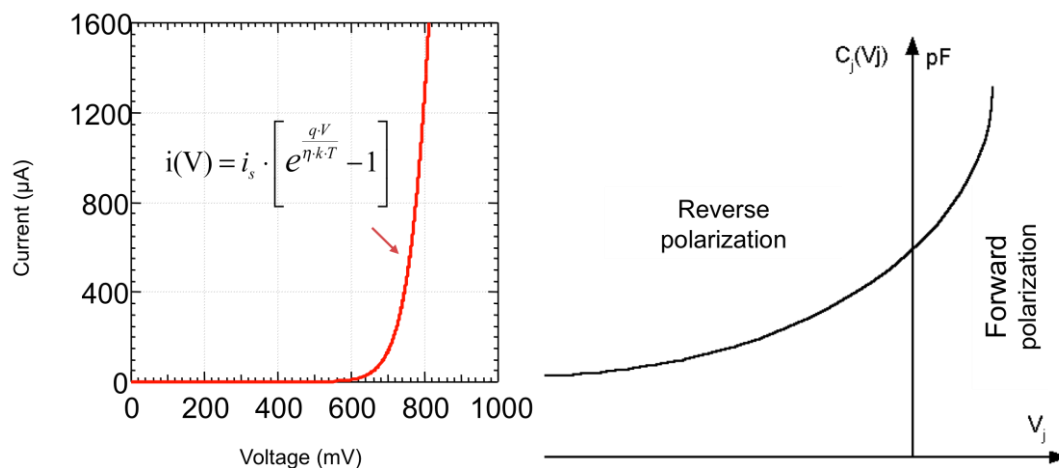
Figure 1.9: Nonlinear I/V characteristic for varistor diode (left) and nonlinear C/V curve for varactor diode (right).

1.3.4 Planar Schottky diode technology

GaAs Schottky barrier diodes continue being the key element for mixers and frequency multipliers in the millimeter and submillimeter wavelength because no

expensive cryogenic cooling system is required to operate them. In order to overcome the drawbacks of the whisker-contact devices, planar diodes technology has been successfully advanced over the past two decades. GaAs discrete planar diodes flip-chip mounted onto the quartz microstrip circuit have been widely employed with good performances in millimeter and submillimeter mixers [Hesler96, Hesler99, Thomas05] and frequency multipliers [Erickson98]. However, the assembly of the circuit is a challenge as the frequency increases. More recently, integrated Schottky diodes circuits have been successfully developed, either the diodes and the microstrip circuit are both integrated on the GaAs substrate, which is the commonly case, or the integration of the GaAs diode directly on the quartz circuit with a very thin GaAs epilayer.

High quality planar Schottky diodes working at millimeter and submillimeter wavelength have been fabricated for more than a decade at the University of Virginia, now at Virginia Diodes Inc. [VDI], and later at the Jet Propulsion Laboratory [Martin01]. Currently, in Europe, only the Technical University of Darmstadt (TUD) in Germany, and the Rutherford Appleton Laboratory (RAL) in the UK have made significant progress towards fabricating high quality and selling planar Schottky diodes. The process developed in Darmstadt is based on a quasi-vertical structure that mimic whisker-contacted diodes but with an integrated process [Simon93]. RAL Schottky process is very similar to VDI process, with air-bridges formed by wet etching underneath the diodes fingers [Alderman07].

Another industrial Schottky process is available from the French-German company United Monolithic Semiconductors [UMS]. This process does not provide air-bridges for the anodes and has numerous limitations that make its use very difficult at frequencies above 180 GHz [Maestrini04b].

More recently, LERMA and the Laboratiore de Photonique et Nanostructures (LPN) in France have initiated a common research and technology program to develop a Schottky process entirely based on E-beam lithography. Presently, significant progress toward fabricating diodes with nano-dimension and with air-bridges entirely patterned with E-beam lithography has been achieved [Jung08].

1.3.5 Applications

Schottky diodes are solid-state devices that can work at room temperature up

to several THz. In addition, these devices are robust enough to work in hostile environments like in space. All these qualities make Schottky diodes irreplaceable for numerous applications, including Earth's atmosphere, planetary science, astronomy, radar and security.

Atmospheric scientists are interested in observing the upper atmosphere with remote sensing from either airborne platforms or satellites. Whisker-contact Schottky diodes were used on the Upper Atmosphere Research Satellite (UARS) of NASA to study the Earth's atmosphere, particularly the protective ozone layer at 205 GHz [Waters93]. At submillimeter wavelength, the Swedish satellite Odin is orbiting the Earth's atmosphere with four cooled Schottky diode heterodyne radiometers since 2001. Even up to THz frequencies, a low noise Schottky diode mixer at 2.5 THz [Gaidis00] implanted in the Microwave Limb Sounder (MLS) was recently employed on NASA's Aura satellite to measure microwave thermal emission from the limb of Earth's upper atmosphere. It was the first space-based heterodyne observations at THz frequency. In the very near future, the Indo-French space experiment Megha-Tropiques will be in operation for understanding tropical meteorological and climatic processes, SAPHIR is a sounding instrument carrying six Schottky diode receivers working near the absorption band of water vapor at 183 GHz. These channels provide relatively narrow weighting functions (see Figure 1.10) from the surface to about 10 km, allowing retrieving water vapor profiles in the cloud free troposphere.
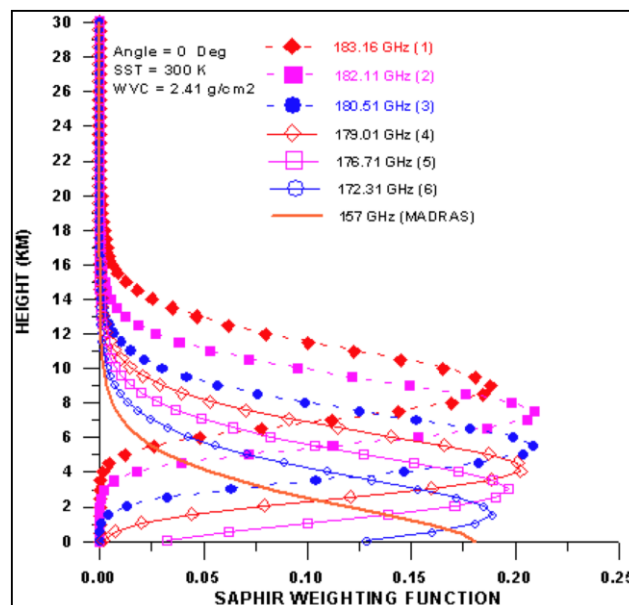
Figure 1.10: Example of weight functions of the 6 channels at Nadir view with a dry atmosphere.

Airborne observation is another approach for the Earth atmosphere science and astronomy. Recently in 2005, Millimetre-Wave Airborne Receivers for Spectroscopic CHaracterisation in Atmospheric Limb Sounding (MARSCHALS) [Moyna06] was successfully flown. MARSCHALS has been designed to be an airborne simulator of a future ESA space instrument MASTER and is the first limb sounder to be explicitly designed and built for the purpose of Upper Troposphere (UT) composition sounding. The principal and most innovative objective of MARSCHALS is to simulate MASTER's (ESA future airborne project) capability for upper troposphere sounding of O3, H2O and CO in the 300, 325 and 345 GHz bands.

For planetary observations, the microwave instrument MIRO [Gulkis06] for the ESA Rosetta Orbiter was launched in 2004, MIRO has two channels at 190 GHz and 560 GHz and employ room temperature planar Schottky diode receivers. Rosetta is devoted to study the comet 67P/Churyumov-Gerasimenko and discover the origins of the solar system and life.

Schottky diodes technology will fly on Herschel and SOFIA, which should be in operation before the end of this decade. They are also candidates for several future planetary missions as TSSM (TITAN), EJSM (Europa Jupiter), and mission for Mars and Earth explorer.

Other applications of Schottky diodes technology include biological and biomedical areas [Siegel04], security and weapons detection, communication, high-resolution radar and imaging, plasma diagnostics by using high resolution imaging system. A high resolution imaging radar at 580GHz has been reported recently [Cooper08], this active submillimeter imager employs all-solid-state devices based on Schottky diode sensors and sources and operates at room temperature avoiding cryogenic system.

It is concluded that the planar Schottky diode technology is a strategic technology for millimeter and submillimeter wave instruments dedicated to the study of the Earth's atmosphere, the study of planets and astrophysics.

2 Millimeter wavelength monolithic Schottky diode-based circuits

This chapter presents a novel method for designing two-pixel integrated heterodyne receiver front-end. To create a compact sub-array, a frequency multiplier and two mixers were integrated within a same mechanical block, a simple waveguide power divider was used for the LO source contribution. The design of the frequency multiplier and the mixer used in this integrated receiver are described individually, experimental results are discussed.

2.1 Modeling tools

The proper design and optimization methods used in this work have been implanted on two software suites: Ansoft High Frequency Simulation Software (HFSS) [HFSS] and Agilent Advanced Design System (ADS) [ADS].

HFSS is a software package that analyzes the electrodynamics behavior of passive structures by using the finite element method. It computes scattering parameter (S-parameter) response and electromagnetic field distributions for passive and three-dimensional structures at high frequency. The final result is an S-parameter matrix that allows the electromagnetic amplitude and the phase of transmitted and reflected signals to be computed directly from a given set of inputs, reducing the full three-dimensional electromagnetic behavior of a structure to a set of high frequency circuit values.

ADS is a powerful electronic design software system. It can offer complete design integration to designers of products such as cellular and portable phones, pagers, wireless networks, and radar and satellite communications systems. The Harmonic Balance simulation method has been used in this work, which is a frequency-domain analysis technique for simulating distortion in nonlinear circuits and systems. Harmonic balance simulation obtains frequency-domain voltages and currents, directly calculating the steady-state spectral content of voltages or currents in the circuit. This method allows one to determine the performance of correspondent circuit.

Figure 2.1 shows the design flow chart for the design and optimization of each circuit by using these two simulators. The three-dimensional structure was first

constructed and the numerical analysis was performed by using HFSS. Thereafter, the physical characteristics of nonlinear element and the numerical results were both implanted in ADS for optimization and determination of the circuit's performance.
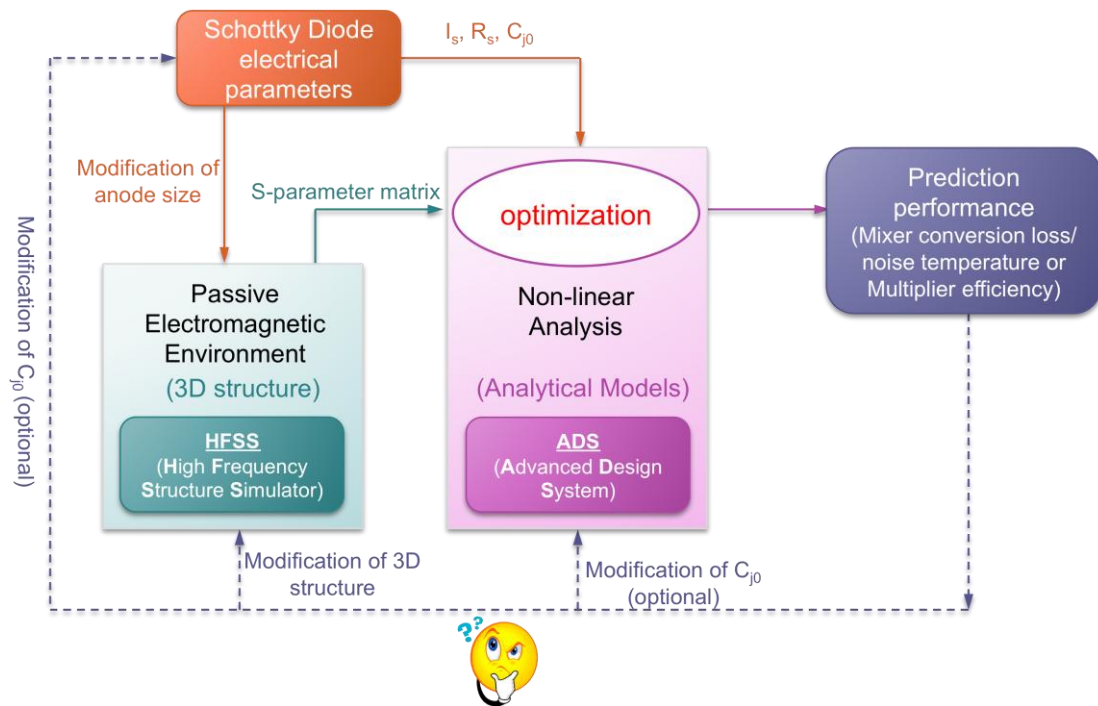
Figure 2.1: Design flow based on two simulators suite.

2.2 UMS Planar Schottky diode

The circuits designed within this work are all based on the UMS MMIC Schottky diode process; Figure 2.2 shows the photo of a single anode Schottky diode from UMS, compared to other typical planar Schottky diode process, no air-bridge to the anode is provided by this process. The epilayer doping and the epilayer length are fixed by UMS BES (Buried Epitaxial Schottky) process.
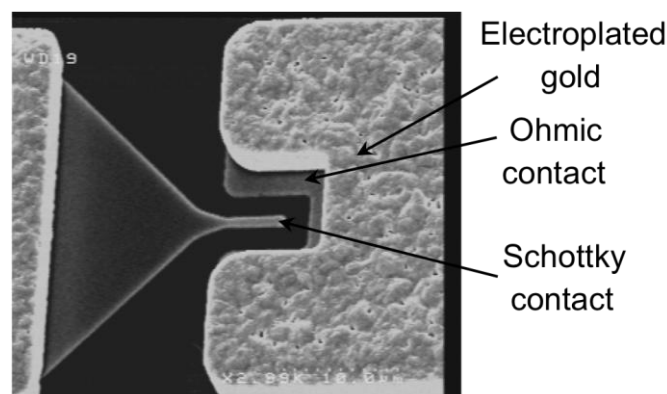
Figure 2.2: Photo of a single anode Schottky diode with 5 μm anode length from UMS.

27

The physical structure of planar Schottky diodes with different layers is shown in Figure 2.3.
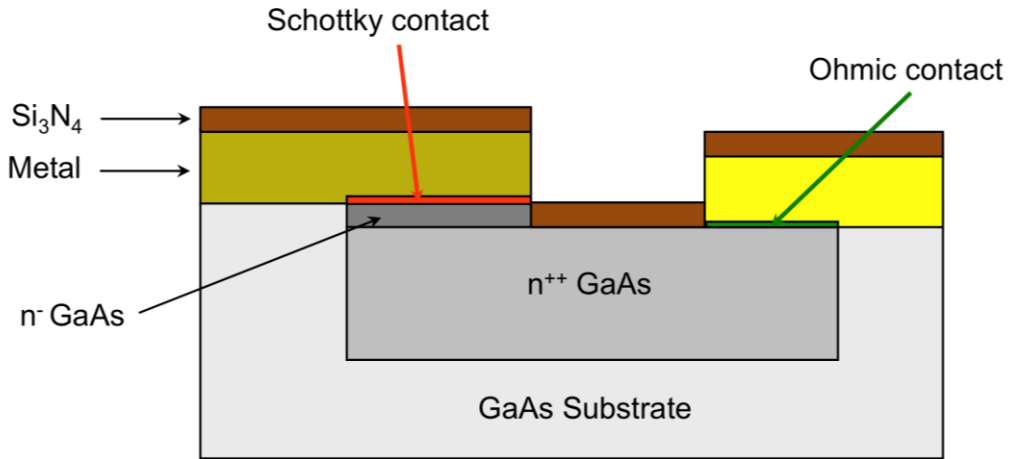
Figure 2.3: Physical structure of Schottky diode of UMS.

As only measurements of diodes (anode gate width) of 4.0 μm, 4.5 μm and 5.0 μm were available when the study started, we used a preliminary study "Report on the Evaluation of the Capabilities of the United Monolithic Semiconductors to Produce Schottky Diodes Based Mixers in the Band 100-380GHz" [Maestrini04b] to estimate the electrical parameters of smaller diodes based on anode dimensions, doping level and edge effects.

a) ideality factor $\eta = 1.2$

b) zero voltage junction capacitances based on the anode dimensions, the doping level and edge effects. [Maestrini04b]:

L (*um*)	Cj0 (*fF*)
1	1.9
2	3.5
3	5.1
4	6.8
5	8.4
6	10.0
7	11.6

Table 2.1 Intrinsic capacitance dependence versus the length of anode.

c) Series resistance Rs [Maestrini04b]:

Anode size (um)	Series resistance
1.0	11Ω (estimated)
3.0	7 Ω (estimated)
4.0	5.5 Ω (measured)
4.5	4.7 Ω (measured)
5.0	5 Ω typical (specs)

Table 2.2 Series resistance dependence versus the length of anode.

2.3   30/90 GHz MMIC Frequency Tripler

Fundamental sources in W-band (75-110GHz) are the key components for various applications including atmospheric remote sensing, radar system and radio astronomy. Many types of multipliers can be used in this frequency region, including active multipliers using transistors and wave-guide varactor diode multipliers. We chose the latter solution in particular. A 6-anode Schottky diode balanced tripler was designed and fabricated. The design of the 90GHz balanced tripler is based on [Maestrini05a]. The tripler uses the so-called open-loop configuration that allows more than two diodes to be easily implanted on chip, increasing the power handling capabilities of the frequency multiplier. This section describes the design method, the simulation results and the experimental results.

2.3.1   30/90GHz Tripler Design

2.3.1.1   Tripler topology

Frequency triplers are complex circuit to design; simultaneous impedance matching has to be achieved in three frequency bands (input frequency, idler frequency and output frequency).

A set of general relations between the real powers at all mixing frequencies in a nonlinear capacitor have been developed by Manley and Rowe [Manley56]. The Manley-Rowe relations are valid for any nonlinear capacitor driven by one or two signals having no commensurate frequencies. They have been applied to parametric amplifiers and up converters as well as to varactor frequency multipliers, and

establish limits to the gain or loss of such components [Maas03]. The two Manley-Rowe relations are:

$$\sum_{m=0}^{\infty}\sum_{n=-\infty}^{\infty}\frac{mP_{m,n}}{mf_1+nf_2}=0 \qquad\qquad (2\text{-}1)$$

$$\sum_{n=0}^{\infty}\sum_{m=-\infty}^{\infty}\frac{nP_{m,n}}{mf_1+nf_2}=0 \qquad\qquad (2\text{-}2)$$

where f_1 and f_2 are the frequencies of the two excitation signals, and $P_{m,n}$ is the average real power into the capacitor at the frequency $|mf_1 + nf_2|$, with m, n are integers. Then for a frequency multiplier, there is only one excitation signal f_1, two equations above becomes

$$\sum_{m=0}^{\infty}P_m=0 \qquad\qquad (2\text{-}3)$$

where P_m is the power in the diode at frequency mf_1. In the ideal case, all the input power must be converted into output power at the harmonics of f_1, which indicates from the equation (2-3). In a frequency multiplier of order m, the highest value of the output power P_m at the frequency mf_1 occurs when only P_1 and P_m are nonzero, therefore the output power P_m is equal to the input power P_1, the theoretical conversion efficiency of the multiplier is 100% as shown in [Penfield62].

In order to achieve this optimum conversion efficiency, there must be no real power in the circuit at any of the unwanted harmonic frequencies. The only way to meet this requirement is when the diode's junction is terminated in a pure reactance at all harmonics other than the desired one. In practice, however, much of the power could be dissipated in the series resistance of the diode or in the passive circuit. Consequently, the theoretical efficiency can't be achieved in a real design.

Two different approaches [Maas03] could be used to eliminate power dissipation in the series resistance, one might be tempted to open-circuit the diode at all unwanted harmonics; then the unwanted harmonic currents in the series resistance would be zero and no power would be dissipated. Another approach would be to short-circuit the diode at all unwanted harmonics; a short circuit would not eliminate the dissipation in the series resistance, but would prevent harmonic power dissipation in the output network.

Consequently, the topology of the frequency multiplier plays an important role in the multiplier design. Several efficient topologies of Planar Schottky diode balanced frequency triplers were demonstrated in [Bradley92, Erickson00] at millimeter and submillimeter wavelength, and more recently at THz frequencies [Maestrini01, Maestrini04a]. As described previously, the matching at the second harmonic is particularly critical when designing a frequency tripler: the impedance at the second harmonic should be as close as possible to a pure reactance [Maestrini05b]. This condition is met when the circuit is balanced and the second harmonic is trapped in a virtual loop.

In our design, this loop shows is created by 6 diodes that are in series at DC but appear to be in an anti-parallel configuration at the RF, due to the symmetry of the excitation and the symmetry of the circuit (see Figure 2.4). This virtual loop can only work if the suspended microstrip line that the diodes are connected to cannot propagate the parasitic (TE) mode at the second harmonic. The matching of the diode is performed both by a succession of high and low impedance sections printed on chip and by the input and the output probes with their respective back shorts. To widen the bandwidth, the circuit features additional matching elements in the input and output waveguides, made with a succession of waveguide sections of different heights and lengths.
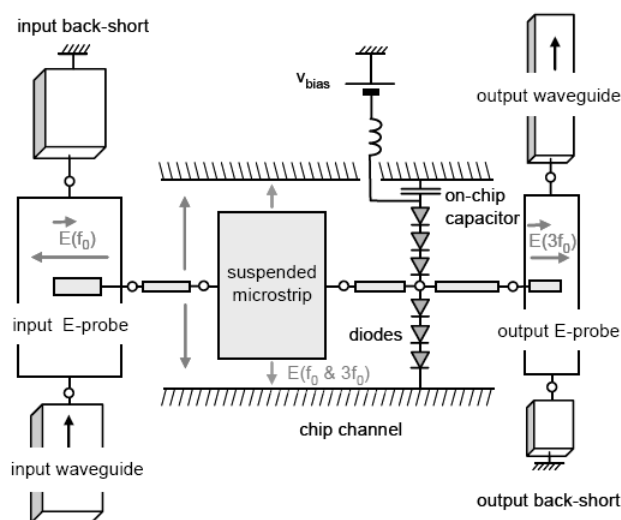
Figure 2.4: Block diagram of the 90 GHz tripler. Additional waveguide sections are used for the input and output matching is not shown (reproduced from [Maestrini05b]).

2.3.1.2 Tripler optimization

To achieve the optimum efficiency in a frequency multiplier, it requires to use a varactor that has low series resistances and select a capacitance that is appropriate for the frequency and power level at which it is to be operated, as well to match the input and output impedance. Detailed design steps are described in this section. The tripler chip is composed of different parts that are shown in Figure 2.5. The chip is suspended in the waveguide channel shown in the right corner of Figure 2.5.
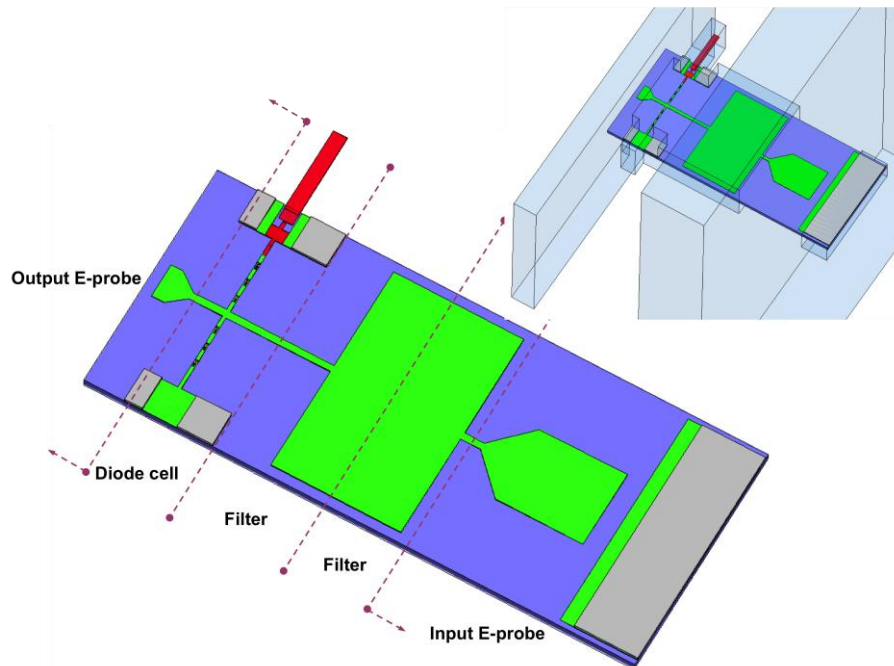
Figure 2.5: Different parts of the tripler circuit when it is been optimized; the chip in the waveguide view is shown on the right corner.

a) Optimization of the diode cell

The first step is to optimize the diode cell that consists in the part of the circuit, which includes the diodes, a section of the chip-channel and two sections of the propagating line at the centre of the chip. A custom three-dimensional model (as shown in Figure 2.6) was constructed using the Ansoft HFSS 9.2 suite and the custom optimization bench was implanted in Agilent ADS. The optimum diode junction capacitance and bias voltage are determined at the same time during this optimization.

The thickness of the substrate was chosen to be 50μm, the nominal thickness of the standard Schottky process of UMS is 100μm, processing the wafer at different thicknesses constitutes an amendment to the standard process and therefore

introduces additional costs and constraints. On the other hand, for best performance, generally it is preferable to work with a thinner substrate, especially when working with high dielectric constant material like gallium arsenide. The choice of 50um seems to be a good compromise between performance, flatness (too thin substrate should produce warpage) and feasibility.

The diode cell features six Schottky diodes using UMS BES process with wide gate width (>10μm) and modified finger shape (see Figure 2.7) with respect to UMS classic diode structure (see Figure 2.2). In this work we call the gate width as the anode length. Compare to the diodes used in the subharmonic mixer (presented later in Chapter 2.4), greater capacitance is needed that implies a much larger junction area. Such a large area also improves heat dissipation; since most of the input power is dissipated in the diodes. Considering that the width of the anode (gate length for UMS) is a fixed parameter imposed by the UMS process, only a change of the anode length can be operated. According to the study of UMS Schottky diode [Maestrini04b], the junction capacitance is estimated in function of the anode length and doping level.
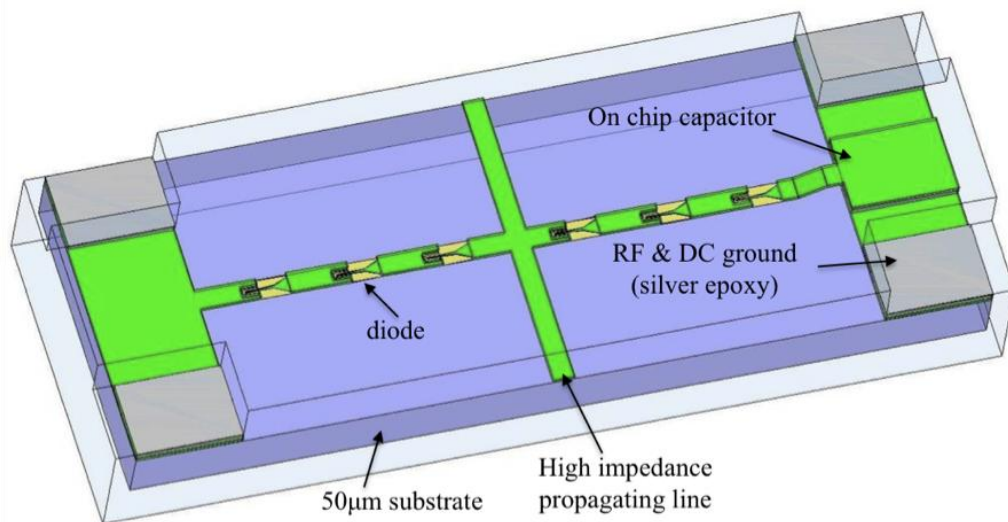
Figure 2.6: Diode cell used to optimize the channel cross-section dimensions, the location of the 6 anodes and the anode size.

Accurate three-dimensional model of diodes shown in Figure 2.7 were drawn with HFSS that features all the relevant details such as the exact shape of the finger, pads and different layers of materials that define the diode. It is important to take into account the ohmic and dielectric losses of the circuit during the simulations. The

definition of the wave ports and the plane of de-embedding in HFSS are two crucial points to achieve a correct simulation.
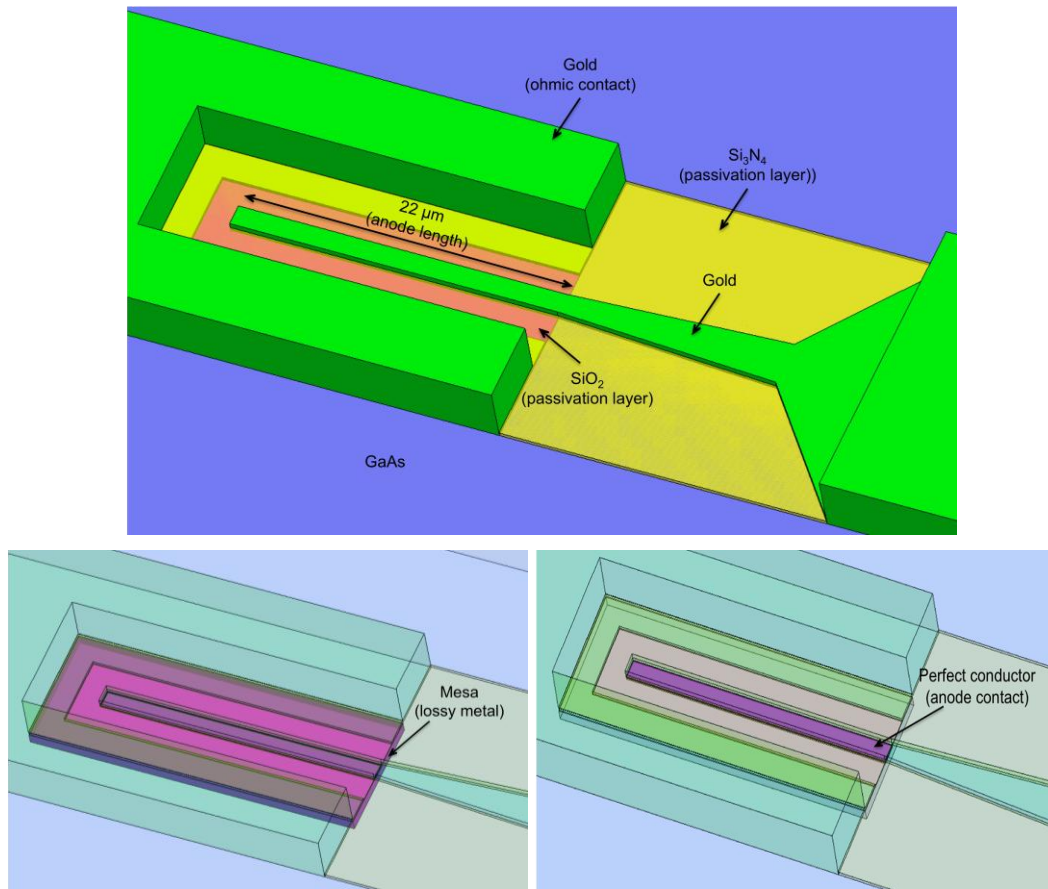
Figure 2.7: Three-dimensional schematic of modified UMS Schottky diode structure with a long anode. Different colours present different layers of diode.

Wave ports definition:

Wave ports in HFSS represent places in the geometry through which excitation signals enter and leave the structure. They are essential to calculate the S-parameters of the structure. As shown in [Thomas04] the definition of the wave port located at the exact location of the Schottky contacts is critical for accuracy. If they are not properly defined, the parasitic capacitance of the diodes is under-estimated. In our simulation, the internal wave port is defined at the location of the anode contact, which is shown in Figure 2.8. A layer of perfect conductor was defined as the port boundary condition; the wave port area was defined at the contact layer between the anode and the diode port. In addition, an integration line is defined as a vector that can represent either the calibration line that specifies the polarity field pattern at a port or the impedance line along which to compute the characteristics impedance for a port. This integration line is critical since it defines the polarity of the diode. If no

line is specified, the polarity will be randomized. A multi-diode circuit with random polarity will produce inconsistent results in nonlinear simulations where the polarity of the diodes connected to the port does matter.
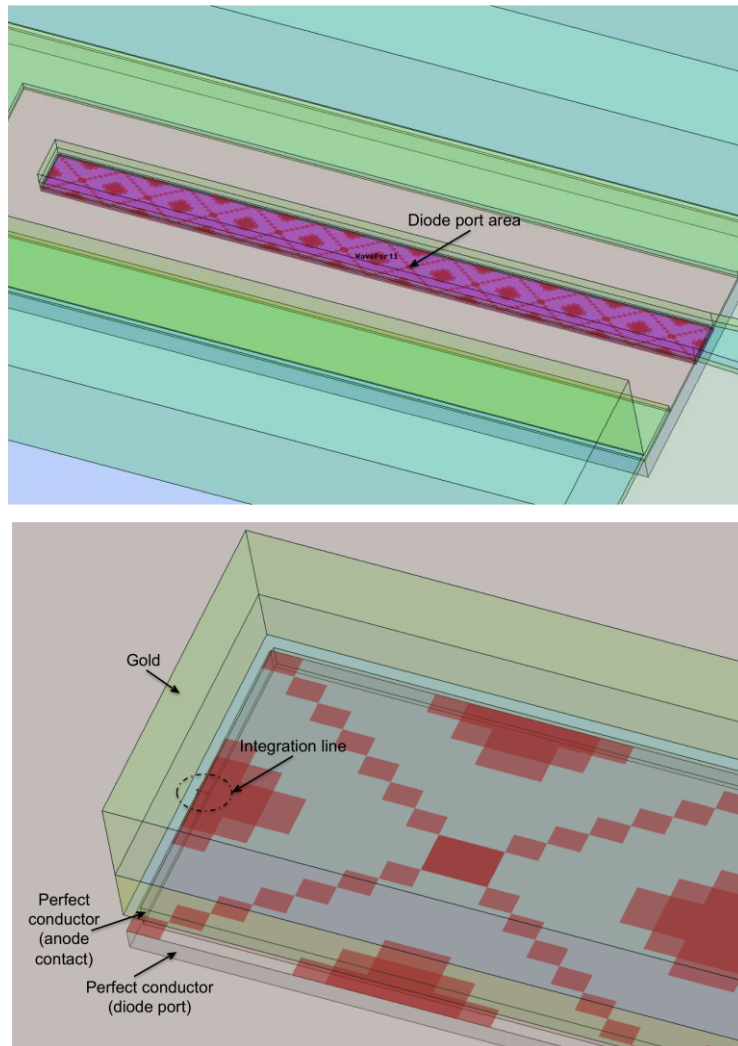
Figure 2.8: Definition of the wave port for the diode contact and the integration line.

De-embedding plane:

The de-embedding plane of a given wave port (see Figure 2.9 blue flash) is a virtual plane inside the structure, orthogonal to the propagation line connected to this port. The S-parameters are recalculated as if the wave port was physically moved towards the location of this virtual plane i.e. as if the propagation line was shorter by the amount of the de-embedding distance. De-embedding is a pure mathematical transformation of the S-parameters matrix. It is an essential operation that enables precise modeling: actually if the ports are too close to discontinuities they can

interfere with the near field around these discontinuities (presence of evanescent modes) and therefore alter the calculations.
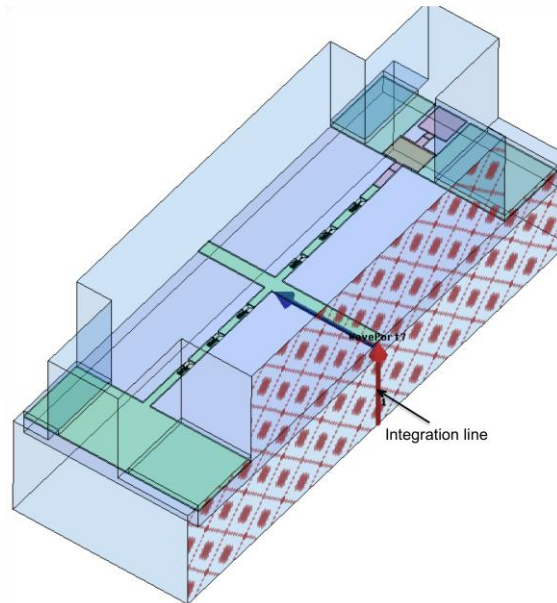
Figure 2.9: Definition of the wave port of a suspend microstrip, the red flash represent the integration line and the blue flash represent the de-embedding plane.

Figure 2.9 shows the 3D model of the diode cell with one defined wave port, this eight-port diode cell structure is simulated in HFSS and its calculated eight-port S-parameter data are then imported into the harmonic-balance simulation bench (see Figure 2.10). This harmonic balance bench has been developed in ADS to determine which junction capacitance and bias voltage give the maximum output power. This is a one-tone nonlinear analysis; harmonic generation will occur in the nonlinear devices. The voltages and currents across the diodes related to desired harmonic products generated by the diodes are measured to calculate the performance of the tripler. Only a limited number of harmonic orders are included in the harmonic balance calculation. The number of harmonics needs to be sufficiently large to represent nonlinear signals. An increase in the order slows down the simulation considerably or results in excessive memory usage. The lower the order, the greater the Harmonic Balance truncation errors as a result of the Fourier truncation in the solution representation. Eleven harmonics have been considered in the tripler optimization to avoid the truncation error while producing an efficient calculation.

The optimization is performed for a given input power and output frequency. Due to the expected limitations induced by the thin epilayer of 100nm and a low doping level of $10^{17} cm^{-3}$, only 50-60mW of input power could be safely handled by

36

six diodes (expected breakdown voltage is -7V per diode). The doping level defines the breakdown voltage, which mainly controls the power handling capability per anode [Maestrini05a].
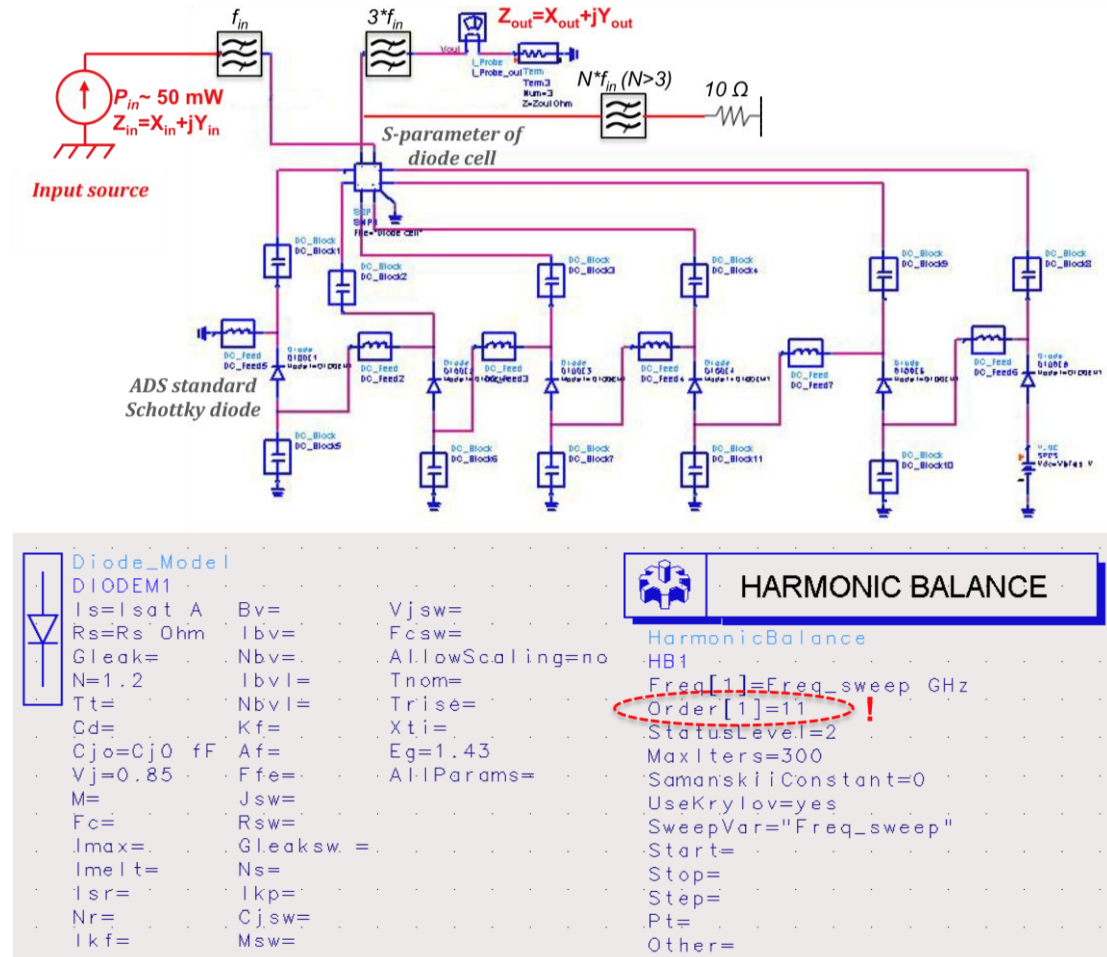
Figure 2.10: Simplified equivalent schematic developed in ADS for the diode cell optimization.

The optimization is semi-empirical since no equivalent model of the diode cell has been built. For the first iteration of the design, the standard Schottky diodes model (see Figure 2.10) in the ADS component library has been used, which is a simple analytical model for Schottky diodes, where the series resistance, the zero-voltage junction capacitance and the saturation current can be defined. Several different configurations have been studied, the final diode cell is shown in Figure 2.11, with the following characteristics: an ideality factor $\eta = 1.2$, saturation current $I_{SAT} = 4.10^{-15}$ A, series resistance $R_s = 5\ \Omega$, the optimum junction capacitance $C_{j0} = 37$ fF (optimized) and the anode length of 22μm. The 6 diodes are connected in series and integrated on a 1360μm wide substrate, suspended in a channel with a width of

1400μm and a height of 550μm. Considering an available input power of 50mW at 30GHz and a bias voltage of -13V for 6 diodes, the compromise between efficiency and bandwidth was found with the above characteristics.

For this topology the rule found in [Maestrini05b] was used: the optimum C_{j0} per diode is linked to the channel cross-section perimeter; the longer the perimeter the smaller the junction capacitance.
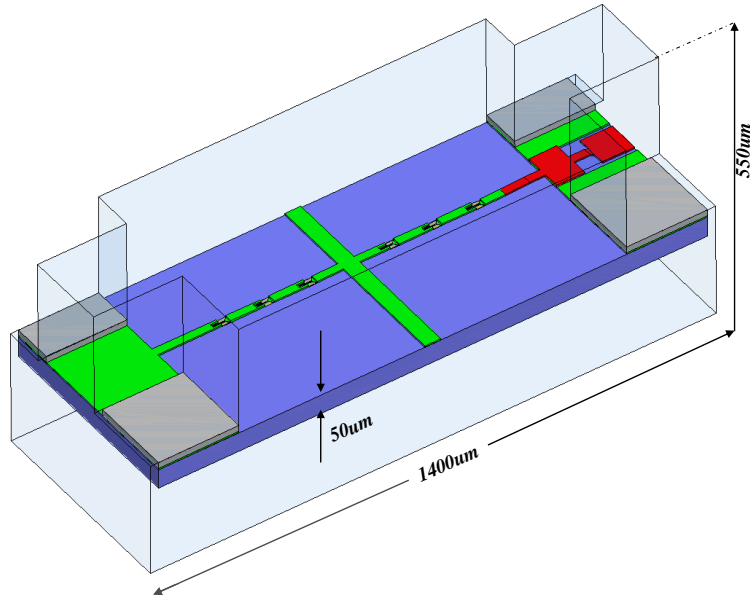
Figure 2.11: Schematic of the final diode cell inside the chip channel with 6 diodes in series (C_{j0} = 37 fF each diode).

It is noticed that the height of the channel is a parameter that has a great influence on the matching of the diodes but much less on the cut-off frequency of the parasitic modes inside the chip-channel. It can therefore be easily adjusted to optimize the performances. The other rule is that the diodes should be separated by slightly uneven distance (due to the physical size of the mesas that breaks partially the symmetry).

b) **Matching circuit – Input, Output probes and waveguides**

Once the size of the anodes and the dimension of the channel are determined, the matching circuits to the diode cell that include the suspended microstrip lines (detailed in Chapter 2.4.2.3), the input and output E-probes will be optimized. The input and output probe are used to get the maximum matching at the input and output sides. In order to reduce the chip dimensions and the losses, a minimum number of

matching circuits are used in the design. Figure 2.12 shows the three-dimensional model of the output probe inside the reduced height output waveguide.
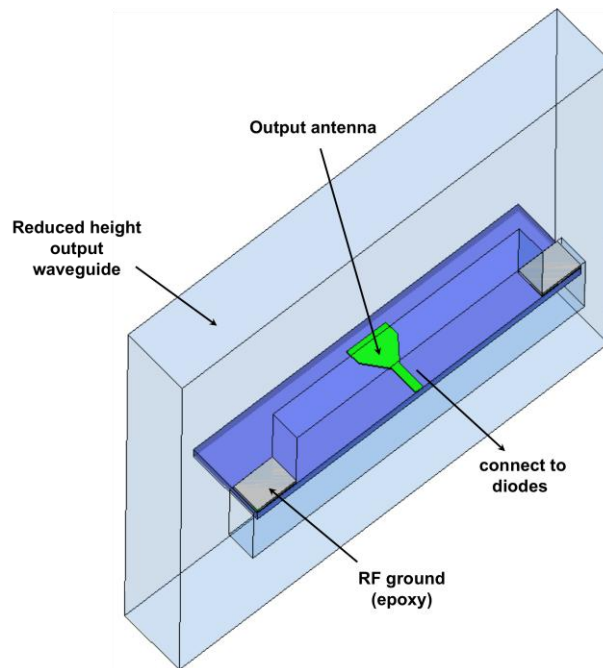
Figure 2.12: Schematic of output antenna with the reduced height output waveguide.

To widen the bandwidth, the circuit features additional matching elements in the input and output waveguides, made with a succession of waveguide sections of different heights and lengths. Reducing the height of waveguide was found to be necessary in order to achieve broadband operations [Hesler97, Shi97]. Two sections of reduced height waveguide were used at the input and output waveguide. The reduced width of output waveguide was used to prevent the second harmonic propagating to the output.

c) DC bias scheme

Special attention was put on the biasing scheme that is usually tricky for high frequency circuits. UMS BES process provides on-chip capacitors that can be small enough to fit on the multiplier chip. This capacitor could provide for RF short and the DC decoupling. The RF grounding to the block will be made by silver epoxy glue; the DC line will be connected to the on-chip-capacitor via a wire-bond. If beam-leads were available, a direct connection to the DC line would be possible without the use of a wire-bond, and the RF grounding could be provided directly via its beam-leads by shorting to the block.

d) Global optimization

The electrical structures of different parts of the tripler were calculated separately in HFSS, which include the input and output E-probe, the diode cell and the microstrip filter (see Figure 2.5). To optimize and analyze the performance of the tripler, an equivalent circuit composed of different parts of the tripler was created in ADS, which is similar to the circuit shown in Figure 2.10. The simplified version is shown in Figure 2.13, additional filters are needed to decouple the input, output and idler frequency signals. Separated frequency band (the fundamental frequency f_0, the second harmonic frequency $2f_0$ and the third harmonic frequency $3f_0$) simulations have been applied for the input and output circuit.
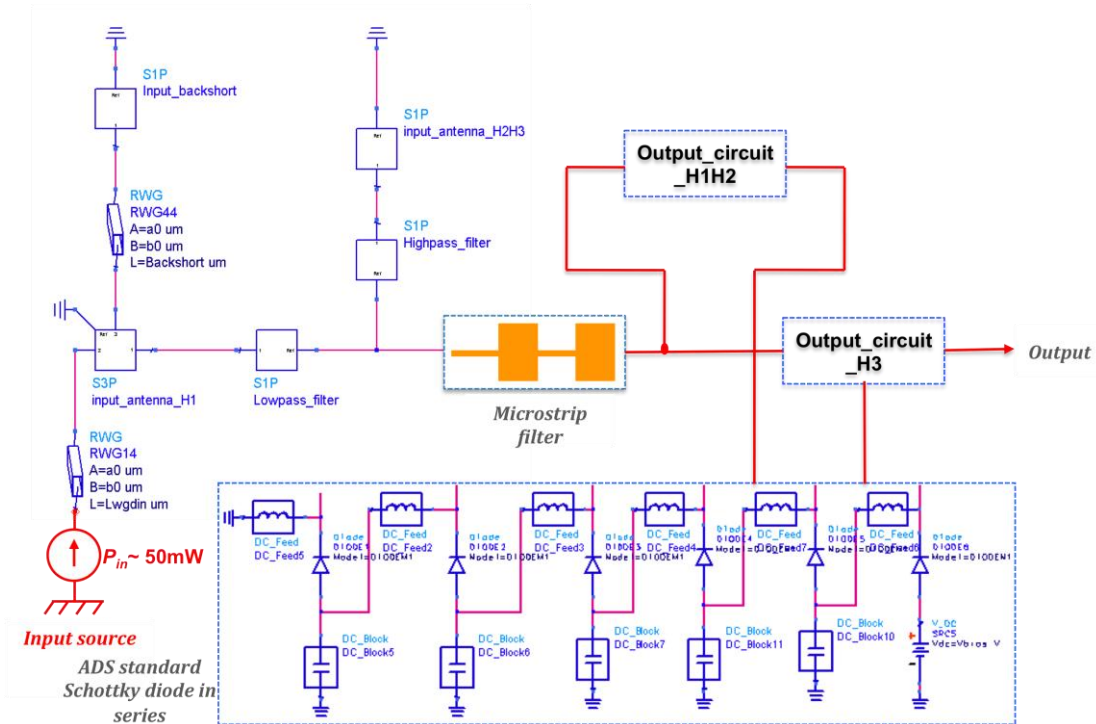
Figure 2.13: Equivalent nonlinear schematic of the tripler in ADS for the global circuit optimization.

Certain parameters should be optimized to achieve the best efficiency over a broadband: the distance of the diodes to the output waveguide (shown in Figure 2.14), the length of different suspended microstrip sections, the position of waveguide back shorts etc.
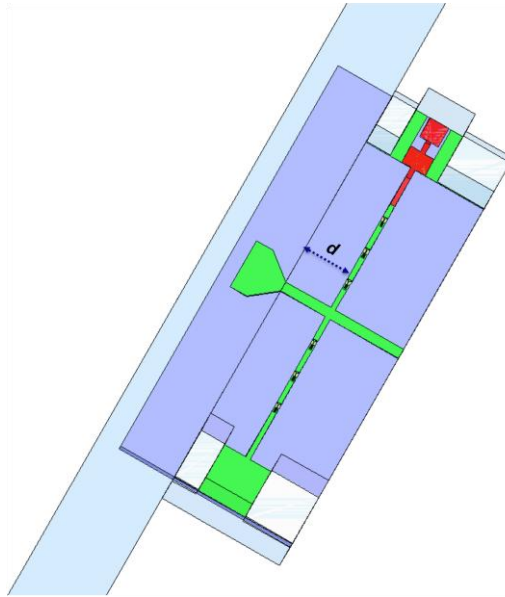
Figure 2.14: The distance from the diodes to the board of the output waveguide.

The distance of the diode to the output waveguide board ***d*** is proposed to be as small as possible. Best performance is obtained with the smallest distance; simple simulation with different distance is shown in Figure 2.15, as the distance is increased, the efficiency of the tripler is decreased significantly. However, the mechanical machining and the circuit processing limit the minimum value of d.
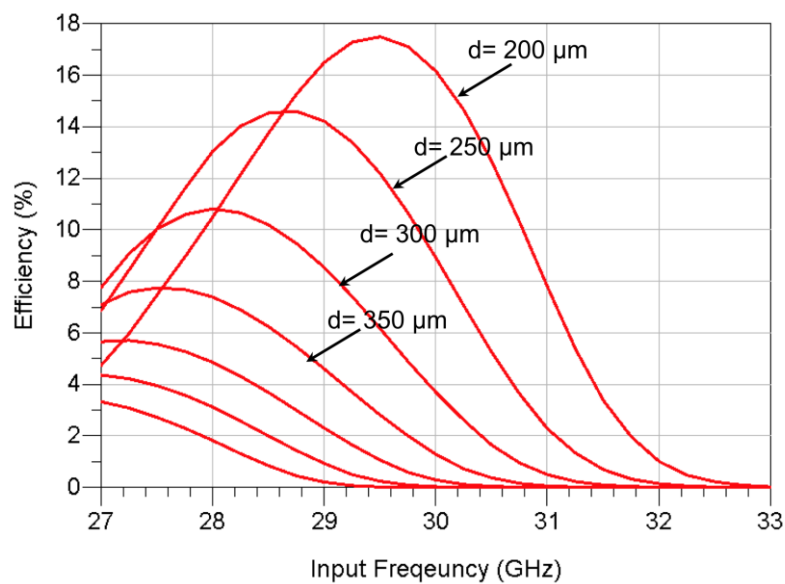
Figure 2.15: Influence on the efficiency of the tripler by the distance of the diodes to the output waveguide d.

41

2.3.1.3 Complete tripler

The tripler block is split in the E-plane of the input and output waveguides, thus simplifying the assembly of the tripler chip and reducing waveguide losses. The planar Schottky diodes are monolithically fabricated on the 50μm-thick GaAs substrate and connected in series. The tripler chip is suspended in a microstrip channel of 1400μm*550μm cross-section, inside this channel, only a quasi TEM mode can propagate at all the frequencies up to 100GHz. A schematic of the tripler chip and the chip with its waveguide are shown respective in Figure 2.16 & Figure 2.17. An E-plane probe is located in the input waveguide to couple the input signal into the suspended microstrip line, these suspended microstrip lines have different impedances and are used to prevent the third harmonic frequency signal from coupling into the input waveguide. Another E-plane probe couples the third harmonic signal that produced by the planar diodes into the output waveguide.

The housing block of this 90GHz tripler was drawn as well with Ansoft HFSS 9.2. Half bottom part of the waveguide block is shown in Figure 2.18 (a), the tripler chip is flip mounted in the block and a number of capacitors are used for the DC bias lines connection via a wire bond. Two close views were shown in Figure 2.18 (b) & (c).
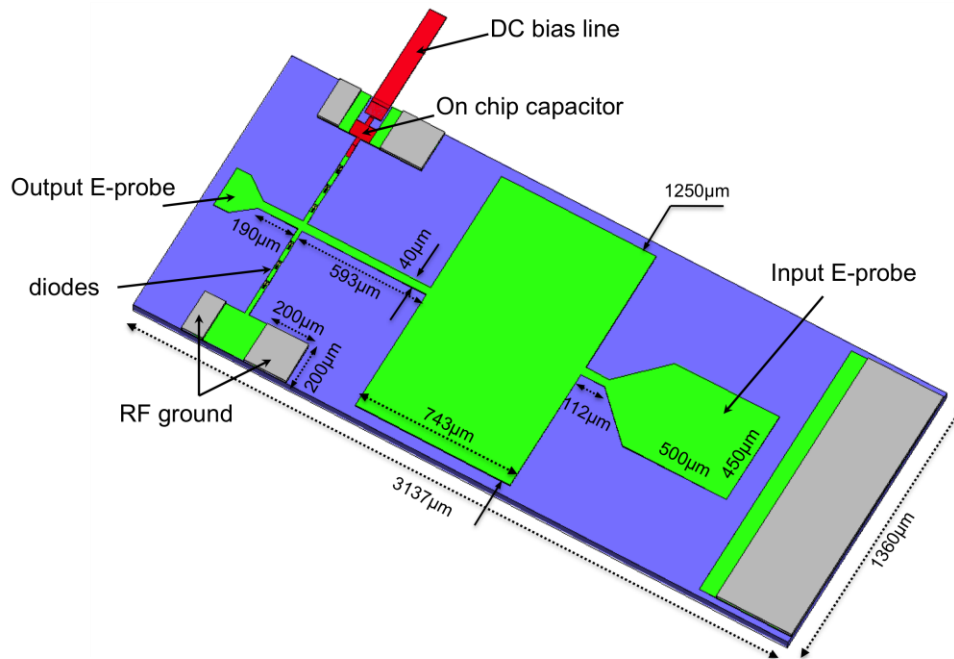
Figure 2.16: Schematic of the final tripler chip on 50um-thick GaAs substrate.
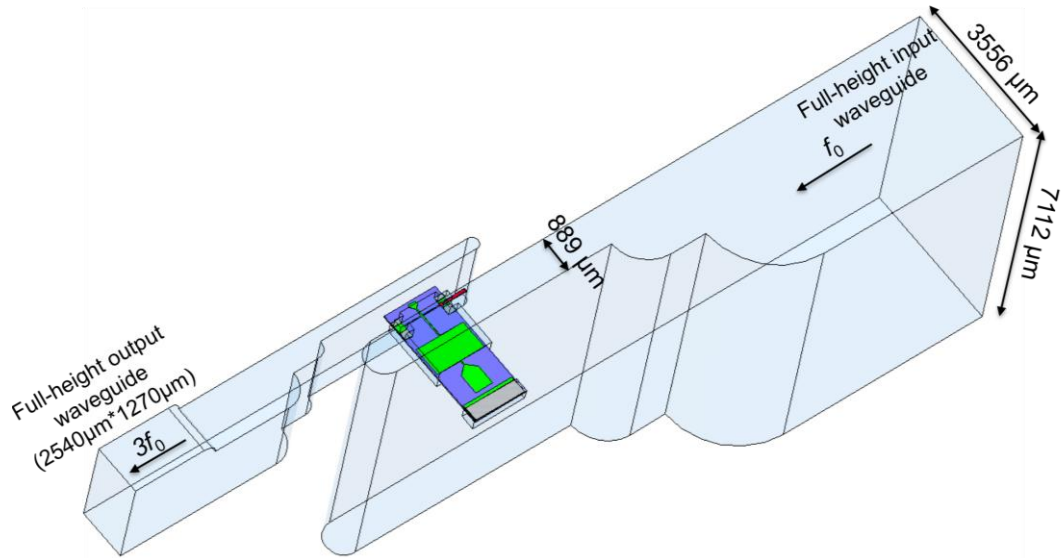
Figure 2.17: Schematic of the 90GHz tripler with input and output waveguide matching circuit.

(a)

43

(b)   (c)
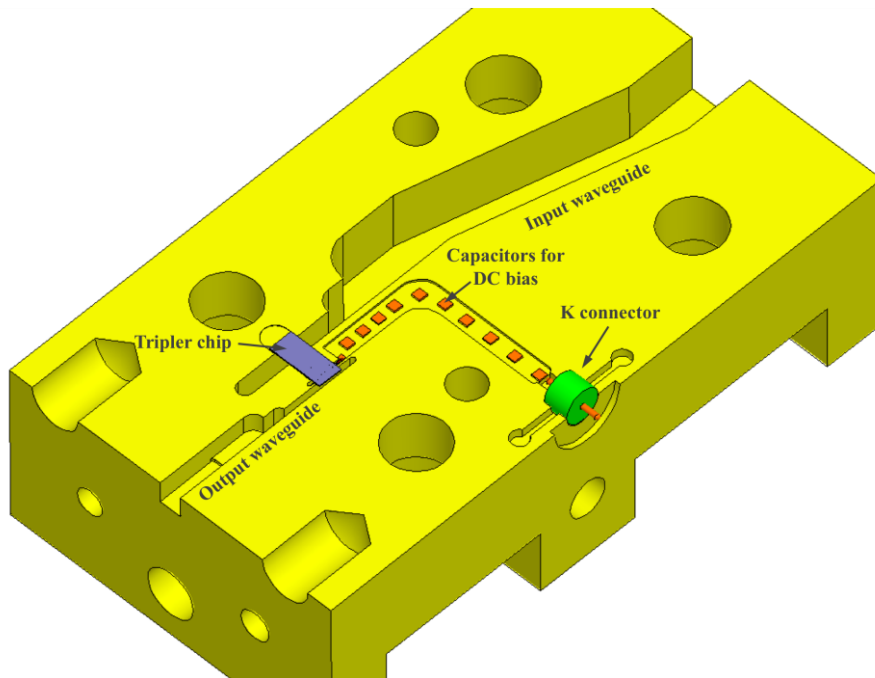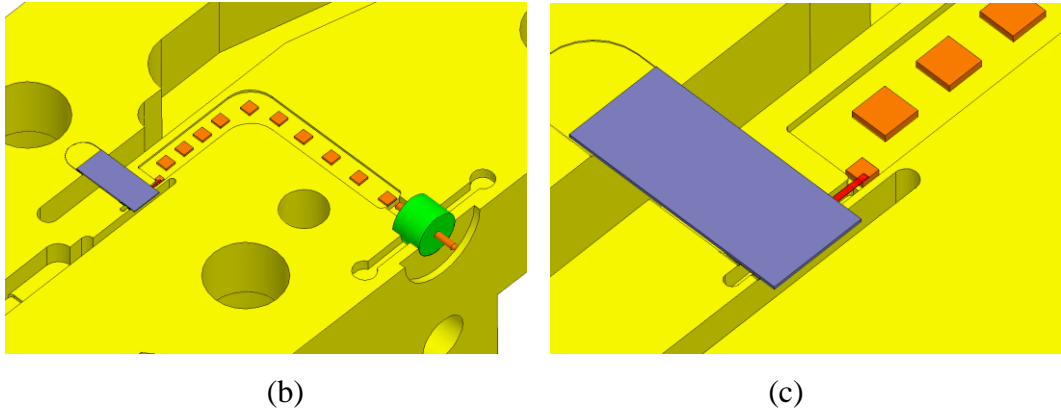
Figure 2.18: (a) 3D view of the bottom part of the waveguide block with the tripler chip, (b)&(c) close up views in the block.

2.3.1.4 Predicted Results

The predicted performance of the tripler is presented in Figure 2.19. As shown in Figure 2.19 (a), the coupling at the input frequency for each diode has a good balance between them, the output matching is above 90% over the band. The efficiency is more than 12% from 87- 97GHz and with the output power over 6mW for an input power of 50mW and 13V inverse bias for six diodes.
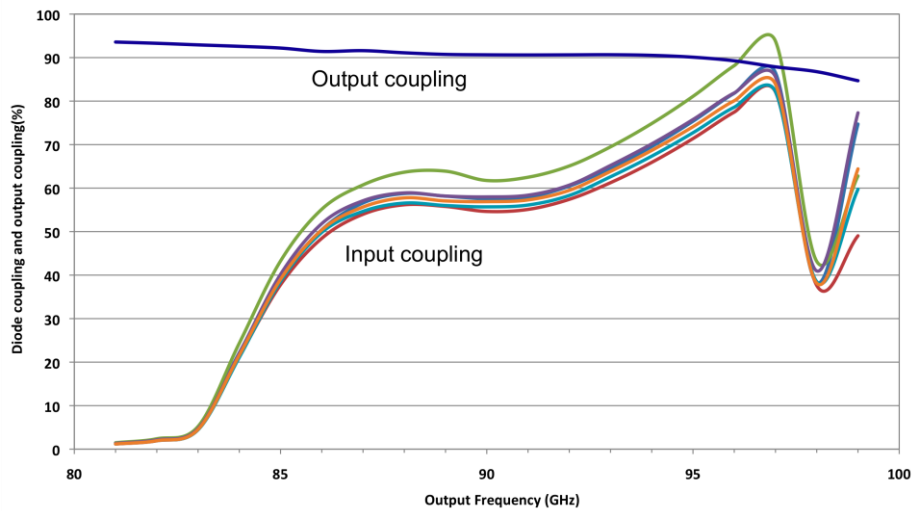
(a)
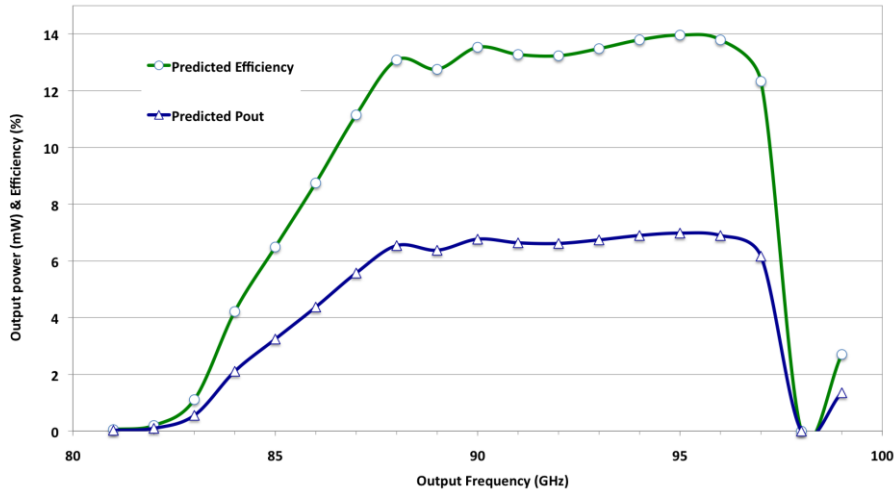
(b)
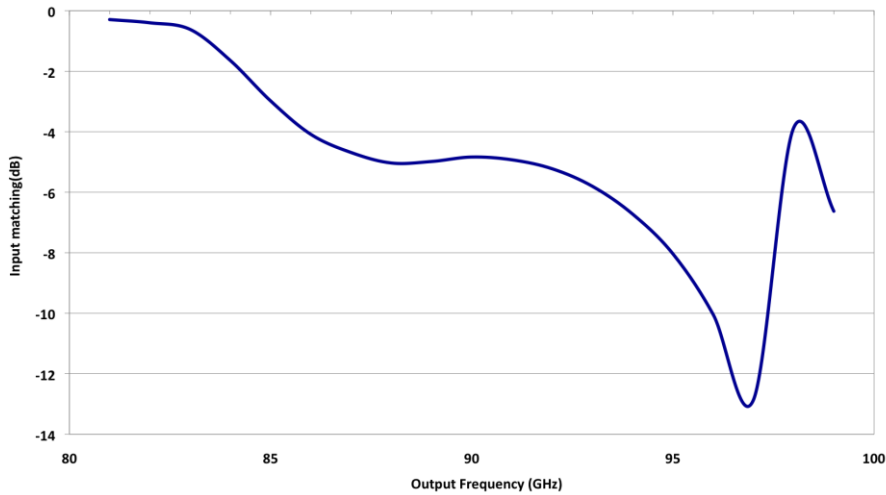
(c)

Figure 2.19: Predicted performance of the 90GHz tripler (a) Power coupling for each diode (%) at the input frequency and the output coupling versus output frequency, (b) predicted efficiency (%) and output power (mW) versus output frequency for a constant input power of 50mW, (c) Predicted input return loss (dB) versus input frequency.

2.3.2 Measurement of UMS MMIC 30/90 GHz Frequency Tripler

This MMIC 30/90GHz frequency tripler chip was fabricated by UMS. The machining of the block and the mounting of the tripler chip in the housing block have been performed at RAL. Figure 2.20 shows several photos during the assembly process.
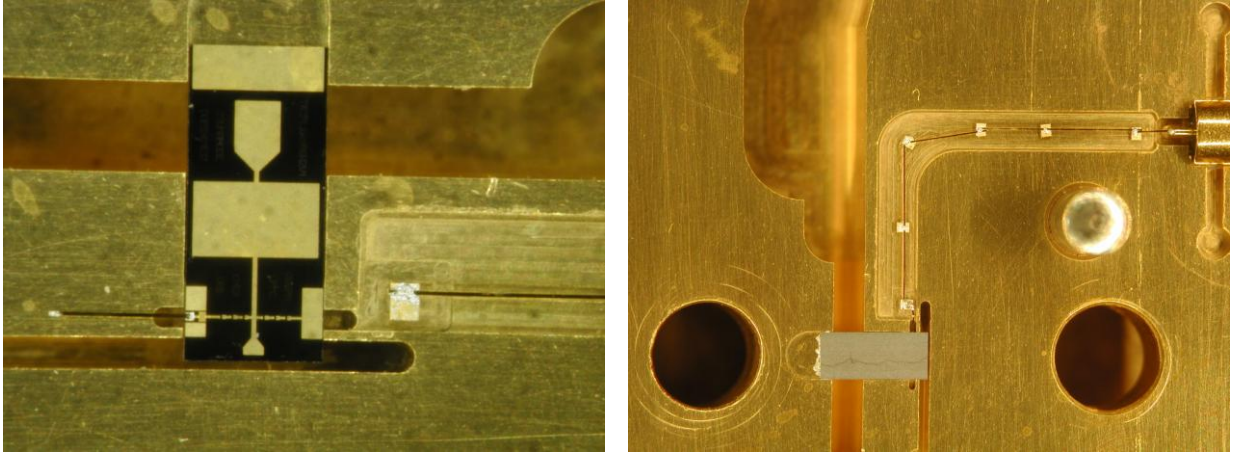
Figure 2.20: Photo of the half block with the tripler chip in the channel before mounting (left) and the tripler chip mounted on the block with its DC bias (right).

2.3.2.1 Test bench

For the experiments, a 20-40GHz source chain has been set up by using several commercial components. Figure 2.21 and Figure 2.22 show a schematic and photograph of the test setup for 30/90GHz tripler measurement at LERMA. The input signal from 8.0 to 18.8GHz was generated by the internal tunable sources from AB Millimetre Vector network Analyzer, which was used to drive an active frequency doubler (Miteq model MAX2M200400-20P). This commercial active doubler can provide more than 100mW from 20 to 40GHz, the isolator has an insertion loss of maximum 1 dB and the directional coupler has an insertion loss less than 1.3 dB.
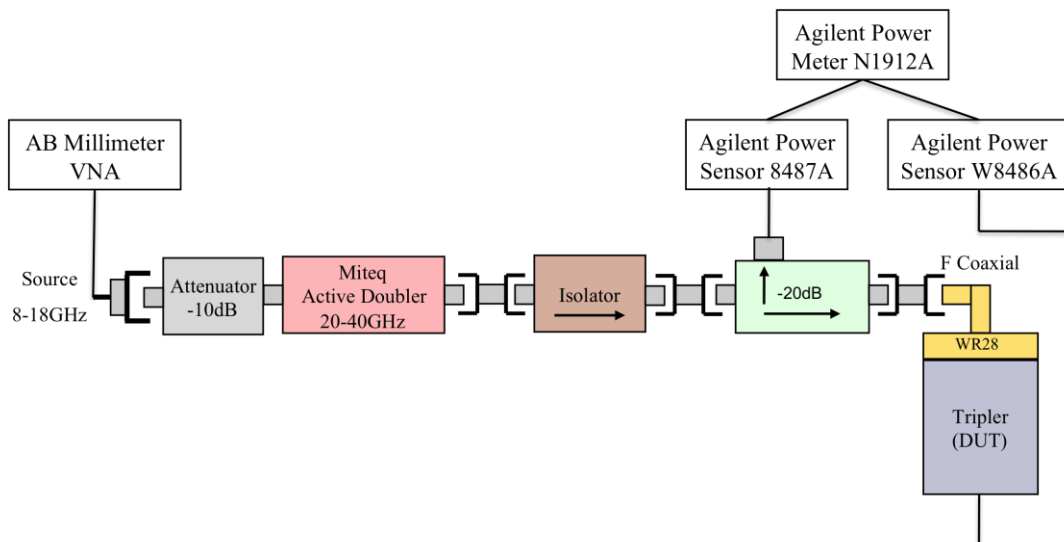
Figure 2.21: Diagram of the test setup for 30/90 GHz tripler measurements.
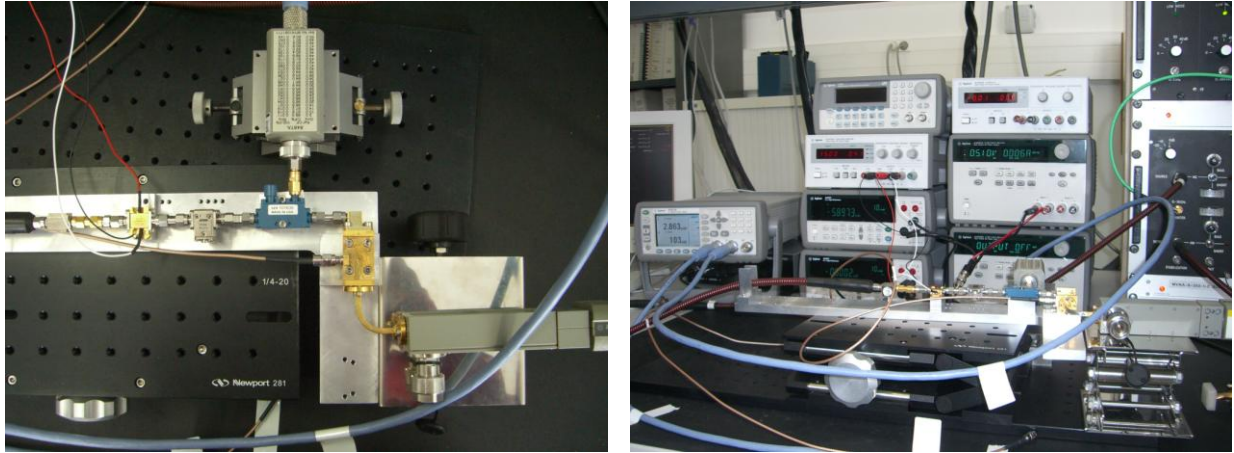
Figure 2.22: Photos of the test setup for 30/90GHz tripler measurements.

The output power of the 30/90GHz tripler was measured with an Agilent power sensor W8486A that covers W-band. An Agilent power sensor 8487A was used to measure the injection power coupled into the directional coupler; with this measured coupling power the injection power into the tripler can be extracted. Nevertheless, a difficulty was observed with the measurement setup described above. Since there is no isolator between the coupler and the tripler, the reflected signal at the input port of the tripler could couple into the coupler; therefore the measured power at the coupled port was a combination of the power of the injected signal and partly of the reflected signal from the tripler. To avoid this source of inaccuracy, the tripler is therefore disconnected; the injection power was measured directly at the output of the coupler.

2.3.2.2 Measured results

Two triplers with different anode size have been measured; T90 SN1 is the one with an anode length of 22µm and T90 SN2 with an anode length of 17µm. Though the tripler chip was optimized for the 22 µm anode-length diode, two variations of the anode size were proposed for the circuit fabrication, the nominal one (22µm long anode) and the smaller one (17µm long anode), in order to take into account a possible underestimation of the diode capacitance.

Input power, output power and efficiency versus output frequency are shown respectively in Figure 2.23 and Figure 2.24 for two triplers with different anode size. The bias was optimized for each frequency, ranging from -8 to 0V across six diodes in series at DC. The measured DC currents were in the range 2-8mA. The calibrated input power was 60-125mW from 75 to 98GHz. For the tripler with 22µm long

47

diodes, a peak output power of 3.67mW at 84GHz was measured; the efficiency was calculated to be about 3.4% at this frequency. And peak efficiency was measured at 4.2% at 86GHz (see Figure 2.23). Then for the tripler with 17μm long diodes, the measured output power was more than 3mW in the band 83-92GHz, with a peak efficiency of 5% at 86GHz. The band of the tripler was shifted to the lower frequency range compared to the predicted result.

Figure 2.25 shows the comparison of the efficiency between two triplers with different anode size. The tripler with 17μm long anode has better performance than the one with the larger anode, which suggests that the capacitance of the diode was underestimated during the simulation.
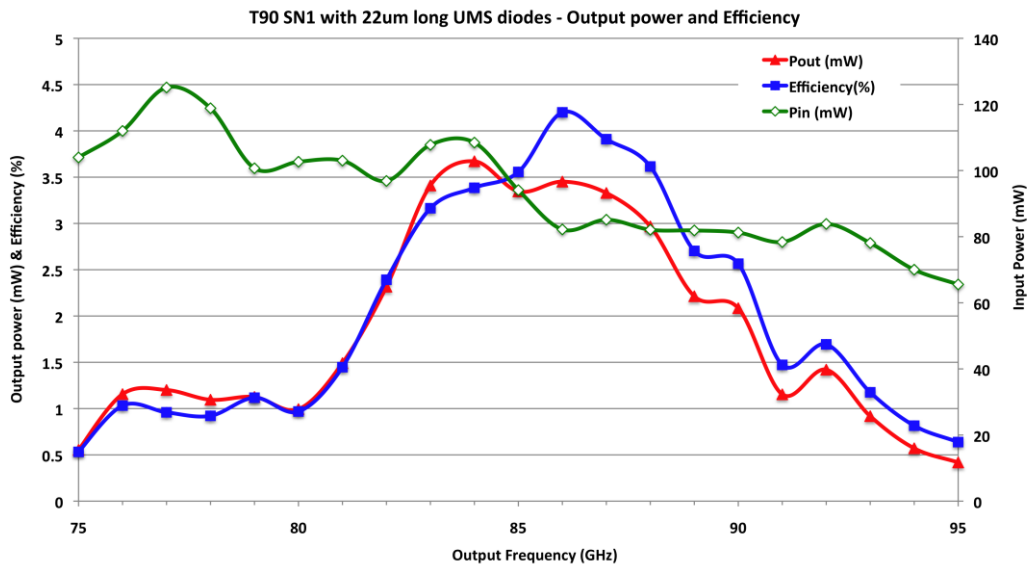
Figure 2.23: The plain curve with filled square markers and the plain curve with filled triangle show respectively the measured efficiency and the output power of the 90GHz tripler with optimized bias for each frequency, the plain curve with opened square markers shows the input power injected into the tripler.
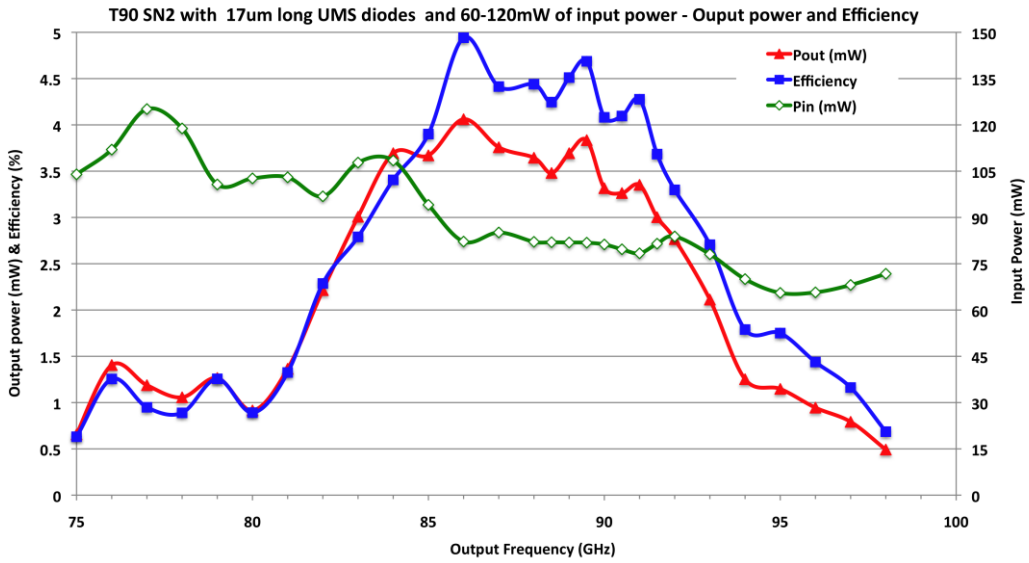
Figure 2.24: The plain curve with filled square markers and the plain curve with filled triangle show respectively the measured efficiency and the output power of the 90GHz tripler with optimized bias for each frequency, the plain curve with opened square markers shows the input power injected into the tripler.
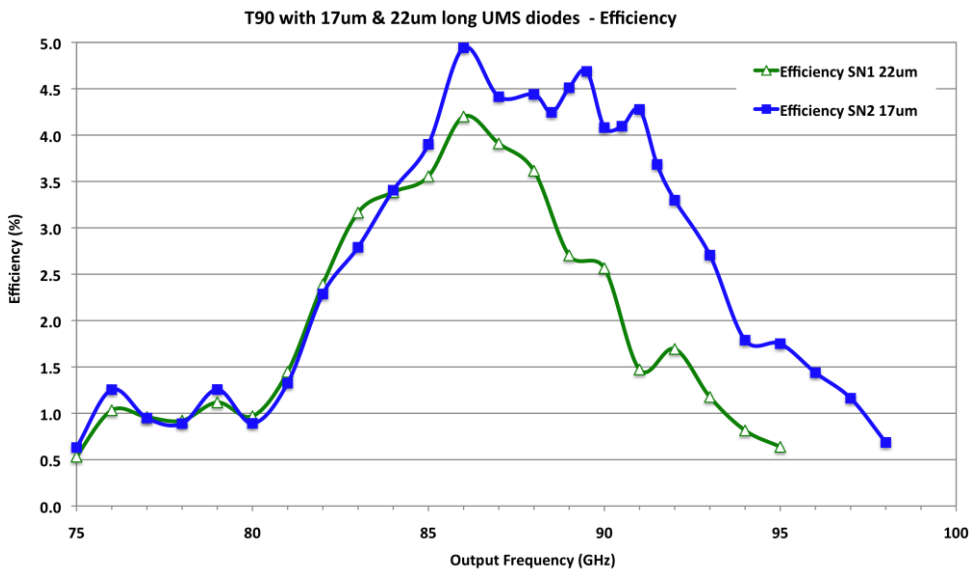
Figure 2.25: The top curve with filled square markers and the plain curve with opened triangle show respectively the measured efficiency of the tripler with 17μm long anode and 22μm long anode.

Further measurements on the input matching have been performed. Figure 2.26 and Figure 2.27 show respectively the return loss of tripler with two different anode sizes.
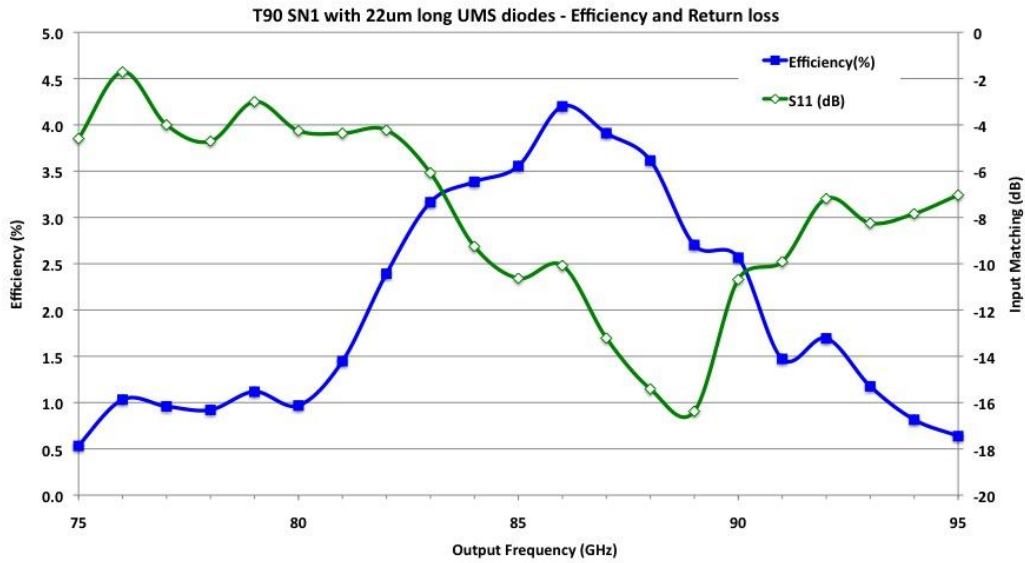
Figure 2.26: The plain curve with filled square markers and the plain curve with opened square markers show respectively the measured efficiency and the return loss of the 90GHz tripler with 22µm long diodes.
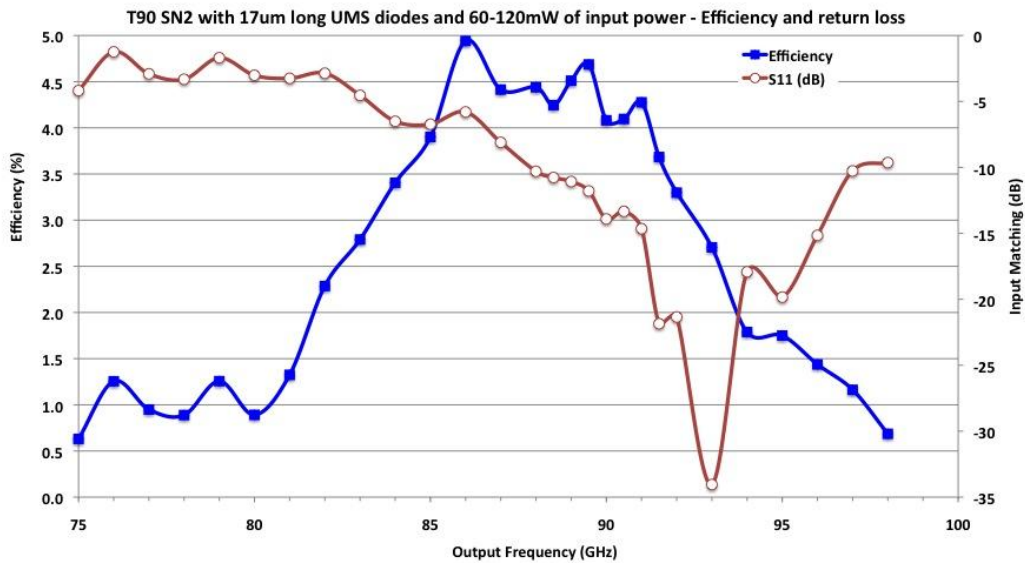
Figure 2.27: The plain curve with filled square markers and the plain curve with opened circle markers show respectively the measured efficiency and the return loss of the 90GHz tripler with 17µm long diodes.

Additional tests were performed to characterize the output power of the tripler with smaller anode size. A 3dB RF (20-40GHz) attenuator was inserted before the tripler to achieve lower input power. The input power with attenuator was 30-60mW from 75-125mW. The measured results are shown in Figure 2.28 and Figure 2.29 with lower input power. Higher efficiency was measured with reduced input power,

flat output power in order of 2mW was gotten from 83 to 91GHz. The input matching showed similar form in Figure 2.27 above.
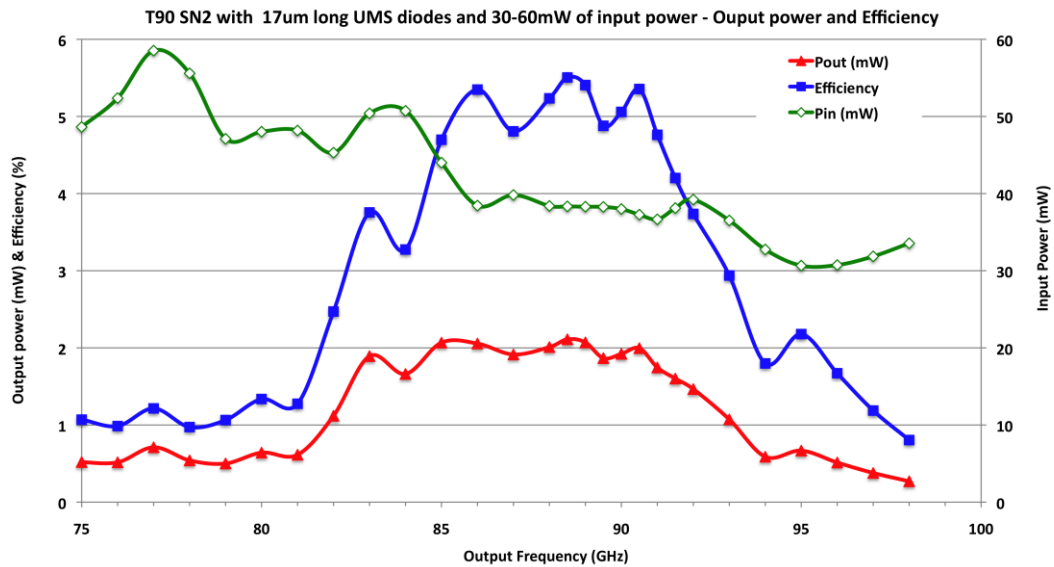
Figure 2.28: The plain curve with filled square markers and the plain curve with filled triangle show respectively the measured efficiency and the output power of the 90GHz tripler with optimized bias for each frequency, the plain curve with opened square markers shows the input power injected into the tripler.
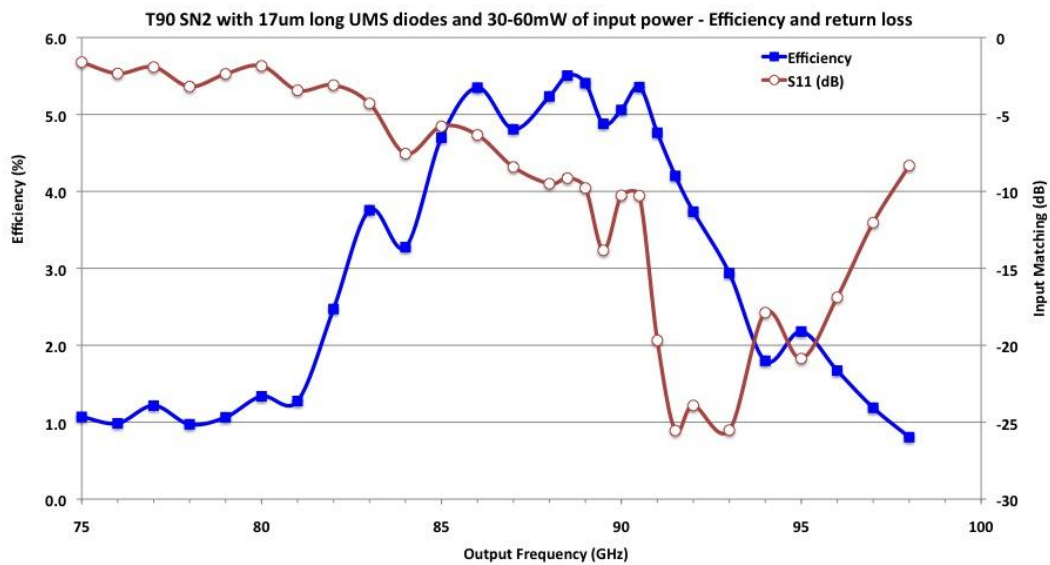
Figure 2.29: The plain curve with filled square markers and the plain curve with opened circle markets show respectively the measured efficiency and the return loss of the 90GHz tripler with 17μm long diodes.

2.3.3 Predicted and Measured results

Differences between the measured results and the model predictions are displayed in Figure 2.30. The measured efficiency and the output power are lower than the predictions, contrary to the better measured input matching (see in Figure 2.31). Note that the simulated performance of the tripler was obtained with constant input power of 50mW and bias of -13V (for six diodes) over the band, and the measured performance was obtained with optimized bias for every frequency point and inconstant input power. The difference between the predicted and measured results is assumed from the inaccurate diode model that was used for the modeling, further analysis is detailed in next section.
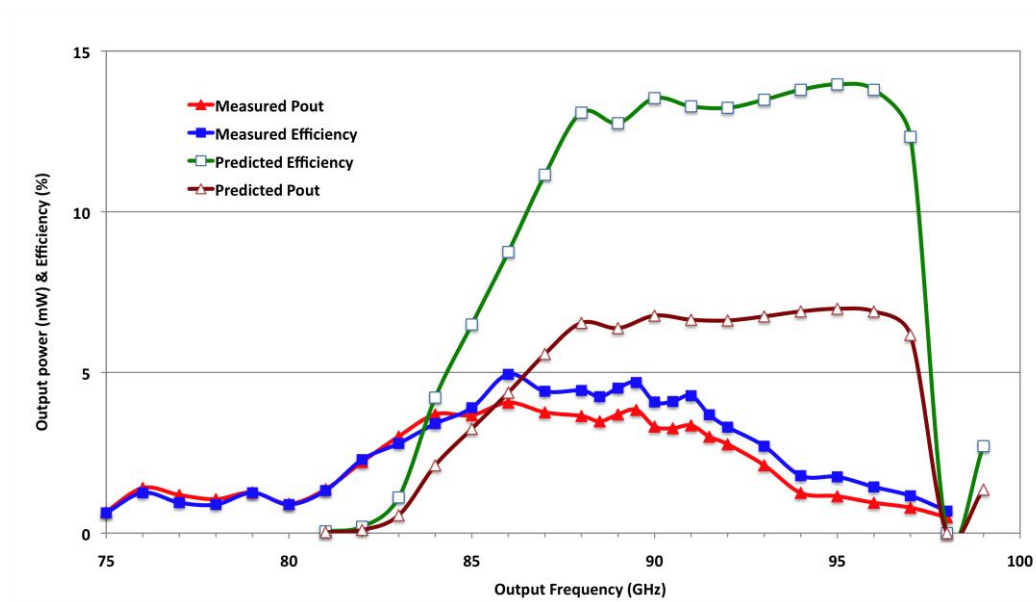
Figure 2.30: The plain curve with filled square markers and the plain curve with opened square markets show respectively the measured efficiency and the predicted efficiency. The plain curve with filled and opened triangle markers respective to the measured output power and the predicted output power.
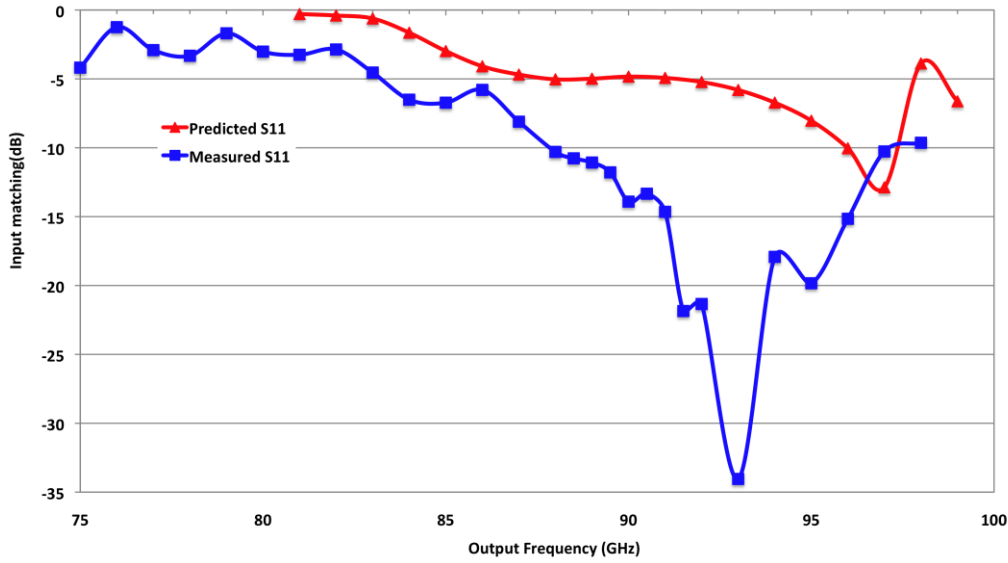
Figure 2.31: The plain curve with filled square and triangle markers show respectively the measured return loss and the predicted one.

2.3.4 Importance of using accurate UMS diode model

A simulation was performed by using a CAD tools based on very accurate physics-based models of the nonlinear device developed at University Polytechnic of Madrid (UPM) detailed in [Siles08a]. Figure 2.32 shows the predicted efficiency with the input power of 50mW and the impedance matched at 90GHz. A maximum 8% efficiency was predicted by using this physics-based diode model for a ideal tripler. Figure 2.33 shows the predicted efficiency in sweep of the input power.
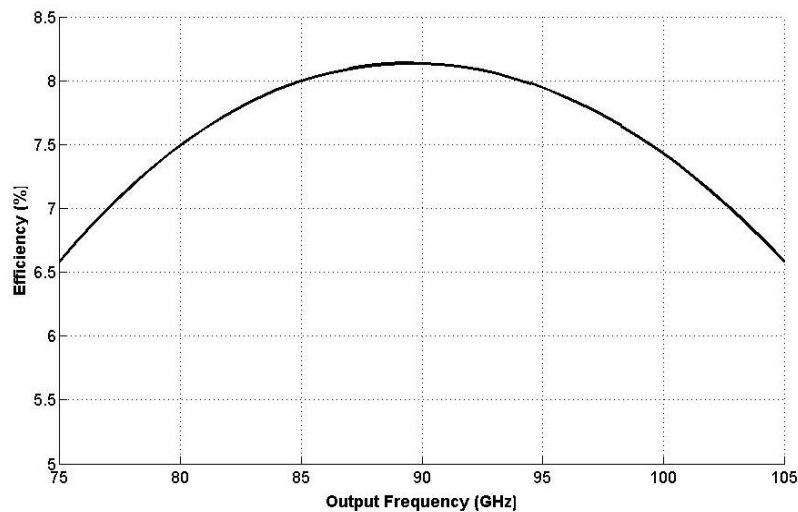
Figure 2.32: Predicted efficiency versus output frequency using physics-based numerical simulation of the 90GHz tripler, with matching impedance optimized at 90GHz.

53
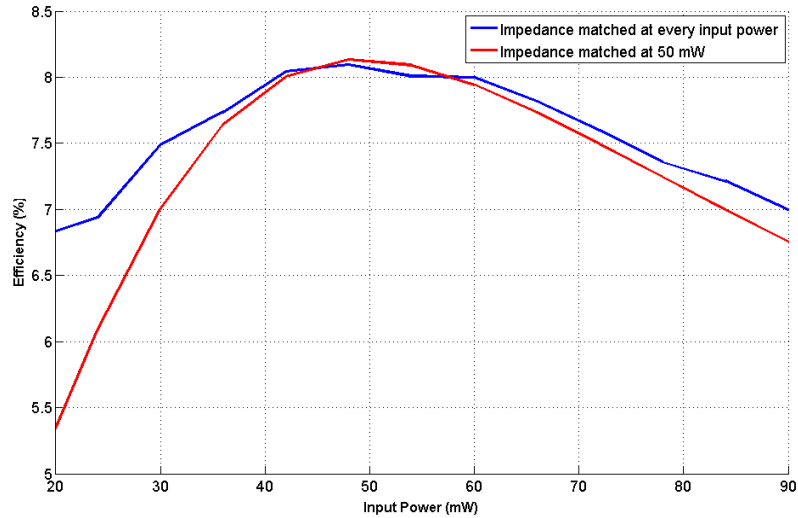
Figure 2.33: Predicted efficiency versus input power using physics-based numerical simulation of the 90GHz tripler.

The inaccuracies induced by the use of the standard Schottky diode model of ADS could explain the difference between the measurements and the initial simulations. The nonlinear circuit simulator like ADS provides simple analytical models for the semiconductor devices, which are impossible to perform a precise optimization of the characteristics of the UMS diodes due to the negligence of the important physical phenomena [Siles08a]. In order to prove this, the ADS standard Schottky diode model used for the tripler design were all replaced by a user-defined electrical model described in [Thomas08b]. This model was been developed particularly for UMS Schottky diode that makes possible to model accurately the I/V and C/V characteristics of the UMS Schottky barrier. Owing to the reduced epitaxial layer thickness in UMS BES process, the capacitance swing between reverse and forward bias is reduced compared to a traditional varactor diode. Edge effects [Louhi95] are not taken into account by the standard ADS Schottky diode model and this model does not correctly predict the response of Schottky diodes when flat band conditions are reached [Siles08a], which is shown in Figure 2.34.
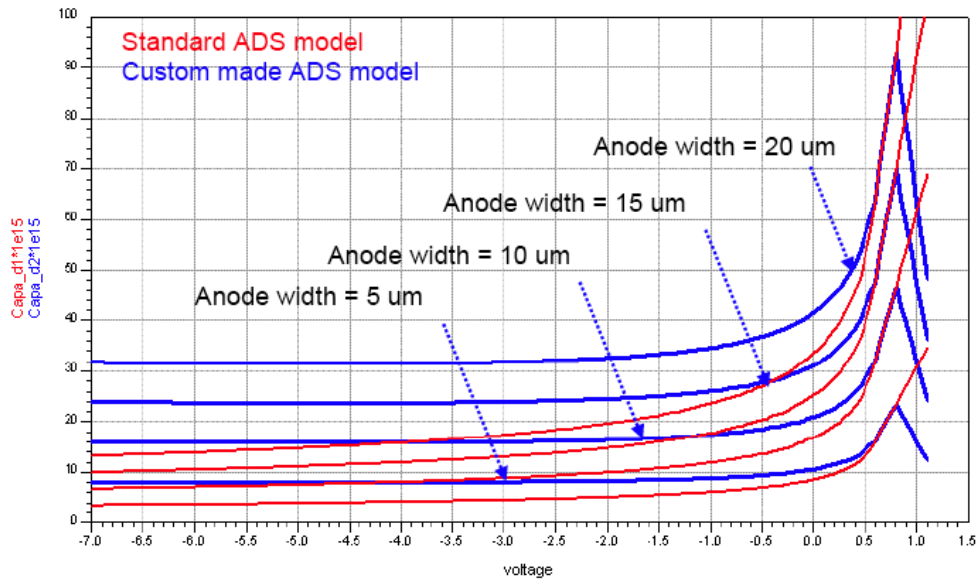
Figure 2.34: Comparison between the C/V characteristics of a custom UMS BES Schottky diode model and a standard ADS Schottky diode model for various anode sizes (Reproduced from [Thomas08b]).

First the ADS standard Schottky diode model underestimates the diode capacitance, in consequence, the impedance of the diode is different and mismatch occurs with the optimized matching circuit obtained with the ADS standard Schottky diode model. Secondly, the conversion efficiency is changed with different modulation of the nonlinearity C/V characteristic. Meantime, the roll-off effect is taken into account with this corrected model, this effect play an important role for a forward biased mixer design.

Further simulations have been performed using the more accurate UMS Schottky diode model reported in [Thomas08b]. The simulated conditions are summarized in Table 2.3. Figure 2.35 & Figure 2.36 show the comparison between the measured efficiency and the predicted efficiency respectively to the tripler with 17µm long anode and 22µm long anode. The predicted results agree better with the measured results except for the predicted band shifted to lower frequency. All these comparisons proved that the ADS standard Schottky diode model isn't accurate enough for the frequency multiplier design with UMS Schottky diode. Figure 2.37 shows the predicted efficiency with two different Schottky diode model, the ADS standard one and the corrected one with different bias and input power conditions. Although the initial diode model was not accurate for the design, optimizing the bias voltage for each frequency allows recovering part of the predicted performances.

Table 2.3 Summary of simulated conditions for Figure 2.35 - Figure 2.37.

	Figure 2.35		Figure 2.36		Figure 2.37		
	Measured	Predicted with corrected model	Measured	Predicted with corrected model	Predicted with ADS model	Predicted with corrected model	
						1	2
Rs (*ohms*)	2.3		1.77		5	1.77	
Anode length (*um*)	17		22		22		
Vbias (*V*)	Optimized for every frequency		Optimized for every frequency		-13	Optimized for every frequency	
Pin (*mW*)	60-125		60-125		50	60-125	
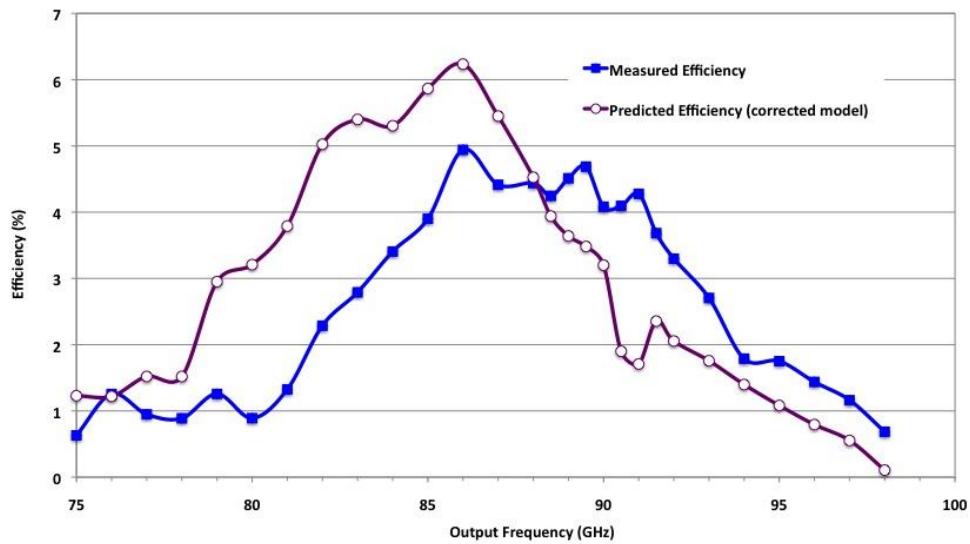
Figure 2.35: The plain curve with filled square and opened circle markers show respectively the measured efficiency and the predicted efficiency by using the corrected diode model for T90 SN2 (17μm long anode).
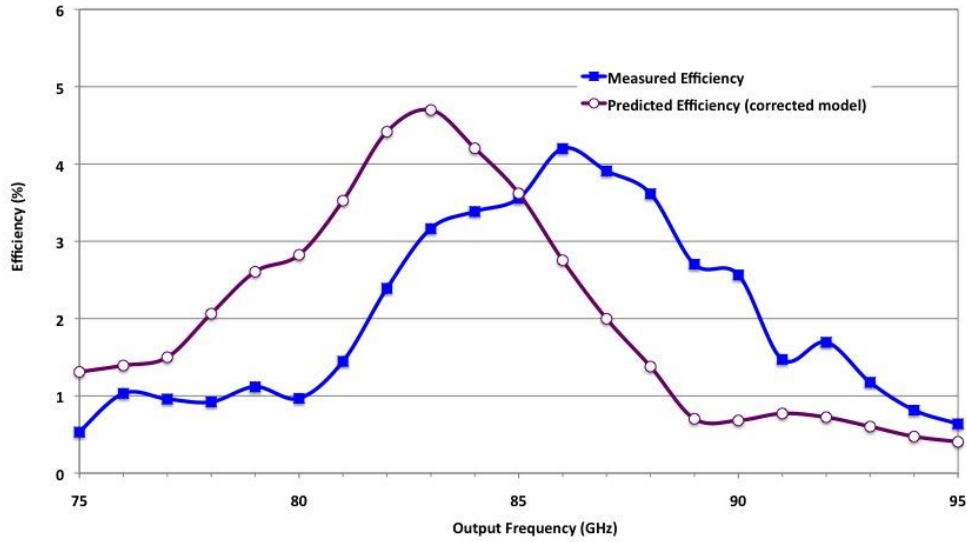
Figure 2.36: The plain curve with filled square and opened circle markers show respectively the measured efficiency and the predicted efficiency by using the corrected diode model for T90 SN1 (22 µm long anode).
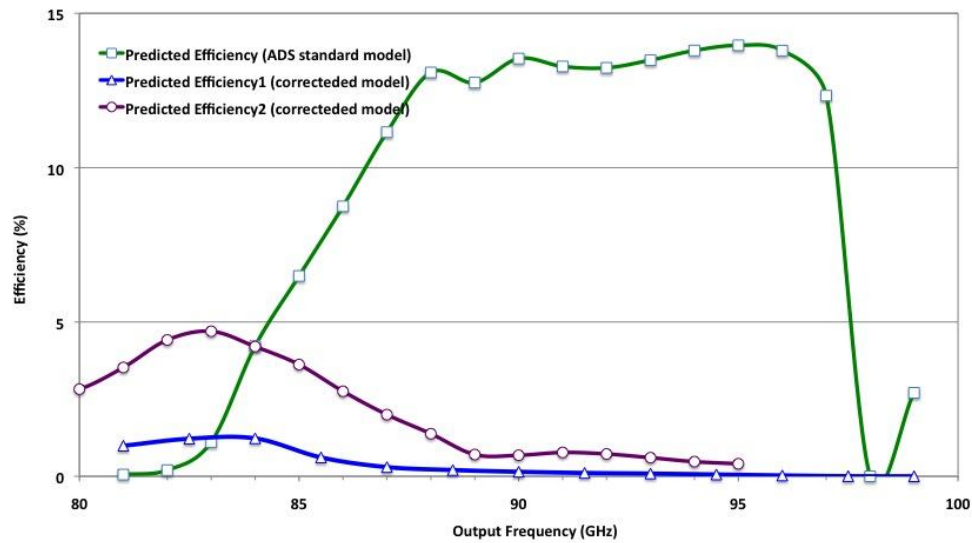
Figure 2.37: The plain curve with opened square and opened triangle/circle markers show respectively the predicted efficiency by using the ADS standard diode model and the corrected diode model for T90 SN1 (22 µm long anode). Note that the simulation conditions are different for efficiency 1 and efficiency 2.

In order to improve and guarantee the good matching between the measured and simulated results for UMS-BES Schottky diode circuits, another model has been proposed and developed by José Siles [Siles08b] at LERMA, the model has been tuned by using measurements results at both DC and RF from the 30/90GHz tripler and a 190GHz doubler chips on the same wafer, as well as physics-based simulation results with the DD Schottky diode model developed at UPM [Siles08a].

This model does not differ significantly from that proposed in [Thomas08b], but it presents some important advantages or improvements. On the one hand, the use of a fitted expression for the junction capacitance instead of the charge leads to a better convergence of the HB algorithm in ADS since the problems with calculation of the capacitance as the derivative of the charge has been removed. The model proposed in [Siles08b], the continuity of the equations that describe the junction capacitance has been imposed, making it faster the convergence of the HB algorithms. On the other hand, the C/V curve above 0.6V, where UMS measurements are not longer valid, has been derived from numerical physics-based simulations. Hence, the roll-off of the capacitance is well modeled. Finally, the physical parameters that describe the I/V response of the diodes has been extracted from DC and RF measurements performed at LERMA (Observatory of Paris) to guarantee a good matching between the simulation results and the measurements.

Figure 2.38 shows the comparison between the junction capacitance obtained by means of the UMS fit (solid lines), the physics-based simulations (dot lines) and the second proposed model (dashed lines). It can be noticed that the proposed model shows a very good agreement with both the UMS fit below 0.6V, and those results obtained with the physics-based simulator.
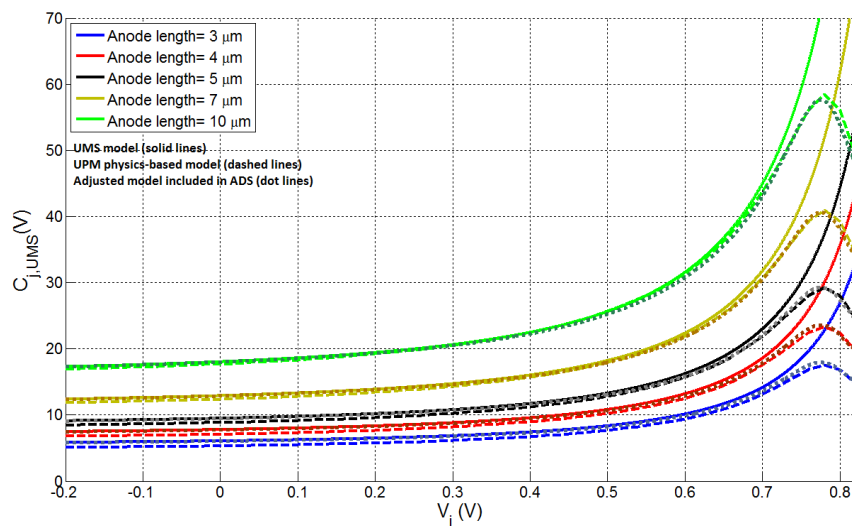
Figure 2.38: Comparison between the UMS model for the Schottky diode junction capacitance (solid lines), the capacitance curves obtained by means of the physics-based Schottky diode simulator developed at UPM (dashed lines), and the proposed fit for ADS (dot lines) (Reproduced from [Siles08b]).

A comparison between simulated and measured results for the 30/90GHz tripler is shown in Figure 2.39 and Figure 2.40 respectively for the 17μm long anode

and 22 μm long anode. It can be noticed that the simulated results obtained with the second proposed UMS Schottky diode model are in better agreement with measured results. The results obtained with this model show a certain improvement with respect to those obtained by using [Thomas08b]. Although DC simulation results (see Figure 2.38) obtained with the [Siles08b] model match pretty well with the available measurement results at DC. However, other important physical effects like the variation of the series resistance with the width of the depletion region of the epilayer have not been included. Hence, discrepancy between measurement and simulation is still presented in Figure 2.39 and Figure 2.40.
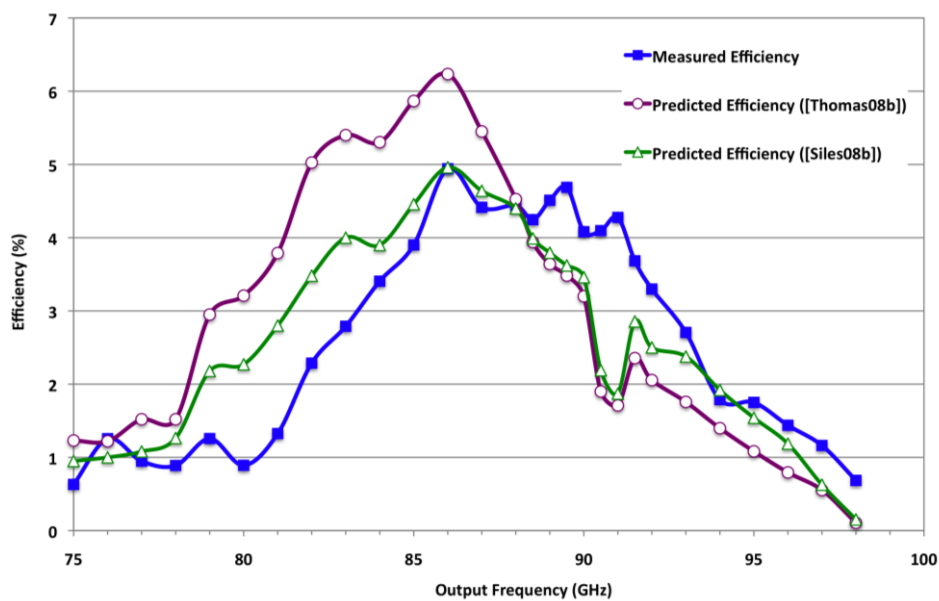
Figure 2.39: Comparison between measurements and simulation results using the UMS Schottky diode model described in [Thomas08b] and [Siles08b](17μm long anode).

59
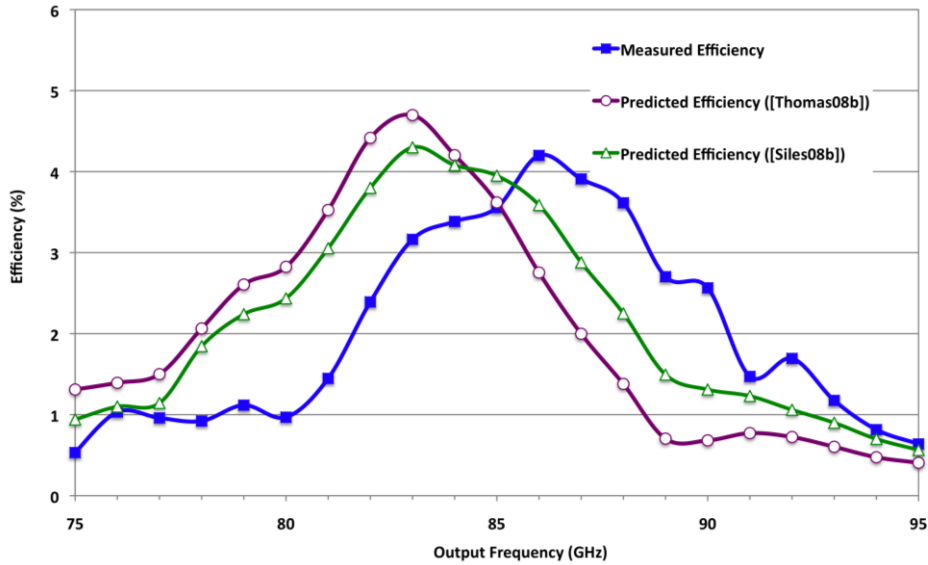
Figure 2.40: Comparison between measurements and simulation results using the UMS Schottky diode model described in [Thomas08b] and [Siles08b](22μm long anode).

2.3.5 Conclusion and perspective

Different W-band triplers have been reported in the past few years, the summary of these reported W-band triplers is shown in Table 2.4. The active type multiplier using transistors [Fudem98, Campos-Roca00, Lin02, Campos-Roca06] can have improved conversion gain, however broadband operation is difficult to achieve. While the diode multipliers are more usable in the millimeter wave range, owing to improved frequency response and stability [Morgan03]. There are also available components proposed by commercial companies like [Millitech], [Pacific], [VDI], [RPG], while no publications have been reported.

MMICs are often preferable to waveguide circuits due to the compactness, repeatable performance and low-cost fabrication in large quantities of waveguide circuits. While MMIC multipliers in transistors are appropriate for integrated circuit such as LNA or power amplifier, interconnect to common millimeter wave component should need a microstrip to waveguide transition, which is an extra concern for the design.

A MMIC 30/90 GHz tripler realized with industrial foundry from UMS was presented in this section, maximum efficiency of 5% and more than 1mW output power has been measured over the band from 80 to 95GHz. This tripler can be used as local oscillator for a subharmonic mixer working around 183GHz. Meanwhile, this

tripler was designed as the local oscillator for a two-pixel heterodyne Schottky diode receiver at 183GHz, which will be presented in sub-Chapter 2.5. The 183GHz subharmonic mixers integrated in the two-pixel receiver are described in the following sub-chapter.

Table 2.4 Summary of previously reported W-band MMIC triplers and this work. (Adapted from [Lin02])

Paper	[Cohn94]	[Campos-Roca00]	[Morgan01]	[Lin02]	[Campos-Roca06]	This work
Frequency multipliers	x3	x3	x3	x3	x3	x3
Device	Schottky vertical diode-4*72 diode arrays	AlGaAs/InGaAs /GaAs PHEMT	BES Schottky diode	GaAs diode PHEMT MMIC Process	MHEMT	BES Schottky diode
Transmission line	Microstrip line	Microstrip line	Microstrip line and GCPW	GCPW	CPW	Microstrip line
Output frequency range (GHz)	97	69-84	75-100	87-102	120-145	75-98
Output power (mW)	79.4	>1.58	>0.35	>0.316	>0.11	>0.27
Input power (dBm)	31	10	16	15.2-16	8	14-18
Input power (mW)	1259	10	40	33-40	6.3	30-60
Conversion loss over the band (dB)	-	<8	<20.6	<20	<17.5	<21
Best conversion loss	12dB @97 GHz	4.3dB @77 GHz	17.3dB @85 GHz	18.1dB @87GHz	11dB @140GHz	12.6dB @88.5GHz
Best efficiency	6.3% @97 GHz	5.36% @77 GHz	1.86% @85 GHz	1.54% @87GHz	7.86% @140GHz	5.5% @88.5GHz

2.4 183GHz Integrated Subharmonic Mixer

At millimeter and submillimeter wavelength, the mixer is the component that most significantly limits the overall receiver performance (shown in Figure 1.5). Therefore, low noise mixer design is important for developing a sensitive receiver. In this section a broadband low noise fix-tuned subharmonically pumped mixer using planar Schottky diode is described, which was integrated in the two-pixel compact receiver front-end described in Chapter 2.5.

2.4.1 General description of a subharmonic mixer

The mixer described in this section is not a fundamental mixer, but rather a subharmonic mixer. A subharmonic mixer performs the same task as a fundamental mixer i.e. it brings the signal down in frequency, but operates as a frequency doubler for the LO signal at the meantime.

For a fundamental mixer working at double sideband (DSB) detection (see Figure 2.41), it can detect two different RF signals in a band of Δf around: $f_{RF}(LSB) = f_{LO} - f_{IF}$ and $f_{RF}(USB) = f_{LO} + f_{IF}$, hence the ability of the mixer to receive in two separate bands, the Lower Side Band (LSB) and the Upper Side band (USB). This ability is usually a disadvantage since the spectrum of two distinct signals could be superimposed at the IF frequency. In practice, it is often necessary to eliminate one of the bands by using a pre-selector filter in front of the DSB mixer; such kind of image rejection mixer is called a single sideband (SSB) mixer. In some cases the ability of receiving in two separate bands is used to reduce the bandwidth of the spectrometer that analyses the IF signal. This is the case of a number of heterodyne receivers dedicated to planetary sciences.

While a subharmonic mixer of order N mixes the Nth harmonic of the LO with the signal (see Figure 2.42). Therefore, the IF signal is at the frequency $f_{IF} = |f_{RF} - N \cdot f_{LO}|$. In the case of N=2, the IF signal is at $f_{IF} = |f_{RF} - 2f_{LO}|$, where $2f_{LO} \approx f_{RF}$. For N=2, it is possible to build a sub-harmonic mixer with a single Schottky diode but its performance will be largely higher if an anti-parallel pair of diodes is used instead.
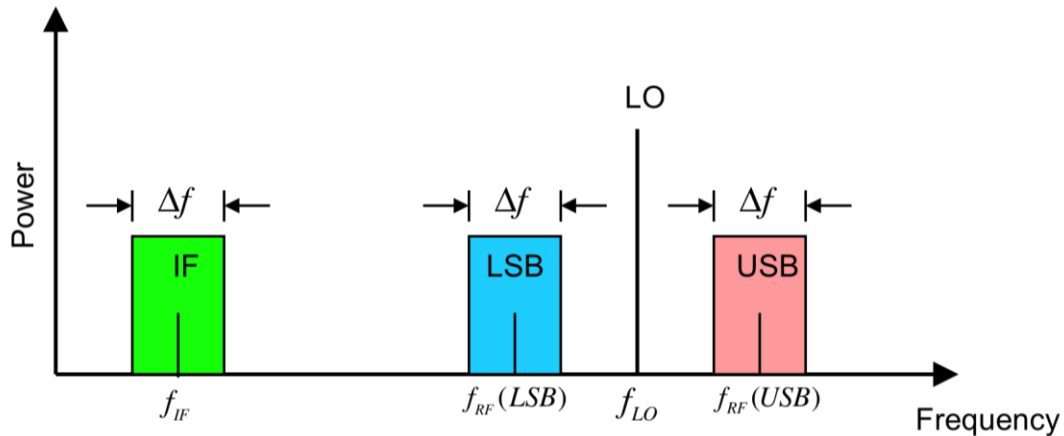
Figure 2.41: Principle of a fundamental mixer. The output IF has two possible frequencies: up conversion and down conversion, and $f_{IF} = |f_{RF} - f_{LO}|$. For a down converter $f_{IF} << f_{RF}$ and is in the MHz-GHz range, so $f_{LO} \approx f_{RF}$.
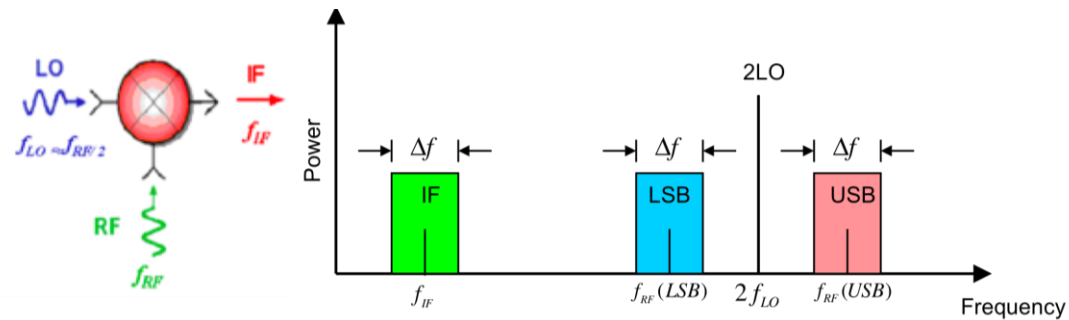
Figure 2.42: Principle of a subharmonic mixer.

Subharmonic mixers that use an anti-parallel pair of diodes produce odd harmonics of the input signals; the even products are trapped inside the anti-parallel pair of diodes due to the anti-symmetry. For a subharmonic mixer of order 2, the RF signal is mixed with the second harmonic of the LO inside the anti-parallel pair of diodes.

Some advantages and disadvantages of a subharmonic mixer of order 2 compared to the fundamental mixer are listed below:

Advantages:

- Subharmonic mixers make it possible the use of a local oscillator at a reduced frequency of a factor *2* compared to that of a fundamental mixer, $2f_{LO} \approx f_{RF}$.

- If ($m+n$) is even, the frequency ($mf_{RF} \pm nf_{LO}$) is removed at the output. This natural rejection is based on the direct interconnection of the anti-parallel diodes.

63

- There is an increased IF bandwidth, due to lower impedances of the diodes at the IF frequency.
- f_{LO} is easily filtered and coupled.

Disadvantages:

- The conversion loss is generally higher for a subharmonic mixer than for a fundamental mixer.
- The power of the local oscillator must be more important because it is necessary to pump two Schottky diodes instead of one and because the pair of diodes is usually unbiased.
- The noise generated by two diodes should be higher than that of one single diode.

Two parameters are mainly used to characterize the sensitivity of a mixer /receiver: the conversion loss and the Equivalent Noise Temperature (ENT).

The conversion loss L_c is defined by the ratio between the power of the RF signal at the input of the mixer to the output power of the IF signal produced by the mixer. L_c is often expressed in dB:

$$L_c(dB) = P_{RF}(dB) - P_{IF}(dB) \tag{2-4}$$

If two sidebands are useful, then the conversion loss is 3dB lower than the single sideband (SSB) case:

$$L_{DSB}(dB) = L_{SSB}(dB) - 3dB \tag{2-5}$$

The mixer, as any type of electronic circuit, generates noise. The noise can have various sources:

- Shot noise: Caused by random fluctuations in current superimposed upon the DC value and exists in all electronic amplifying devices. This type of noise exists in Schottky junctions.
- Thermal noise created from the random free electron movement in a conductor (resistor) due to thermal agitation. In a mixer, the diodes' series resistance and other resistive elements of the embedding network (such as transmission lines) generate the thermal noise. This is the main noise source

present in the mixer, minimize the series resistance of diode could eventually reduce the mixer noise temperature.

- Quantum noise is generated by the fluctuations in the stream of LO photons to the device, which is generated before the mixer.

- Flicker noise: Observed at very low frequencies, and is thought to be due to fluctuation in the conductivity of semiconductor devices. It is regarded as negligible at high frequencies.

The ENT is proportional to power; the total noise temperature of two or more noise sources combined is the sum of the noise temperature of all of the sources, which can be expressed as:

$$T_e = T_0(nf - 1) \qquad (2\text{-}6)$$

where T_0 is the room temperature in Kevin, and nf is the Noise Factor (NF) of the device. The Noise Factor is the ratio of the Signal to Noise Ratio (SNR) at the output compared to the SNR at the input, measured at T_0. The mixer noise temperature can be measured by using Y factor method (described in Appendix A), in practice the SSB mixer noise temperature is generally twice of the DSB mixer noise temperature, in theory the SSB mixer noise temperature could be less when the diode has a good matching at desired frequencies.

If there are multiple noisy components in cascade with respective noise temperature and gain of each stage (see Figure 2.43), the cascade noise temperature can be written using the Friis formula:

$$T_{out} = T_1 + \frac{T_2}{G_1} + \frac{T_3}{G_1 G_2} + ... + \frac{T_n}{G_1 G_2 ... G_n} \qquad (2\text{-}7)$$
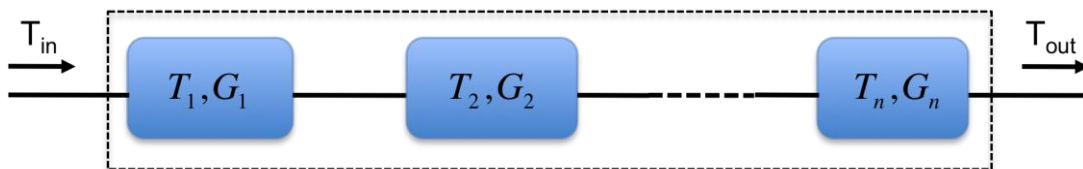
Figure 2.43: A system with cascaded components.

For a detection chain, the receiver noise temperature will relate to all the components in the chain such as the antenna, the mixer, the low noise amplifier etc. A receiver's sensitivity is a measure of its ability to discern low-level signals. In radio

astronomy, the sensitivity of a system can be defined as the smallest change of temperature of the signal can be detected with a signal to noise of n :

$$\Delta T_{\min}(n\sigma) = \frac{nT_{sys}}{\sqrt{B\tau}} \qquad (2\text{-}8)$$

where T_{sys} is the noise temperature of the system, B is the bandwidth of the receiver, τ is the integration time and $n \geq 1$. This analysis is assumed that the receiver gain was constant, while in practice gain variation are unavoidable, the sensitivity is therefore reduced due to receiver instability [Kraus86]. To improve the sensitivity of a system, the system noise temperature T_{sys} need to be as low as possible.

2.4.2 183GHz mixer design

To reduce the conversion loss of the mixer, it is crucial to have adequate matching circuits to the diodes at desired frequencies. For a subharmonic mixer, the RF, LO and IF are involved in the circuit, therefore matching circuits at respective frequency need to be analyzed to optimize the performance of the mixer. The design procedure is discussed below.

2.4.2.1 Ideal mixer analysis

An ideal mixer composed of an anti-parallel pair of diodes and ideal matching elements as in [Thomas04] was analyzed firstly. This analysis is performed in nonlinear mode, i.e. using the harmonic balanced code of ADS. This is a two-tone nonlinear analysis that enables us to measure the voltages across the diodes and the currents through the diodes, related to all mixing products generated by the diodes. This enables us to calculate the impedances of the diodes at all the frequencies $f_{m,n} = |m \times f_{RF} + n \times f_{LO}|$ (m, n relative integer). In practice, only a limited number of mixing products are considered i.e. $|m| \leq 3$ and $|n| \leq 9$ (as the power of the LO signal is much stronger than the power of the RF signal, it is necessary to consider more harmonics of the LO). The equivalent circuit in ADS is shown in Figure 2.44. Two set of impedances are important for the modeling of the circuit, which are the impedances of the diodes Z_{diode1_RF}, Z_{diode2_RF}, Z_{diode1_LO} and Z_{diode2_LO} at $f_{RF} = f_{1,0}$ and $f_{LO} = f_{0,1}$, and the embedding impedances Z_RF and Z_LO presented to the pair of diodes at f_{RF} and f_{LO} respectively. These embedding impedances are the input

impedances, looking into the diodes mounted in the circuit. Z_RF has an impact on the conversion loss, therefore on the noise performance of the mixer; Z_LO impacts the amount of LO power needed to pump the mixer. Hence, the simulation consists in optimizing the impedances Z_RF and Z_LO to maximize the coupling of diodes at RF and LO.
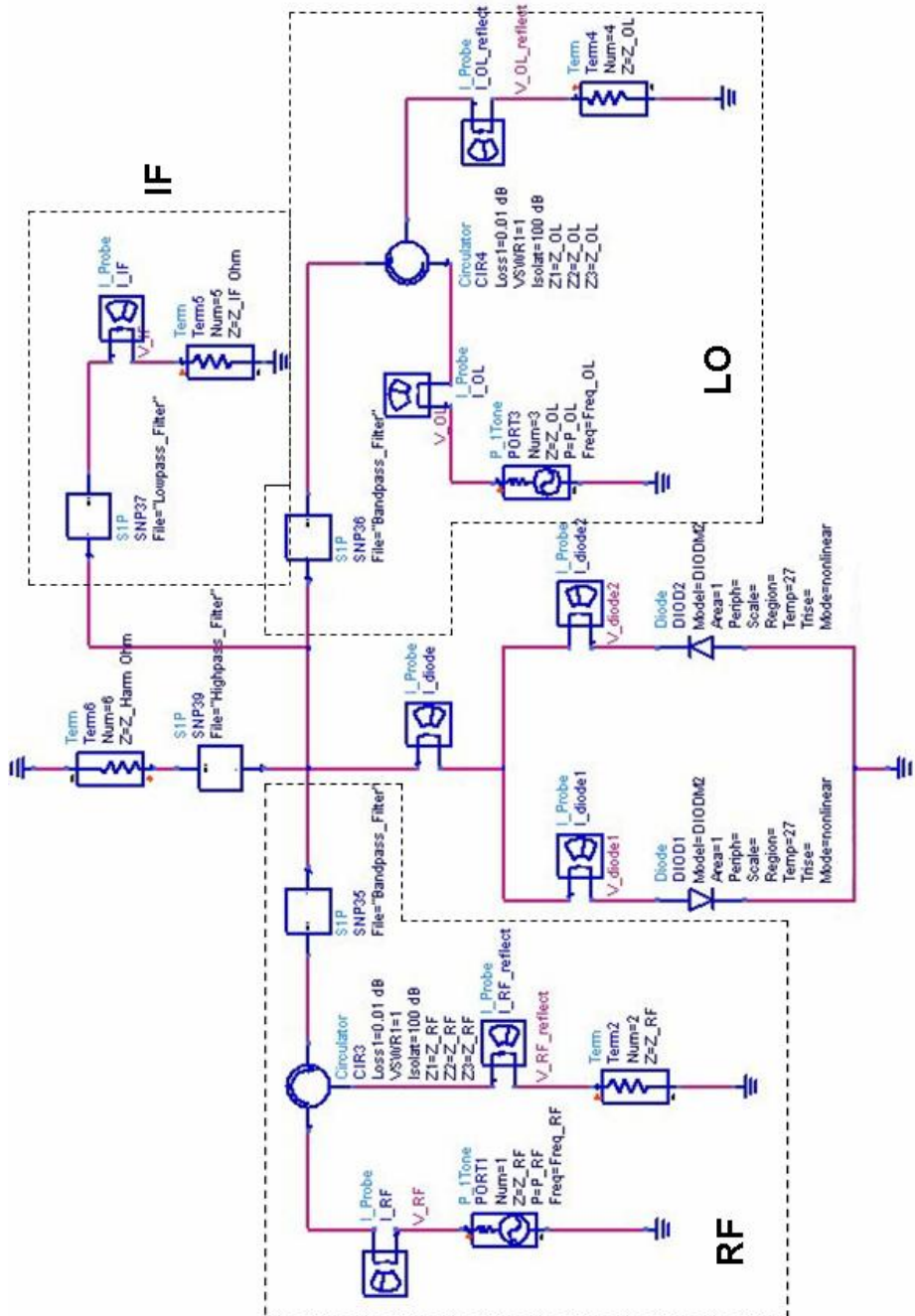
Figure 2.44: Equivalent circuit of an ideal subharmonic mixer with pair of diodes in nonlinear mode.

The optimum $Z\_RF = \left(Z_{diode1\_RF}//Z_{diode2\_RF}\right)^*$ and $Z\_LO = \left(Z_{diode1\_LO}//Z_{diode2\_LO}\right)^*$ were obtained, with these impedance the mixer provides the minimum conversion loss and requires the minimum LO power. For the ideal mixer, the impedance of each diode is the same, therefore $Z\_RF = \left(Z_{diode1\_RF}/2\right)^*$ and $Z\_LO = \left(Z_{diode1\_LO}/2\right)^*$.

The values of Z_RF and Z_LO will be used thereafter to synthesize the real mixer: the real matching circuit of the mixer will have to provide to the diodes embedding impedances as close as possible to Z_RF at f_{RF} and as close as possible to Z_LO at f_{LO}.

Meantime, this study can determine the impedance of each diode at RF and LO frequency rang. In theory, pair of diodes are identical, therefore $Z_{diode1\_RF} = Z_{diode2\_RF}$ and $Z_{diode1\_LO} = Z_{diode2\_LO}$. In order to analyze the matching between the diodes and other part of the mixer, the linear analysis such as the transmission and reflexion between the diodes and sources could be useful. To realize this simulation, the standard nonlinear diode model that used in Figure 2.44 need to be replaced by its impedance at desired RF and LO frequency range. A Data Access Component (DAC) was used to represent the impedance of diode at different frequency range, as shown in Figure 2.45. With this linear analysis, the transmission coefficient and reflection coefficient between the diodes and the RF or LO source can be obtained. For a ideal mixer, the maximum transmission coefficient between the
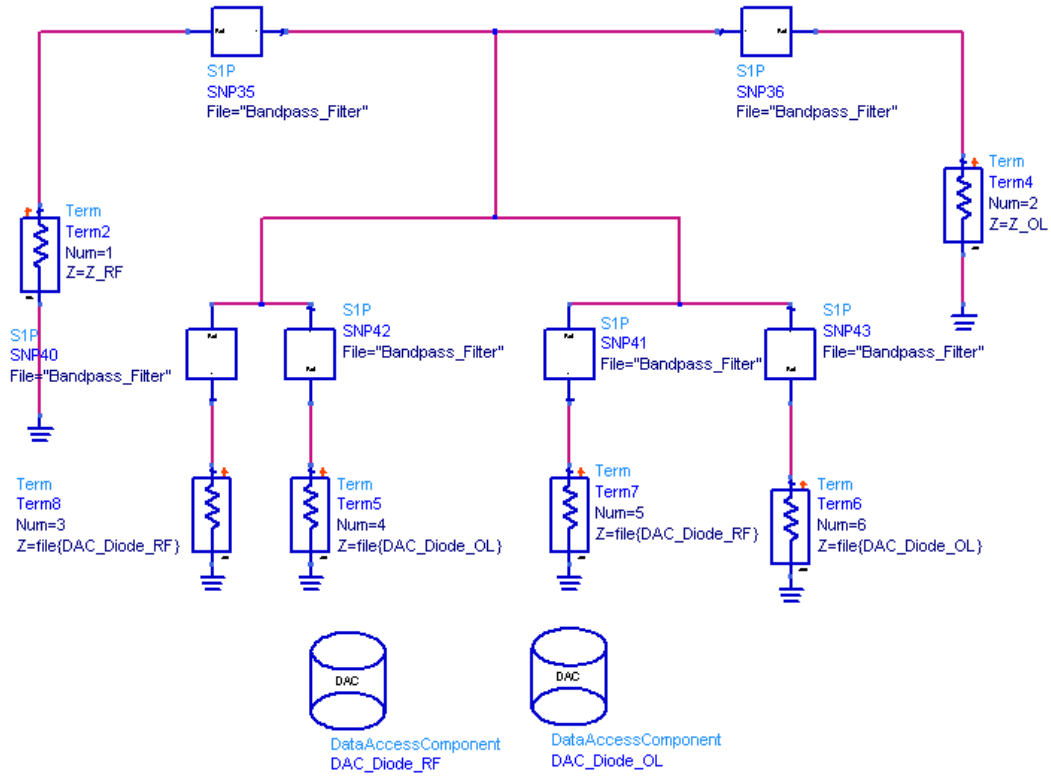
Figure 2.45: Equivalent circuit of an ideal subharmonic mixer with pair of diodes in linear mode.

diode and RF or LO source is $\sqrt{0.5} \approx 0.707$, therefore $\left|S_{31}\right|_{max} = \left|S_{51}\right|_{max} = 0.707$ between the diodes and the RF source, $\left|S_{42}\right|_{max} = \left|S_{62}\right|_{max} = 0.707$ between the diodes and the LO source.

2.4.2.2 Anti-parallel pair of diodes optimization

The configuration of the pair of diodes was studied before the complete mixer was optimized. Two different diode configurations are commonly used for subharmonic mixer design: either the diodes are in the open loop configuration shown in Figure 2.46(a), or the diodes are in anti-parallel configuration shown in Figure 2.46(b). The open loop configuration is often used in frequency multiplier designs due to its convenient structure for DC polarization. The anti-parallel configuration has been employed in this mixer design, as this mixer is unbiased. The equivalent circuit for these two configurations is identical, which is shown in Figure 2.44.

69
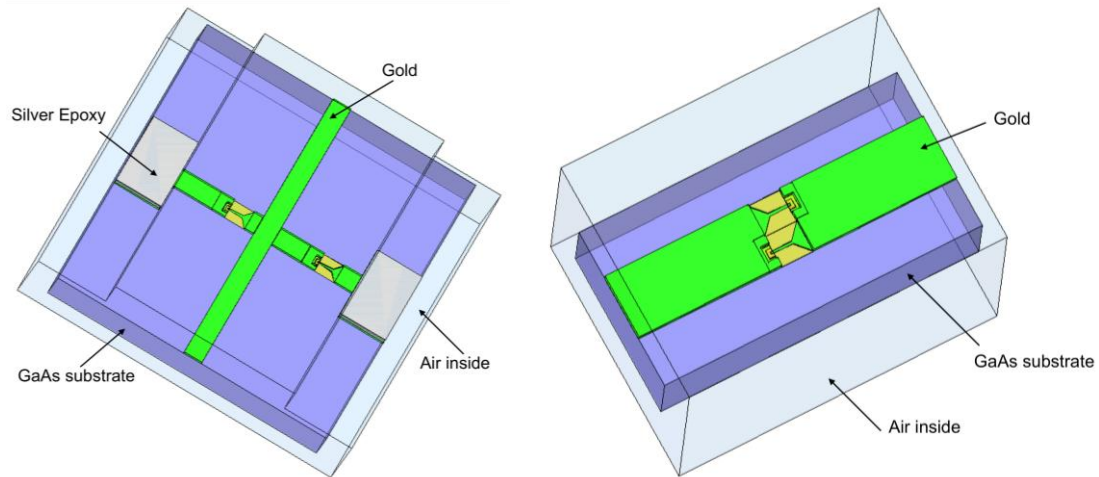
Figure 2.46: (a) Open loop configuration; (b) Anti-parallel configuration.

In order to optimize the diode configuration, three-dimensional electromagnetic simulations were performed using the finite-element method of HFSS. An accurate three-dimensional model of the pair of diodes was drawn that features all the relevant details such as the exact shape of the finger, pads, and passivation layers… The definitions of the wave ports for the diode configuration are shown in Figure 2.47.
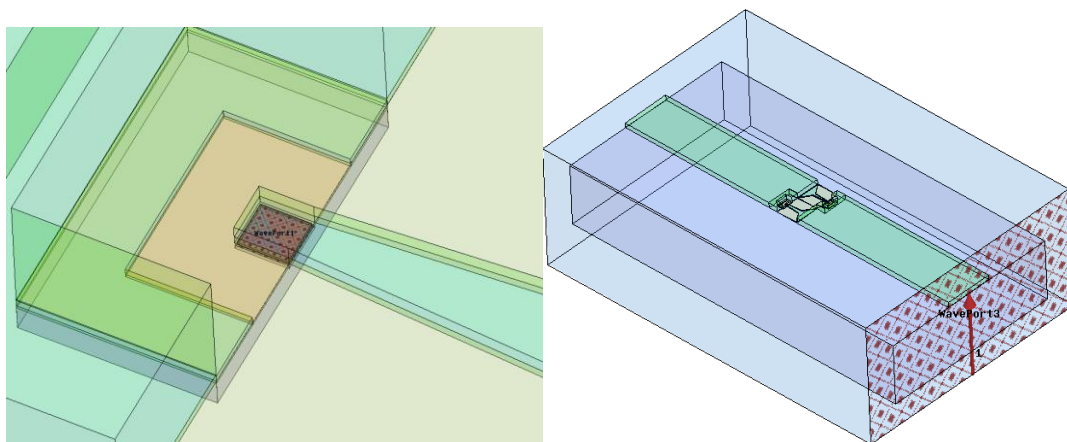
Figure 2.47: Wave port definition in anode and the transmission line.

Optimization of the configuration of the pair of diodes have been performed by modifying the geometry of the structure, for instance the length of the anode, the thickness and the width of the substrate, the length and the width of the finger, the dimension of the channel etc... The width of the anode is fixed to the nominal value given by UMS; it is in the order of 1um. A 50 μm of substrate thickness has been chosen for the same reason described for 90GHz tripler. Small anode diodes have

been chosen for eliminating the shunt effect of the junction capacitance [Crowe92, Siles08a].

Dozens of configurations with different channel dimensions have been studied using HFSS and our custom simulation bench in ADS, the anti-parallel configuration shown in Figure 2.48 was chosen for the complete mixer design, with diodes that have an ideality factor $\eta = 1.2$, a saturation current $I_{SAT} = 4 \times 10^{-15} A$, an estimated series resistance $R_s = 10\,\Omega$, and a zero bias junction capacitance $C_{j0} = 2\,fF$. The simulations gave an optimum LO power of 2mW for the pair of diodes, with the embedding impedances $Z\_RF = 82 + j44.7$ at $f_{RF} = 183\,\text{GHz}$ and $Z\_LO = 197.5 + j182$ at $f_{LO} = 89.5\,\text{GHz}$. The impedance at $f_{IF} = 4\,\text{GHz}$ was set to $Z\_IF = 100\,\Omega$ (detail is described in Chapter 2.4.2.5). The higher harmonics were modeled with embedding impedance $Z\_Harm = 10\,\Omega$ as in [Hesler96].

In fact, for the fabricated version, another configuration as in [Hesler00] was employed: one of the pads is connected to a microstrip line with a width larger than the line of the opposite pad (see Figure 2.49), which achieved a broader bandwidth.
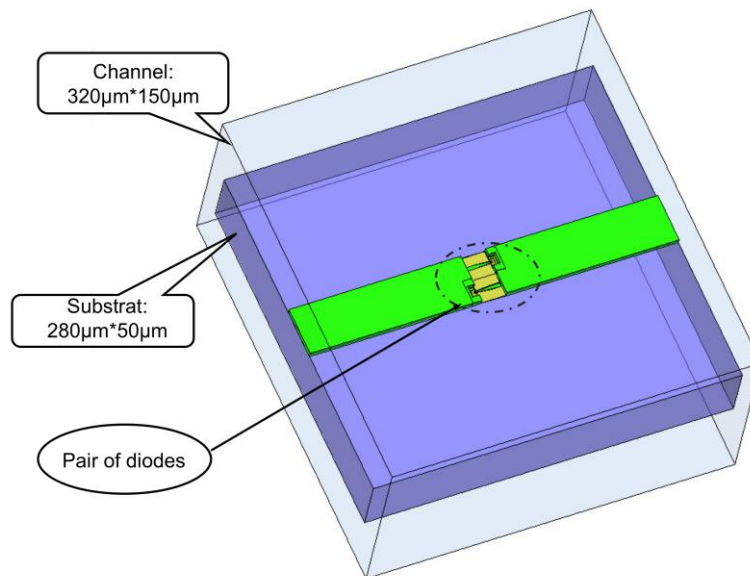
Figure 2.48: The anti-parallel configuration with optimized dimension was chosen for the design of the mixer.
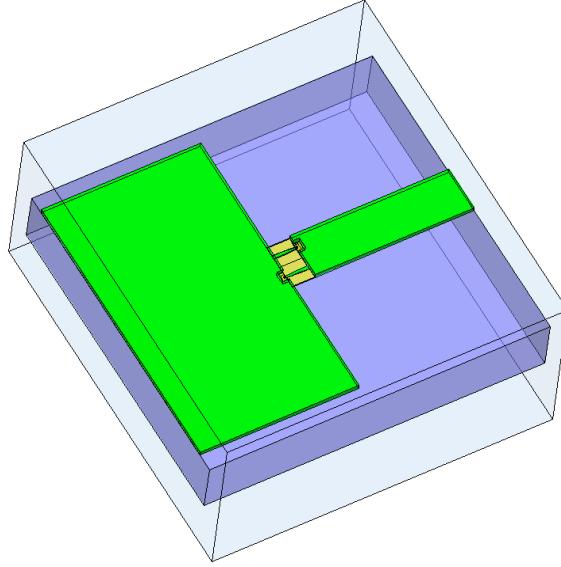
Figure 2.49: Actual configuration used in the final fabrication.

2.4.2.3 Complete Mixer Design

After the completion of pair of diodes configuration optimization, the design of broadband matching circuits at f_{RF} and f_{LO} can start. They are synthesized using a method similar to the one defined in [Hesler96].

The mixer block is split in the E-plane of the RF and LO waveguides described in [Raisanen93, Hesler00] with fixed RF and LO backshorts, thus simplifying the assembly of the mixer and reducing waveguide losses. The planar diodes are integrated on a 50um-thick GaAs circuit containing the embedding circuitry and suspended in a microstrip channel. Inside this channel, only a quasi TEM mode can propagate up to 210GHz. The microstrip channel is perpendicular to the RF and LO waveguides. Schematics of the mixer block are shown in Figure 2.50 & Figure 2.51. Two-sided waveguide-to-microstrip transitions are used to couple both the RF and LO signal into the channel. The microstrip metallization transitions across each guide; third reduced-height waveguide were used for both the RF and LO rectangular waveguides to achieve broad bandwidth [Hesler97, Shi97]. Two band-pass microstrip filters are used to prevent the RF signal from coupling to the LO waveguide, and a short-circuited half-wave stub is used to provide the LO termination. Details on the design of the different parts of the mixer will be given thereafter in this section.
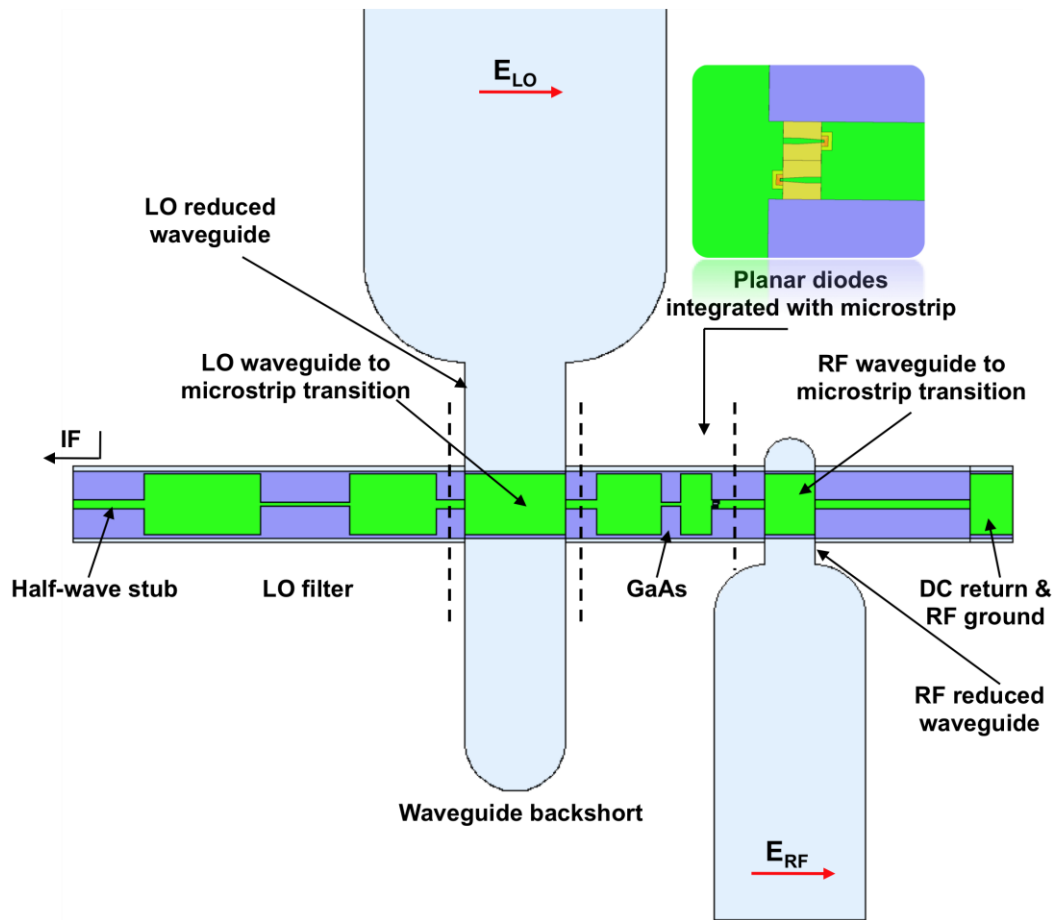
Figure 2.50: Schematic of the MMIC mixer circuit and waveguide matching elements, a photograph of an anti-parallel pair of UMS diodes is shown on the top right.
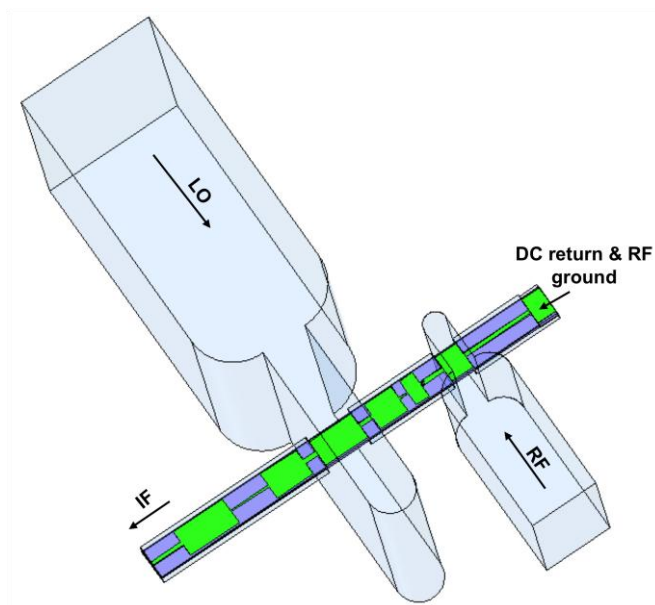
Figure 2.51: Cross section of the fixed-tuned subharmonic mixer.

a) Global circuit optimization bench implanted in ADS

It is necessary to create an electrical model of each independent part of the mixer (the LO and RF waveguide to microstrip transitions, the pair of diodes …) and create a global equivalent circuit of the mixer by connecting the independent parts in a proper way. The electrical models of the independent parts of the mixer are constructed and simulated respectively using HFSS. The calculated S parameters data of each part is imported to the global optimization bench developed in ADS, a certain number of elements can be optimised: the position of the waveguide backshorts; the lengths of the different sections of the LO and RF filters (see Figure 2.52).
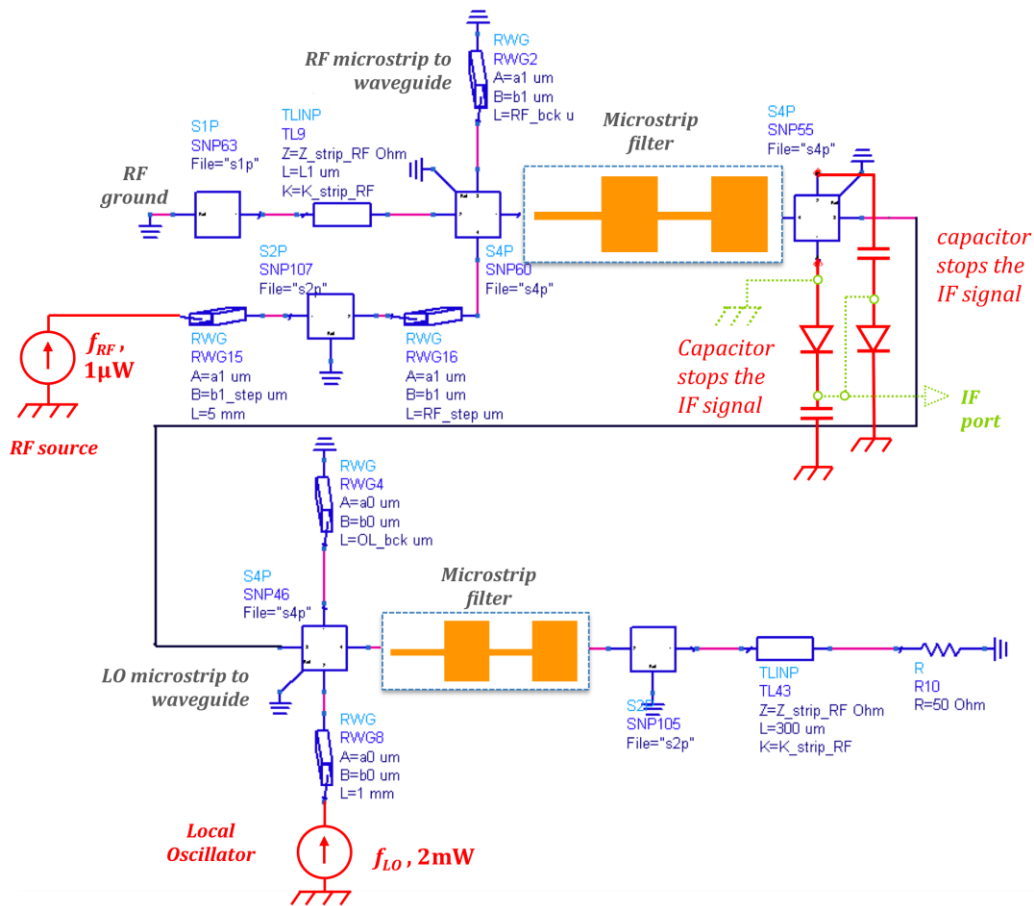
Figure 2.52: Global nonlinear optimization schematic implanted using ADS. The IF circuit is represented in green dashed-lines. Additional ideal filters are needed to decouple the IF signal to RF and LO signals.

b) Design of suspended microstrip filters

Microstrip lines of different widths present different impedances. If the difference of impedances between two juxtaposed lines is large, they present an important discontinuity at their interface that can be used to create a high rejection

filter. A succession of microstrip lines of different widths and lengths can constitute a filter; Figure 2.53 (above) shows the physical layout of the microstrip low pass filter. This is the topology used for the RF and LO filters of this mixer, the model of one step in suspended microstrip line is shown in Figure 2.53 (below), illustrated with the electromagnetic field at the low impedance port. The fields in the three-dimensional model of the microstrip step were calculated using HFSS; the electrical characteristics of the low and high impedance microstrip line were solved at the same time, which will be implanted in the ADS optimization.

Since the electrical characteristics of the microstrip lines are frequency dependent, separated band simulation for the RF/LO filter at f_{RF} and f_{LO} are performed to carry out an accurate optimization. The equivalent circuit in ADS is shown in Figure 2.54.
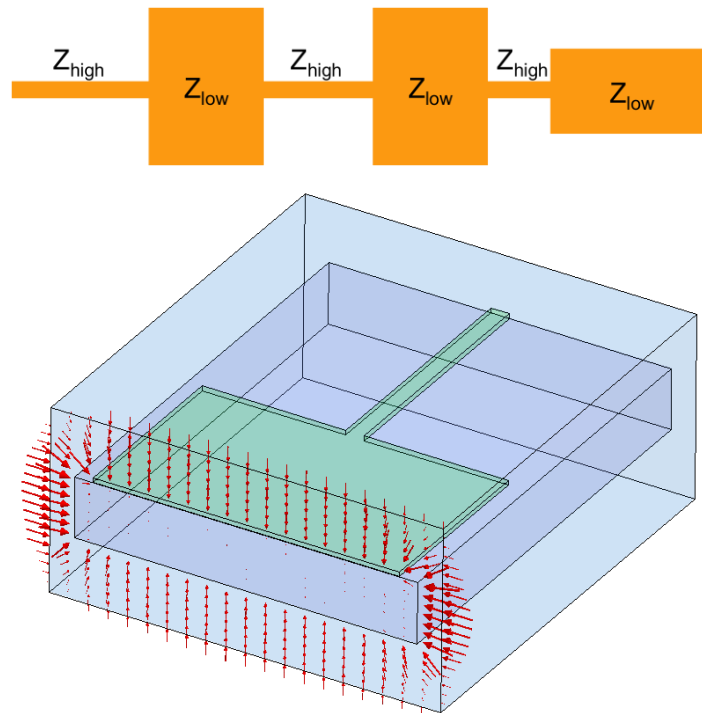
Figure 2.53: Layout of the microstrip low pass filter (above); suspended microstrip filter model constructed using HFSS (below). The calculated two-port S-parameter matrix is imported into the global optimization bench.
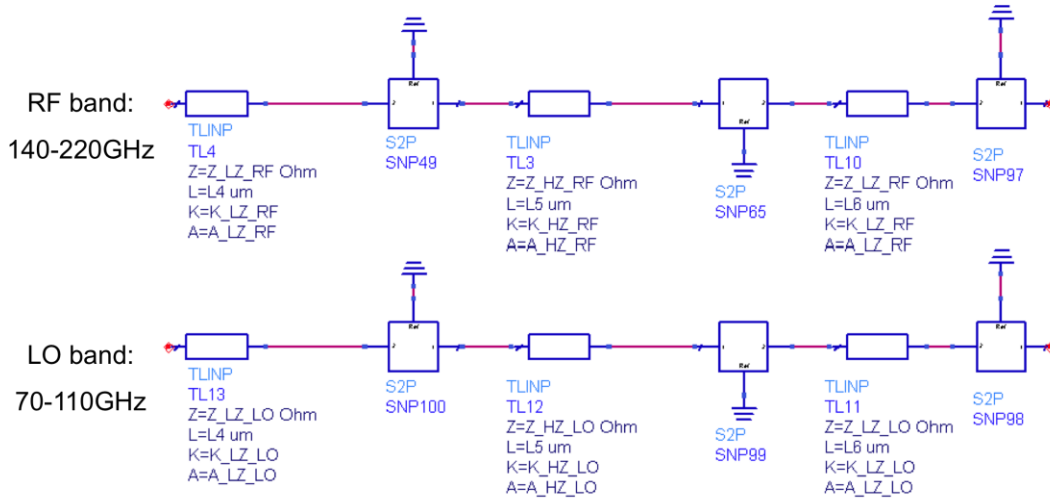
Figure 2.54: Example of the equivalent circuit of RF filters implanted using ADS at f_{RF} (top) and f_{LO} (bottom).

c) **Design of the waveguide to microstrip transition**

Many mixers and multipliers use waveguide at their input due to the availability of waveguide flanges and horns. This allows for efficient coupling of power into the waveguide over a broad bandwidth. Once inside the waveguide, it is often convenient to transfer into a shielded microstrip channel in order to simplify the integration of filters and nonlinear devices into the mixer or multiplier.

The LO and RF waveguides to microstrip transitions can be designed independently from the microstrip circuit around the diode. The transitions are designed to match the microstrip line to the waveguide. Two main transition geometries are possible [Hesler97], the transition in which the substrate circuit is oriented parallel with the E-plane of the waveguide has been used in our design. A view of the RF waveguide to microstrip transition is shown in Figure 2.55, the LO waveguide transition has the same structure but a different waveguide due to the different operating frequency, so the LO waveguide is $1270\,\mu m \times 2540\,\mu m$ and the LO reduced waveguide is $420\,\mu m \times 2540\,\mu m$. The reduced waveguide height for both geometries was chosen to be the third of the normal height. Reducing the height was found to be necessary in order to achieve broadband operation with this type of transition [Hesler97, Shi97]. A fixed-tuned bandwidth of approximately 20% was achieved in our design (the bandwidth is defined as the range of frequency where $L_C \leq 10$ dB).
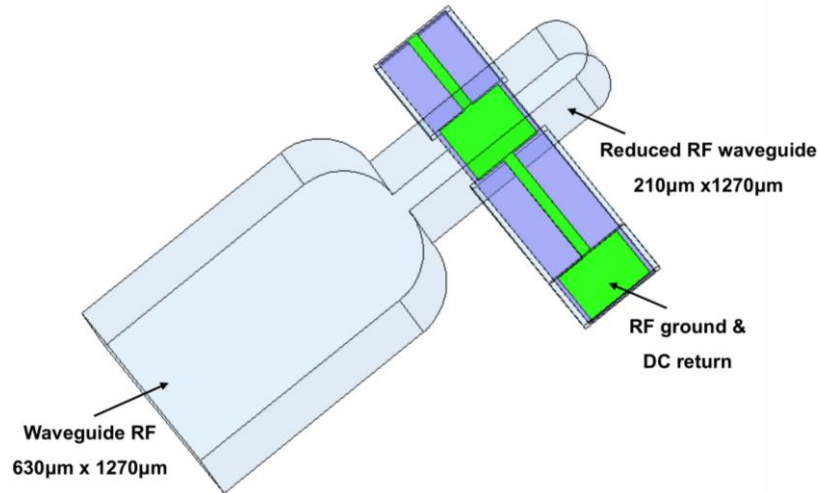
Figure 2.55: 3D model of the RF waveguide to microstrip transition with corresponding waveguide dimensions.

d) Optimization procedure

To optimize and determine the performance of the complete mixer composed of different matching circuits described previously, the equivalent circuit in nonlinear mode in ADS shown in Figure 2.52 has been used to optimize and predict the performance of the mixer. Considering the heavy and arduous calculation due to the large number of optimized variables with harmonic balance code, the optimization of the complete mixer was performed in linear mode (see Figure 2.45).

Therefore the purpose of the optimization is to maximize the coupling between the diodes and RF/LO source. Certain variable parameters were optimized, such as the step length of microstrip line filters, the distance between the diode and RF waveguide to microstrip transition, the position of the backshort and the length of reduced RF/LO waveguide. After the optimization with respective distributed components, all the optimized parameters except the length of reduced RF/LO waveguide and the position of backshort are considered as constant, two half-mixers shown in Figure 2.56 are constructed with these optimized values, one is composed of the RF ground, the RF waveguide to microstrip transition and the cell of diodes, another half of the mixer is the rest part. Thereafter, the second optimization with the same method was used to adjust the backshort and the reduced waveguide position.
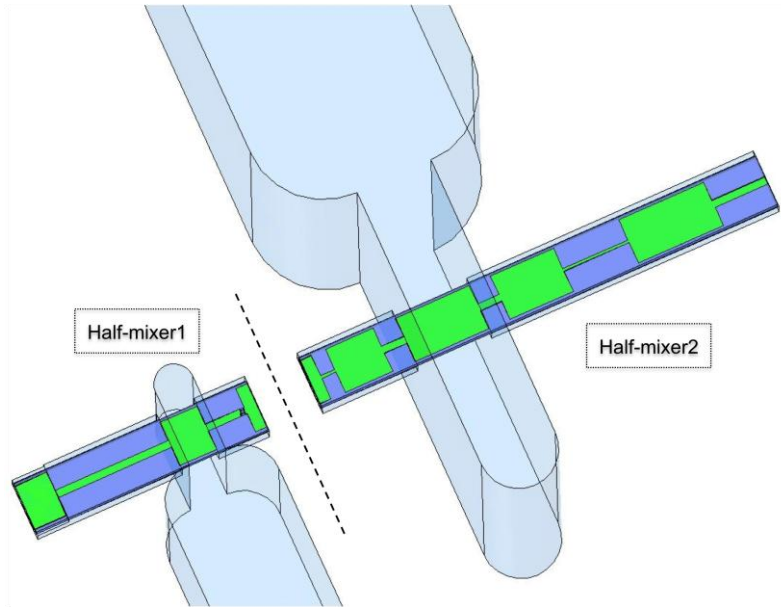
Figure 2.56: 3D model of two half part of the mixer.

Figure 2.57 shows the optimized transmission coefficient between two diodes and RF source (left) and LO source (right) for the complete mixer.
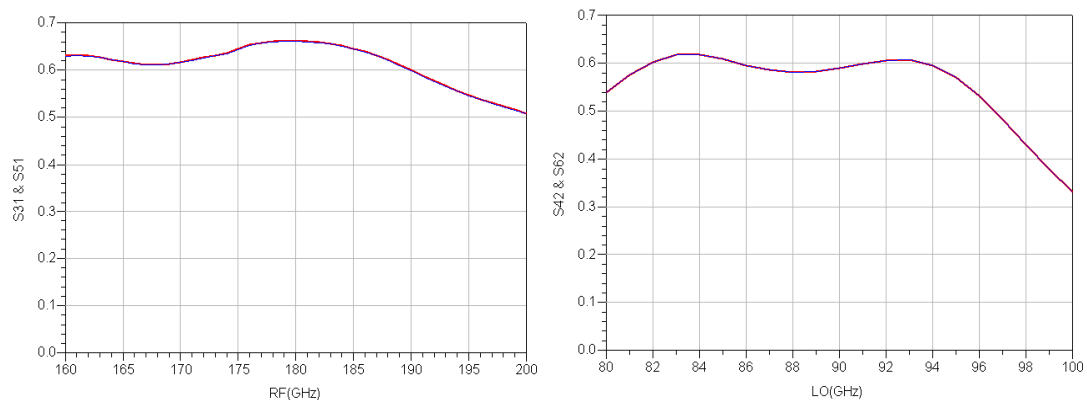
Figure 2.57: Coupling of the diodes and RF source (left) and LO source (right).

2.4.2.4 Predicted results

The performance of the mixer can be predicted by using the harmonic balance code. The LO power coupling for this mixer was optimized at 183GHz, and this mixer required 2-3mW of LO power. The expected mixer DSB conversion loss is about 3dB. A sweep of DSB mixer conversion gain (no extra losses has been taken into account) versus RF with different LO pump power is shown in Figure 2.58, the mixer has a good performance and a broader bandwidth with LO power of 2mW. According to Figure 2.59, where DSB mixer conversion loss is shown in sweep of LO power at 183GHz, it can be noticed that there is an optimum LO pump power to obtain the minimum conversion loss at a given frequency. The mixer requires enough

pump power but not too much, as the mixer conversion loss increased when the LO power increased after the optimum power value.
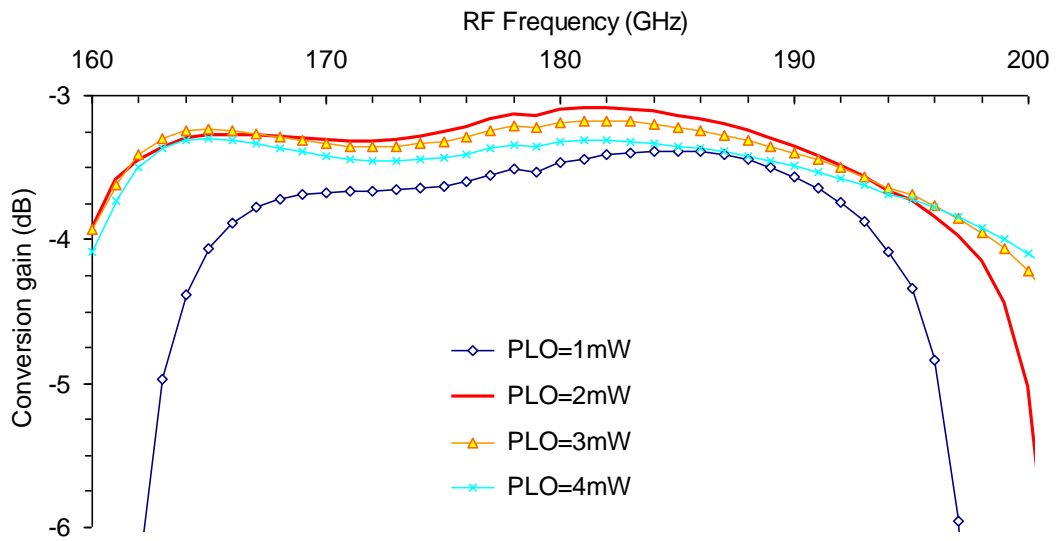
Figure 2.58: DSB mixer conversion gain dependence versus different LO power.
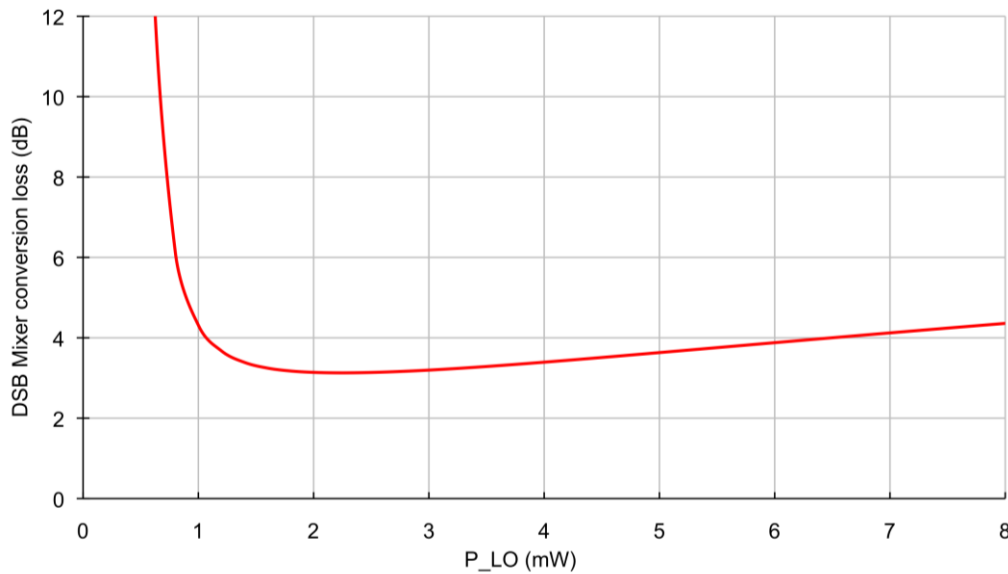
Figure 2.59: DSB mixer conversion losses versus LO pump power at 183GHz.

A margin of 2dB takes into account losses introduced by the external feed horn and mismatches between the mixer and the low noise amplifier (LNA). If the LNA equivalent noise temperature is $T_{LNA}=100K$, then the expected DSB receiver noise temperature is about 500K i.e. at the state-of-the-art. Figure 2.60 shows the DSB receiver noise temperature in a sweep of the RF frequency. The RF and LO return loss is shown in Figure 2.61.

Expected DSB receiver temperature with P_{LO}=2mW and T_{LNA}=100K at F_{IF}=1.5 GHz (Extra loss margin=2dB)
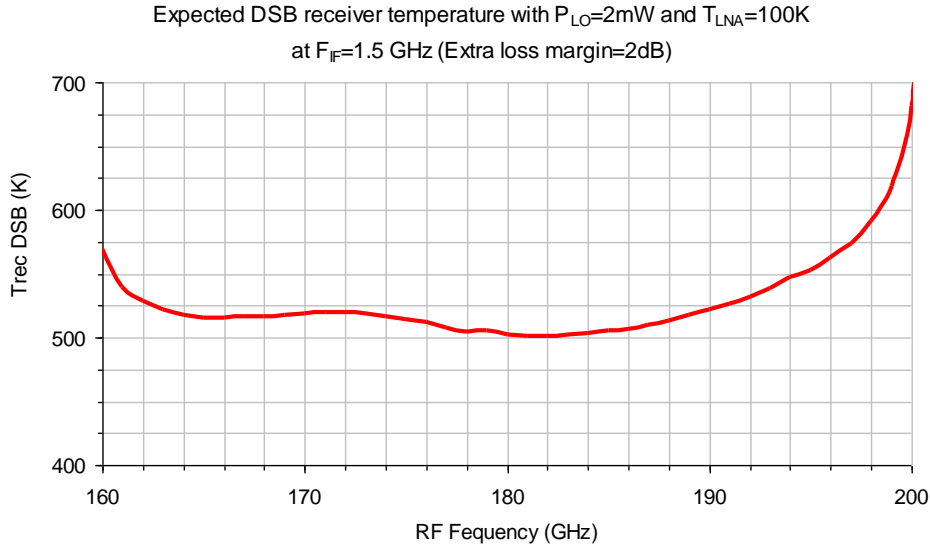
Figure 2.60: Estimated receiver DSB noise temperature depending on RF frequency. T_{LNA} is assumed to be 100K at 1.5GHz. An extra loss of 2dB was added to the DSB mixer conversion loss to take into account the losses introduced by the horn antenna and the mismatch between the mixer and the LNA.
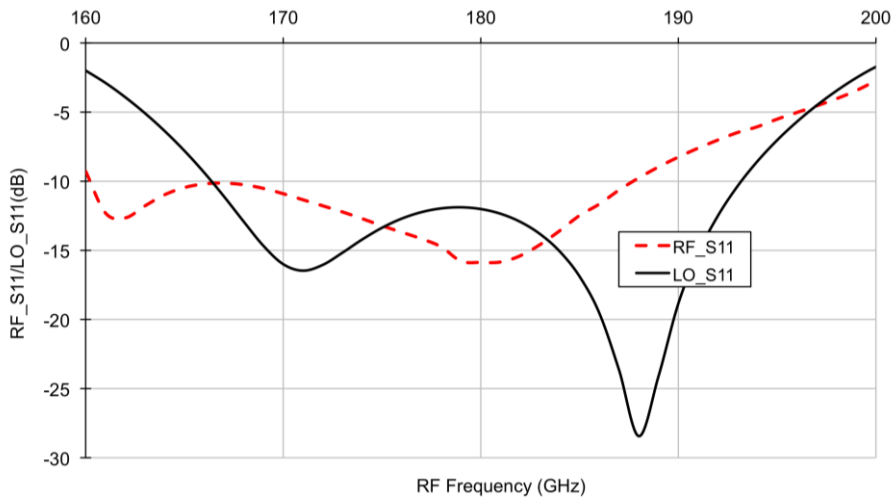
Figure 2.61: Predicted RF and LO input return losses (dB) VS RF frequency (GHz) with P_LO=2 mW.

2.4.2.5 IF impedance - Z_IF

In the 183GHz MMIC SHP2 mixer design, the output impedance of the pair of diodes at intermediate frequency (IF) was set to 100Ω as described in [Hesler99, Thomas05]. Typically in a heterodyne receiver, the IF output of the mixer is connected to an IF low noise amplifier (LNA) chain. The input impedance of the IF amplifier chain is expected to be 50Ω, which is the standard impedance for coaxial connector. The typical IF impedance of the pair of Schottky diodes is expected to be about 150Ω at the frequency range that we are working. This value has been brought

into question in certain discussions. Further study has been performed to determine which Z_IF is optimum for the mixer design. This additional investigation should be useful to improve the current design method on the millimeter wave and submillimeter wave Schottky diode mixer [Thomas 04].

This study is based on the 183GHz MMIC SHP2 Mixer (detailed in this section). The whole mixer including the IF circuit was simulated using HFSS at lower frequency range from 1 to 20GHz with three ports (see Figure 2.62), which corresponds to the model of mixer working at IF band. The matching circuit respective at RF, LO and IF to the pair of diodes were implanted into the equivalent circuit shown in Figure 2.52.
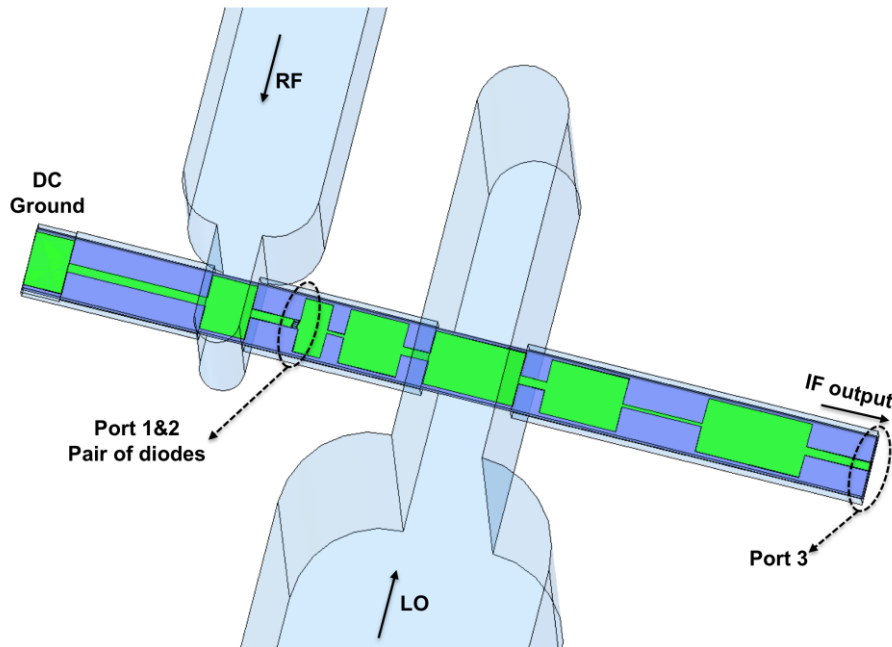
Figure 2.62: Three-dimensional model of the whole mixer composed of three waveguide ports for the IF impedance study.

Four different IF impedances have been studied to characterize the performance of the mixer. Z_IF=100Ω was the nominal value used for the design. Z_IF=143.8 Ω is the IF impedance optimized at 183 GHz with a given LO power of 2mW. The simulated DSB mixer conversion gain with four different Z_IF is shown in Figure 2.63. Four simulations were performed in the same condition of LO power and intermediate frequency. It can be noticed that the predicted result with 100Ω, 150Ω and 143.8 Ω are almost identical. There are around 1dB difference between the IF impedance of 50Ω and 100Ω, which supported the 1 to 1.5dB of discrepancy

between the measured and predicted result mentioned in [Thomas05]. This discrepancy could be explained by the mismatch between the mixer and the IF LNA chain.
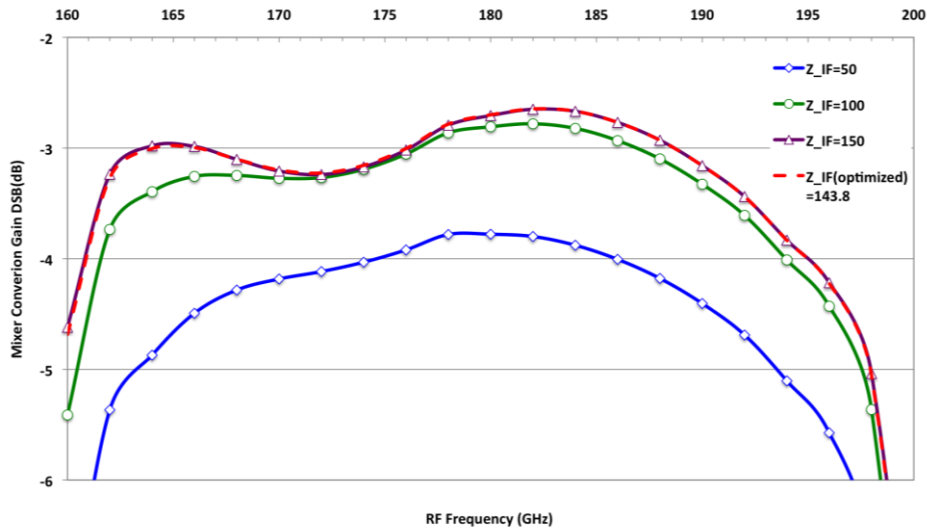
Figure 2.63: Comparison of the mixer DSB conversion gain between four different Z_IF, with P_LO=2 mW and $f_{IF}=1.5GHz$.

The IF impedance is sensitive to the LO power [Siles08a], additional simulations have been performed with higher LO power and IF shown in Figure 2.64 and Figure 2.65. Better mixer conversion gain are obtained with higher LO power and higher intermediate frequency with IF impedance of 50Ω. The performance predicted by Z_IF=100Ω and the optimized Z_IF are always similar to each other. All the results above revealed that there is a compromise in the choice of the output impedance of the pair of diodes at IF (Z_IF) between 50Ω and 100Ω for the design of Schottky diode mixer working at millimeter wavelength. By using 100Ω as the Z_IF, less LO pump power is needed for the optimized mixer, but around 1dB mismatch is present between the mixer and the IF LNA chain. In order to get a good matching, an impedance transformer could be added between two parts. If 50Ω is used for the IF impedance, more LO power is needed to get better mixer conversion gain and more noise will be produced by the diodes.
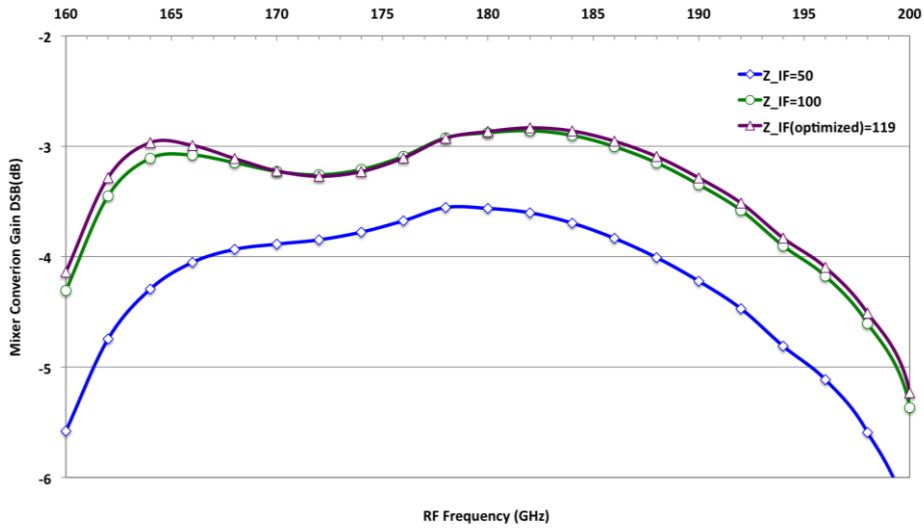
Figure 2.64: Comparison of the mixer DSB conversion gain between three different Z_IF, with P_LO=3mW, f_{IF}=1.5GHz. The optimized IF impedance is optimized at 183GHz.
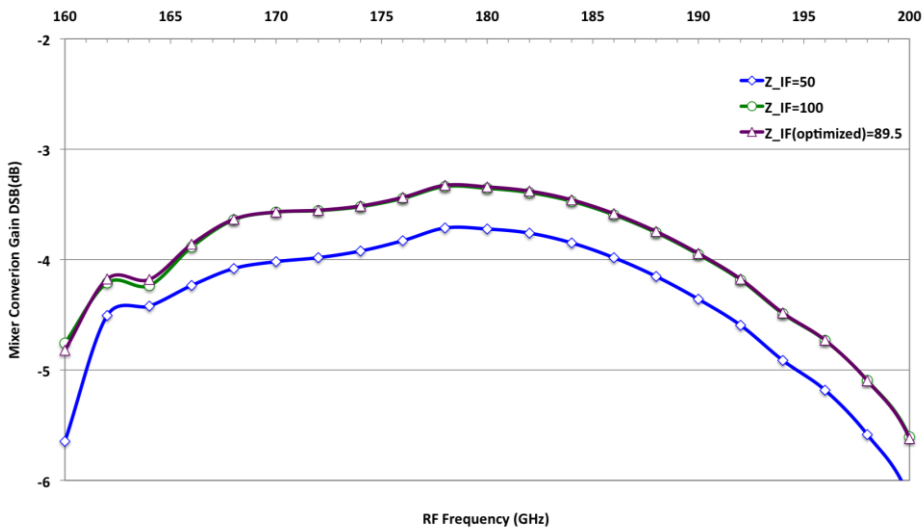
Figure 2.65: Comparison of the mixer DSB conversion gain between IF impedance of 50 and 100 with P_LO=3mW, f_{IF}=3GHz. The optimized IF impedance is optimized at 183GHz.

2.4.3 RF measurement and results

2.4.3.1 Mixer fabrication

As described previously, the mixer chips were fabricated by UMS on the same wafer that contained the tripler chips and other circuit within the research project. The mechanical block machining and the construction of the mixer have been both carried out at RAL.

Figure 2.66: Photo of the mixer chips with three different anode sizes on a tile of the UMS fabricated wafer.
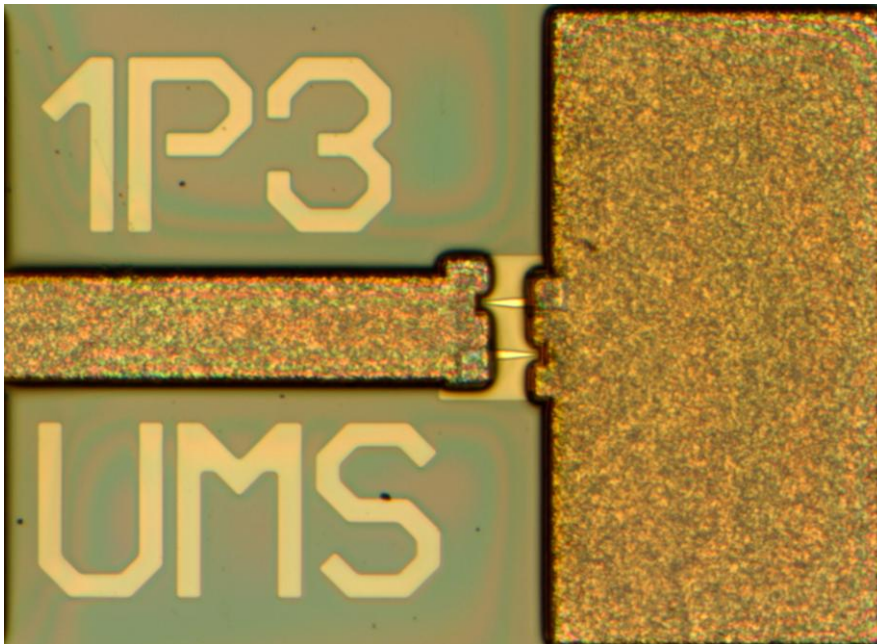
Figure 2.67: Close view of the anti-parallel diodes with 1.3 μm anode length that was labelled on the chip.

The designed anode dimensions were bracketed to include larger and smaller anodes to allow for variations in the actual anode size as well as doping density and modeling errors. Hence, three different anode sizes have been included on the wafer for the mixer chip; Figure 2.66 shows the photo of these three anode size variations, the label can identify the dimension of the anode size for each chip. Detailed view of the anti-parallel diodes is shown in Figure 2.67, which corresponds to a mixer chip with 1.3μm anode length diodes.

On-wafer measurements of the discrete diode characteristics have been performed at RAL. The small area anodes generally present high resistance values with a significant offset between the polarities of the diodes. At the UMS BES foundry, it is the first fabrication of small area diodes (anode length less than 3μm). UMS has been investigating the cause of this discrepancy and a solution has been proposed to reduce the systematic error for the second running. Based on preliminary on-wafer diode measurement results, the mixer chip with a larger anode size has been chosen for the mixer performance test. Owing to misalignments, all the diodes with different orientations (anti-parallel) present an asymmetry in the active area and therefore present imbalanced characteristics.
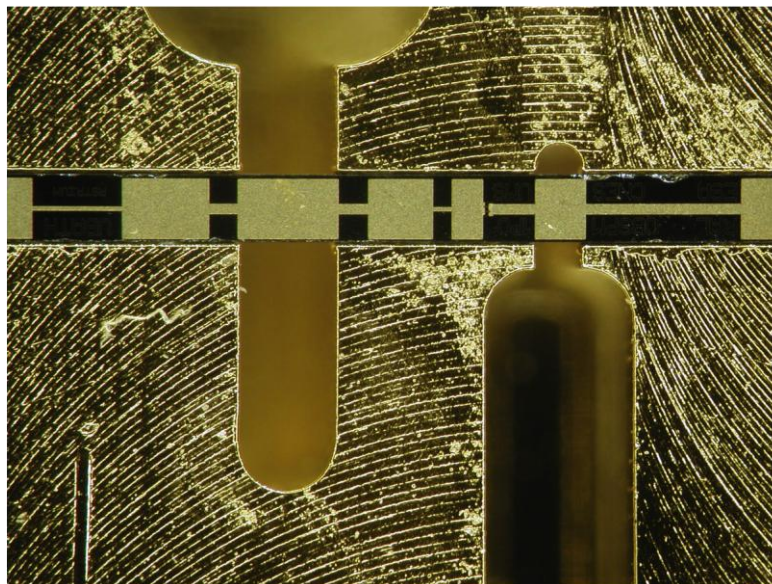
Figure 2.68: Photograph of the bottom block with the 183GHz integrated mixer chip. The circuit is about 4mm long, 0.28mm width.

The measured mixer chip with 1.3μm anode size has imbalanced diodes with measured series resistance of 21Ω and 12.5Ω. Figure 2.68 shows a photo of the mixer chip mounted in the bottom block.

2.4.3.2 Mixer measurement

For the experiments, the LO fundamental source was provided by a 8-18GHz Yig oscillator from an AB Millimetre Network Vector Analyzer [ABmm], which was used to drive a commercial sextupler followed by a power amplifier, both from Radiometer Physics GmbH; this LO source chain could provide about 10mW from 75GHz to 100GHz. This source chain was calibrated with an Erickson power meter [Erickson99]. A W band waveguide attenuator was used to adjust the pump power for the mixer. A directional coupler inserted before the mixer measured the pump power coupled into the mixer. Photo of this test setup is shown on the left of Figure 2.69.
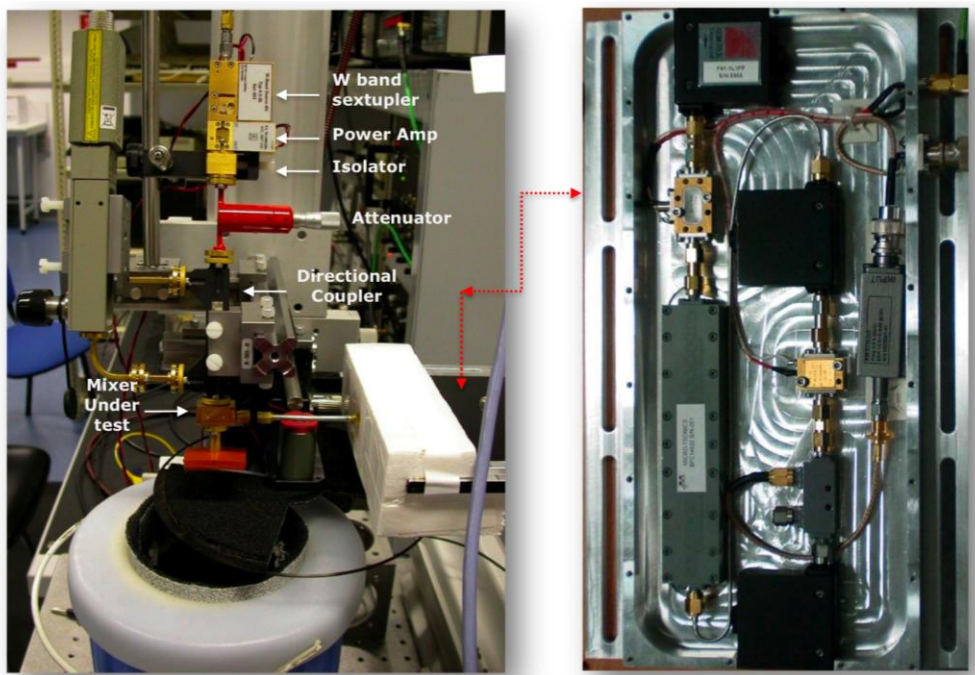
Figure 2.69: Test setup for mixer measurement (left) and LERMA 2-4GHz IF chain before closing the top cover (right)

A 2-4GHz IF chain (see Figure 2.69 and detailed in Appendix A) has been used for the measurement, which includes a low-loss isolator at its input and an internal noise source that can be switched ON and OFF to modify the noise factor of the IF chain. The equivalent noise temperature of the IF chain is 194.4K when the internal noise source is ON, and 81.2K when the internal noise source is OFF.

The equivalent noise temperature of the receiver was measured by presenting alternatively a room temperature and a liquid nitrogen-cooled blackbody in front of the mixer feed-horn. Two independent receiver equivalent noise temperature measurements are performed: one with the internal noise source ON the other with

the internal noise source OFF. The receiver noise temperature is calculated using the classic Y factor method. The Y factor was measured with an Agilent E9325A (0.05-18GHz) power sensor corrected from its non-linearity in a separate calibration procedure. This test bench can achieve an excellent accuracy resolution of 0.001dB for the Y factor measurement. Details can be found in Appendix A.

All the measurements were performed at room temperature. Mixer DSB noise temperatures, mixer conversion losses and the LO pump powers as a function of RF frequency are presented below in Figure 2.70 and Figure 2.71. The optimum pump power in the band 160-190GHz is however in very good agreement with the simulation results.
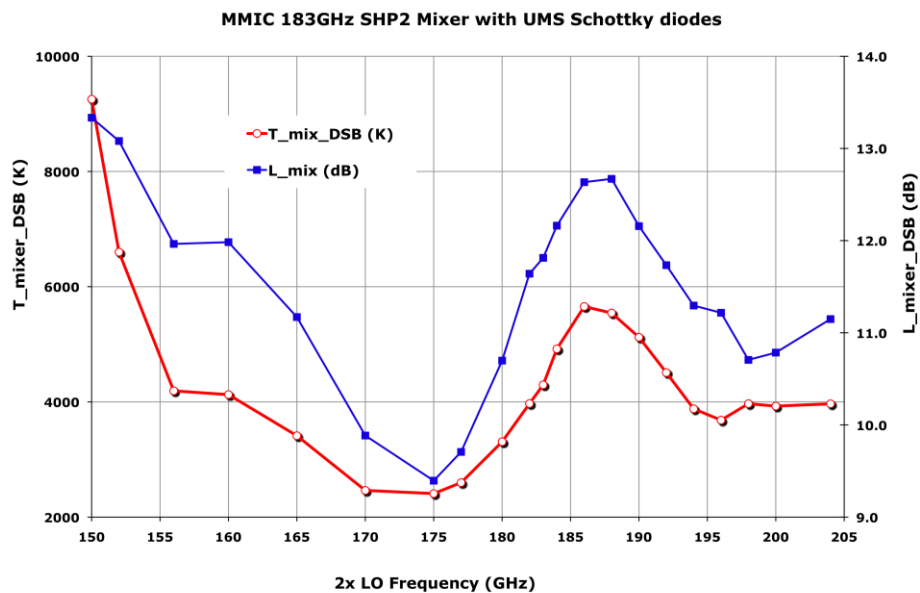
Figure 2.70: The top plain curve with filled square markers and the bottom plain curve with open circles show respectively the measured DSB mixer noise temperature and the measure DSB mixer conversion loss.
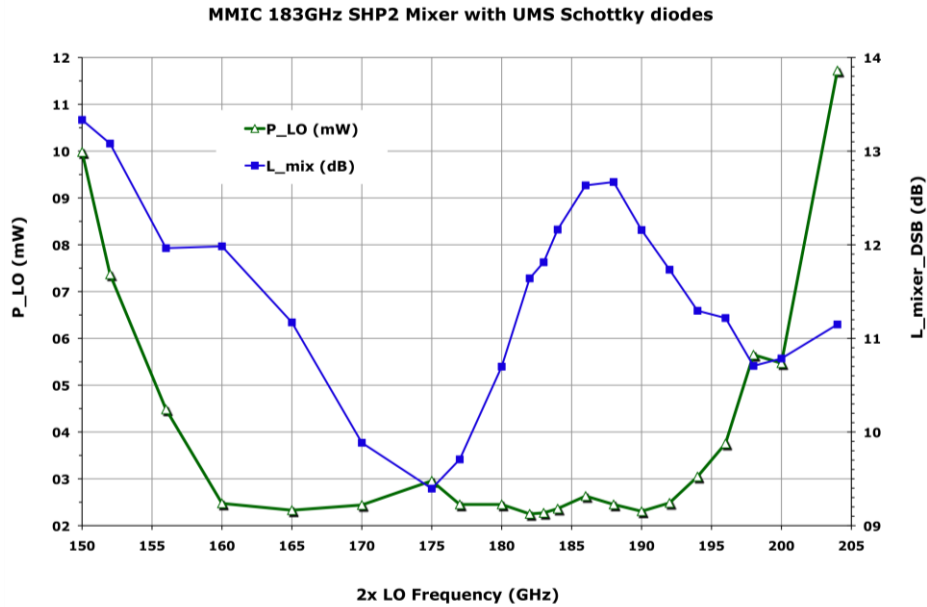
Figure 2.71: The top plain curve with filled square markets shows the measured DSB mixer conversion losses, the bottom plain curve with open circles show the optimum LO pump power for each frequency.

Additional measurement on the LO return loss has been performed at ABmm with the network vector analyzer. Figure 2.72 (below) shows the measured LO return loss. The LO pump power is delivered by a W-band sextupler, with the measured LO power injected into the mixer shown in Figure 2.72 (top). As the mixer was optimized for 2mW of LO power, to measure the LO return loss at the proper power, an attenuator was used to reduce the LO power remaining around 2mW.

88
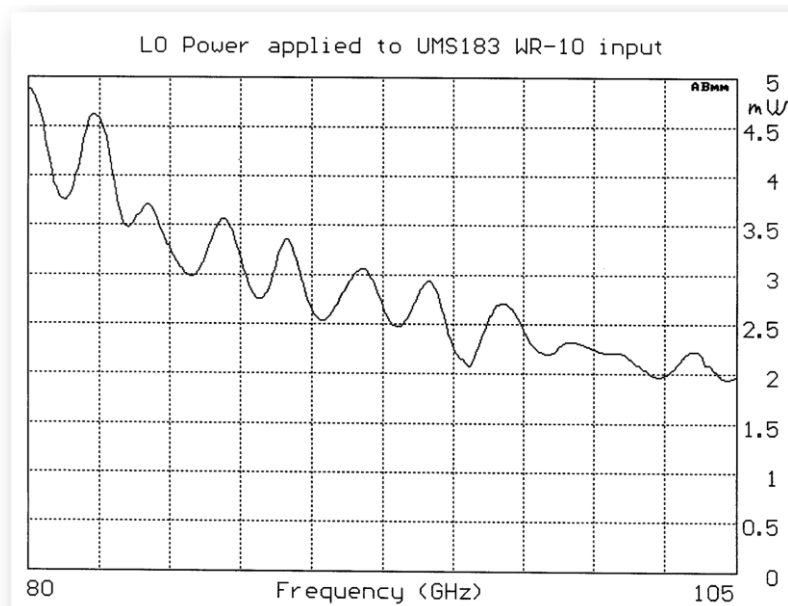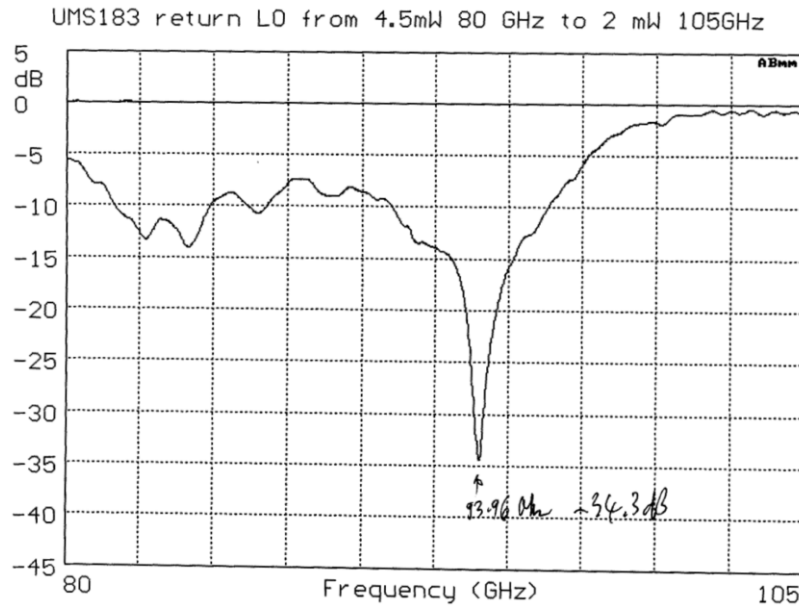
Figure 2.72: LO pump power as function of LO frequency using for the return loss measurement (top) and measured LO return loss as function of LO frequency (below).

2.4.4   Comparison of the measured and predicted results

Table 2.5 shows the predicted mixer performance and the measured results presented previously. The measured noise temperature and conversion loss is significantly higher than the predicted values. This could be partly due to the unbalance of the diodes. The diode model of the nominal design and the measured one is summarized in

Table 2.6. The diode characteristics of the simulated model were estimated from measurements of diodes with larger anode.

Table 2.5 Comparison of the measured with the predicted results for the 183 GHz mixer, 2 dB estimation of mixer losses introducing by the horn losses and the mismatch between the mixer and the IF LNA chain.

	Predicted (with loss)	Measured
Best DSB mixer conversion loss (dB)	5.1@183GHz	9.4@175GHz
Best DSB mixer noise temperature (K)	500@183GHz	2409@175GHz
LO pump power (mW)	2	~2

Table 2.6 Comparison of the diode model for the simulation and the measured mixer chip.

Diode electrical parameters	Specific	Simulated	Measured
Anode length (um)	5	1.5	1.3 (?)
$R_S(\Omega)$	5	10	$R_{s1} = 12.5$ $R_{s2} = 21$
η	1.2	1.2	~1.26
$C_{j0}(fF)$	8	2	?

Some of the potential reasons for the discrepancy between the measured and predicted results include:

- Variations in diode characteristics (e.g. epitaxial layer doping, anode area);

- Variations in substrate thickness;

- Variations in mixer chip mounting (e.g. position of the microstrip to waveguide transition);

The variations in diode characteristics include changes in anode area and epitaxial layer doping, which led to the variations in the diode's electrical properties. When the diode embedding impedance changes, the matching circuits are no more appropriate to the actual diodes. These variations are expected to affect the mixer performance. In order to determine the effect from these variations, series simulations were performed on the variations in several diode electrical parameters. These simulations were based on the 183GHz mixer discussed previously, and the variations of each parameter were independent.

Figure 2.73 shows the SSB mixer conversion gain as a function of the series resistance with 5Ω steps. It can be noticed that an offset of 5Ω on the series resistance can potentially account for about 0.5dB on the predicted conversion gain. Meanwhile, the predicted mixer noise temperature can be changed approximately by

120K for each increment, which is shown in Figure 2.74. As the series resistance is measured by experiment, each research group will have its own method, uncertainty of this measured value is causing by different measured methods. As measuring the series resistance of small-anode diodes is not performed in a standardized manner, experimental values of series resistance can have an important error bar, depending on the laboratory and method used.
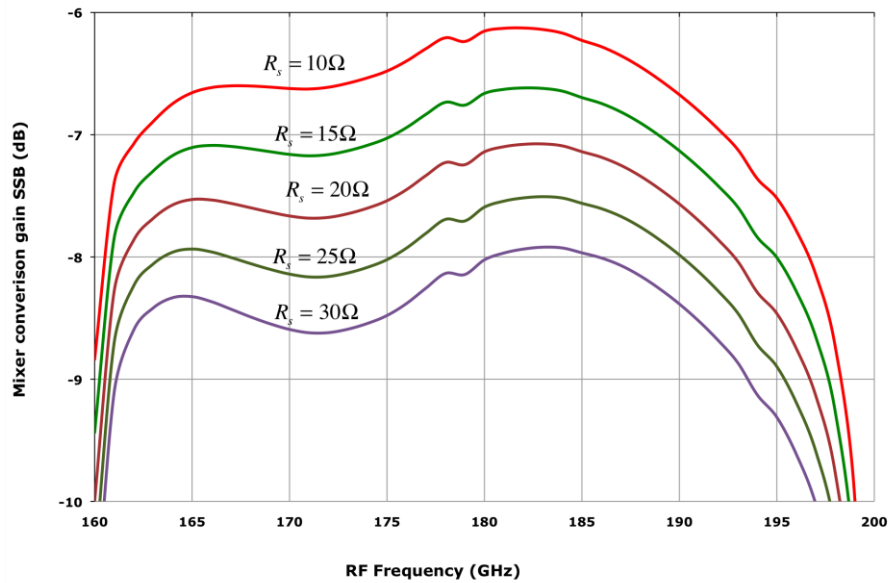
Figure 2.73: SSB mixer conversion gain dependence versus different Rs.
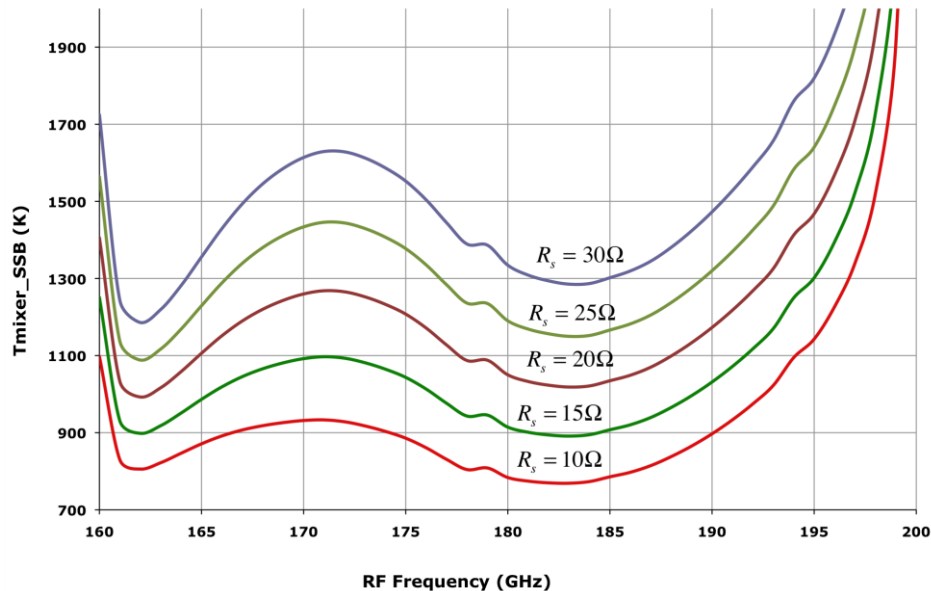
Figure 2.74: SSB mixer noise temperature dependence versus different Rs.

Figure 2.75 shows the effect on the mixer conversion gain introduced by the variation of the diode ideality factor. The mixer performance decreased when the

diode ideality factor increases. Another important parameter is the zero voltage junction capacitance, as discussed previously; it is important to minimize the junction capacitance for a mixer diode, which is shown in Figure 2.76 and Figure 2.77. According to Figure 2.76, the conversion gain is degraded at least 0.5dB with difference of 2fF zero voltage junction capacitance, this degradation increases by increasing the value of the capacitance. The mixer operating frequency band is shifted at the same time to lower frequency. The effects of the variations of the diodes characteristics on the mixer performance are summarized in Table 2.7.
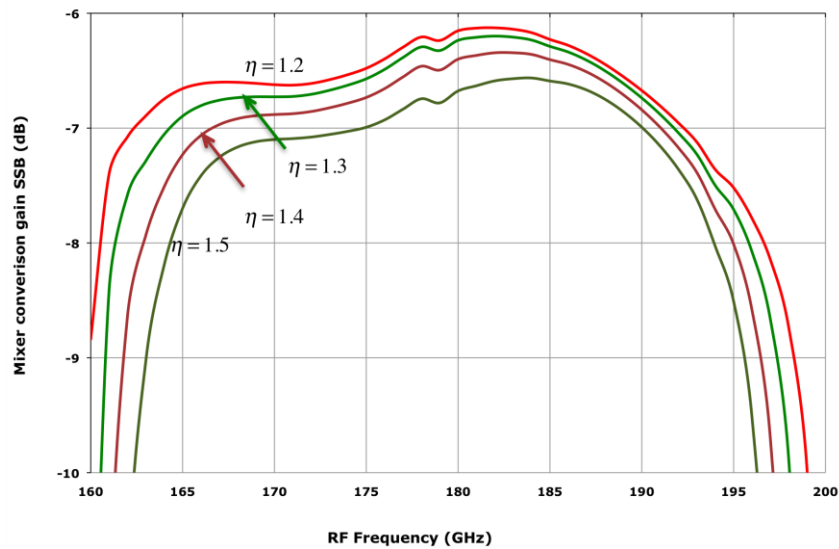
Figure 2.75: SSB mixer conversion gain dependence versus variation of ideality factor.
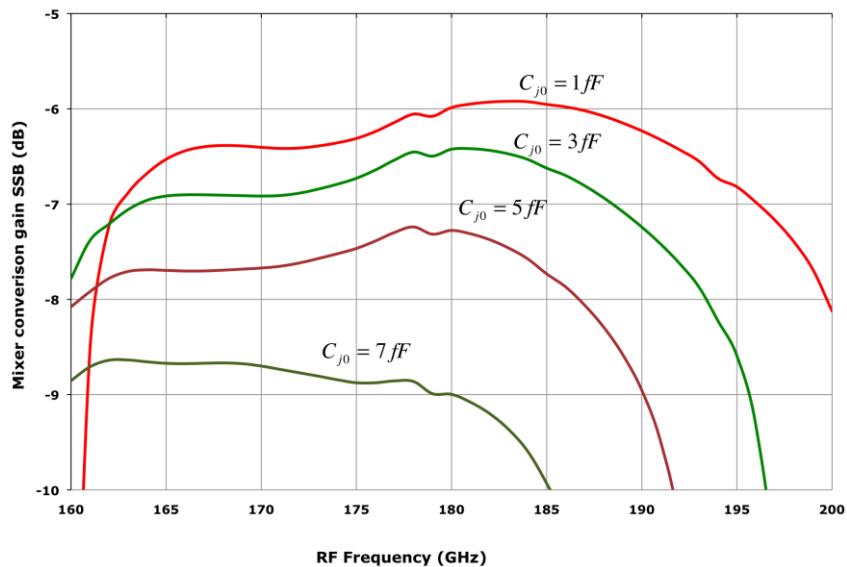
Figure 2.76: SSB mixer conversion gain dependence versus variation of C_{j0}.
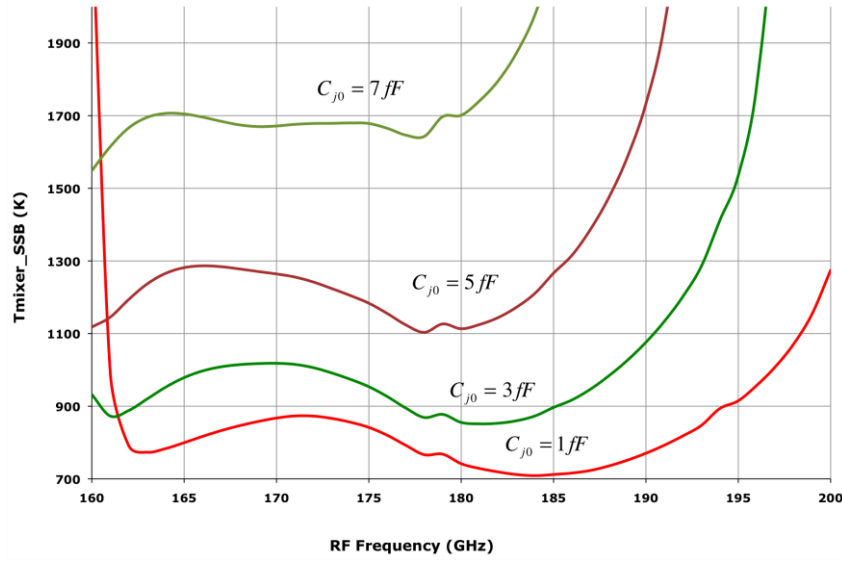
Figure 2.77: SSB mixer noise temperature dependence versus variation of C_{j0}.

Table 2.7 Summary of the variations in diode characteristics on the effect of the 183GHz mixer performance.

Diode electrical parameters	Predicted SSB mixer conversion gain (dB)	Predicted SSB mixer noise temperature (K)
$\Delta R_S = 5\Omega$	~0.5	~120
$\Delta \eta = 0.1$	>0.08	-
$\Delta C_{j0} = 2\,fF$	>0.4	>87

As described in [Crowe86] conversion loss may be divided into intrinsic loss L_0 and parasitic loss L_p. Intrinsic loss is the amount of loss that would occur if there were no parasitic elements, i.e. series resistance and junction capacitance, in the diode. Parasitic loss is defined as the increase in conversion loss due to the presence of non-zero parasitic elements, and is generally approximate by,

$$L_p = (1 + R_s / R_{IF})(1 + R_s / R_{RF} + \omega^2 C_j^2 R_{RF} R_s) \qquad (2\text{-}9)$$

Equation (2-9) assumes that the diode is optimally pumped by the LO source. Where R_s is the constant series resistance, C_j is the constant junction capacitance and equivalent impedances R_{RF} and R_{IF} at the signal and image frequencies. When the series resistance increased or decreased, the mixer conversion loss is changed

93

proportionally. The effective noise temperature of the series resistance was expressed as in [Crowe87]

$$T_e = A(f)R_s I^2 \qquad (2\text{-}10)$$

where I is the current through the epilayer and $A(f)$ is a frequency-dependent coefficient. Apparently, the effective noise temperature of the series resistance is increased proportionally to the series resistance. So it is important to minimize the series resistance of the diode in order to decrease the mixer noise temperature.

Mixer with imbalanced diodes has been analyzed with electrical parameters values listed in Table 2.8. Owing to the misalignment, the anti-parallel diodes present an asymmetry in the anode areas; therefore different capacitance value of each diode is used for this analysis. The comparison of the predicted mixer conversion gain and noise temperature between the mixer with nominal designed diodes and imbalanced diodes were shown in Figure 2.78 and Figure 2.79, at least 2dB discrepancy of the mixer conversion gain is accounted by this imbalance in the series resistance, furthermore the mixer noise temperature is approximately doubled with the imbalanced diodes. Although the discrepancy between the measured results and the predicted results is partly due to the imbalanced UMS diodes, part of this difference cannot be explained at the current stage of this work. The comparison between the predicted mixer results with identical diodes and imbalanced diodes is shown in Table 2.9.

Table 2.8 Imbalanced diode electrical parameters used for the simulation.

Diode electrical parameters	Diode1	Diode2
$R_S (\Omega)$ Measured value	12.5	21
η	1.26	1.26
$C_{j0} (fF)$ Estimated value	6.5	3.8
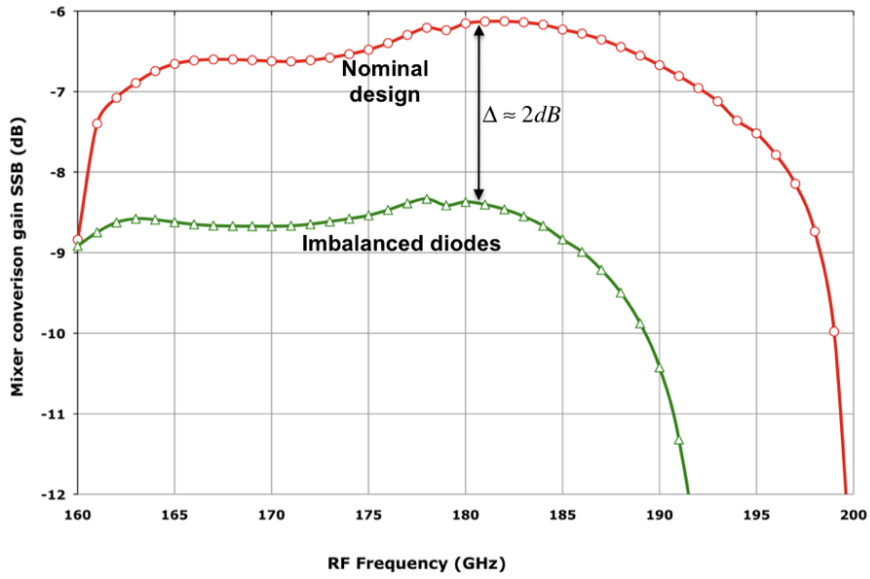
Figure 2.78: Predicted SSB mixer conversion gain with nominal diodes and imbalanced diodes.
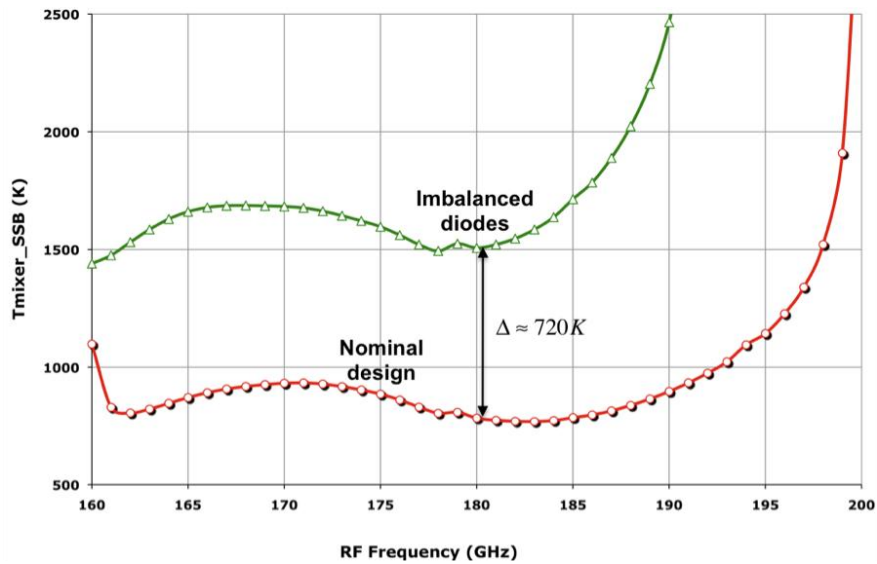
Figure 2.79: Predicted SSB mixer noise temperature with nominal diodes and imbalanced diodes.

Table 2.9 Comparison of the predicted results for the 183 GHz mixer at 183 GHz, with identical diodes and imbalanced diodes, excluding the losses.

	Predicted SSB mixer conversion loss (dB)	Predicted SSB mixer noise temperature (K)
Identical diodes	6.14	769
Imbalanced diodes	8.55	1585
Discrepancy	2.41	816

The mounting of the mixer circuit in the block is generally performed manually under a microscope. Two series of simulations were performed the effect of these mounting inaccuracies on the mixer performance. One is concerning the variation of the substrate thickness; the substrate thickness was reduced to 40μm from the designed thickness of 50μm, the comparison of the mixer performance between the variations of the substrate thickness is shown in Figure 2.80 and Figure 2.81. The offset of the substrate thickness does not significantly affect the mixer performance, but reduces the bandwidth.
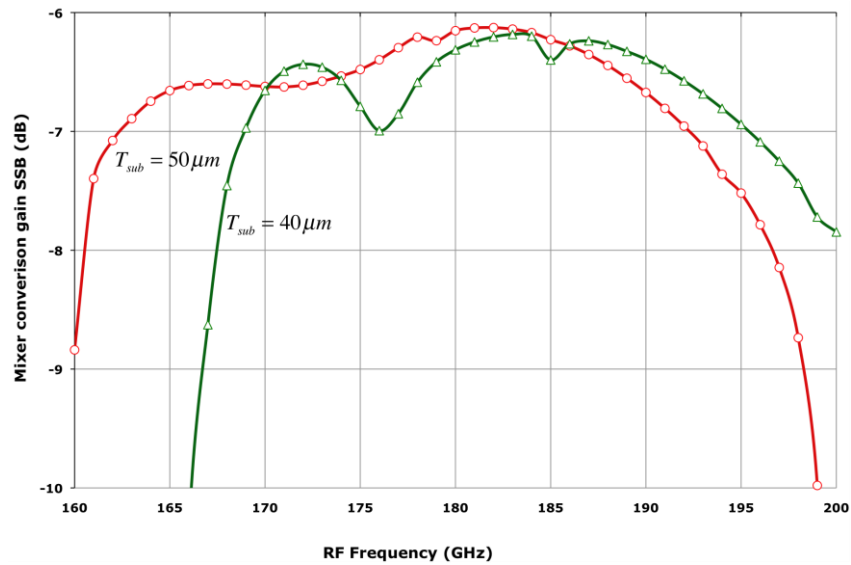
Figure 2.80: Predicted SSB mixer conversion gain by reducing the substrate thickness to 40μm.
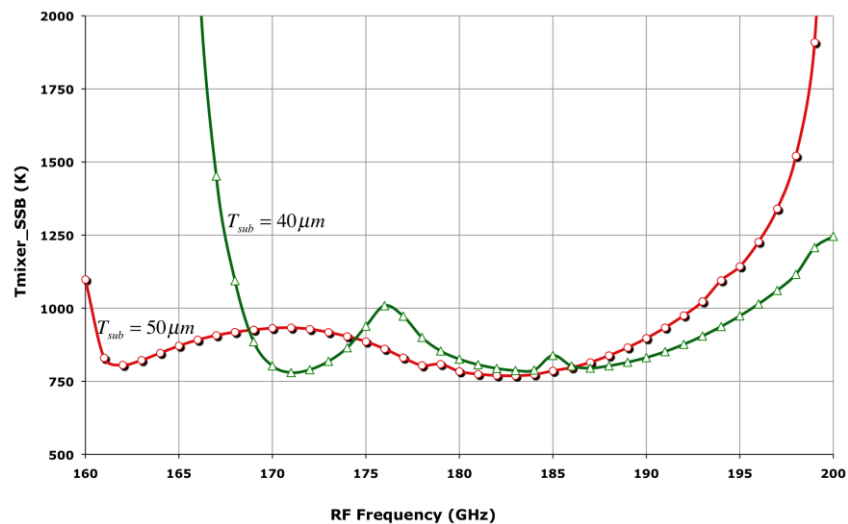
Figure 2.81: Predicted SSB mixer noise temperature by reducing the substrate thickness to 40μm.

Another series of simulation was performed on the variations of the position of the microstrip to waveguide transition (see Figure 2.82), therefore the diodes are closer or away to the RF waveguide. As the mixer chip is flipped and mounted in the block, offset could be presented from the design position. Two variations have been analyzed with $\pm 10\mu m$ offset; $+10\mu m$ indicating the diodes are closer to the RF waveguide. The loss caused by these variations is really small, around 0.02 dB.
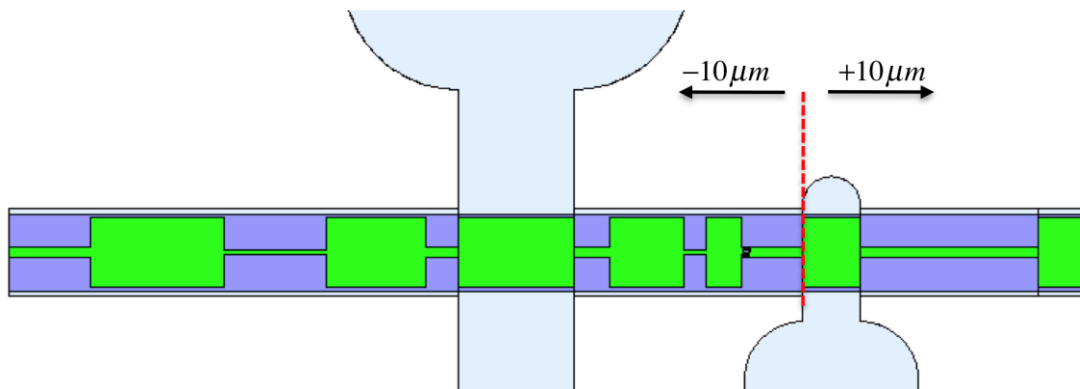
Figure 2.82: Schematic showing offset of the designed position of the mixer circuit in the block.

2.4.5 Perspectives

The circuits designed within this work are all using the industrial foundry process from UMS, which rely on its guarantied quality and repeatability. They provide a Schottky diode process without an air-bridge to the anode, compared to the traditional air-bridge Schottky diode process. The purpose of the air-bridge is to reduce the parasitic elements around the diode. In consequence, an interesting study has been taken on to compare the process with or without air-bridge for a same circuit based on Schottky diodes. The 183GHz MMIC SHP2 mixer described in this section has benefited two other European Schottky diode processes in collaboration programs. Prototypes of this mixer have been fabricated at the University of Bath and thereafter at the RAL in UK, both using a process that allow air-bridging of the diodes to decrease the parasitic capacitance. They share the same chip-layout and waveguide block as the mixer designed for UMS BES process. Simulations show that the presence of the air-bridges does not significantly change the matching of the diodes; therefore the same block is expected to be optimum for both circuits allowing a direct and relevant comparison between the processes, furthermore this could be the

first time such a study is carried out. With this approach, we could also study the repeatability of the design with different process.

2.4.5.1 183GHz mixer using the diodes from University of Bath

Three-dimensional integrated diode structure is shown in Figure 2.83, detailed description of the mixer fabrication was given in [Rollin06].
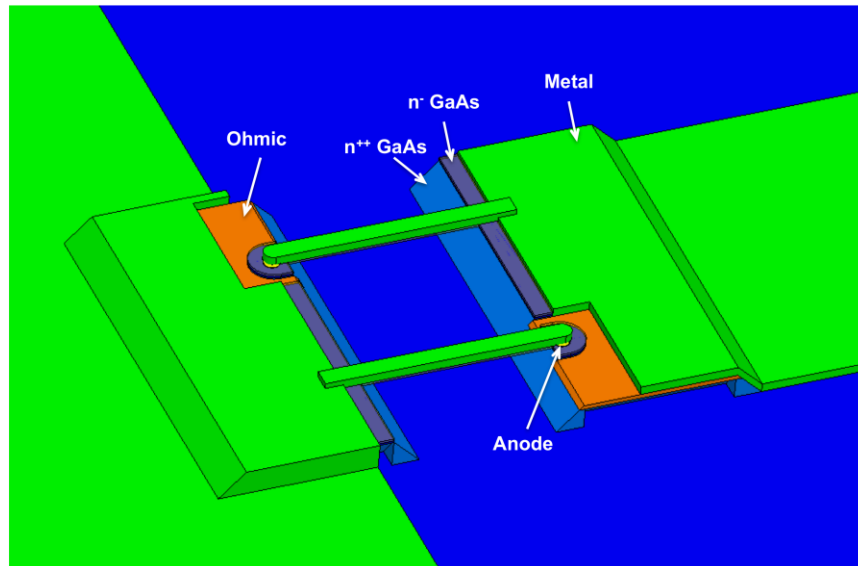
Figure 2.83: Three-dimensional view of the integrated diode structure and air-bridge configuration.

Simulated mixer performance with the diodes from the University of Bath is shown in Figure 2.84. The simulated result shows that the presence of the air-bridges does not significantly change the matching of the diodes. Within this simulation, the diodes of University of Bath have the same electrical parameters for the UMS diodes except the diodes structure. The simulated diodes have an ideality factor $\eta = 1.2$, saturation current $I_{SAT} = 4 \times 10^{-15} A$, a series resistance $R_s = 10\Omega$, and a zero bias junction capacitance $C_{j0} = 2 fF$.
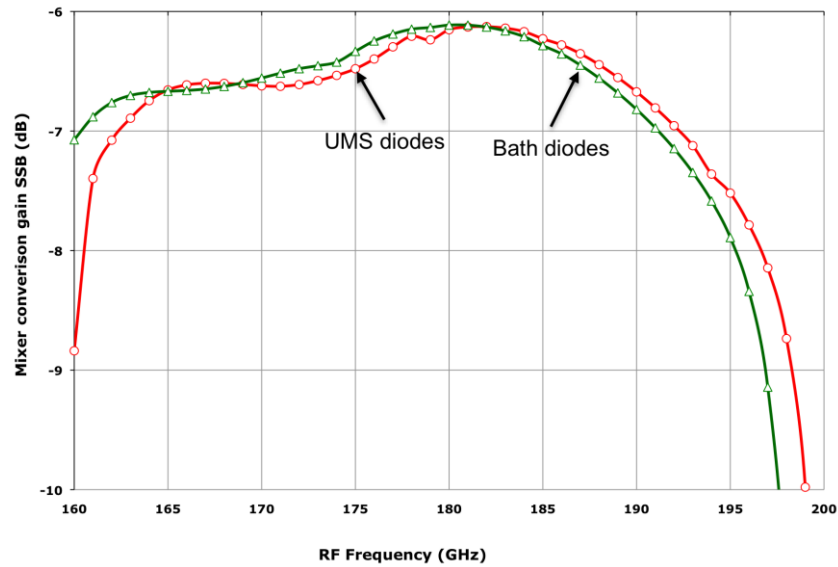
Figure 2.84: Predicted SSB mixer conversion gains with UMS diodes and Bath diodes; diodes have the identical electrical parameters.

Complete devices were fabricated on GaAs substrate with an epilayer doping of $2 \cdot 10^{17} cm^{-3}$, having anode diameters of 1μm, expected ideality factors $\eta = 1.15$ and series resistance of around 15Ω per anode. An SEM image of the on wafer complete mixer circuits is shown in Figure 2.85.
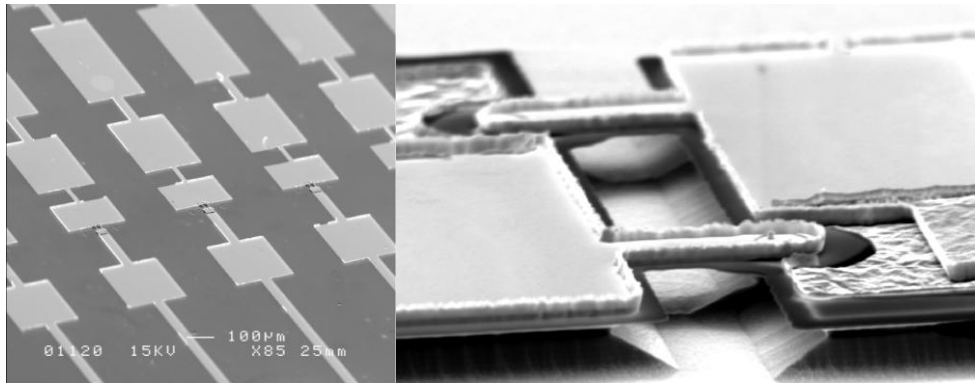
Figure 2.85: SEM images of complete mixer chips on wafer and close view of the anti-parallel pair of diodes.

Figure 2.86 shows the mounted mixer chip in the bottom mixer block (above), from the figure below, it can be noticed that the mounted chip in the block is curved. This deformation was due to the extremely thin substrate of the chip (around 20μm) compared to the length of the complete chip of more than 4mm. However, the nominal design is for the chip substrate of 50μm. Owing to this deformation of the mixer chip, part of the circuit could probably touch the block when closing the split half block. A preliminary measurement on this mixer block has been performed at

RAL; the preliminary experiment shows that LO coupling was good, but the mixer performance was degraded due to the diode characteristics degradation.
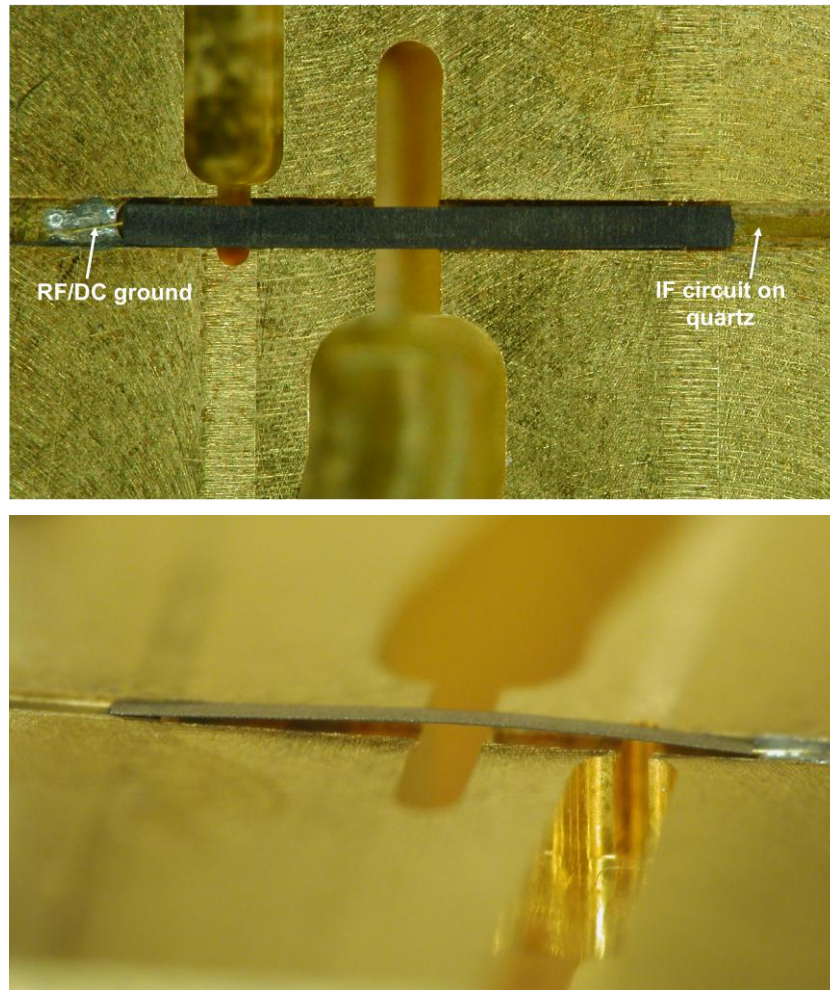
Figure 2.86: The photograph of the mixer chip mounted in the bottom block (above) and side view of the mounted chip (below).

2.4.5.2 183GHz mixer with the diodes from RAL

Thereafter the same mixer layout has been fabricated with RAL Schottky diode process; the RAL diodes structure is very similar to that of the University of Bath. Figure 2.87 and Figure 2.88 show respectively the photograph of the mixer chip during dicing and the mixer chip mounted in the bottom block.
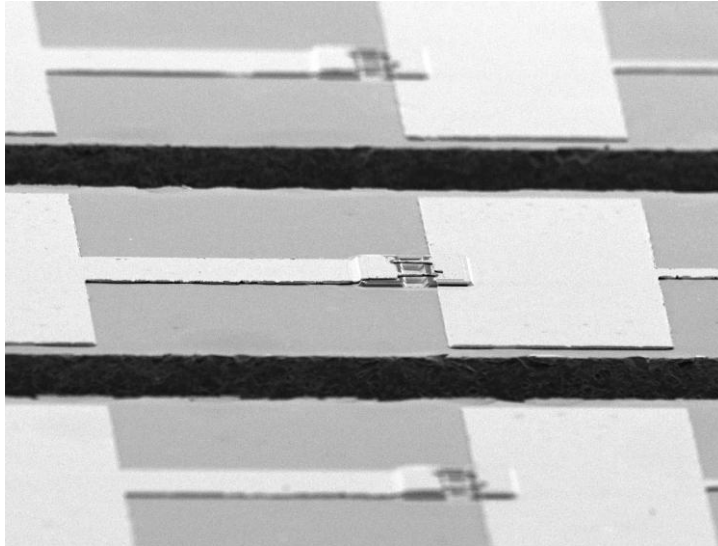
Figure 2.87: Photograph of the mixer chip during dicing.
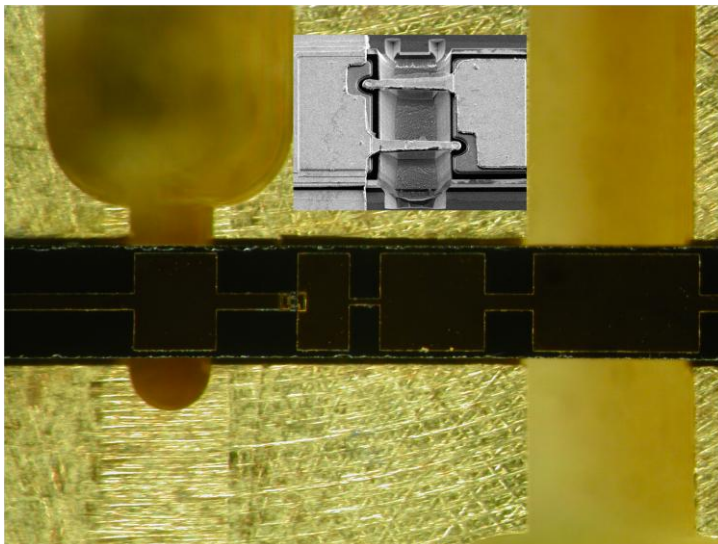
Figure 2.88: Photograph of the bottom block with the 183GHz mixer chip. The circuit is about 4mm long, 0.28mm width. Top middle shows the anti-parallel diodes of RAL.

a) 1st RF measurement of 183GHz mixer with 1st run from RAL diodes

The first series of the 183GHz mixer chip has been fabricated on a higher doping epilayer GaAs wafer with $N_{epi} = 4 \cdot 10^{17} cm^{-3}$ compared to the nominal doping epilayer of $1 \cdot 10^{17} cm^{-3}$, the diodes having a diameter of 1.3 μm, hence these diodes do not have the same electrical parameters for the nominal design, they have higher zero bias junction capacitances (40% higher than the nominal value) and smaller series resistance.

The mixer performance has been measured at LERMA by using the same method described in Chapter 2.4.3. The measured DSB mixer conversion loss and

noise temperature are shown in Figure 2.89, a minimum DSB mixer conversion loss of 4.8dB and correspond with the minimum noise temperature of 793K were measured at 161GHz. The measured optimum LO pump power is shown in Figure 2.90, at least 4.3mW LO pump power is needed to apply for the mixer, which is higher than the expected LO power of 2mW. Meantime, the frequency band has been shifted towards much lower frequency due to the higher zero voltage junction capacitance.
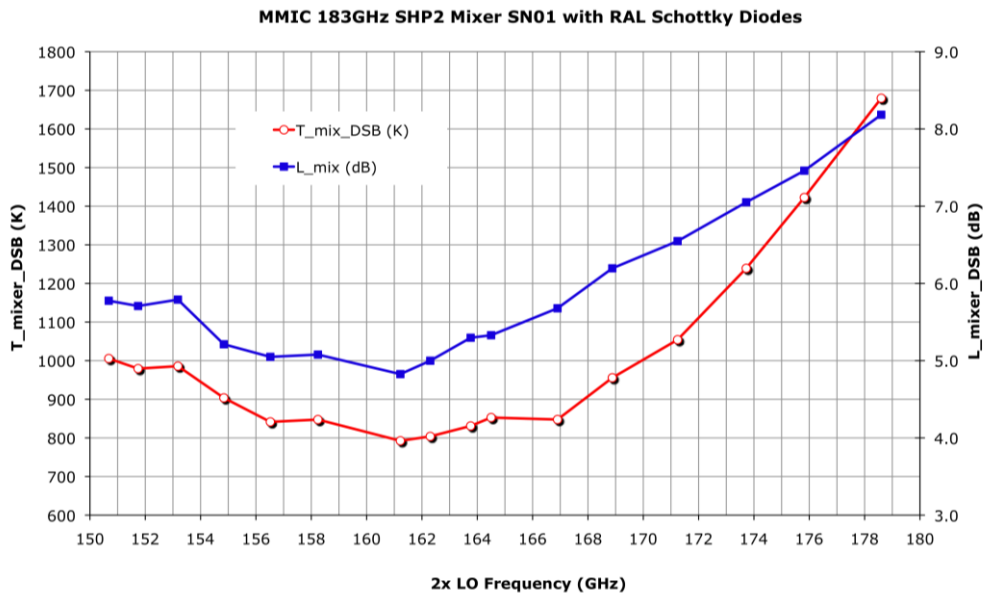
Figure 2.89: The plain curve with filled markers and opened markers show respectively the measured DSB mixer conversion loss and DSB mixer noise temperature.
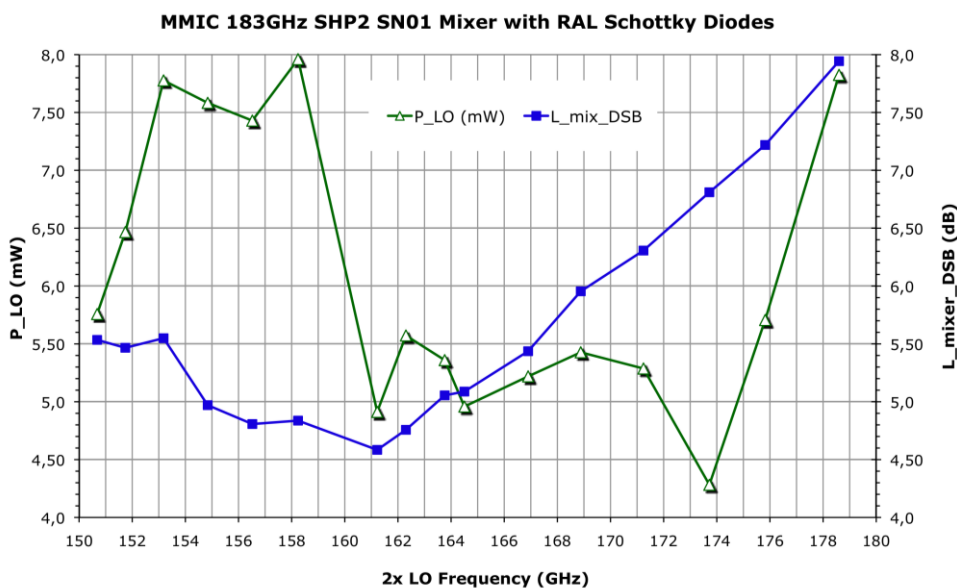
Figure 2.90: The plain curve with filled markers and opened markers show respectively the measured DSB mixer conversion loss and the optimum LO pump power.

Further measurement has been performed to characterize the requirement of LO pump power, by tuning the LO pump power at $f_{LO} = 80 GHz$, the measured mixer performance in function of LO pump power is shown in Figure 2.91.

MMIC 183GHz SHP2 Mixer SN01 with RAL Schottky Diodes
2x LO Frequency =160 GHz IF Frequency= [2GHz,4GHz]
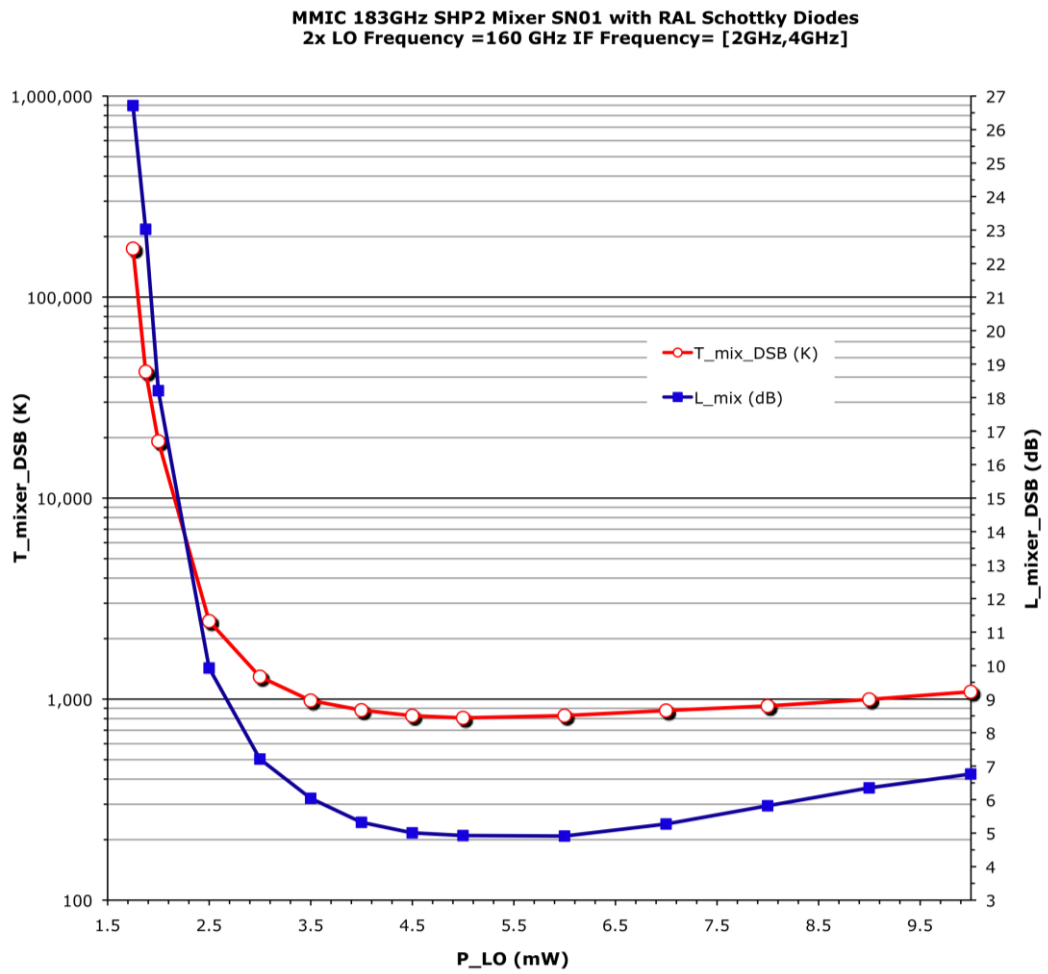
Figure 2.91: The plain curve with filled markers and opened markers show respectively the measured DSB mixer conversion loss and DSB mixer noise temperature versus LO pump power.

b) 2nd RF measurement of 183GHz mixer with 2nd run from RAL diodes

The second series of the 183GHz mixer chip have been fabricated on a GaAs wafer with $N_{epi} = 1 \cdot 10^{17} cm^{-3}$, which is the same as the nominal design, the diodes having a diameter of 1.3μm. The measured DSB mixer conversion loss and noise temperature are shown in Figure 2.92, a minimum DSB mixer conversion loss of

6.6dB corresponding the minimum noise temperature of 1038K were measured at 183 GHz. The measured optimum LO pump power is shown in Figure 2.93, at least 2.6mW LO pump power is needed to apply for the mixer. The mixer exhibits good performance at the simulated frequency range from 160GHz to 200GHz.
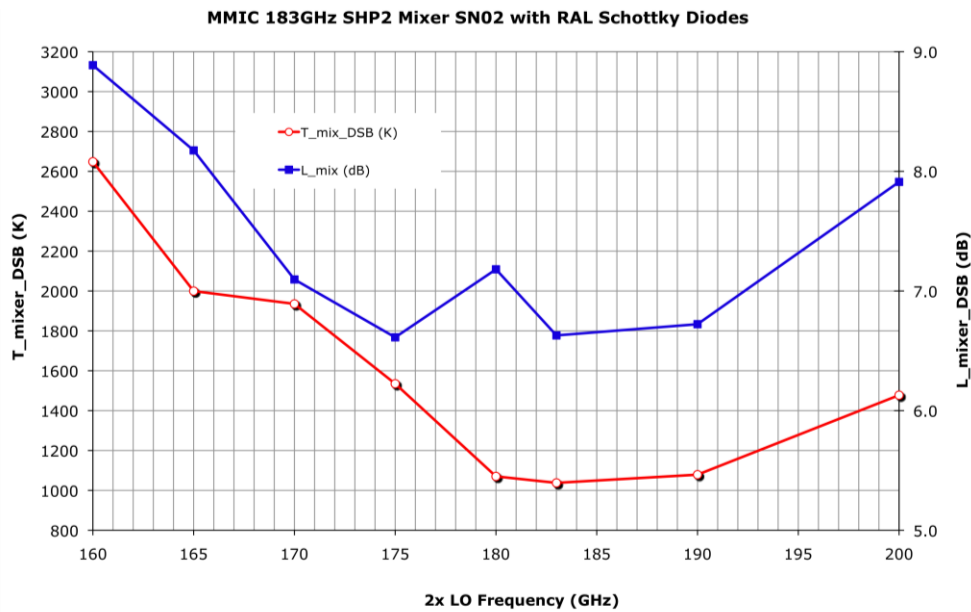
Figure 2.92: The plain curve with filled markers and opened markers show respectively the measured DSB mixer conversion loss and DSB mixer noise temperature.
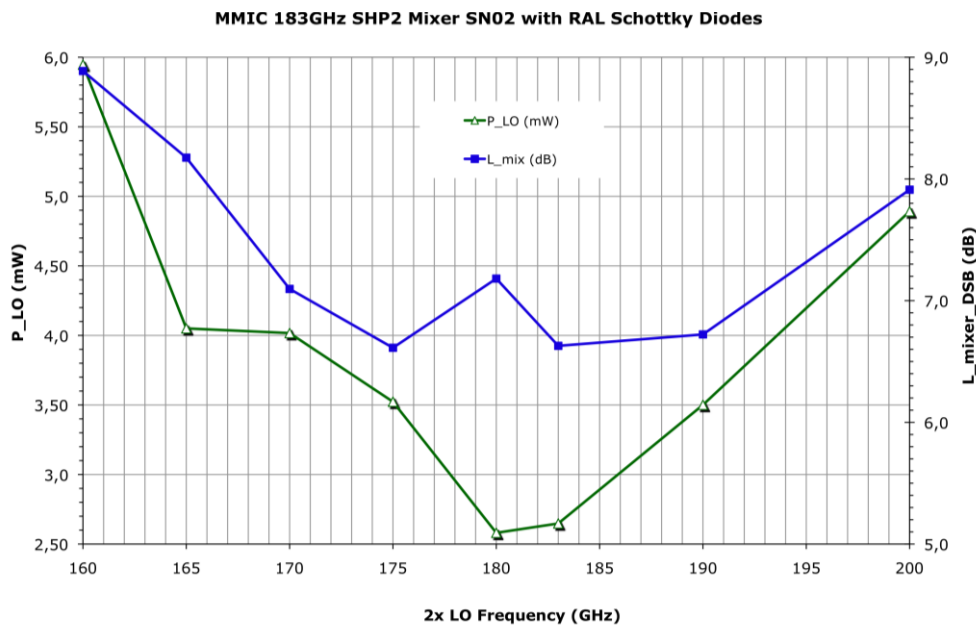
Figure 2.93: The plain curve with filled markers and opened markers show respectively the measured DSB mixer conversion loss and the optimum LO pump power.

Since this perspective is not the main objective in the thesis, only one measurement has been performed, some of the potential reasons for the discrepancy between the measured and predicted results could probably be due to the degraded diodes characterization of the measured mixer chip or the assembly problem. Further analyzes and more chip measurements are needed to find out this discrepancy. However, it can be concluded that the design is almost correct, several measurements have shown that the mixer works correctly, but the performance depends only on the diodes characteristics.

2.4.6 Conclusion

The design of a fixed-tuned subharmonic mixer based on a pair of UMS Schottky diodes in anti-parallel configuration was presented. The fundamental principles were introduced in a simple way and the most important details of the design method were given. Simulations have been used to determine some of the potential reasons for the discrepancy between the measured and predicted results. This discrepancy was partly cause by the imbalanced diodes on the mixer chip. The variations in diodes characteristics influenced dramatically on the predicted mixer performances, hence an accurate design require accurate diode electrical parameters. A universal method to measure and calculate the characteristics of diodes should be useful for an efficient design (detailed in Appendix B).

This mixer layout has been fabricated using two other planar Schottky diode technologies that are available in Europe. Measured results showed that a same mixer design could have a repeatable performance by using different diode process, but the diodes within different process require same diode characteristics.

2.5 Two-pixel integrated heterodyne Schottky diode receiver front-end at 183GHz

Although the standard deployed heterodyne instruments at millimeter and submillimeter wave around the world are based on a single pixel, increasing requirement of array receivers for higher mapping speed and consistency have been pushed with the significantly improvement and progress of a variety of millimeter and submillimeter wave techniques. In planetary and atmospheric sciences Schottky diode-based heterodyne array receiver can offer these advantages while avoiding the use of cryogenic system. Which could eventually reduce the size, weight and complexity of the instrument, and improvement of the lifetime. The purpose of this work is to demonstrate a two-pixel integrated heterodyne Schottky diode-based receiver front-end working at 183GHz, and contribute to provide a new way for receiver circuit implementation at higher frequency and appropriate for larger number of pixels.

2.5.1 Concept description

Many challenges and considerations are concerned in developing large array of heterodyne receivers, which include the array configuration, mixer configuration, local oscillator power injection, IF layout, remote tuning, monitoring capability and calibration etc.

Fix-tuned integrated subharmonic Schottky diode mixer was investigated as the detector of this demonstrator receiver front-end. The integrated fixe-tuned Schottky diode mixer eliminates the complex mobile backshort tuning or E-plane tuner and the cryostat, and simplifies the assembly work for multiple arrays. A fix-tuned bandwidth of around 20% can be achieved with good sensitivity.

Local oscillator power distribution is a main concern for heterodyne array receivers, as the LO power need to be coupled efficiently and equally into each pixel. Furthermore, Schottky diode mixers require high local oscillator pump power. To improve the power distribution and reduce the losses, only highly integrated components make building large array receiver possible. The Schottky diode-based frequency multipliers are the candidates as the last stage of the local oscillators in this demonstrator, because they are compact, tunerless, broadband and reliable.

Several potential techniques can be used for multiplexing local oscillator power to a number of pixels simultaneously. Quasi-optical techniques can be complex; can introduce losses or alignment difficulties, While waveguide techniques can be also complex, difficult to implement due to losses and fabrication, they are compact and can be integrated in the whole array. To overcome the losses in the LO circuit, an approach has been proposed in [Narayanan02], it is to integrate the stages of the frequency multiplier chain in the array mixer blocks. Two approaches have also been discussed in [Chattopadhyay04]; either use individual LO sources for each mixer or one LO source used to pump several mixers.

Two different configurations can be used to integrate the mixer and the frequency multiplier; either combine the mixer and the frequency multiplier on a single substrate [Thomas08c], or integrate the mixer and multiplier that are based on separate substrate via waveguide component. Obviously the integration of a mixer and multiplier on a single substrate offer a simpler assembly work and higher integration level, which are suitable for large array development. However the optimum performance of the mixer and the frequency multiplier generally require respectively different epitaxial doping layer of the substrate. Compare to the single substrate configuration, the mixer and the frequency multiplier on separate substrate can remain optimum performance by using the respective optimum epilayer. Meantime, the mixer and the frequency multiplier could be measured and operated independently.

In our concept, the mixer and the frequency multiplier on separate substrate has been used. One single solid state LO source pump two mixers simultaneously by using a waveguide LO multiplexer. Furthermore, the two mixers and the frequency multiplier are integrated in the same waveguide block to create a compact sub-array.
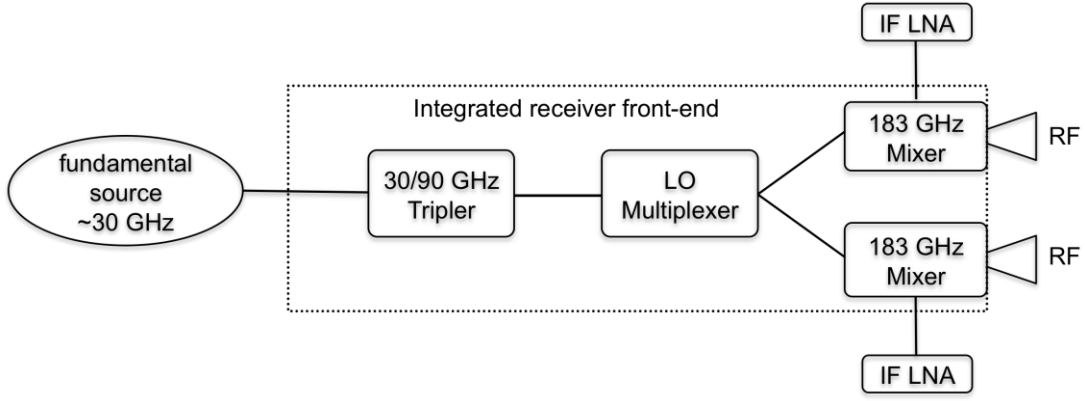
Figure 2.94: Block diagram of the two-pixel heterodyne receiver. Components shown within dotted line are integrated in a same waveguide block.

The two-way waveguide LO multiplexer shown in Figure 2.94 can be a three-port coupler or a quadrature hybrid coupler with the fourth port terminated by a load. The quadrature hybrid couple has been widely used in sideband-balanced mixers, which separate a microwave signal into two equal parts with a 90-degree phase difference. To eliminate this phase shift between two mixers, a simpler in phase waveguide power divider is used in our concept.

One of the most important advantages of developing large array receiver is to improve the mapping speed when compared to a single pixel receiver. Hence it is crucial to make a realistic estimation of how well it will perform and to look at the performance of the array when compared to an upgraded single pixel instrument, since it will always be much easier to upgrade a single pixel instrument than an array [Russell95]. For a N-pixel receiver, the integration time required to reach a given noise level is proportional to $(T_{sys})^2$:

$$t_{int} = (\frac{T_{sys}}{\Delta T})^2 \frac{1}{\beta} \qquad (2\text{-}11)$$

ΔT is the system sensitivity, β is the bandwidth of the receiver, and T_{sys} is the DSB system noise temperature, which given in [Russell95],

$$T_{sys} = \frac{2T_{rec} + T_{background}}{\eta_{ap}\eta_l\eta_{sky}\sqrt{N}} \qquad (2\text{-}12)$$

T_{rec} is the DSB mixer noise temperature referenced to the input of the receiver, $T_{background}$ is the background temperature due to radiation by the sky and the telescope. N is the number of pixels. $\eta_{ap}, \eta_l, \eta_{sky}$ are the aperture efficiency, the transmission

from the receiver through the telescope to the bottom of the atmosphere, and the transmission of the atmosphere, respectively.

In order to increase the mapping speed, the integration time has to be reduced, and hence the system noise temperature needs to be reduced. The aperture efficiency of the array is lower than that of the single pixel receiver [Padman87, Erickson92, Russell95]. The required number of pixels of an array to have a certain factor improvement in mapping speed can be derived from the equation 2-12. For the mapping speed advantage of a small, single polarization array to be realized, the performance of each pixel in the array must be very close to the performance of an optimized single pixel instrument.

2.5.2 Design procedure

2.5.2.1 Preliminary study

In order to explore the harmonic balance method used for more complex circuit optimization. A preliminary study of the integrated mixer/tripler was firstly performed. The study was based on the stand-alone mixer and tripler circuits described previously. The objective is to analyze the integrated mixer/tripler by integrating them via a straight waveguide (shown in Figure 2.95).
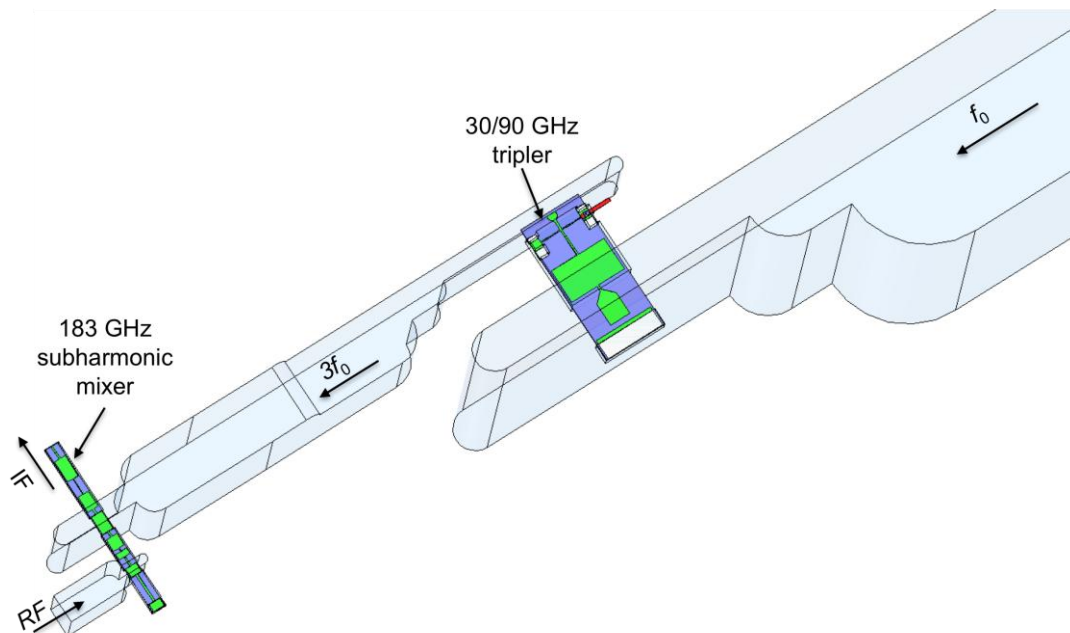
Figure 2.95: Three-dimensional model for integrated mixer/tripler.

The equivalent nonlinear circuit of this integrated mixer/tripler was developed and implanted in ADS suite, which is shown in *Figure 2.96*. Compared to the stand-

alone mixer circuit, the LO source is replaced by the tripler; hence the fundamental source of the integrated mixer/tripler is the LO input source of the tripler at f_0. The power produced at the third harmonic from the input source is the LO pump power of the mixer. Meantime the LO frequency of a subharmonic mixer is around half the RF frequency, therefore $f_{RF} \approx 6f_0$. This is a two-tone nonlinear analysis, one is the LO input source and the other one is the RF source; mixing products will appear with this two sources. The voltages and currents across the diodes related to the desired mixing products generated by the diodes are measured to calculate the performance of the mixer. As described in Chapter 2.3, only a limited number of mixing products are included in the harmonic balance calculation. The number of harmonics needs to be sufficiently large to represent nonlinear signals. For this integrated mixer/tripler, maximum nine harmonics of f_{LO} are considered for the mixer performance prediction, 24 harmonics of f_0 and three harmonics of f_{RF} are included for the simulation to achieve a compromise between the accuracy and the simulation speed. Figure 2.97 shows an example of the simulated result that was obtained by using the harmonic balance optimization and the simulation bench developed in ADS suite shown in *Figure 2.96*.

Pair of diode in anti-parallel

183 GHz subharmonic mixer

6 diodes in series

RF source

30/90 GHz tripler

LO input source

A

B

C

D

111
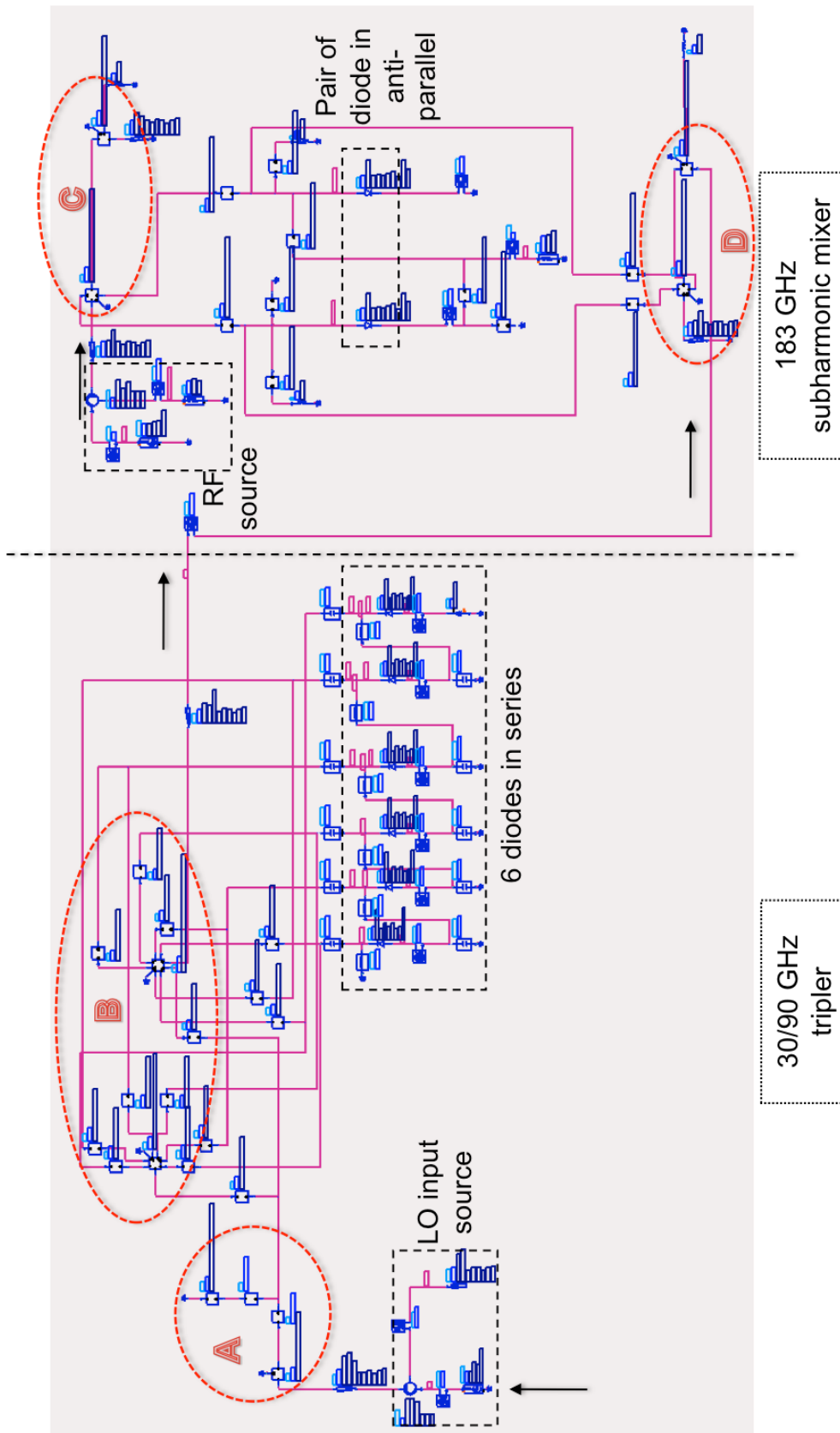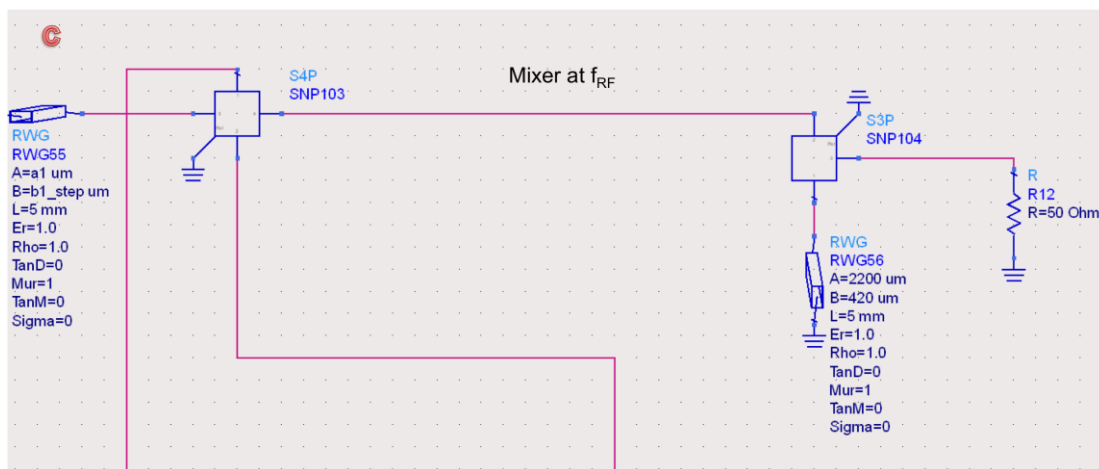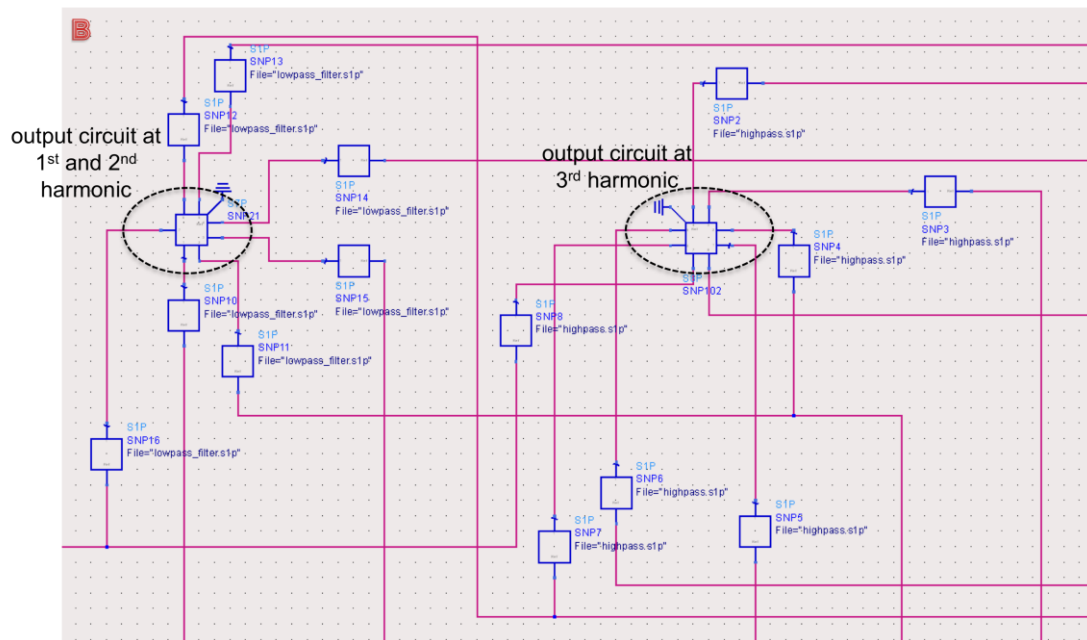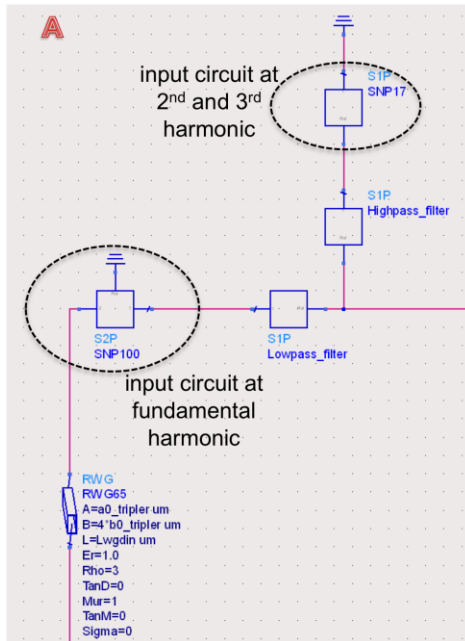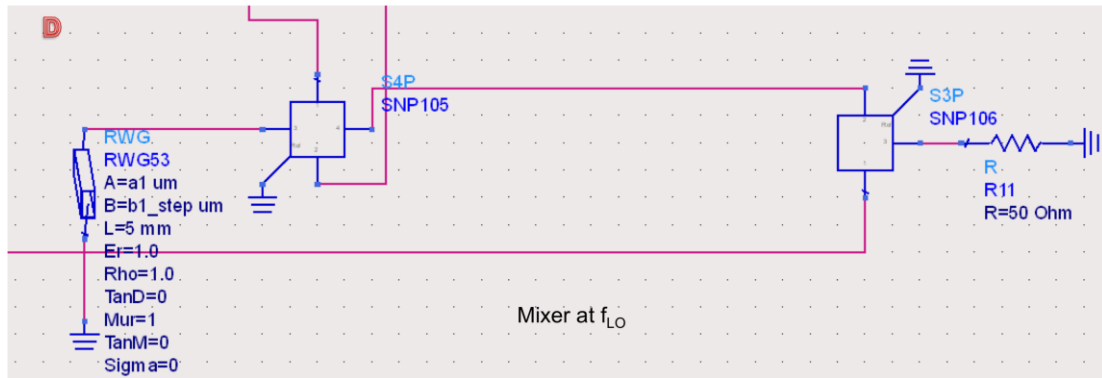
Figure 2.96: Equivalent nonlinear circuit of integrated mixer/tripler developed for the performance optimization and prediction. Close views for different parts present separately.
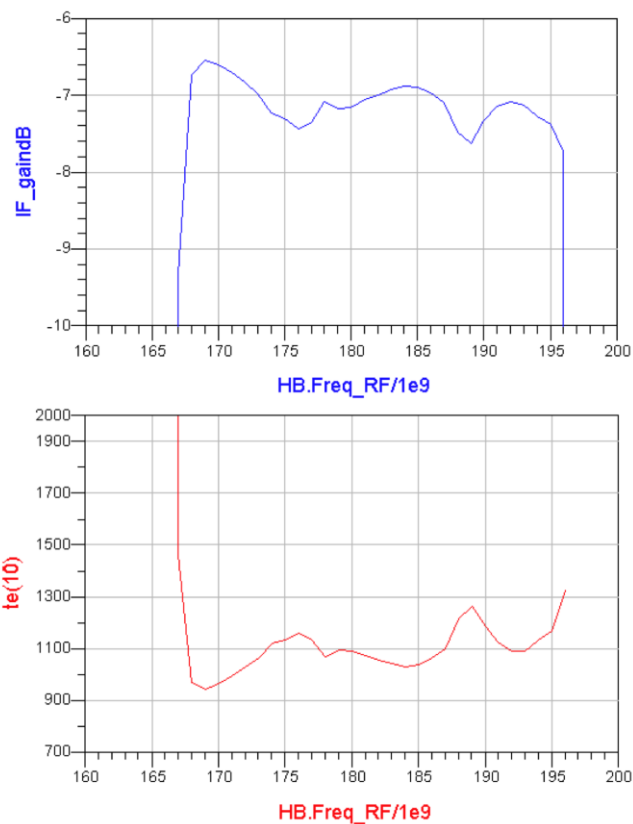
Figure 2.97: Predicted performance of the non-optimized integrated mixer/tripler obtained by using our developed harmonic balanced optimization bench shown in Figure 2.96.

2.5.2.2 Two-pixel demonstrator design

The two-pixel integrated receiver front-end shared the same mixer and tripler chips as for the stand-alone 183GHz mixer in Chapter 2.4 and 30/90GHz tripler in Chapter 2.3. Several detailed steps below performed the design and optimization of the two-pixel integrated receiver.

a) 183 GHz subharmonic mixer re-optimization

The mixer chip i.e. the suspended matching circuits and the diodes integrated on the GaAs substrate was been kept the same one for previous optimized stand-alone mixer in Chapter 2.4. In order to reduce the size of the integrated receiver, the height of the LO waveguide of the mixer was reduced contrary to the stand-alone version that had full height waveguide. Meantime, the width of the LO waveguide was changed to be 2200µm (the same width of the tripler output waveguide) instead of 2540µm. Therefore, the RF waveguide backshort, the RF waveguide step and the LO waveguide backshort of the mixer were re-optimized as a new stand-alone circuit (see Figure 2.98) to have an optimized matching with the new waveguide dimensions. The same method detailed in Chapter 2.4 for the mixer design has been used for this re-optimization. The re-optimized dimensions are shown in Figure 2.98.
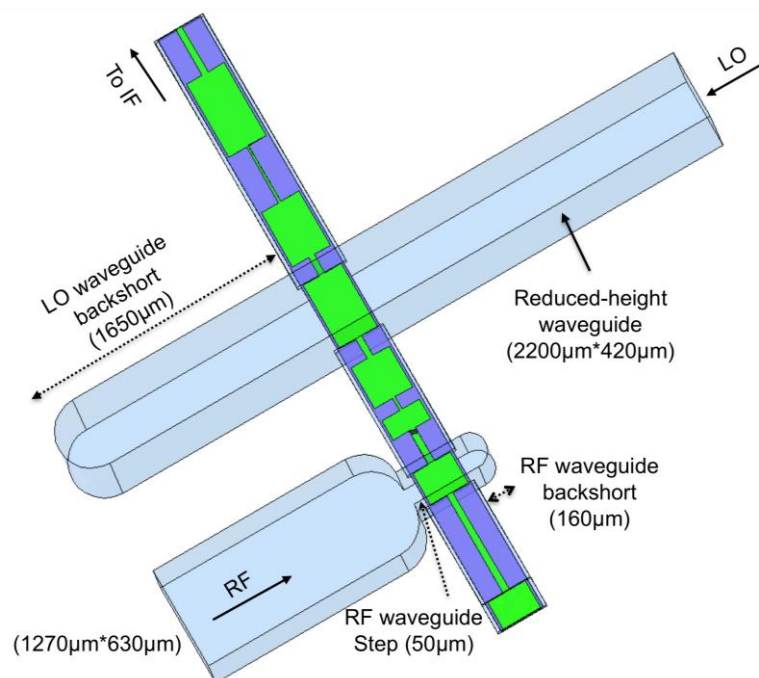
Figure 2.98: Re-optimized mixer with reduced height LO waveguide for the two-pixel receiver.

The predicted performance of the re-optimized mixer is shown below, which is very similar to the stand-alone mixer shown in Chapter 2.4. A sweep of DSB mixer conversion gain (no extra losses have been taken into account) versus RF with different LO pump power is shown in Figure 2.99. The DSB mixer noise temperature versus RF is shown in Figure 2.100.
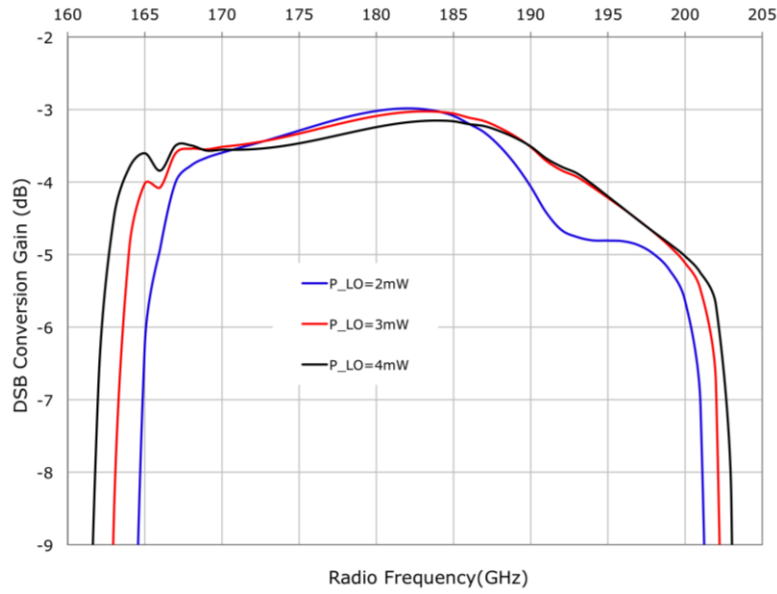
Figure 2.99: Predicted DSB re-optimized mixer conversion gain dependence versus different LO power, excluding any losses.
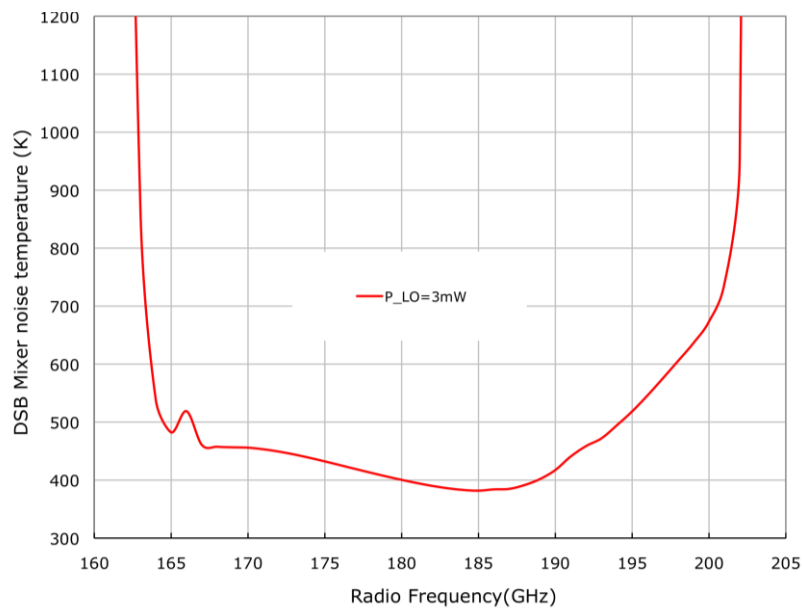
Figure 2.100: Predicted DSB re-optimized mixer noise temperature versus RF, excluding any losses.

b) 30/90 GHz Tripler re-optimization

For the same reason, the height of the output waveguide of the tripler was reduced contrary to the stand-alone version that had full height waveguide. Hence, the input waveguide backshort, the input waveguide steps and the output waveguide backshort of the tripler were re-optimized as a new stand-alone circuit (see Figure

2.101). The predicted performance of the re-optimized tripler is shown in Figure 2.102. ADS standard diode model was used for this simulation.
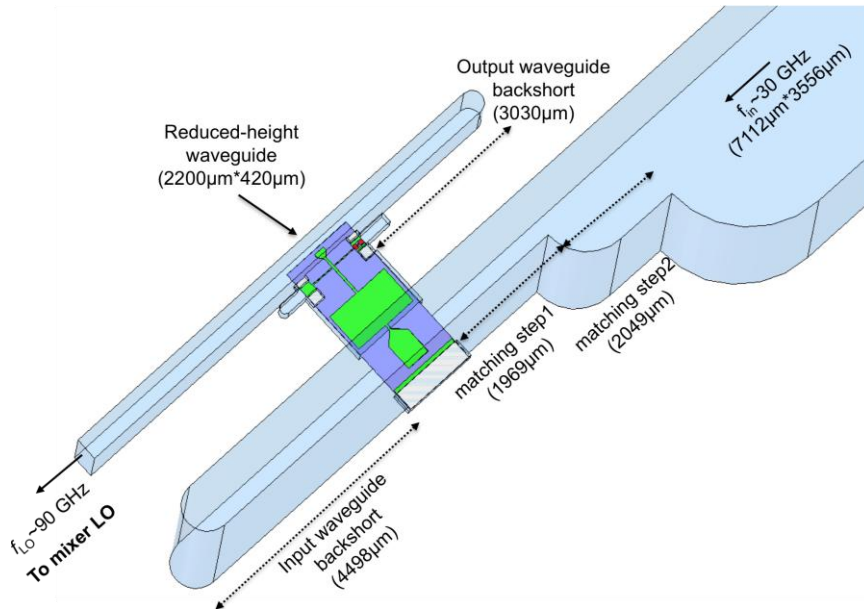
Figure 2.101: Re-optimized tripler with reduced height output waveguide for the two-pixel receiver.
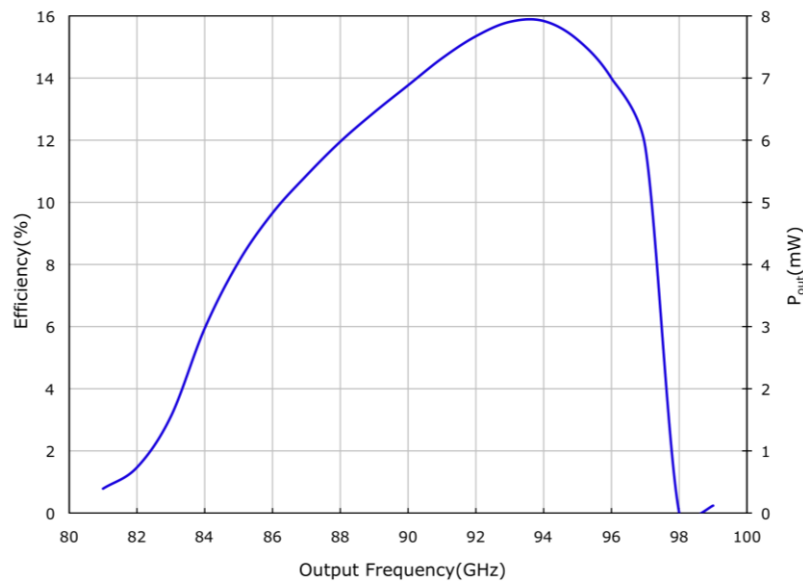
Figure 2.102: Predicted re-optimized tripler efficiency and output power versus output frequency with $P_{in} = 50mW$ and $V_{bias} = -11V$.

c) In phase waveguide power divider design

The power divider used in our design is also called a Y junction, and is shown in Figure 2.103. The LO power at the input port of the Y junction is split in two even parts and is delivered in phase at its output ports. If the Y junction is excited in phase

at its output ports, the power will combine and deliver to its matched input port; in this case, it works as a power combiner.
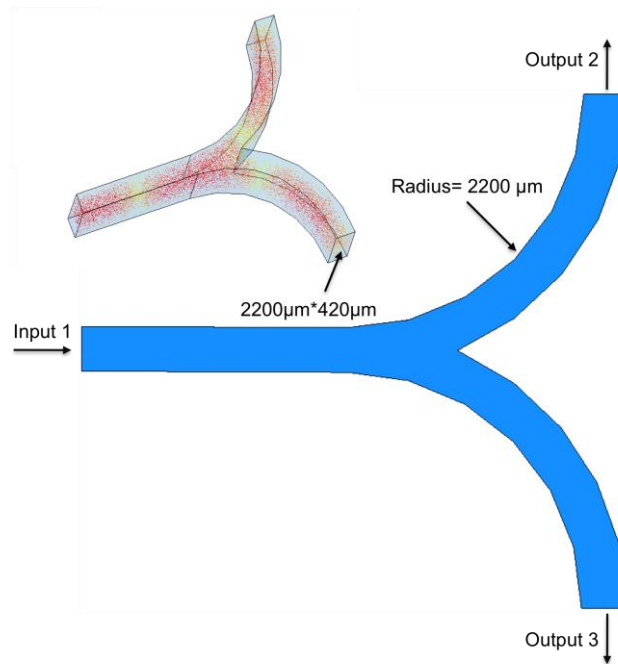
Figure 2.103: Three-dimensional model of the waveguide Y junction, with the electrical fields displayed on top left.

The design and optimization of the Y junction was performed by using three-dimensional electromagnetic simulator HFSS. The objective is to maximize the coupling between the input and the two output ports, and minimize the reflection at its input port. The three-dimensional model is shown in Figure 2.103, the waveguide dimension is the same of the output waveguide of the tripler and the LO waveguide of the mixer. The radius was optimized at 2200μm to get the best matching between the input and output ports. The simulated performance of the Y junction is shown in Figure 2.104.
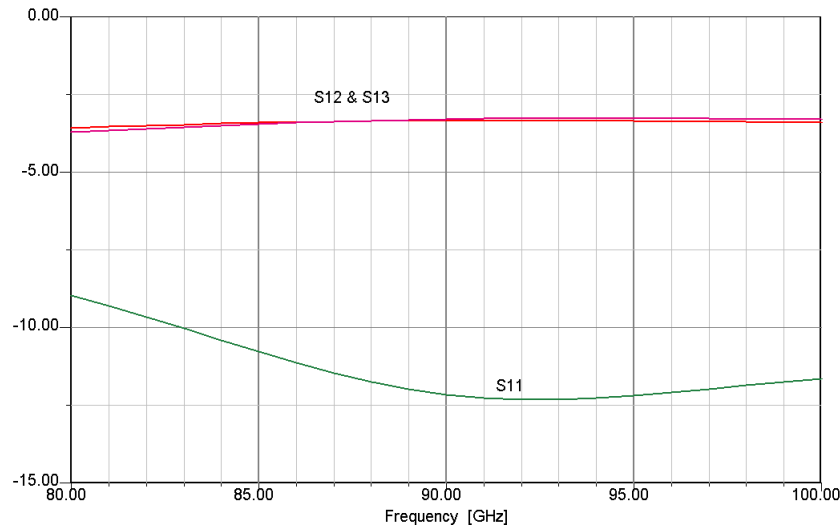
Figure 2.104: Simulated performance of the Y junction, showing the coupling between input and output ports S_{12} & S_{13} and the input return loss S_{11}.

d) Complete receiver front-end optimization

Once the mixer, the tripler and the waveguide Y junction were optimized independently, the optimization of the complete receiver was performed by tuning both the distance d_1 between the output probe of the tripler and the Y junction, and the distance d_2 & d_3 between the LO waveguide of the mixer and the Y junction, theoretically $d_2 = d_3$. Figure 2.105 shows the schematic of the two-pixel complete integrated receiver front-end. These distances were optimized to achieve an optimum LO power coupling and minimize the reflexion, because the Y junction is a reciprocal component, if the LO source is mismatched, an additional reflected component will affect the incident LO power.

The equivalent nonlinear circuit of the complete two-pixel receiver was developed and implanted in ADS suite, which is based on the preliminary study discussed in *Figure 2.96*. This optimization bench using harmonic balance code makes optimizing and predicting the performance of the complete receiver possible. Compared to the integrated mixer/tripler bench, another identical mixer is inserted, hence there are ten nonlinear diodes in total and at least 72 harmonic mixing produces included; this should be a long and arduous calculation.

118
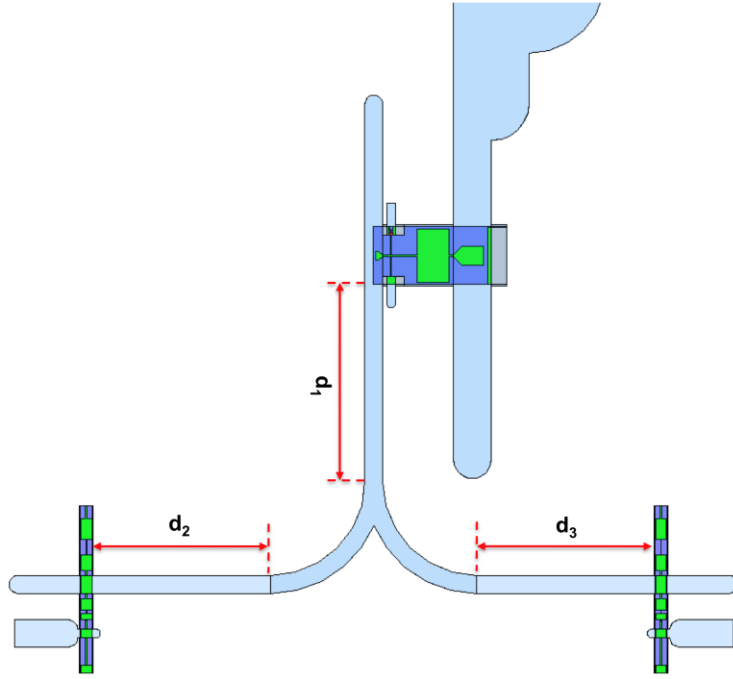
Figure 2.105: Schematic diagram of the two-pixel complete receiver composed of optimized mixer, tripler and Y junction.

2.5.3   Proposed two-pixel integrated receiver front-end prototype

The physical dimensions of the integrated receiver were optimized in previous section; several considerations have to be taken into account to configure a practical and compact prototype of a two-pixel receiver. Firstly, the electrical connector for DC and IF connections need to be constructed in an area close enough to the waveguide to allow the mounting of neighbouring waveguides and connectors in the array. Secondly, there are well-known limitations for the smallest beam spacing that are reported in [Yngvesson83], since placing the feed elements too close together results in interaction via electromagnetic fields [Goldsmith93]. These can be discussed in terms of the spacing Δx of adjacent pixels in the array.

If each element in the array illuminates a telescope at an f-number of f/D, then full sampling of the focal plane for incoherent illumination of the scene and measurement of the intensity in the focal plane requires that $\Delta x = 1/2 \cdot (f\lambda/D)$ [Rutledge83, Goldsmith93]. Where focal ratio or f-number relates to the brightness of the image and the width of the field of view and focal ratio is the focal length of the objective lens or primary mirror divided by the aperture size. There is no type of feed element that has been reported in practice, which is capable

119

to be so close while still achieving a good illumination efficiency of the telescope. For example, corrugated horns, which have excellent beam efficiency, must be spaced about $2 \cdot f\lambda / D$ reported in [Goldsmith92]. Studies of optimum feed horns for array systems have been reported in [Ardenn87, Payne88, Yngvesson88].

There are two different configurations to compose our two-pixel integrated receiver, which are shown respectively in Figure 2.106 and Figure 2.107. Figure 2.106 shows the configuration with two mixers located parallel to the tripler circuit, an extra quarter circle waveguide bend is needed between the Y junction and the mixer LO waveguide transition for the connection, and the mixer IF output connections are proposed to be collected respectively from the side. With this configuration, the extension of the array is limited vertically by the lateral IF connections.
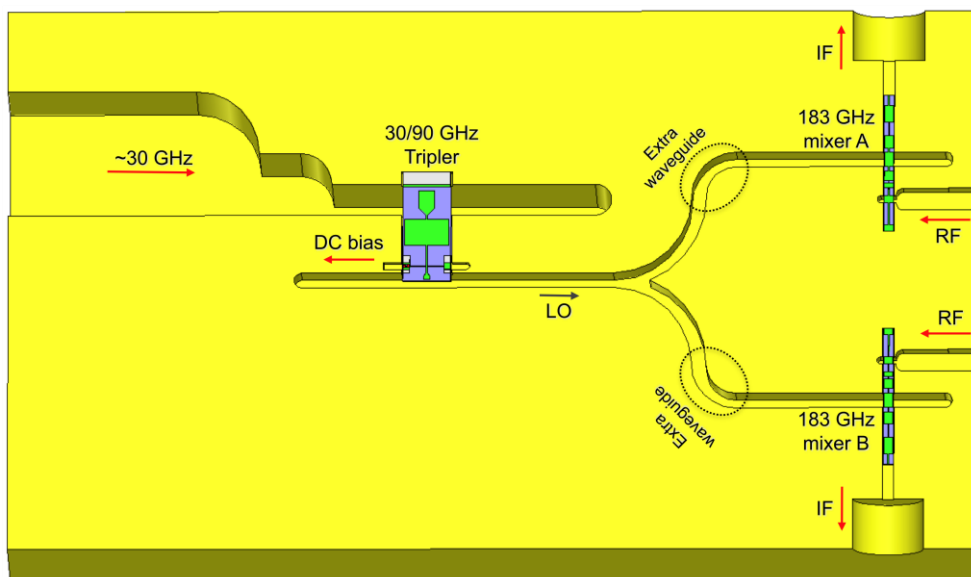
Figure 2.106: Layout of the two-pixel integrated receiver configuration (1).

To construct a more flexible, efficiency and compact prototype of sub-array receiver, another configuration layout is shown in Figure 2.107, the mixers are connected directly to the output of the Y junction, no extra waveguide bends are needed, hence no extra losses introduced. The mixer IF output connections of each pixel and the tripler DC bias have been chosen to be collected vertically from the top of the two-pixel receiver block for the final two-pixel integrated receiver. This final block is shown in Figure 2.108, three red SSMA connector flanges on the top block are respectively for the two mixer IF output connections and for the tripler DC bias.

Space around the waveguide was optimized to maximize the performance and minimized assembly "real-life" issues.
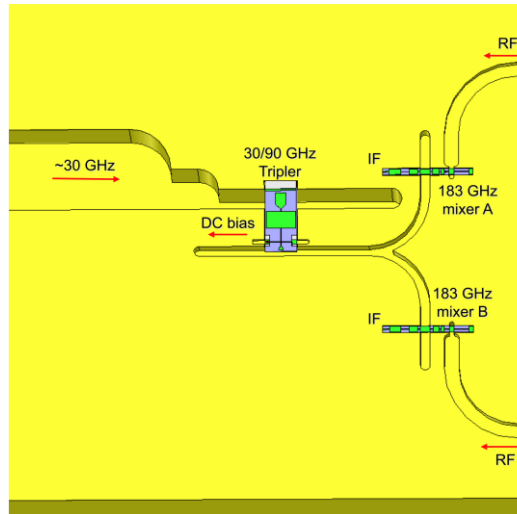
Figure 2.107: Layout of the two-pixel integrated receiver configuration (2).

The spacing between adjacent pixels in this array was chosen to be 20 mm, in order to not only avoid any crosstalk between radiating elements but also provide two different flange connections (standard one and smaller one). This spacing is not the closest value for a compact array, but make possible for alterable experimental study using this demonstrator. The final optimized complete block size is $40mm \times 37mm \times 20mm$.
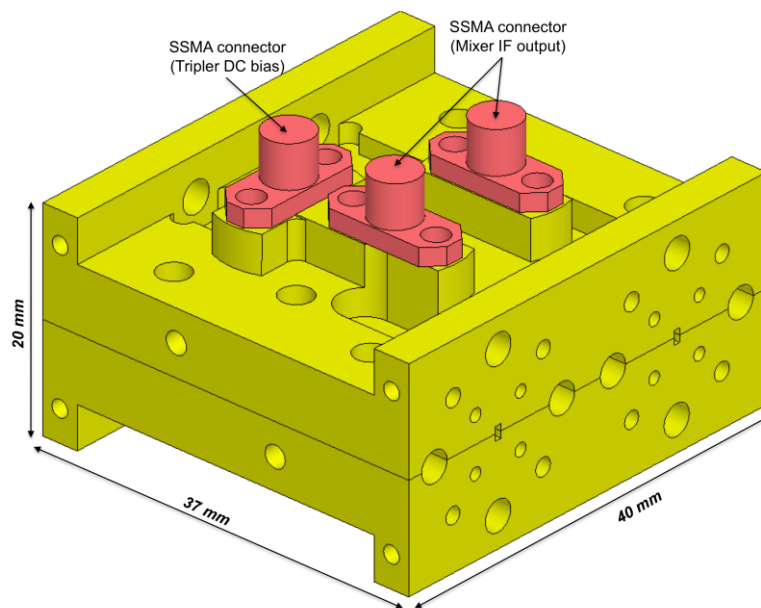
Figure 2.108: Final two-pixel integrated receiver split waveguide block.

The inside view of the bottom block containing the mixer and tripler chips is shown in Figure 2.109. The mixer chip is inverted and mounted on the block; one end of the circuit is directly soldered to the bottom of half block using silver-epoxy, which provides a precise RF ground. The end of the mixer circuit towards the IF output is connected to a broadband IF circuit with silver-loaded epoxy or solder. This IF circuit is fabricated from a 50Ω suspended microstrip line deposited on a quartz substrate, which connects to the vertical SSMA connector. The tripler circuit is also inverted and mounted on the block, the DC bias is provided via wire bonding through Metal-Insulator-Metal (MIM) capacitors.
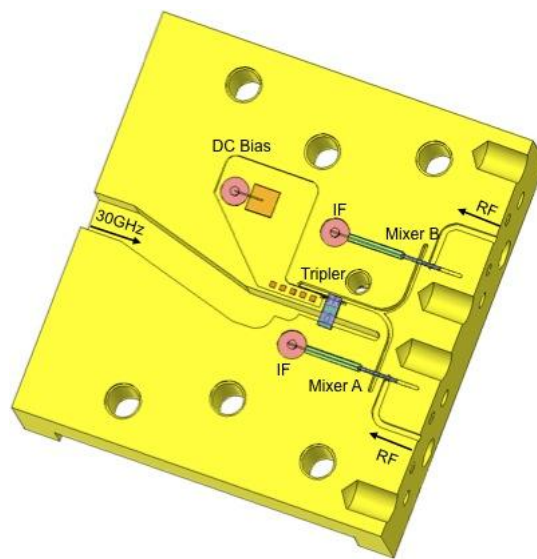
Figure 2.109: Schematic of the bottom block of the two-pixel integrated receiver. Two mixers IF signals and tripler DC bias are collected vertically with SSMA connector.

2.5.4 Predicted results

2.5.4.1 Optimization and predicted results using ADS standard diode model

The predicted DSB mixer conversion gain of the optimized two-pixel integrated receiver is presented in Figure 2.110. Two mixers in the array have almost identical conversion gain, discrepancies relate only to numerical errors in the HFSS/ADS simulations. By tuning the input power of the receiver from 30mW to 100mW, the optimum input power of the receiver for each frequency point can be found. Figure 2.110 shows the DSB conversion gain of each mixer with the optimum input power to each frequency. These predicted results exclude any extra losses; a

minimum conversion loss of 3dB is expected at 183GHz, which present very close performance compared to a single optimized mixer (detailed in Chapter 2.4). Figure 2.111 shows the predicted DSB mixer noise temperature versus RF, and the optimum input power versus RF.
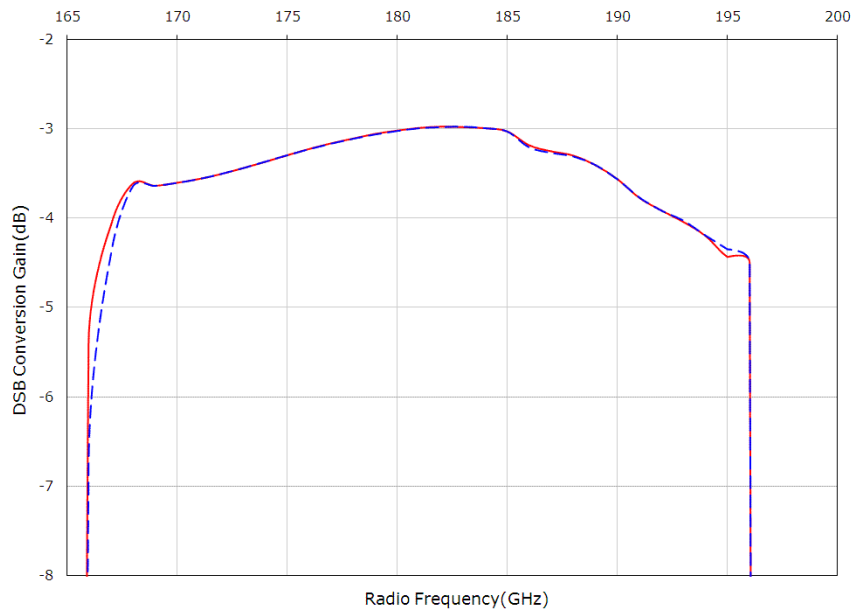
Figure 2.110: Predicted DSB mixer conversion loss versus RF excluding any extra losses, with the receiver optimum input power at each frequency in the range 30mW~100mW.
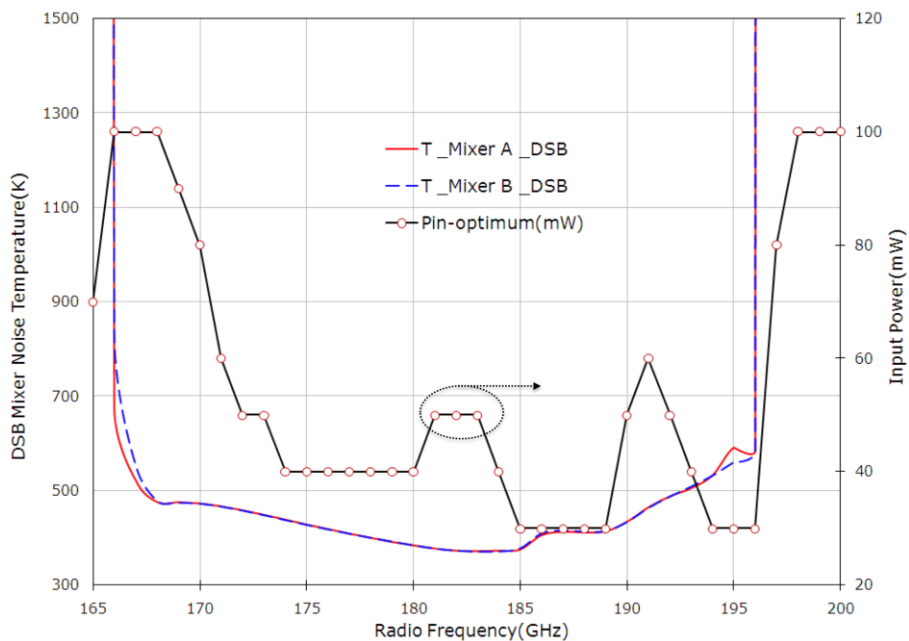
Figure 2.111: The plain curve and the dashed curve show respectively the predicted DSB mixer noise temperature of each pixel versus RF, and the plain curve with open circle markers shows the optimum receiver input power at each frequency in the range 30mW~100mW.

123

2.5.4.2 Optimization and predicted results using adjusted diode model

In order to guarantee the adequacy of the design, the optimization of the two-pixel integrated receiver was re-optimized by using the adjusted Schottky diode model described in [Siles08b]. The predicted DSB mixer conversion gain of the optimized two-pixel integrated receiver is presented in Figure 2.112. By tuning the input power of the receiver from 30mW to 100mW, the optimum input power of the receiver for each frequency point can be found. Figure 2.112 shows the DSB conversion gain of each mixer with the optimum input power to each frequency. These predicted results exclude any extra losses; a minimum conversion loss of 3dB is expected at 183GHz. Figure 2.113 shows the predicted DSB mixer noise temperature versus RF, and the optimum input power versus RF. A minimum mixer noise temperature of 750K is predicted at 183GHz including extra losses. The two-pixel receiver is biased inversely with 5V.
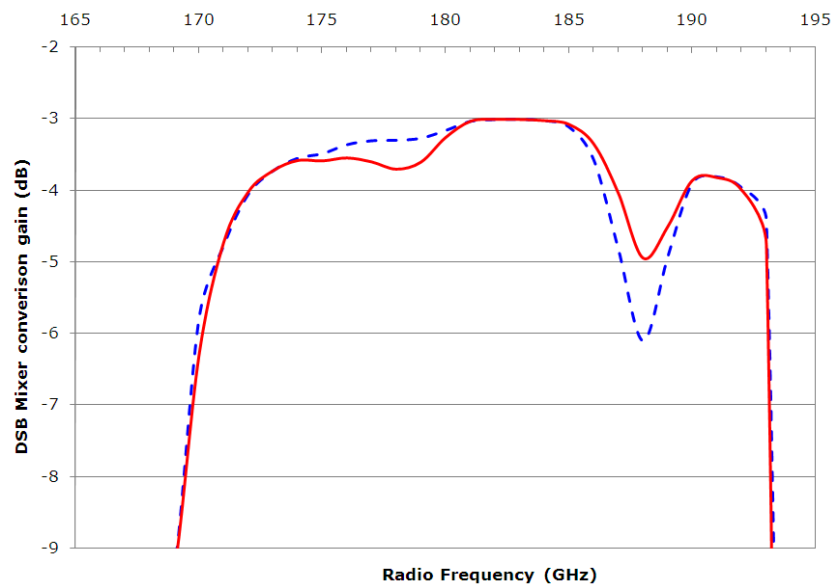
Figure 2.112: Predicted DSB mixer conversion gain versus RF excluding any extra losses, with the receiver optimum input power at each frequency in the range 30mW~100mW.
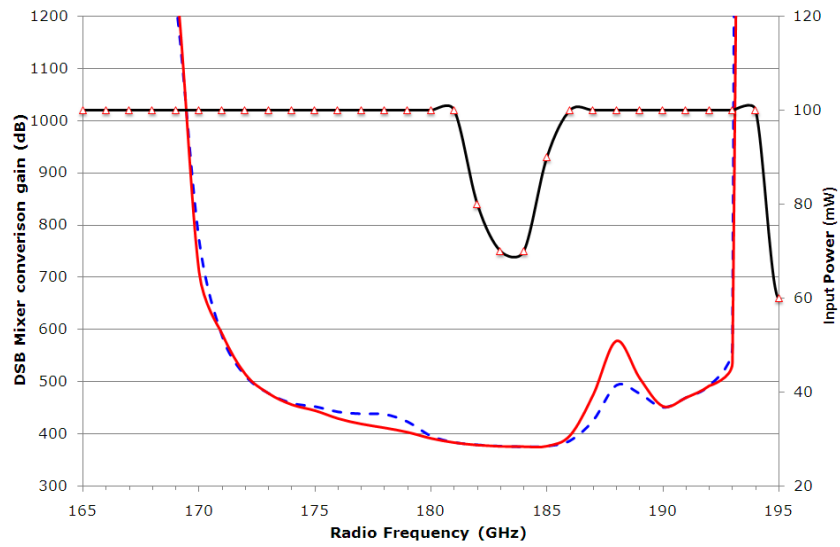
Figure 2.113: Predicted DSB mixer noise temperature versus RF excluding any extra losses, with the receiver optimum input power at each frequency in the range 30mW~100mW.

3   Conclusions and suggestions for future work

Novel techniques intended to improve further the performance of receivers or to provide new ways for receiver circuit implementation have been studied in this thesis. A compact two-pixel integrated Schottky diode receiver front-end was proposed and studied. This is the first demonstration of the integration of frequency multiplier and several mixers in a same block employing Schottky diode technology.

Large arrays of millimeter and submillimeter wave heterodyne Schottky diode-based receivers can offer higher mapping speed and mapping consistency while avoiding the use of cryogenic receivers. To improve the mapping speed of a large array heterodyne receiver compared to a single pixel receiver, the performance of each pixel in the array must be very close to the performance of an optimized single pixel receiver. The Schottky diode receiver can operate at room temperature but requires a large amount of LO power compared to SIS or HEB, to develop a large array heterodyne receiver based on Schottky diode will require more LO power, specially for higher frequencies, which could be a concern.

To reduce the size, the weight and the power consumption of a multi-pixel receiver it is necessary to optimize the interface between the mixers and the local oscillator unit. Only higher-level integration components make possible to build large array heterodyne receivers, MMICs offers this advantage. One solution consists in integrating in the same mechanical block a frequency multiplier and one or several mixers to create a compact sub-array. A novel approach to design multi-pixel heterodyne receiver is demonstrated in this thesis. In our configuration, one single solid state LO source pump two mixers simultaneously by using an in phase waveguide Y junction. In addition, the mixers and the frequency multiplier are integrated in a same waveguide block. Furthermore, the frequency multiplier and the mixer were both optimized independently for two stand-alone circuits. The optimization method for developing an integrated multi-pixel Schottky diode receiver has been explored, due to the complexity and the non-linearity of the circuit; certain procedures have been studied and proposed to improve the efficiency and the accuracy of the design. The optimization of such a complex circuit is suggested to optimize in different parts the contrariety of the global optimization (the whole circuit is optimized at the same time). The global optimization method has been studied as

an initial method, but owing to the complexity of the calculation, it is unpractical and unrealizable.

3.1   Summary and Conclusions

This dissertation discusses the development of a 183GHz two-pixel integrated heterodyne receiver front-end at room temperature. The 183GHz subharmonic mixer and the 30/90GHz frequency tripler used in the two-pixel integrated receiver were both been fabricated using European industrial Schottky diode process of UMS and measured independently. The measured best DSB mixer noise temperature was 2409K with a minimum DSB mixer conversion loss of 9.4dB at 175GHz. Big discrepancies are presented compared to the expected DSB mixer noise temperature of 500K and conversion loss of 5.1dB. These discrepancies are mostly due to the imbalance in anode and high series resistance. Better performance relies on the quality of the diodes.

Regarding to the 30/90 GHz tripler, measurements were performed for two different anode sizes. The best efficiency of 5% and more than 1mW output power has been measured over the band 80-95GHz for 17μm length anode tripler. Owing to the inaccurate diode model that used for the tripler design, lower power efficiency was obtained compared to the expected efficiency of 14%. Corrected diode models that take into account the flat-band effects have been developed for the integrated receiver optimization.

These two measured circuits were used to build up the two-pixel integrated receiver; the DSB mixer noise temperature of 750K was expected at 183GHz for single pixel.

3.2   Suggestions for Future work

Based on the approach and study of the two-pixel integrated receiver front-end in this dissertation, several considerations and suggestions could be useful for improving and developing a larger array receiver in the future.

In order to improve the isolation between the mixers stage and the tripler stage, another type of power divider could be used – a waveguide quadrature hybrid. A quadrature hybrid is a four-port directional coupler, power incident is divided equally between two others ports with a 90° phase different, and the fourth port is

isolated and terminated by a load. The waveguide quadrature hybrid consists of two parallel waveguides coupled through a series of apertures or branches waveguide, while the branch-line coupler is preferred because of its compability with split-block and its simplicity of fabrication. For higher frequencies the waveguide hybrid coupler involves numbers of manufacturing concerns. Another concern is the waveguide load terminated the fourth port. The only purpose of the waveguide load is to absorb all the energy in a waveguide without causing standing waves. It needs to be as compact as possible and usually contained inside the waveguide. For large array receiver, the waveguide quadrature hybrid is less compact than a Y junction, and the complexity of fabrication is much higher.

Two different configurations of four-pixel receiver can be composed by using two identical two-pixel integrated receivers as the one proposed in this work. One solution consist in stacking them to compose a two by two array as shown in Figure 3.1; the other consists in placing them side-by-side, which is shown in Figure 3.2. Consequently, an eight-pixel receiver front-end shown in Figure 3.3 could be composed by combining the stacked and side-by-side structure.
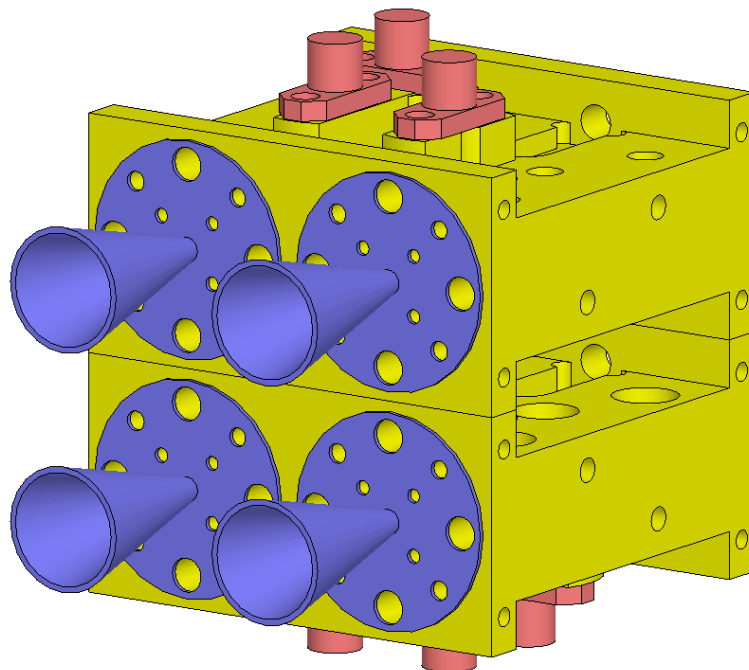
Figure 3.1: Two by two array receiver based on two identical two-pixel integrated sub-array receiver.
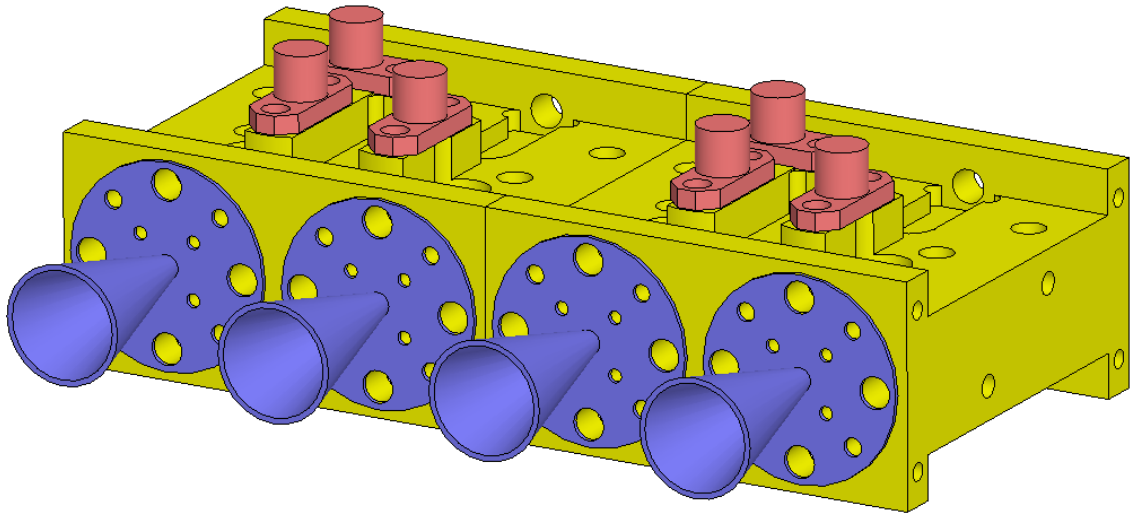
Figure 3.2: One by four array receiver based on two identical two-pixel integrated sub-array receiver.
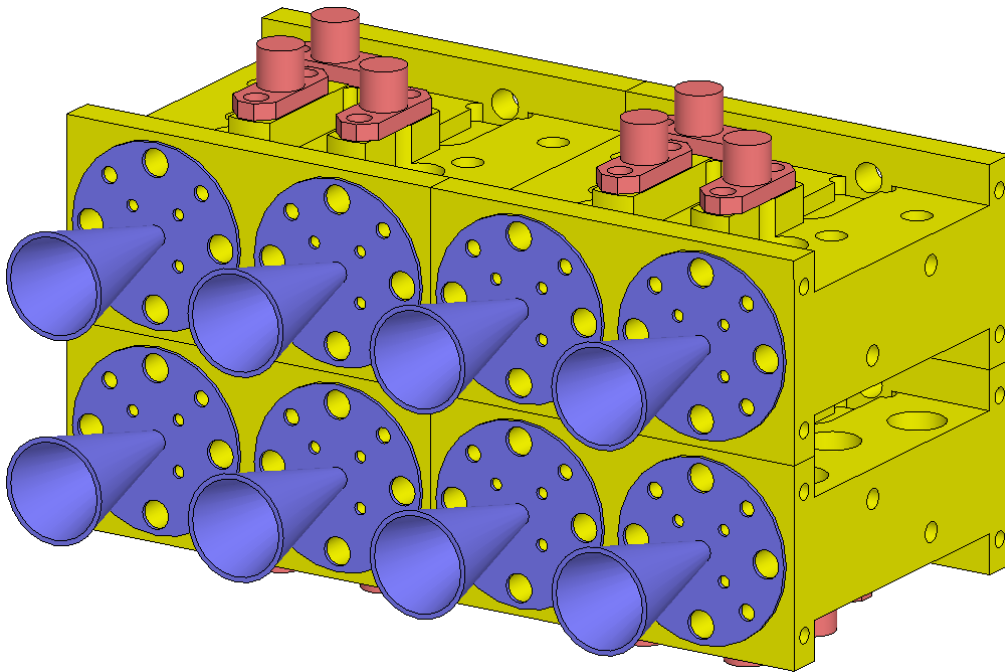
Figure 3.3: Two by four array receiver based on four identical two-pixel integrated sub-array receiver.

Appendix

Appendix A – Mixer test setup at LERMA

1. Y-factor measurement

The Y-factor method is the most common method to calculate the receiver equivalent noise temperature. Y-factor is a ratio of two noise power levels. The measurement of a receiver (see Figure A.1) is performed with two loads having different physical temperature connected at the input of the receiver. The output power of the receiver is recorded as P_{out} (cold) and P_{out} (hot) respectively to the input connected with a matched load at the physical temperature T_{cold} and T_{hot}.
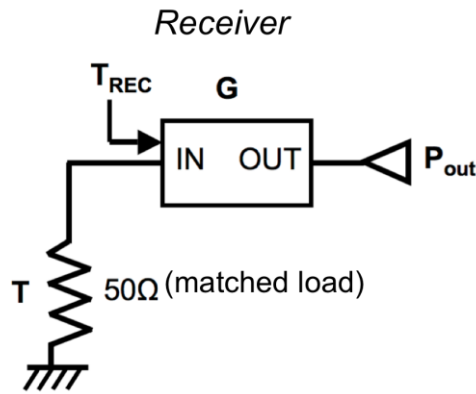
Figure A.1: A simplified receiver chain under test.

The Y-factor is defined as:

$$Y = \frac{P_{out}(T_{hot})}{P_{out}(T_{cold})} \qquad (A\text{-}1)$$

At any temperature above absolute zero the thermal noise power generated in a conductor is proportional to its physical temperature on the absolute scale (measured in Kelvin). The basic relationship between thermal noise power P_N, temperature T and bandwidth β is:

$$P_N = kT\beta \qquad (A\text{-}2)$$

Consequently, for the receiver shown in Figure A.2, the relationship between the thermal noise output power and the receiver equivalent noise temperature is:

$$P_{out} = k(T_{rec} + T_{signal})\beta G \qquad (A\text{-}3)$$

where *k* is Boltzmann's constant, β is the receiver bandwidth and G is the receiver power gain.
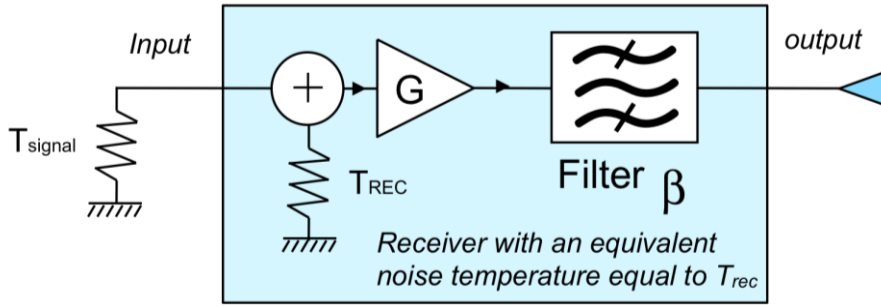
Figure A.2: Receiver equivalent noise temperature.

Therefore, combining the equation (A-1) and (A-3) gives us:

$$Y = \frac{P_{out}(T_{hot})}{P_{out}(T_{cold})} = \frac{k(T_{rec} + T_{hot})\beta G}{k(T_{rec} + T_{cold})\beta G}$$

$$\Rightarrow Y = \frac{(T_{rec} + T_{hot})}{(T_{rec} + T_{cold})}$$

$$\Rightarrow Y \times (T_{rec} + T_{cold}) = T_{rec} + T_{hot}$$

The receiver equivalent noise temperature is derived by the following formula:

$$T_{rec} = \frac{T_{hot} - Y \times T_{cold}}{Y - 1} \qquad (A\text{-}4)$$

For a cascade receiver chain as shown in Figure A.3, according to the Friis formula the receiver noise temperature depends on the mixer noise temperature, the gain of the mixer and the equivalent noise temperature of the IF chain.
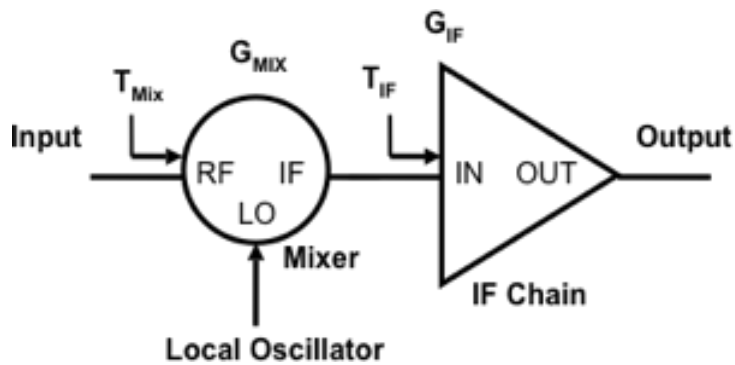
Figure A.3: A receiver chain is composed of a mixer and IF chain.

$$T_{rec} = T_{mix} + \frac{T_{IF}}{G_{mix}} \qquad (A\text{-}5)$$

To extract the mixer equivalent noise temperature and the mixer conversion losses, a dual noise factor IF chain has been used in our measurement. This IF chain has an internal noise source that can be switched on and off to modify its noise factor. This feature is very useful since two independent Y-factor measurements are necessary to extract both the equivalent noise temperature of the mixer and its conversion losses. Two independent receiver equivalent noise temperature measurement are performed with the internal noise source ON and OFF:

$$T_{rec\_ON} = \frac{T_{hot} - Y_{ON} \times T_{cold}}{Y_{ON} - 1} \qquad (A\text{-}6)$$

$$T_{rec\_OFF} = \frac{T_{hot} - Y_{OFF} \times T_{cold}}{Y_{OFF} - 1} \qquad (A\text{-}7)$$

T_{cold} is set to 77 K, the temperature of liquid nitrogen. This is correct only if the RF calibration target is an ideal black body in the RF band. In practice, 77 K≤T_{cold}≤80 K for a calibration load with 99% emissivity. T_{hot} is set to 297.15K for an experimental temperature of T_{room}=24°C. The mixer noise temperature T_{mix} and conversion loss G_{mix} can be determined from (A-5)(A-6)(A-7):

$$T_{mix} = T_{rec\_ON} - \frac{T_{IF\_ON}(T_{rec\_ON} - T_{rec\_OFF})}{T_{IF\_ON} - T_{IF\_OFF}} \quad (A\text{-}8)$$

$$G_{mix} = \frac{T_{IF\_ON} - T_{IF\_OFF}}{T_{rec\_ON} - T_{rec\_OFF}} \quad (A\text{-}9)$$

Simple manipulation of equations above give the expression for G_{mix} and T_{mix},

$$T_{mix} = \frac{(T_{hot} - Y_{OFF} \times T_{cold})(T_{IF\_ON} - T_{IF\_OFF})(Y_{ON} - 1) - T_{IF\_OFF}(T_{hot} - T_{cold})(Y_{OFF} - Y_{ON})}{(T_{IF\_ON} - T_{IF\_OFF})(Y_{ON} - 1)(Y_{OFF} - 1)} ($$

$$A\text{-}10)$$

$$G_{mix} = \frac{(Y_{ON} - 1)(Y_{OFF} - 1)(T_{IF\_OFF} - T_{IF\_ON})}{(T_{hot} - T_{cold})(Y_{ON} - Y_{OFF})} \quad (A\text{-}11)$$

2.   IF chain description

The schematic of the 2-4GHz IF chain is given in Figure A.4 and a picture of its inside view is shown in Figure A.5. The chain is fully isolated at the input and at the output. An isolator is also placed between the LNA and the IF band pass filter.

The losses of the isolators and the 20dB coupler are about 0.25dB (better than specified). The noise factor of the LNA is 0.35dB. The ENR of the noise source is 15.5dB. The total gain of the IF chain is about 77dB. The 1dB compression point of the second stage amplifier is +13dBm (under normal test conditions, the IF chain output dynamic ranges between -3dBm and +3dBm).
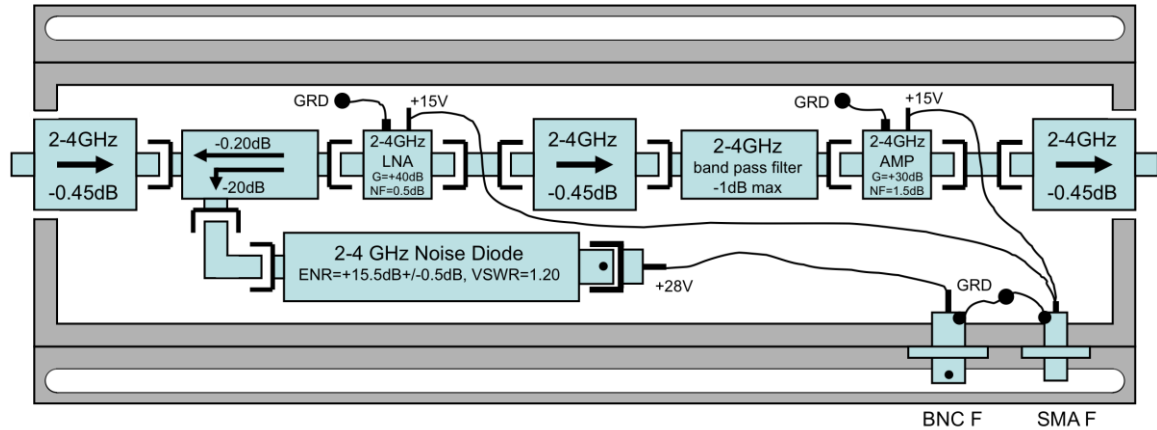
Figure A.4: Schematic of LERMA 2-4GHz IF Chain.
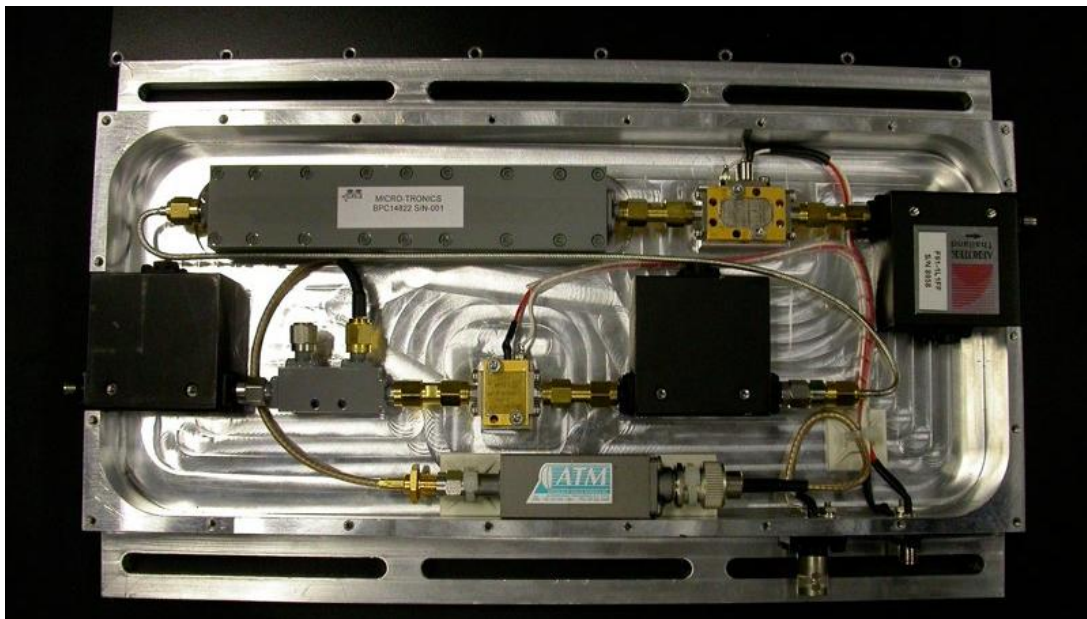
Figure A.5: Picture of LERMA 2-4GHz IF Chain before closing the top cover.

The measure of the IF chain noise figure was made using the Y-factor method. A 50Ω cable thermally grounded near the input of the IF chain and a 50Ω resistor were used for the calibration load. The cable and the 50 Ω resistor was either maintained at 297K or plunged in liquid nitrogen (77K). The resistance of the 50Ω resistor at 77K was found to be 52Ω insuring a good match with the cable. The Y factor was measured with an Agilent E9325A 0.05-18 GHz power sensor in

AVERAGE mode and an Agilent N1912A power meter that integrates the whole 2-4 GHz band. The measured equivalent noise temperature of the IF chain are $T_{IF\_ON}(K) = 194.8 \pm 1.1$ when the internal noise source is ON and $T_{IF\_OFF}(K) = 81.6 \pm 0.5$ when the internal noise source is OFF. The standard deviation is obtained based on a statistic of 6 measurements made at different period of time. The room temperature is stabilized at $23.5° \pm 0.5°$.

3. Measure of receiver noise temperature using the Y-factor method

The mixer measurement setup at LERMA uses an Agilent N1912A power meter and an Agilent E9325A peak power sensor for measuring the power delivered by the IF chain. The power meter is externally synchronized with a mechanical chopper used to present alternatively a blackbody at room temperature and a blackbody at liquid nitrogen temperature in front of the mixer feed horn. The chopper has two blades that cut the RF beam of the mixer at about 30Hz. A thick layer of RF absorber is tapped onto the blades to define the room temperature calibration target. The free path of the mixer RF beam points to an RF absorber plunged into liquid nitrogen (see Figure A.6).
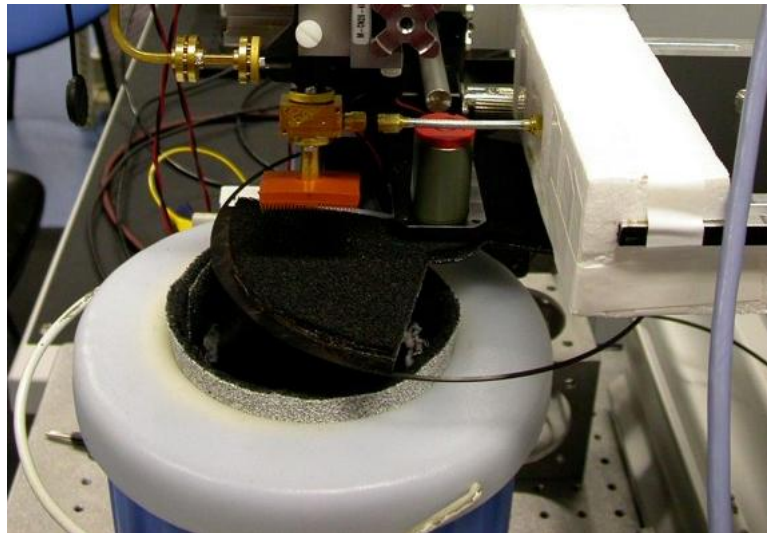
Figure A.6: A two-blade chopper is used to cut the beam of the mixer and define the room temperature calibration target. The nitrogen-cooled calibration target is placed below the chopper and in the free-path of the mixer beam.

With the above configuration, the Agilent N1912A power meter is able to give the integrated IF power over the entire 2-4GHz IF band versus time, with time

steps of a few microseconds. The Agilent E9325A peak power sensor is configured in normal mode and bandwidth is set to off. On the N1912A power meter two time gates are defined: one corresponds to the room temperature black body being totally in front of the mixer feed horn, the other corresponds to the 77K black body being totally in front of the mixer feed horn (see Figure A.7).
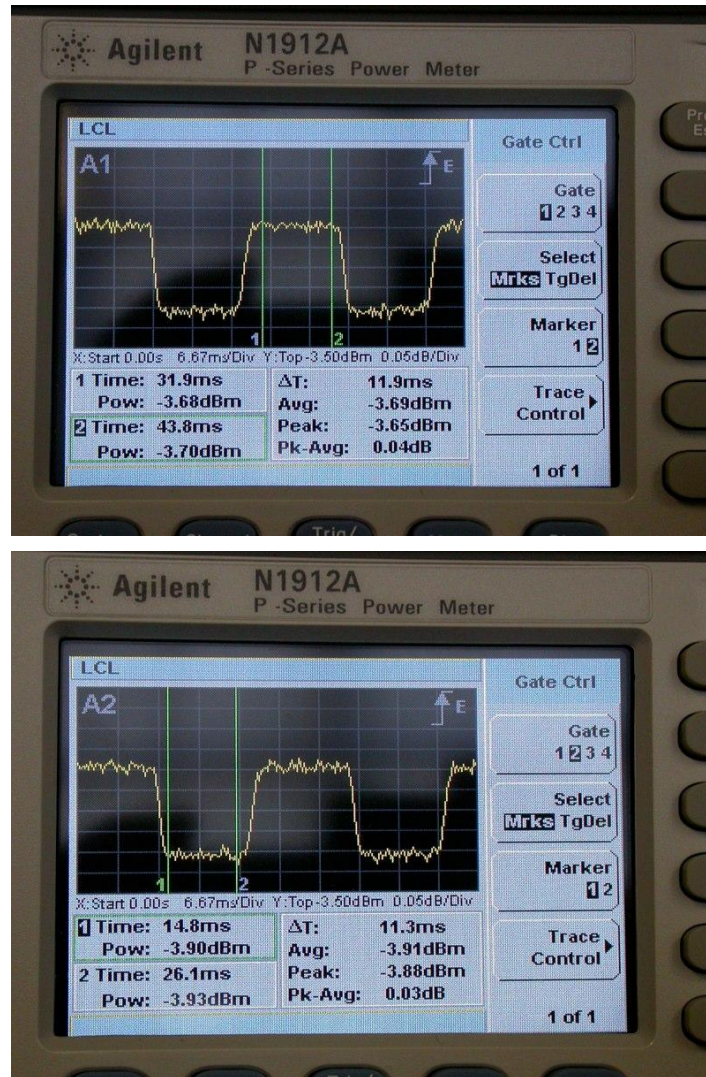
Figure A.7: Gate definition of measured IF output average power when mixer looks at the room temperature calibration target (top) and the nitrogen-cooled calibration target (bottom).

For each gate, the Agilent N1912A power meter measures the average IF power and then calculates the ratio of the two average IF power that is the value of the measured Y-factor. The power meter gives directly the value of the Y-factor with a resolution of 0.001dB (see Figure A.8) and a noise floor of 0.000dB after video averaging over 256 periods.

Figure A.8: The measured Y-factor value displayed with 0.001dB resolution.

While the measured Y-factor value directly from the power meter is not correct, due to the non-linearity of the Agilent E9325A peak power sensor. Since the Agilent E9325A power sensor has a narrow bandwidth of 300kHz (ideal for telecommunication applications), it is not calibrated for measuring white noise signals of several gigahertz of bandwidth. It is necessary to calibrate the power sensor against a sensor with unlimited bandwidth like the Agilent 8482A thermocouple sensor. Hence the calibration procedure is able to correct the Y-factor with an estimated remaining non-linearity error below 0.005 dB/dB. For white noise signals in the 2-4GHz bands and for powers ranging from -5dBm to -1dBm, the uncorrected Y factor is biased by a systematic error of +0.097 dB/dB. For power in the -10dBm to -5dBm, the uncorrected Y factor is biased by a systematic error of +0.093dB/dB. Note that the non-linearity of the E9325A sensor decreases if it is configured in average only mode but in this case time gating is not available. The measured Y-factor value is corrected by introducing the non-linearity factor. For the 183GHz subharmonic mixer, around 60K error has been corrected.
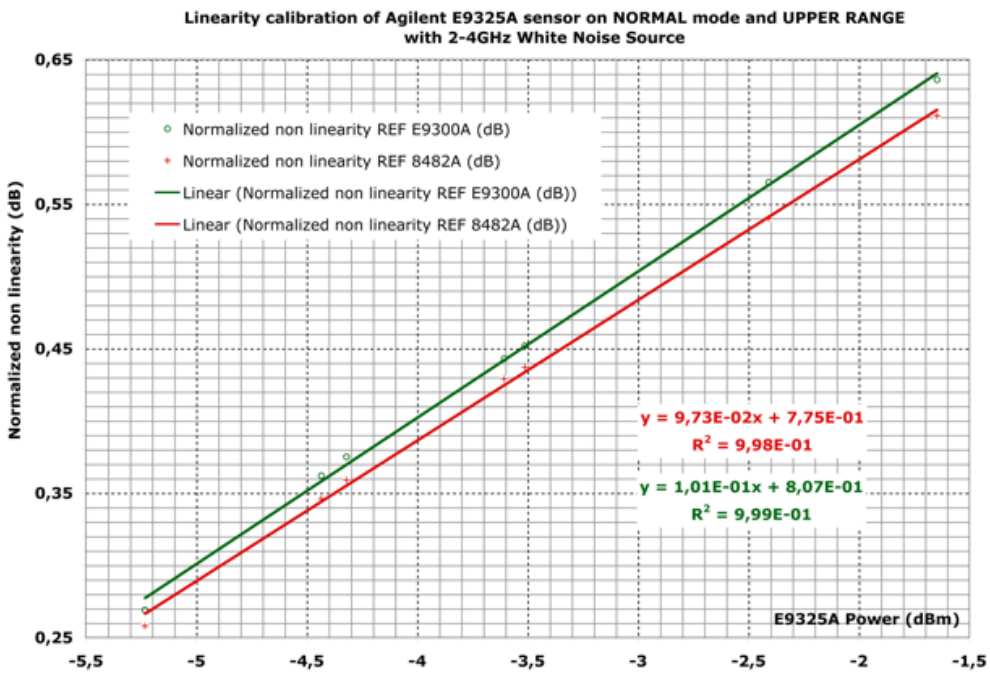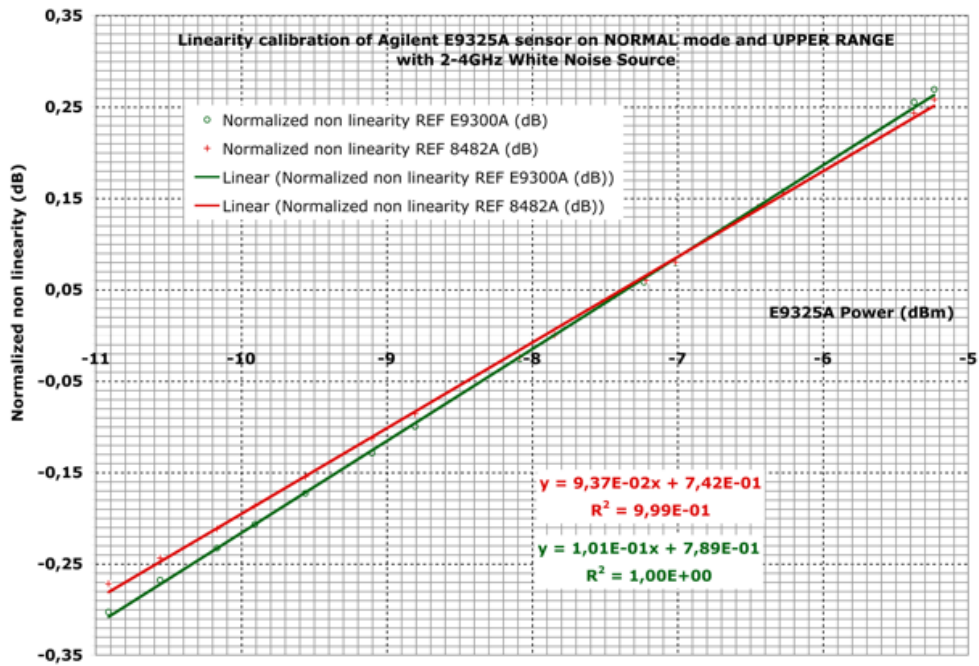
Figure A.9: Linearity calibration of the Agilent E9352A power sensor.

Appendix B - Diode I/V Measurement

The Schottky diode can be characterized by its built-in voltage V_b, the zero voltage junction capacitance C_{j0}, the ideality factor η, the saturation current I_0 and the series resistance R_s. These characterizations can be determined by measurements detailed in [Maas92].

The I/V characteristics can be measured directly with a semiconductor curve tracer, or by point-by-point measurement. A measuring device with current resolution below $1.0\mu A$ is recommended, which make possible to detect reverse leakage and to examine the I/V characteristics at low currents. Current should be recorded from the lowest possible value to a level where at least a few mV are developed across R_s. The data could be plotted on semi log graph, and the points for low currents are linear in function of applied voltage. A typical Schottky diode I/V curve is shown in Figure B.1, with a summary of I/V calculations. As one can see on the I/V curve, at the high current $I > 100\mu A$, the curve deviates noticeably from the extended straight line. This deviation is due to the voltage drop across the series resistance.
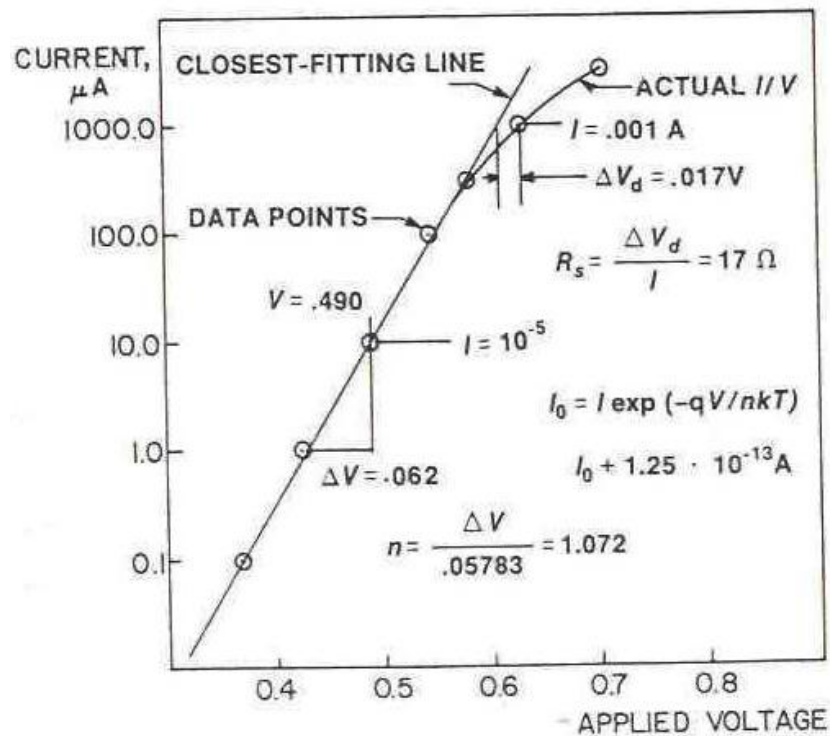
Figure B.1: Schottky diode I/V curve and DC parameter calculations (Reproduced from [Maas92]).

The ideality factor η, saturation current I_0, and series resistance R_s can be extracted from the I/V curve. At low currents, little voltage drop occurs across the series resistance, and the change in voltage per decade of current is constant.

When $I > I_0$,

$$I(V) = I_0 \left[\exp\left(\frac{qV}{\eta kT}\right) - 1 \right] \approx I_0 \cdot \exp(\frac{qV}{\eta kT}) \qquad (B\text{-}1)$$

And for $I ? I_0$,

$$I(V) = I_0 \cdot \exp(\frac{qV}{\eta kT}) \qquad (B\text{-}2)$$

On a semi log graph, there is

$$\ln(I) = \ln I_0 + \frac{qV}{\eta kT} \qquad (B\text{-}3)$$

Let's take two points $I_1 = 1\mu A$ and $I_2 = 10\mu A$ at low current, in order to neglect the voltage drop across series resistance, with respectively voltage of V_1 and V_2.

$$\ln(I_1) = \ln I_0 + \frac{qV_1}{\eta kT} \qquad (B\text{-}4)$$

$$\ln(I_2) = \ln I_0 + \frac{qV_2}{\eta kT} \qquad (B\text{-}5)$$

(B-5) - (B-4):

$$\ln(\frac{I_2}{I_1}) = \frac{q(V_2 - V_1)}{\eta kT}$$
$$\Rightarrow \eta = q\Delta V_{21} / kT \ln(10)$$
$$\Rightarrow \eta = 17.19 \Delta V_{21} \qquad (B\text{-}6)$$

Suppose that $\Delta V_{21} = V_2 - V_1$, with $q/kT = 39.585$, $T = 293.15K$ (absolute temperature), k is Boltzmann's constant $1.38 \cdot 10^{-23} J/K$.

The saturation current I_0 can be calculated at low current by knowing the ideality factor,

$$I_0 = I(V) \cdot \exp(-\frac{qV}{\eta kT}) \qquad (B\text{-}7)$$

R_s can be found from the deviation at the high current ($\Box$ $100\mu A$) end of the curve.

LERMA uses a source meter Keithley 2635 with probe heads Suss Microtec PH150, a LEICA stereo microscope M205C with Planapo lenses 1.0x and 2.0x. Special algorithm has been developed by Yamina Dekali and Alain Maestrini at LERMA for the extraction diode parameters (the ideality factor, the saturation current and the series resistance) from an I/V curve, the data acquisition was performed by using a custom LabView application (developed by Yamina Dekali and Alain
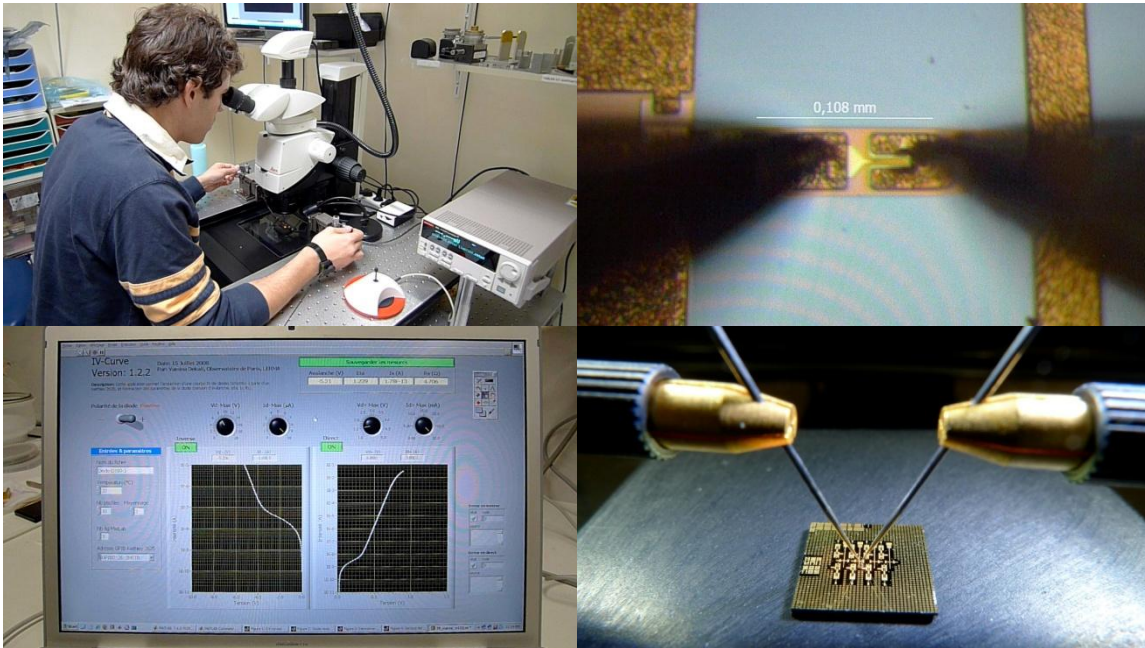
Maestrini at LERMA). Close-up photo of the test bench, showing the employed instrumentation, the chips under test and the probe heads, are presented in Figure B.2.

Figure B.2: Close-up photos of the test bench showing the source meter, the microscope, the circuits under test and the probe heads, and the custom LabView application employed for data acquisition.

The DC measurement results for both the I/V curves and the extraction of the resistance are shown in Figure B.3 and Figure B.4 respectively for a big ($21\mu m$ anode length) and a small anode ($1\mu m$ anode length).
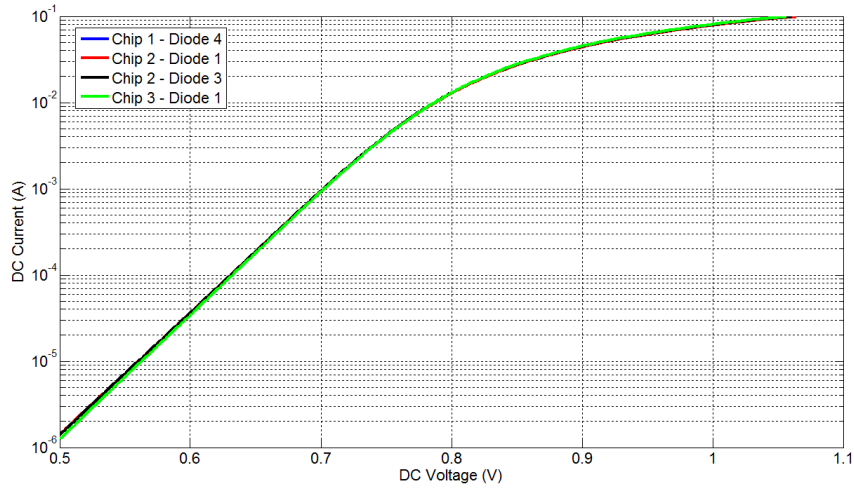
Figure B.3: (a) Measured I/V response as a function of applied voltage (anode length=21μm).
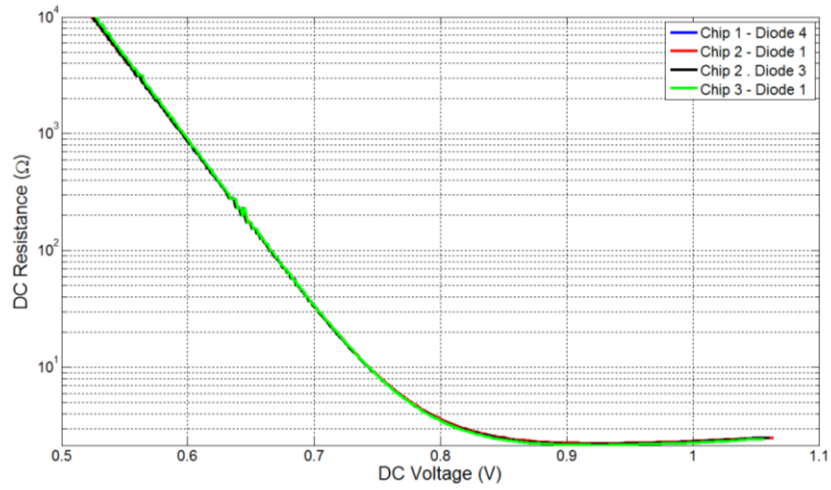
Figure B.3: (b) Measured DC Resistance as a function of applied voltage (anode length=21μm).
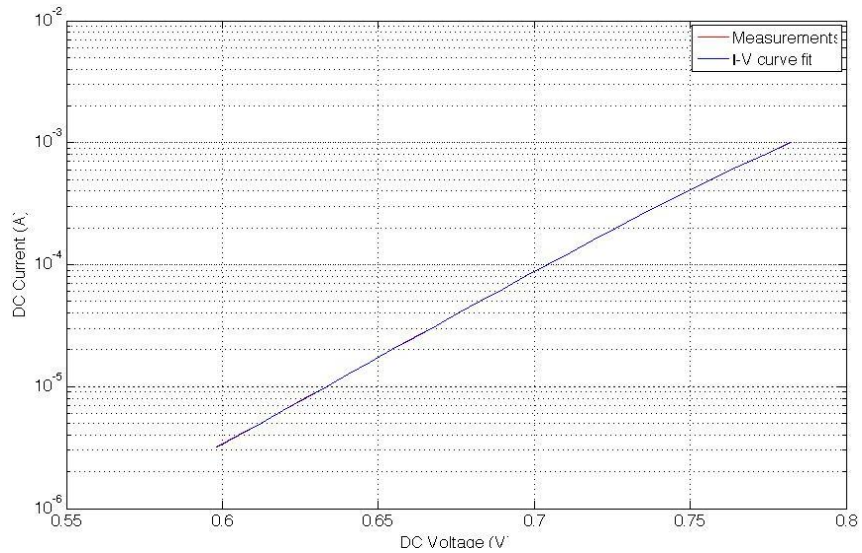
Figure B.4: (a) Measured I/V response as a function of applied voltage (anode length=1μm).
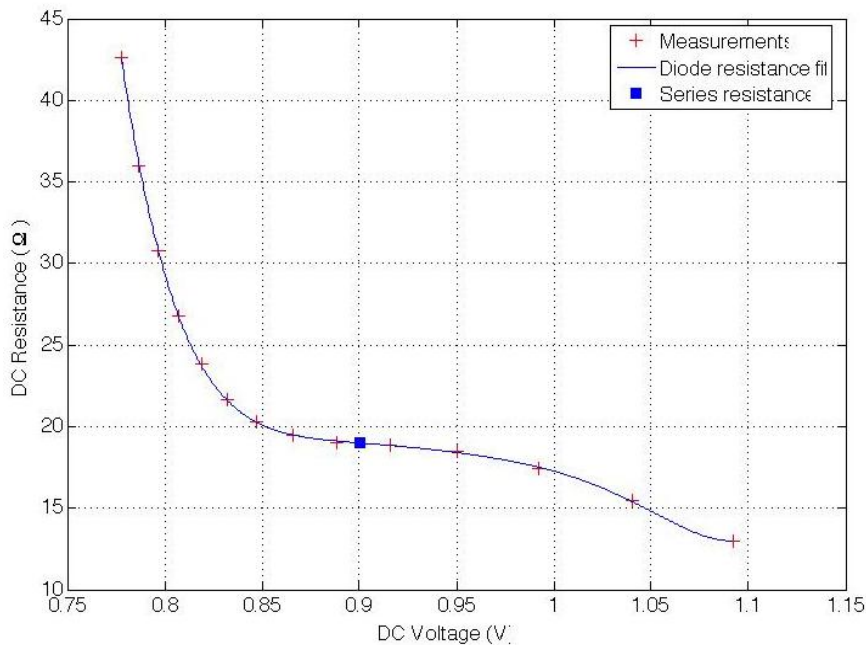
Figure B.4: (b) Measured DC Resistance as a function of applied voltage (anode length=1μm).

Using the results presented in Figure B.3 (a) and Figure B.4 (a), it is possible to extract the main DC parameters of the Schottky diodes (ideality factor, series resistance, and saturation current). The series resistance can be directly obtained from the results provided in Figure B.3 (b) and Figure B.4 (b), as it is directly the value of the DC resistance under flat-band conditions, i.e. when the Schottky barrier disappears and the junction resistance becomes equal to zero. However, in order to have an accurate value for the DC series resistance, it is necessary to take into account the probe heads resistance. The probe heads resistance can be calculated by

143

measuring the resistance of a single diode, two diodes in series, and three diodes in series.

Appendix C – List of Publications

H.Wang, J. Siles, A.Maestrini, B.Alderman and G.Beaudin, *"30/90 GHz Tripler using United Monolithic Semiconductors Schottky diode Process"*, IEEE Microwave and Wireless Components Letters 2009 (in preparation).

B. Alderman, H. Sanghera, B. Thomas, D. Matheson, A. Maestrini, **H. Wang**, J. Treuttel, J. V. Siles, S. Davies, T. Narhi, *"Integrated Schottky Structures for Applications Above 100 GHz"*, to appear in the proceedings of the 38th European Microwave Conf., European Microwave Week, Amsterdam, October 27-31,2008.

H.Wang, A.Maestrini, B.Thomas, B.Alderman and G.Beaudin, *"Development of a Two-pixel integrated heterodyne Schottky diode receiver at 183GHz"*, in the proceedings of the 19th International Symposium On Space THz Technology, ISSTT2008, pp.490-493, Groningen, the Netherland, April 2008.

C.Jung, **H.Wang**, A.Maestrini and Y.Jin, *"Fabrication of GaAs Schottky nano-diodes with T-Anodes for submillimeter wave mixers"*, in the proceedings of the 19th International Symposium On Space THz Technology, ISSTT2008, pp.517-518, Groningen, the Netherland, April 2008.

H.Wang, B.Alderman, B.Thomas, A.Maestrini, and G.Beaudin, *"A low noise integrated sub-harmonic mixer at 183GHz using European Schottky diode technology"*, the European Summer School On New Trends In Terahertz Imaging NTTI2007, Paris, France, July 2007.

J.-M.Rollin, **H.Wang**, B.Thomas, A.Maestrini, and S. Davies, *"A low noise integrated sub-harmonic mixer at 183GHz"*, in Proceedings of the 17th Int. Symp. On Space THz Technology, ISSTT2006, Paris, France, May 2006.

H. Wang, J.-M. Rollin, B. Thomas, S. Davies, B. Alderman and A. Maestrini, *"Design of a low noise integrated sub-harmonic mixer at 183 GHz using European Schottky diode technology"* in Proceedings of the 4th ESA workshop on Millimetre-Wave Technology and Applications, pp.249-252, Espoo, Finland, February 2006.

J.-M. Rollin, **H. Wang**, A Maestrini and S. Davies, *"Integrated Schottky diodes for a sub-harmonic mixer at millimetre wavelengths"*, in Proceedings of the 4th ESA workshop on Millimetre-Wave Technology and Applications, pp.117-121, Espoo, Finland, February 2006.

Abbreviations

ADCs	Analog to Digital Converters
ADS	Advanced Design System
CMB	Cosmic Microwave Background
CNES	Centre National D'Etudes Spatiales
CNRS	Centre National de la Recherche Scientifique
DAC	Data Access Component
DSB	Double Side Band
ESA	European Space Agency
FPGAs	Field Programmable Gate Arrays
GHz	Gigahertz
HB	Harmonic Balance
HBV	Heterostructure Barrier Varactor
HEB	Hot Electron Bolometer
HFSS	High Frequency Simulation Software
HIFI	Heterodyne Instrument for the Far Infrared
IF	Intermediate Frequency
JPL	Jet Propulsion Laboratory
LERMA	Laboratoire d'Etude du Rayonnement de la Matière en Astrophysique
LO	Local Oscillator
LPN	Laboratoire de Photonique et Nanostructures
LSB	Lower Side Band
MIM	Metal-Insulator-Metal
MIRO	Microwave Instrument for the Rosetta Orbiter (for the Rosetta orbiter)
MLS	Microwave Limb Sounder
MMIC	Monolithic Microwave Integrated Circuit
MNVA	Microwave Vector Network Analyzer
NASA	National Aeronautics and Space Administration
NF	Noise Factor
PAs	Power Amplifiers
QCL	Quantum Cascade Laser
RAL	Rutherford Appleton Laboratory
RF	Radio Frequency
SHP	Subharmonically Pumped (mixers)

SIS	Superconductor-Insulator-Superconductor junction
SNR	Signal to Noise Ratio
SOFIA	Stratospheric Observatory for Infrared Astronomy
SSB	Single Side Band
THz	Terahertz
TUD	Technique University of Darmstadt
UARS	Upper Atmosphere Research Satellite
UMS	United Monolithic Semiconductors
UPM	University Polytechnic of Madrid
USB	Upper Side Band
UT	Upper Troposphere
VDI	Virginia Diodes Inc.

List of References

[ABmm] http://www.abmillimetre.com/

[ADS] Advanced Design System, Agilent Technologies, 395 Page Mill Road, Palo Alto, CA 94304, USA.

[Alderman07] B. Alderman, H. Sanghera, C. Price, B. Thomas and D.N. Matheson, "Fabrication of Reproducible Air-Bridged Schottky Diodes for use at Frequencies Near 200 GHz," in *proceedings of the 2007 Joint 32nd International Conference on Infrared and Millimeter Waves and 15th International Conference on Terahertz Electronics*, pp. 848-849, Cardiff, UK, September 3-7, 2007.

[Archer01a] J. W. Archer, R. Lai, and R. Gough, "Ultra-low-noise indium-phosphide MMIC amplifiers for 85-115 GHz," *IEEE Trans. Microwave Theory and Techniques*, Vol. 49, No. 11, pp. 2080-2085, Nov.2001.

[Archer01b] J. W. Archer, R. Lai, R. Grundbacher, M. Barsky, R. Tsai, and P. Reid, "An indium phosphide MMIC amplifier for 180-205 GHz," *IEEE Microwave and Wireless Components Letters*, Vol. 11, No. 1, pp. 4-6, Jan.2001.

[Ardenn87] A. van Ardenne, "Design considerations for a Multibeam receiver for millimeter wave astronomy," *International Journal of Infrared and Millimeter Waves*, Vol.8, No. 2, pp. 107-117, 1987.

[Belkin08] M. A. Belkin, S. P. Khanna, J. A. Fan, S. Hormoz, M. Lachab, F. Capasso, A. G. Davies, and E. H. Linfield, "Terahertz frequency quantum cascade lasrs operating up to 178 K with copper metal-metal waveguides," to appear in the *proceeding of the Joint 33th International Conference on Infrared and Millimeter Waves and 16th International Conference of Terahertz Electronics*, Pasadena, CA, Sep.2008.

[Benz05] A. O. Benz, P. C. Grigis, V. Hungerbuhler, H. Meyer, C. Monstein, B. Stuber, and D. Zardet, "A broadband FFT spectrometer for radio and millimeter astronomy," *A&A*, Vol. 442, pp. 767-773, Nov.2005.

[Betz96] A.L. Betz and R.T. Boreiko, "A Practical Schottky Mixer for 5 THz," in

Proceedings of the 7th International Symposium on Space Terahertz Technology, pp. 503-510, Charlottesville, VA, March 1996.

[Blaney78] T. G. Blaney, "Radiation detection at submillimeter wavelengths," *J. Phys.E:Sci. instrum.*, Vol. 11, pp. 856-881, Sep.1978.

[Boreiko96] R.T. Boreiko, and A.L. Betz, "Heterodyne Spectroscopy of the 63 μm OI Line in M42," *Astrophys. J.*, vol. 464, pp. L83–L86, Jun. 1996.

[Bradley92] R. F. Bradley, "*The application of planar monolithic technology to Schottky varactor millimeter-wave frequency multipliers*," Ph.D. dissertation, Sch. Eng. Appl. Science, Univ. of Virginia, Charlottesville, May 1992.

[Brown95] E. R. Brown, K. A. Mcintosh, K. B. Nichols, and C. L. Dennis, "Photomixing up to 3.8 THz in low-temperature-grown GaAs," *Appl. Phys. Lett.,* vol. 66, no. 3, pp. 285-287, Jan.1995.

[Bruneau08] P. J. Bruneau, H. D. Janzen, and J. S. Ward, "Machining of Terahertz Split-Block Waveguides with Micrometer Precision," to appear in the *proceeding of the Joint 33th International Conference on Infrared and Millimeter Waves and 16th International Conference of Terahertz Electronics*, Pasadena, California, Sep.2008.

[Campos-Roca00] Y. Campos-Roca, L. Verweyen, M. Fernandez-Barciela, E. Sanchez, M.C. Curras-Francos, W. Bronner, A. Hulsmann, and M. Schlechtweg, "An optimized 25.5-76.5 GHz PHEMT-based coplanar frequency tripler," *IEEE Microwave Guided Wave Letter*, vol. 10, pp. 242-244, June 2000.

[Campos-Roca06] Y. Campos-Roca, C. Schworer, A. Leuther, and M.Seelmann-Eggebert, "G-Band Metamorphic HEMT-Based Frequency Multipliers," *IEEE Trans. Microwave Theory and Techniques*, Vol. 54, No.7, pp. 2983-2992, July 2006.

[Charlstrom96] J. Charlstrom, and J. Zmuidzinas, "Millimeter and submillimeter techniques," in *Review of Radio Science 1993-1996*, W. R. stone, Ed. Oxford University Press, pp.839-882, June 1996.

[Chattopadhyay04] G. Chattopadhyay, I. Mehdi, J. S. Ward, E. Schlecht, A. Skalare, and P. H. Siegel, "Development of Multi-Pixel Heterodyne Array Instruments at

Submillimeter Wavelengths," *Invited Paper – in Proceedings of the Asia Pacific Microwave Conference*, New Delhi, India, December 15-18, 2004.

[Chattopadhyay05a] G. Chattopadhyay, "Future of heterodyne receivers at submillimeter wavelength," *The Joint 30th International Conference on Infrared and Millimeter Waves and 13th International Conference of Terahertz Electronics*, Vol.2, pp.461-462, September 2005.

[Chattopadhyay05b] G. Chattopadhyay, "Heterodyne Arrays at Submillimeter Wavelengths" *Invited Paper – In Proceedings of the XXVIIIth. General Assembly of International Union of Radio Science (URSI)*, New Delhi, India, October 2005.

[Cohn94] M. Cohn, R. Freitag, H. Henry, J. Degenford, and D. Blackwell, "A 94 GHz MMIC tripler using anti-parallel diode arrays for idler separation," in *IEEE MTT-S Intl. Microwave Symp. Digest*, pp. 763-766, San Diego, CA, 1994.

[Cooper08] K. B. Cooper, R. J. Dengler, G. Chatopadhyay, E. Schlecht, J.Gill, A. Skalare, I. Mehdi, and P. H. Siegle "A High-Resolution Imaging Radar at 580GHz," *IEEE Microwave and Wireless Components Letters*, Vol. 18, No. 1, pp. 64-66, Jan.2008.

[Crowe86] T.W.Crowe and R.J.Mattauch, "Conversion loss in GaAs Schottky-barrier mixer diodes," *IEEE Trans. Microwave Theory and Techniques*, Vol. MTT-34, No. 7, pp. 753-760, July 1986.

[Crowe87] T.W.Crowe and R.J.Mattauch, "Analysis and Optimization of Millimeter and Submillimeter-Wavelength Mixer Diodes," *IEEE Trans. Microwave Theory and Techniques*, Vol. MTT-35, No. 2, pp. 159-168, Jan.1987.

[Crowe92] T.W.Crowe, R.J.Mattauch, H.P.Röser, W.L. Bishop, W.C.Peatman, and X.Liu, "GaAs Schottky diodes for THz mixing applications," in *Proceedings of the IEEE*, Vol.81, No. 11, pp. 1827-1841, Nov.1992.

[David02] T. David, S. Arscott, J.M. Munier, T. Akalin, P. Mounaix, G. Beaudin, and D. Lippens, "Monolithic Integrated Circuits Incorporating InP-based Heterostructure Barrier Varactors," *IEEE Microwave and wireless components letters*, Vol.12, No.8, pp.281-283, 2002.

[Deal07a] W. R. Deal, X. B. Mei, V. Radisic, W. Yoshida, P. H. Liu, J. Uyeda, M. Barsky, T. Gaier, A. Fung, L. Samoska, and R. Lai, "Demonstration of a S-MMIC LNA with 16-dB gain at 340GHz," in *IEEE Compound Semiconduct. Integr. Circuits Symp.*, pp. 1-4, Oct.2007.

[Deal07b] W. R. Deal, X. B. Mei, V. Radisic, W. Yoshida, P. H. Liu, J. Uyeda, M. Barsky, T. Gaier, A. Fung, L. Samoska, and R. Lai, "A 245-GHz MMIC amplifier with 80-um output periphery and 12-dB gain," in *IEEE MTT-S Intl. Microwave Symp. Digest*, pp. 329-332, June 2007.

[Deal07c] W. R. Deal, X. B. Mei, V. Radisic, W. Yoshida, P. H. Liu, J. Uyeda, M. Barsky, T. Gaier, A. Fung, L. Samoska, and R. Lai, "Demonstration of a 270-GHz MMIC amplifier using 35-nm InP HEMT technology," *IEEE Microwave and Wireless Components Letters*, Vol. 17, No. 5, pp. 391-393, May 2007.

[Deal08] W.R.Deal, X. B. Mei, V. Radisic, B. Bayuk, A. Fung, W. Yoshida, P. H. Liu, J. Uyeda, L. Samoska, T. Gaier, and R. Lai, "A New Sub-Millimeter Wave Power Amplifier Topology Using Large Transistors," *IEEE Microwave and Wireless Components Letters*, Vol. 18, No. 8, pp. 542-544, Aug.2008.

[Dengler07] R. J. Dengler, K. B. Cooper, G. Chatopadhyay, I. Mehdi, E. Schlecht, A. Skalare, C. Chen, and P. H. Siegle, "600 GHz imaging radar with 2 cm range resolution," in *IEEE MTT-S Intl. Microwave Symp. Digest*, pp. 1371-1373, Jun.2007.

[Dent00] W. Dent, et al., "HARP and ACSIS on the JCMT," *in ASP Conference Series,* Vol.217, pp.33-40, 2000.

[Dolan79] G. J. Dolan, T. G. Phillips, and D. P. Woody, "Low noise 115 GHz mixing in superconducting oxide-barrier tunnel junctions," *Appl. Phys. Lett.*, vol. 34, no. 5, pp. 347-349, Mar. 1979.

[Edgar00] M. L. Edgar and J. Zmuidzinas, "CASIMIR: A submillimeter heterodyne spectrometer for SOFIA," in *Airborne Telescope Systems, Proc. SPIE*, vol. 4014, pp. 31-42, 2000.

[Erickson92] N. R. Erickson, P. F. Goldsmith, G. Novak, R.M. Grosslein, P.J. Viscuso, R.B. Erickson, and C. R. Predmore, "A 15 element focal plan array for 100

GHz," *IEEE Trans. Microwave Theory and Techniques*, Vol. 40, No. 1, pp. 1-11, Jan.1992.

[Erickson98] N.R. Erickson, "Wideband High Efficiency Planar Diodes Doublers," in *Proceedings of the 9th International Symposium on Space Terahertz Technology*, pp. 473-480, Pasadena, CA, 1998.

[Erickson99] N.R. Erickson, "A Fast and Sensitive Submillimeter Waveguide Power Sensor," *in Proceedings of the 10th International Symposium on Space Terahertz Technology*, pp. 501-507, Charlottesville, VA, 1999. Available from Erickson Instruments LLC, Amherst, MA.

[Erickson00] N. R. Erickson, R. P. Smith, S. C. Martin, B. Nakamura, and I. Mehdi, "High efficiency MMIC frequency triplers for millimeter and submillimeter wavelengths," in *IEEE MTT-S Int. Microwave Symp. Dig.,* vol. 2, pp.1003–1006, Boston, MA, Jun. 2000.

[Fudem98] H. Fudem, and E. Niehenke, "Novel millimeter-wave active MMIC triplers," *IEEE MTT-S Int. Microwave Symp. Digest*, pp. 387-390, Baltimore, MD, 1998.

[Gaidis00] M. C. Gaidis, H. M.Pickett, C.D.Smith, S.C.Martin, R.P.Smith, and P.H.Siegel, "A 2.5-THz receiver front end for spaceborn applications," *IEEE Trans. Microwave Theory and Techniques*, Vol. 48, No. 4, pp. 733-739, Apr.2000.

[Gaier07] T. Gaier, L. Samoska, A. Fung, W. R. Deal, V. Radisic, X. B. Mei, W. Yoshida, P. H. Liu, J. Uyeda, M. Barsky, and R. Lai. "Measurement of a 270 GHz low noise amplifier with 7.5 dB noise figure," *IEEE Microwave and Wireless Components Letters*, Vol. 17, No. 7, pp. 546-548, July 2007.

[Gao05] J. R. GAO, J. N. Hovenier, Z. Q. Yang, J. J. A. Baselmans, A. Baryshev, M. Hajenius, T. M. Klapwijk, A.J.L. Adam, T. O. Klaassen, B.S.Williams, S. Kumar, Q. Hu, and J. L. Reno, "Terahertz heterodyne receiver based on a quantum cascade laser and a superconducting bolometer," *Appl. Phys.Lett.*, Vol. 86, No 24, 244104, June 2005.

[Gao07] J. R. GAO, M. Hajenius, Z. Q. Yang, J. J. A. Baselmans, P. Khosropanah, R.

Barends, and T. M. Klapwijk, "Terahertz Superconducting Hot Electron Bolometer Heterodyne Receivers," *IEEE Transactions on   Applied Superconductivity*, Vol. 17, No 2, pp. 252-258, June 2007.

[Garnier05] A.Garnier, J.P.Pommereau, P.Cocquerez, G.Held and the Hibiscus partners, "The balloon flights in the tropics of the Hibiscus project," in *Proceedings of the 17th ESA Symposium on European Rocket and Balloon Programmes and Related Research*, pp. 203-206, Norway, Aug. 2005.

[Gillespie79] A.R.Gillespie and T.G.Phillips, "Array Detectors for Millimetre Line Astronomy," *A&A*, 73, 14, 1979.

[Goldsmith93] P. F. Goldsmith, C. -T. Hsieh, G. R. Huguenin, J. Kapitzky, and E. L.Moore, "Focal plane imaging systems for millimeter wavelengths," *IEEE Trans. Microwave Theory and Techniques*, Vol. 41, No. 10, pp. 1664-1675, Oct.1993.

[Goldsmith07] P. F. Goldsmith, "Submillimeter Astronomy and Mauna Kea-An Overview," in *IEEE MTT-S Int. Microwave Symp. Dig.*, pp. 1845-1848, Honolulu, HI, June 2007.

[Gulkis06] S. Gulkis, *et al.*, "MIRO: Microwave Instrument for Rosetta Orbiter," *Space Science Reviews*, Vol. 128, No. 1-4, pp. 561-597, 2006.

[Graf03] U. U. Graf, et al., "SMART: The KOSMA Sub-Millimeter Array Receiver for Two Frequencies,"   *in Proc. SPIE,* Millimeter and Submillimeter Detectors for Astronomy, Vol. 4855, 2003.

[Groppi00a] C. Groppi, C.K.Walker, A. Hungerford, C.Kulesa, K. Jacobs, and J. W. Kooi, "Pole STAR: An 810 GHz Array Receiver for AST/RO," *in ASP Conference Series,* Vol.217, pp.48-49, 2000.

[Groppi00b] C. Groppi, C.K.Walker, A. Hungerford, G. Narayanan, and A. Lichtenberger, "A 345 GHz array receiver for the Heinrich Telescope," *in Proc. SPIE,* Vol. 4015, 2000.

[Groppi07] C.Groppi, C.K.Walker, C.Kulesa, D.Golish, P.Pütz, P.Gensheimer, A.Hedden, S.Bussmann, S.Weinreb, G.Jones, J.Barden, H.Mani, T.Kuiper, J. W.

Kooi, A.W.Lichtenberger, T.Cecil, and G.Narayanan, "Supercam: A 64 pixel superheterodyne camera," *In Proceedings of the 18th International Symposium on Space Terahertz Technology*, pp. 264-269, Pasadena, California, March 2007.

[Gusten98] R. Gusten, et al., "CHAMP: The carbon heterodyne array of the MPIfR," *in Proc. SPIE Advanced Technol. MMW, Radio, Terahertz Telescopes Conf. Kona*, HI, vol. 3357, pp. 167-177, 1998.

[Herschel] http://sci.esa.int/science-e/www/area/index.cfm?fareaid=16

[Hesler96] J.L.Hesler, *Planar Schottky diodes in submillimeter-wavelength waveguides receivers*, Ph.D.Dissertation, University of Virginia, VA, January 1996.

[Hesler97] J. L. Hesler, K. Hui, R.M. Weikle, T. Crowe, "Design, Analysis and Scale Model Testing of Fixed-Tuned Broadband Waveguide to Microstrip Transitions," in *Proc. of Eighth Int. Symp. on Space THz Tech.*, Cambridge, MA, pp. 319-325, March 25-27 1997.

[Hesler99] J. L. Hesler, K. Hui, S. He, and T.W. Crowe, "A Fixed tuned 400 GHz Subharmonic Mixer Using Planar Schottky Diodes," (invited talk) in *Proc. 1999 Int. Symp. On Space THz Tech.*, Charlottesville, VA, pp. 95-99, Mar. 1999.

[Hesler00] J. L. Hesler, "Broadband Fixed-tuned Subharmonic Receivers to 640 GHz," in *Proc. 11th 1999 Int. Symp. On Space THz Tech.*, Ann Arbor, MI, May 2000.

[HFSS] High Frequency Simulation Software, Ansoft Corporation, 225 West Station Square Drive, Suite 200, Pittsburgh, PA 15219, USA.

[Hindle08] F. Hindle *et al.*, "Continuous-wave terahertz by photomixing: applications to gas phase pollutant detection and quantification," *C.R.Physique 9*, pp. 262-275, 2008.

[Hodges77] D. Hodges, F. Foote, and R. Reel, "High-power operation and scaling behavior of CW optically pumped FIR waveguide lasers," *IEEE Journal of Quantum Electronics*, Vol. 13, no. 6, pp. 491-494, June 1977.

[Huang06] P. Huang, R. Lai, R. Grundbacher and B. Gorospe, "A 20 mW G-Band

Monolithic Driver Amplifier using 0.07um InP HEMT," in *IEEE MTT-S Int. Microwave Symp. Dig.*, pp. 806-809, June 2006.

[Hübers05] H.W.Hübers, S.G.Pavlov, A.D.Semenov, R.Köhler, L.Mahler,A. Tredicucci, H.E.Beere, D.A.Ritchie, and E.H.Linfield, "Terahertz quantum cascade laser as local oscillator in a heterodyne receiver," *Optics Express,* vol.13, no.15, pp.5890-5896, July 2005.

[Ito05] H. Ito, F.Nakajima, T.Furuta, and T.Ishibashi, "Continuous THz-wave generation using antenna-integrated uni-travelling-carrier photodiodes," *Semiconductor Science and Technology*, 20, no.7, S191-S198, 2005.

[Jung08] C. Jung, H. Wang, A. Maestrini, and Y. Jin, "Fabrication of GaAs Schottky nano-diodes with T-Anodes for Submillimeter Wave Mixers," to appear in the *proceedings of the 19th Int. Symp. on Space THz Technology*, Groningen, the Netherlands, April 28-30, 2008.

[Kangaslahti06] P. Kangaslahti, T. Gaier, M. Seiffert, S. Weinreb, D. Harding, D. Dawson, M. Soria, C. Lawrence, B. Hooberman, and A. Miller, "Planar Polarimetry Receivers for Large Imaging Arrays at Q-band," *IEEE MTT-S International Microwave Symposium*, pp. 89 − 92, June 2006.

[Karpov07] A. Karpov, D. Miller, F. Rice, J. A. Stern, B. Bumble, H. G. LeDuc, and J. Zmuidzinas, "Low Noise 1 THz–1.4 THz Mixers Using Nb/Al-AlN/NbTiN SIS Junctions," *IEEE Transactions on Applied Superconductivity*, Vol. 17, No 2, pp. 343-346, June 2007.

[Kasemann06] C. Kasemann, R. Güsten, S. Heyminck, B. Klein, T. Klein, S. D. Philipp, A. Korn, G. Schneider, A. Henseler, A. Baryshev, and T. M. Klapwijk, "CHAMP+: a powerful array receiver for APEX," *in Proc. of the SPIE*, Millimeter and Submillimeter Detectors and Instrumentation for Astronomy. Vol. 6275, 2006.

[Khosropanah07] P. Khosropanah, J. R. GAO, M. Laaumen, M. Hajenius, and T. M. Klapwijk, "Low Noise NbN Hot Electron Bolometer Mixer at 4.3THz," *Appl. Phys.Lett*, 91,221111, 2007.

[Kirby06] P. L. Kirty, D. Pukala, H. Manohara, I. Mehdi, and J. Papapolymerou,

"Characterization of micromachined silicon rectangular waveguide at 400 GHz," *IEEE Micr. Wireless Comp. Lett.,* Vol.16, No.6, pp.366-368, June 2006.

[Klein06] B. Klein, S. D. Philipp, I. Kramer, C. Kasemann, R. Gusten, and K. M. Menten, "The APEX digital Fast Fourier Transformation Spectrometer," *A&A*, Vol. 454, pp. L29-L32, Aug.2006.

[Köhler02] R. Köhler, A. Tredicucci, F. Beltram, H. E. Beere, E. H. Linfield, A. G. Davies, D. A. Ritchie, R. C. Iotti, and F. Rossi, "Terahertz semiconductor-heterostructure laser", *Nature 417*, pp. 156-159, 2002.

[Kollberg89] E.L.Kollberg, and A. Rydberg, "Quantum-barrier-varactor diode for high efficiency millimeter-wave multipliers," *IEEE Electronics Letters*, Vol.25, pp. 1696-1698, 1989.

[Kraus86] J. D. Krarus, *Radio Astronomy*. Second edition. Cygnus-Quasar Books, 1986.

[Li08] Y. Li, P. L. Kirty, O. Offranc, and J. Papapolymerou, "Silicon Micromachined W-band Hybrid Coupler and power Divider Using DRIE Technique," *IEEE Micr. Wireless Comp. Lett.,* Vol.18, No.1, pp.22-24, Jan.2008.

[Lin02] K. Lin, H. Wang, M. Morgan, T. Gaier, and S. Weinreb, "A W-band GCPW MMIC diode tripler," *2002 European Microwave Conference*, Vol.1, pp.441-444, Milan, Sep.2002.

[Louhi95] J.T. Louhi and A.V.Raisanen, "On the Modeling and Optimization of Schottky Varactor Frequency Multipliers at Submillimeter Wavelengths", *IEEE Transactions On Microwave Theory And Techniques*, vol.43, no.4, pp.992-926, Apr. 1995.

[Lubecke98] V. M. Lubecke, K. Mizuno, and G. M. Rebeiz, "Micromachining for terahertz applications," *IEEE Transactions Microwave Theory and Techniques,* Vol.46, No.11, pp.1821-1831, Nov.1998.

[Maas92] S. A. Maas, *Microwave Mixers*. Norwood, MA: Artech House, 1992.

[Maas03] S. A. Maas, *Nonlinear Microwave and RF Circuits*. Second edition.

Norwood, MA: Artech House, 2003.

[Maestrini99] A. Maestrini, *Modélisation et conception de multiplicateurs de fréquences utilisant des diodes planaires aux longueurs d'onde millimétriques et submillimétrques*, Ph.D.Dissertation, Université de Bretagne Occidentale, Feb.1999.

[Maestrini01] A. Maestrini, J. Bruston, D. Pukala, S. Martin, and I. Mehdi, "Performance of a 1.2 THz frequency tripler using a GaAs frameless membrane monolithic circuit," in *IEEE MTT-S Int. Microwave Symp. Dig.*, Vol. 3, pp. 1657-1660, Phoenix, AZ, May 2001.

[Maestrini04a] A. Maestrini, J. Ward, J. Gill, H. Javadi, E. Schlecht, G. Chattopadhyay, F. Maiwald, N. R. Erickson, and I. Mehdi, "A 1.7 to 1.9 THz local oscillator source," *IEEE Microw. Compon. Lett*, vol., 14, no. 6, pp. 253–255, Jun. 2004.

[Maestrini04b] A. Maestrini, and B. Thomas, "Report on the Evaluation of the Capabilities of the United Monolithic Semiconductors to Produce Schottky Diodes Based Mixers in the Band 100-380GHz", 2004.

[Maestrini05a] A. Maestrini, C. Tripon-Canseliet, J. S. Ward, J. J. Gill, H. Javadi, E. Schlecht, G. Chattopadhyay, and I. Mehdi, "Multiple-Anode Broadband Frequency Triplers at Submillimeter Wavelengths," *Proceedings, Sixteenth International Symposium on Space Terahertz Technology*, paper 5-3, Göteborg, Sweden, May 2005.

[Maestrini05b] A. Maestrini, J. S. Ward, J. J. Gill, H. S. Javadi, E. Schlecht, C. Tripon-Canseliet, G. Chattopadhyay, and I. Mehdi, "A 540-640 GHz High Efficiency Four Anode Frequency Tripler," *IEEE Transactions On Microwave Theory And Techniques*, vol.53, no.9, pp.2835-2843, Sep.2005.

[Maestrini08a] A. Maestrini, J. S. Ward, G. Chattopadhyay, E. Schlecht, and I. Mehdi, "Terahertz Sources based on Frequency Multiplication and Their Applications" *Frequenz, Journal of RF Engineering and Telecommunications*, Issue 5/6 2008, Vol. 62, no.3, pp.118-122, May/June 2008.

[Maestrini08b] A. Maestrini, J. S. Ward, C. Tripon-Canseliet, J. J. Gill, C. Lee, H. Javadi, G. Chattopadhyay, and I. Mehdi, "In-Phase Power-Combined Frequency triplers at 300 GHz," *IEEE Microwave and Wireless Components Letters*, vol.18, no.3, pp.218-220, Mar.2008.

[Maestrini08c] A. Maestrini, J. Ward, G. Chattopadhyay, E.Schlecht, J. Gill, C. Lee, H. Javadi, and I. Mehdi, "In-Phase Power Combining of Submillimeter-Wave Multipliers," to appear in the *proceeding of the Joint 33th International Conference on Infrared and Millimeter Waves and 16th International Conference of Terahertz Electronics*, Pasadena, CA, Sep.2008.

[Manley56] J. M. Manley and H. E. Rowe, "Some General Properties of Nonlinear Elements," in *Proc. IRE*, Vol. 44, p. 904, 1956.

[Martin01] S. Martin, B. Nakamura, A. Fung, P. Smith, J. Bruston, A. Maestrini, F. Maiwald, P. Siegel, E. Schlecht, and I. Mehdi, "Fabrication of 200GHz to 2700GHz multipliers devices using GaAs and metal membranes", in *proceedings of the IEEE MTT-S*, Vol.3, pp. 1641-1644, Phoenix, Arizona, May 20-25, 2001.

[Melnick00] G. Melnick, *et al.* "The submillimeter wave astronomy satellite: Science objectives and instrument description," *Astrophys. J. Lett.*, vol.539, no.2, pt.2, pp.L77-L85, Aug.2000.

[Melique00] X. Melique, A. Maestrini, R. Farre, P. Mounaix, M. Favreau, O. Vanbesien, J. Goutoule, F. Mollot, G. Beaudin, T. Nahri, and D. Lippens, "Fabrication and performance of InP-based heterostructure barrier varactors in 250-GHz waveguide tripler," *IEEE Trans. Microw. Theory Tech.*, vol. 48, no. 6, pp. 1000–1006, Jun. 2000.

[Michael02] E. A. Michael, U. U. Graf, C. E. Honingh, K. Jacobs, F. Lewen, R. Schieder and J. Stutzki, "SOFIA Terahertz Array Receiver (STAR)" *in Airborne Telescope Systems, Proceedings of the SPIE*, vol. 4014, 2000.

[Millitech] "Fullband Frequency Triplers-MUT10", Product data sheet, Millitech, Inc. Northampton, MA.

[Morgan01] M. Morgan and S. Weinreb, "A full waveguide band MMIC tripler for

75-110 GHz," in *IEEE MTT-S Int. Microwave Symp. Digest*, pp. 103-106, Phoenix, AZ, 2001.

[Morgan03] M. Morgan, "*Millimeter-Wave MMICs and Applications*," Ph.D. dissertation, California Institute of Technology, Pasadena, California, March 2003.

[Moyna06] B.P.Moyna, *et al.*, "MARSCHALS: airborne simulator of a future space instrument to observe millimetre-wave limb emission from the upper troposphere and lower stratosphere," in *Proc. SPIE European Remote Sensing Conference*, 6361-10, Stockholm, Sept. 2006.

[Mueller98] E. R. Mueller, W. E. Robotham, Jr., R. P. Meisner, R. A. Hart, J. Kennedy, and L. A. Newman, "2.5 THz laser local oscillator for the EOS CHEM 1 satellite," in *Proceedings of the 9th International Symposium on Space Terahertz Technology*, pp. 563–572, Pasadena, CA, 1998.

[Murphy88] J. A.Murphy, R.Padman, and R. E. Hills, "An Experimental Submillimeter Heterodyne Array Receiver," *International Journal of Infrared and Millimeter Waves*, Vol.9, No. 4, pp. 325-350, 1988.

[Narayanan02] G. Narayanan, N. R. Erickson and A. W. Lichtenberger, "Integrated terahertz heterodyne focal plane array receivers," *In Proc. Far-IR, Sub-MM, and MM Detector Technology Workshop*, pp. 203-206, CA, April 2002.

[Odin] http://www.ssc.se/?id=7180

[Pacific] "Frequency Multipliers-W3," Product data sheet, Pacific Millimeter Products, Golden, CO.

[Padman87] R. Padman, J. Murphy and R. Hills, "Gaussian mode analysis of Cassegrain antenna efficiency," *IEEE Transactions On Antennas And Propagation,* Vol.35, No.10, pp.1093-1103, Oct. 1987.

[Paidi05] V. K. Paidi, Z. Griffith, Y. Wei, M. Dahlstrom, M. Urteaga, N. Parthasarathy, M. Seo, L. Samoska, A. Fung, M.J.W. Rodwell, "G-band (140-220 GHz) and W-band (75-110 GHz) InP DHBT medium power amplifiers," *IEEE Trans. Microwave Theory and Techniques*, Vol. 53, No. 2, pp. 598 – 605,Feb. 2005.

[Pardo08] J. R. Pardo, Private communication, 2008.

[Payne88] J.M.Payne, "Multibeam receiver for millimeter-wave radio astronomy," *Rev.Sci.Insrum.*, Vol.59, No.9, pp. 1911-1919, Sep.1988.

[Payne95] J.M.Payne and P.R.Jewell, "The upgrade of the NRAO 8-beam receiver," *ASP Conference Series*, Vol.75, pp. 144-148, 1995.

[Penfield62] P. Penfield and R. P. Rsafuse, Varactor Applications, Harmonic Multipliers. Cambridge, MA: MIT Press, 1962, ch. 8.

[Phillips73] T. Phillips, and K. Jefferts, "A low temperature bolometer heterodyne receiver for millimeter wave astronomy," *Rev. of Sci. Instrum.*, vol.44, no.8, pp.1009-1014, 1973.

[Phillips87] T. G. Phillips, "Techniques of Submillimeter Astronomy," *in Proc. of summer school on millimeter and submillimeter astronomy*, Stirling, Scotland, June 1987.

[Phillips92] T. G. Phillips, and J. Keene, "Submillimeter Astronomy," *Proc. IEEE*, vol. 80, pp. 1662-1678, Nov.1992.

[Phillips02] T. G. Phillips, "The Role of Heterodyne Detection in Future Space Missions," *In the Proceedings of the Far-IR, Sub-MM, and MM Detector Technology Workshop*, J. Wolf, J. Farhoomand and C. Crelght, eds., Montery, CA, pp. 31-37, April 2002.

[Pospieszalski93] M. W. Pospieszalski, "Ultra-low-noise receivers for the 1 to 120GHz frequency range," *in Proc.of 23rd European Microwave Conf.*, Madrid, Spain, pp. 73-79, Sep.1993.

[Pukala08] D. Pukala, L. Samoska, T. Gaier, A. Fung, X. B. Mei, W. Yoshida, J. Lee, J. Uyeda, P. H. Liu, W. R. Deal, and V. Radisic, "Submillimeter-wave InP MMIC amplifers from 300-345 GHz," *IEEE Microwave and Wireless Components Letters*, Vol. 18, No. 1, pp. 61-63, Jan.2008.

[Rabanus02] D. Rabanus, U. U. Graf, S. Heyminck, S. Stanko, and J. Stutzki, "Techniques for Heterodyne Array Receivers," *In Proc. Far-IR, Sub-MM, and MM*

Detector Technology Workshop, J. Wolf, J. Farhoomand and C. Crelght, eds., Montery, CA, pp. 179-182, April 2002.

[Raisanen93] A. V. Raisanen, S. Choudhury, R. J. Dengler, J. E. Oswald, and P. Siegel, "A novel split-waveguide mount design for millimeter and submillimeter-wave frequency multipliers and harmonic mixers," *IEEE Microwave and guided wave letters,* Vol.3, No.10, pp.369-371, Oct.1993.

[Raja01] R. Raja et al., "A 183GHz low noise amplifier module with 5.5 dB noise figure for the conical scanning microwave imager sounder (CMIS) program," in *IEEE MTT-S Intl. Microwave Symp. Digest*, vol.3, pp. 1955-1958, May 2001.

[Richards79] P. L. Richards, T. M. Shen, R. E. Harris, and F. L. Lloyd, "Quasiparticle heterodyne mixing in SIS tunnel junctions," *Appl. Phys. Lett.*, vol. 34, no. 5, pp. 345-347, Mar. 1979.

[Richards94] P. L. Richards, "Bolometers for Infrared and Millimeter Waves," *J.Appli. Phys*, 76, pp. 1-24, 1994.

[Rollin06] J. -M. Rollin, H. Wang, B. Thomas, A. Maestrini and S. Davies, "Integrated Schottky diodes for a Sub-harmonic Mixer at Millimeter Wavelengths," in *proceedings of the 4th ESA Workshop on Millimetre Wave Technology and Applications*, pp. 117-121, Espoo, Finland, February 15-17, 2006.

[Russell95] A. Russell, H. Van de Stadt, B. Hayward and B. Duncan, "JCMT Plans for a Heterodyne Array," *ASP Conference Series*, Vol.75, pp. 179-185, 1995.

[Rutledge83] D. B. Rutledge, D. P. Neikirk, and D.P. Kasilingam, "Integrated-Circuit Antennas," in *Infrared and Millimeter Waves*, Academic Press, Orlando, Vol.10, Chap.2, pp. 1, 1983.

[RPG] http://www.radiometer-physics.de

[Samoska01] L. Samoska, V. Radisic, M. Micovic, M. Hu, P. Janke, and C. Ngo, "InP MMIC Chip set for Power Source Convering 80-170 GHz," in *Proceedings of the 12th International Symposium on Space Terahertz Technology*, paper 11.1, San Diego, CA, Feb.2001.

[Samoska04] L. Samoska, A. Peralta, H. Ming, M. Micovic, and A. Schmitz, "A 20mW, 150GHz InP HEMT Power Amplifier Module," *IEEE Microwave and Wireless Components Letters*, Vol. 14, No. 2, pp. 56-58, Feb.2004.

[Samoska06] L. Samoska, "Towards Terahertz MMIC Amplifiers: Present Status and Trends," in *IEEE MTT-S Intl. Microwave Symp. Digest*, pp. 333-336, Jun.2006.

[Samoska08a] L. Samoska, W. R. Deal, G. Chattopadhyay, D. Pukala, A. Fung, T. Gaier, M. Soria, V. Radisic, X. Mei, and R. Lai, "A Submillimeter-Wave HEMT Amplifier Module With Integrated Waveguide Transitions Operating Above 300GHz," *IEEE Trans. Microwave Theory and Techniques*, Vol. 56, No. 6, pp. 1380-1388, Jun.2008.

[Samoska08b] L. Samoska, D. Pukala, M. Soria, and G. Sadowy, "A G-Band Multi-Chip MMIC T/R Module for Radar Applications," to appear in the *proceeding of the Joint 33th International Conference on Infrared and Millimeter Waves and 16th International Conference of Terahertz Electronics*, Pasadena, CA, Sep.2008.

[Schellenberg07] J. Schellenberg, R.Chedester, and J. McCoy, "Multi-Channel Receiver for an E-band FMCW Imaging Radar," *IEEE MTT-S International Microwave Symposium*, pp.1359-1362, June 2007.

[Schuster00] K. -F. Schuster, J. Blondel, M. Carter, B. Fouilleux, B. Lazareff, F. Mattiocco, F. Morel, A. Perrigouard, and J.-L. Pollet, "The IRAM 230 GHz Multibeam SIS receiver," *in ASP Conference Series,Vol.217:Imaging at Radio through Submillimeter Wavelengths*, pp.25-32, 2000.

[Schuster04] K. -F. Schuster et al. "A 230 GHz Heterodyne Receiver Array for the IRAM 30m Telescope," *A&A 423*, pp.1171-1177, 2004.

[Sequoia] http://www.astro.umass.edu/~fcrao/instrumentation/sequoia/seq.html

[Shi97] S. C. Shi and J. Inatani, "A Waveguide-to-Microstrip Transition with a DC/IF Return path and an Offset Probe", *IEEE Transactions On Microwave Theory And Techniques*, Vol.45, No.3, March 1997.

[Siegel02] P. Siegel, "Terahertz technology," *IEEE Transactions Microwave Theory*

and Techniques, Vol.50, No.3, pp.910-928, Mar.2002.

[Siegel03] P.H. Siegel, "THz Technology: An Overview," *International Journal of High Speed Electronics System,* Vol.13, No.2, pp.351-394, 2003.

[Siegel04] P.H. Siegel, "THz Technology in Biology and Medicine," *IEEE Transactions Microwave Theory and Techniques,* Vol.52, No.10, pp.2438-2448, Oct.2004.

[Siegel06a] P.H. Siegel, and R.J. Dengler, "Terahertz Heterodyne Imaging Part I: Introduction and Techniques," *International Journal of Infrared and Millimeter Waves*, Vol.27, No. 4, pp. 465-480, April 2006.

[Siegel07] P.H. Siegel, "THz Instruments for Space," *IEEE Transactions On Antennas And Propagation,* Vol.55, No.11, pp.2957-2965, November 2007.

[Siles08a] J.V. Siles, *Design and Optimization of Frequency Multipliers and Mixers at Millimeters and Submillimeter-wave Bands*, Ph.D. Dissertation, University Polytechnic of Madrid, April 2008.

[Siles08b] J.V. Siles, "Modeling of UMS-BES Schottky diodes for high frequency MMICs design with ADS", ESA report, Dec.2008.

[Simon93] A. Simon, A. Griib, V. Krozr, K. Beilenhoff, and H. L. Hartnagel, "Planar THz Schottky Diode Based on a Quasi Vertical Diode Structure", *Proc. 4th Int. Symp. Space Terahertz Technol.*, pp, 392-403, 1993.

[SOFIA] http://www.sofia.usra.edu/

[Sunada00] K. Sunada, C. Yamaguchi, N. Nakai, K. Sorai, S. K. Okumura, N. Nakai, and N. Ukita, "Development and First Result from NRAO SIS 25 Beam Array Receiver System (BEARS)," *ASP Conference Series*, Vol.217, pp. 19-22, 2000.

[Tessmann06] A. Tessmann, M. Kuri, M. Riessle, H. Massler, M. Zink, W. Reinert, W. Bronner, and A. Leuther, "A Compact W-Band Dual-Channel Receiver Module," *IEEE MTT-S International Microwave Symposium*, pp. 85-88, June 2006.

[Tessmann07] A. Tessmann, A. Leuther, H. Massler, W. Bronner, M. Schlechtweg, and G. Weimann, "Metamorphic H-band low noise amplifier MMICs," in *IEEE MTT-S Intl. Microwave Symp. Digest*, pp. 353-356, June 2007.

[Thomas04] B. Thomas, *Etude et réalisation d'une tête de reception heterodyne en ondes submillimétriques pour l'étude des atmospheres et surfaces de planètes*, Ph.D.Dissertation, Université Pierre et Marie Curie – Paris6, December 2004.

[Thomas05] B.Thomas, A. Maestrini and G. Beaudin, "A Low-Noise Fixed-Tuned 300-360 GHz Sub-Harmonic Mixer Using Planar Schottky Diodes", *IEEE Microwave and Wireless Components Letters*, vol.15, no.12, pp.865-867, December 2005.

[Thomas08a] B. Thomas, A. Maestrini, D. Matheson, I. Mehdi, and P. de Maagt, "Design of an 874GHz Biasable Sub-Harmonic Mixer Based on MMIC Membrane Planar Schottky Diodes," to appear in the *proceeding of the Joint 33th International Conference on Infrared and Millimeter Waves and 16th International Conference of Terahertz Electronics*, Pasadena, CA, Sep.2008.

[Thomas08b] B. Thomas, J. Treuttel, B. Alderman, D. Matheson and T. Narhi, "Application of transferred substrate to a 190 GHz doubler and 380 GHz mixer using MMIC foundry Schottky diodes," to appear in the *proceedings of the SPIE conf. on Astronomical Instrumentation*, Marseille, France, June 2008.

[Thomas08c] B. Thomas, B. Alderman, D. Matheson and P. de Maagt, "A Combined 380 GHz Mixer/Doubler Circuit Based on Planar Schottky Diodes", *IEEE Microwave and Wireless Components Letters*, vol.18, no.5, pp.353-355, May 2008.

[Tucker79] J. Tucker, "Quantum limited detection in tunnel junction mixers," *IEEE J. Quant. Electron.*, vol. 15, no. 11, pp. 1234-1258, 1979.

[UMS] UMS – MMIC foundry – BES Design Manual, Version 1.0, Orsay, France, 1998.

[VDI] Virginia Diodes: http://www.virginiadiodes.com/

[Vukusic06] J. Vukusic, B. Alderman, T.A.Emadi, M.Sadeghi, A. O. Olsen,

T.Bryllert, and J.Stake, "HBV tripler with 21% efficiency at 102 GHz", *Electronics letters*, vol.42, no.16, pp.355-356, March 2006.

[Vukusic07] J. Vukusic, T. Bryllert, T. A. Emadi, M. Sadeghi, and J. Stake, "A 0.2-W Heterostructure Barrier Varactor Frequency Tripler at 113 GHz", *IEEE Electron Deveice Letters*, vol.28, no.5, pp.340-342, May 2007.

[Walker02] C. K. Walker, C. Groppi, C. Drouet d'Aubigny, C. Kulesa, A. Hedden, D. Prober, I. Siddiqi, J. W. Kooi, G. Chen, and A. W. Lichtenberger, "Integrated Heterodyne Array Receivers for Submillimeter Astronomy" *Proceedings of SPIE, Astronomical Telescopes and Instrumentation*, 2002.

[Wang01] H. Wang, L. Samoska, T. Gaier, A. Peralta, H. H. Liao, Y. C. Leong, S. Weinreb, Y. C. Chen, M. Nishimoto, and R. Lai, "Power Amplifier Modules Convering 70-113 GHz Using MMICs," *IEEE Trans. Microwave Theory and Techniques*, Vol. 49, No. 1, pp. 9-16, Jan.2001.

[Waters93] J. W. Waters, L. Froidevaux, W. G. Read, G. L. Manney, L. S. Elson, D. A. Flower, R. F. Jarnot, and R. S. Harwood, "Stratospheric CIO and ozone from the microwave limb sounder on the upper atmosphere research satellite", *Nature*, vol.362, pp. 597-602, Apr.1993.

[Weinreb88] S. Weinreb et al., "Cryogenic, HEMT, Low-Noise Receivers for 1.3 to 43 GHz Range," *in Proc. NTT-S Int. Microwave Symp.*, New York, pp. 945-948, 1988.

[Weinreb99] S. Weinreb, T. Gaier, R. Lai, M. Barsky, Y. C. Leong, and L. Samoska, "High-gain 150-215 GHz MMIC amplifiers with integral waveguide transitions," *IEEE Microwave and Guided Wave Lett.*, Vol. 9, No. 7, pp. 282-284, July 1999.

[Williams07] B.S. Williams, "Terahertz quantum-cascade laser", *Nature photonics*, Vol.1, pp. 517-525, Sep.2007.

[Xiao04] Q. Xiao, Y. Duan, J. L. Hesler, T.W. Crowe, and R. M. Weikle, II, "A 5-mW and 5% efficiency 210 GHz InP-based heterostructure barrier varactor quintupler," *IEEE Microw. Wireless Comp. Lett.*, vol. 14, no.4, pp. 159–161, Apr. 2004.

[Xiao05] Q. Xiao, J. Hesler, T. Crowe, R. Weikle, II, Y. Duan, and B. Deaver, "High efficiency heterostructure-barrier-varactor triplers using AlN substrates," in *IEEE MTT-S Int. Dig.*, pp.443–446, Long Beach, CA, Jun. 2005.

[Xiao07] Q. Xiao, J. L. Hesler, T. Crowe, B. S. Deaver, Jr. and R. M. WeikLe II, "A 270-GHz Tuner-less Heterostructure Barrier Varactor Frequency Tripler", *IEEE Microwave and Wireless Components Letters*, vol.17, no.4, pp.241-243, April 2007.

[Yamaguchi00] C.Yamaguchi, K.Sunad, Y.Iizuka, H.Iwashita, and T.Noguchi, "Design of the Focal Plane Array Receiver for the NRO 45-m Telescope," *in Proc. SPIE*, "Radio Telescope", Vol. 4015, pp. 614-623, 2000.

[Yngvesson83] K. S. Yngvesson, "Near-Millimeter Imaging with Integrated Planar Receptors: General Requirements and Constraints," in *Infrared and Millimeter Waves (K. J. Button, Ed.),* Vol. 10, pp. 91, 1983.

[Yngvesson88] K. S. Yngvesson, J. F. Johansson, Y. Rahmat-Sami, and Y. S. Kim, "Realizable feed-element patterns and optimum aperture efficiency in multibeam antenna systems," *IEEE Transactions On Antennas And Propagation,* Vol.36, pp.1637-1641, 1988.

[Zmuidzinas04] J. Zmuidzinas and P. L. Richards, "Superconducting detectors and mixers for millimeter and submillimeter astrophysics," in *Proc. IEEE*, vol. 92, no. 10, pp. 1597-1616, Oct. 2004.

[Zmuidzinas07] J. Zmuidzinas, "Technology for Submillimeter Astronomy," in *IEEE MTT-S Int. Microwave Symp. Dig.*, pp. 1861-1864, Honolulu, HI, June 2007.

List of Figures

171

174

List of Tables